EXPERIMENTAL SEARCH FOR TOROIDAL HIGH-SPIN ISOMERS IN COLLISIONS OF ^{28}Si + ^{12}C AT 35 MEV/NUCLEON USING FAUST

A Thesis

by

ANDREW J. HANNAMAN

Submitted to the Graduate and Professional School of
Texas A&M University
in partial fulfillment of the requirements for the degree of

DOCTOR OF PHILOSOPHY

Chair of Committee,	Sherry J. Yennello
Committee Members,	Charles M. Folden III
	Che-Ming Ko
	Xin Yan
Head of Department,	Simon North

May 2023

Major Subject: Chemistry

ABSTRACT

Ground state stable nuclei typically have spherical geometries but may exhibit exotic shapes and form α-particle clusters within their bulk if given excitation energy and/or angular momentum. It is predicted that such clustering can promote the production of angular-momentum stabilized toroidal nuclei. Previously, an experiment was performed using the NIMROD detector array where high-excitation energy peaks were observed in the 7-α particle disassembly of ^{28}Si in collisions of ^{28}Si + ^{12}C at 35 MeV/nucleon; these peaks were attributed to the breakup of toroidal high-spin isomer states. However, the angular resolution of NIMROD is determined by the size of the individual silicon detectors, giving large uncertainties when reconstructing the excitation energy of the fragmenting source. This motivated the present work, where these collisions were measured with improved angular resolution using the Forward Array Using Silicon Technology (FAUST). FAUST is equipped with resistive dual-axis duo-lateral (DADL) position-sensitive silicon detectors capable of sub-millimeter position resolution. Due to the detector charge-splitting mechanism, position dependence of the measured energy as well as distortions in calculated particle positions were observed when using conventional signal processing electronics. A charge determination method has been developed that greatly minimizes these distortions. The performance and response of the array was characterized in detail to accurately predict the expected resolution of measuring narrow resonances. The measured excitation energy distributions for 7- and 8-α disassembly events showed no strong evidence for highly excited states, in contradiction with the NIMROD experiment. Further investigation of collision properties that lead to these exit channels revealed challenges in isolating clean projectile-mass decays, where many 7-α events do not originate from a single ^{28}Si source. A statistical likelihood analysis was performed to determine the sensitivity of the present measurement for confidently determining resonant yield, providing an upper limit to toroidal high-spin isomer cross section as a function of the excitation energy and width of potential states.

DEDICATION

To Cierra and Archie

ACKNOWLEDGMENTS

I must first thank my wife, Cierra, for the incredible amount of patience, love, and support she has shown me over these years. I would also like to thank my son, Archie, for giving me a constant source of inspiration and motivation since he joined the world. I will be forever grateful to Prof. Sherry J. Yennello for giving me the freedom, support, and guidance to explore and pursue my scientific interests to my heart's content. I must thank Dr. Kris Hagel for introducing me to the subject of this work, and for the incredible amount of help he has given me over these years. From finding bugs in my code, to aiding in the physical and mental labor of experimental design, setup, execution, and analysis; there was never a dull moment thanks to his stories, camaraderie, and positive, reassuring attitude. I would also like to thank Dr. Alan McIntosh for both his immense aid and involvement in all aspects of this work, and his guidance in improving my nuclear science intuition, communication, and analytical skills. I'll miss the multi-hour meetings in his office bouncing ideas back and forth. I also must thank Dr. Joseph Natowitz for his support, feedback, and investment in this work. Thanks to Davis Winchester for being a great friend, challenging me to think critically about more than just science, and for helping take care of Archie. Thank you to Bryan Harvey for devoting so much time to this work, both out of his passion for good science and the goodness of his heart. To that end, thanks Maxwell Sorensen, Austin Abbott, and Zachary Tobin for being a crucial part of my entire graduate experience. The growing pains of learning the breadth of skills required for this work was eased by being surrounded by such brilliant and fun people. Thank you to Travis Hankins for being a sounding board and for providing excellent editorial feedback. Thank you to my parents for the unending support they have always shown me — and thank you to my Dad for both brainstorming solutions to the many challenging puzzles of this work and for planting the seed of pursuing a Ph.D. Thanks are also due for Dr. George Kim, Dr. Brian Roeder, and Dr. Henry Clark for the excellent beam quality and flexible scheduling of the many experiments.

CONTRIBUTORS AND FUNDING SOURCES

Contributors

This work was supported by a dissertation committee consisting of Professors Sherry Yennello, Charles M. Folden III, and Xin Yan of the Department of Chemistry and Professor Che-Ming Ko of the Department of Physics.

Experimental data was collected with the help of the SJY group at the Cyclotron Institute. The AMD simulation data in Section 5.1 was provided by Bryan Harvey of the Department of Physics at Texas A&M University. The analyses conducted in Sections 4.1.3 and 5.7 were also developed and executed in part by Bryan Harvey.

All other work conducted for the dissertation was completed by the student independently.

Funding Sources

This work was made possible by support from the Department of Energy (DE-FG02-93ER40773) and the Robert A. Welch Foundation (A-1266). No other outside source of funding was provided.

TABLE OF CONTENTS

Page

LIST OF FIGURES

LIST OF TABLES

TABLE Page

1. INTRODUCTION AND MOTIVATION

1.1 α-particle Clustering in Nuclear Matter

The existence of clustering in complex systems spans many fields of study, from the clustering of stars and galaxies to the clustering of humans into groups. In all cases, there is some driving force for clustering, whether to minimize the potential energy of the system or for some evolutionary advantage. In the case of atomic nuclei, the formation of clusters can, under certain circumstances, favorably increase the binding energy and total stability of the nucleus. Gamow's theory of $\alpha(^4\text{He})$-decay proposed that α-particles may exist preformed within nuclei prior to decay; using this idea, general trends in α-decay half-lives were well reproduced by treating the process as repeated collisions between preformed α-particles and the Coulomb barrier with each collision having a given probability of tunneling through [18]. This notion naturally fueled the study of clustering within atomic nuclei where primary interactions are between clusters of tightly bound protons and neutrons. α-particles are the most promising candidate for clustering due to their high binding energy and high energy of its first excited state; these ensure that α-particle sub-units can persist in nuclei under both normal and extreme conditions [19]. An α-cluster model of nuclei was developed to explore the idea that ground state nuclear matter may spend some time in this configuration [20]. Hafstad and Teller also observed a linear correlation between the binding energy of α-conjugate nuclei and the number of available α-α nuclear "bonds" [21]. Later, Pauling studied and produced a cluster model of nuclei incorporating the shell model that further developed the idea of clustered nuclear structure [22]. While these earlier models suggested the existence of clustering in the ground state of nuclei, it was later proposed that the cluster degree of freedom is only liberated at excitation energies close to the decay threshold as depicted in the Ikeda diagram of Figure 1.1 [23, 24, 25]. In essence, the internal energy of the nucleus must be sufficient to account for the mass difference between the unclustered and

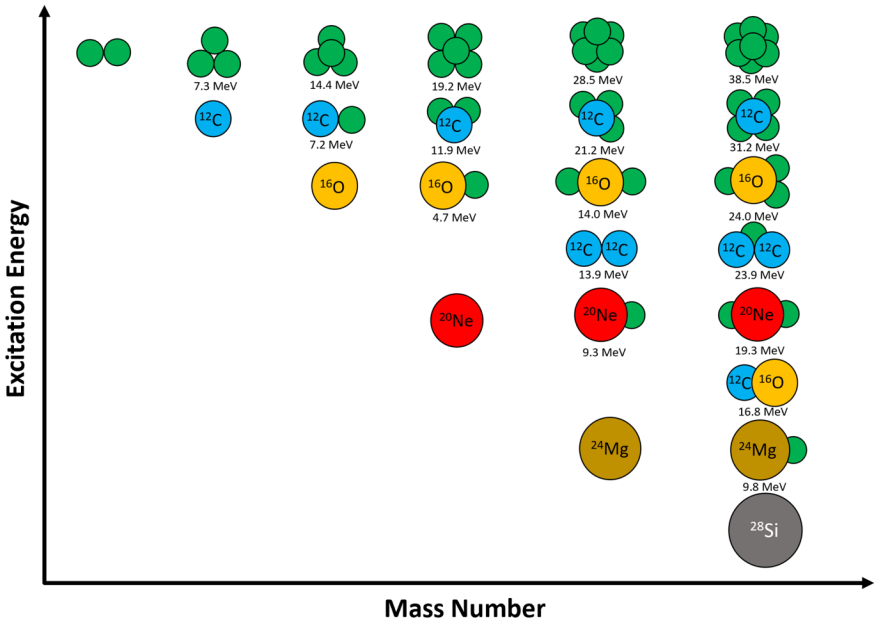

Figure 1.1: Ikeda Diagram for α-conjugate nuclei from ^{8}Be to ^{28}Si showing the relationship between excitation energy, mass number, and α-clustering structures. The quoted excitation energies for each clustering configuration is approximated as the Q-value between the parent nucleus and the constituent clusters. Location of clustered nuclei is relative.

clustered nucleus. While both of these theoretical approaches are oversimplified, experimental evidence and theoretical descriptions exist for clustering in both the ground and excited state [26, 27].

One of the most extensively studied examples of excited state clustering in nuclear physics is the Hoyle state of ^{12}C due to the triple-α process in nucleosynthesis [28]. This state lies only $\sim$380 keV above the 3α decay threshold and is generally believed to consist of α-particle clusters where α-particle degrees of freedom dominate over individual nucleon degrees of freedom. One way that such particle-unbound states are observed experimentally is by measuring the momentum vectors of the decay products - in this case three α-particles. The excitation energy of the decay is then calculated by summing all decay product kinetic

energies in the center-of-mass frame and subtracting the Q-value:

$$E_x = \sum_{i=1}^{M_{dp}} KE_{dp}^{com}(i) - Q \tag{1.1}$$

where M_{dp} is the decay product multiplicity, KE_{dp}^{com} is the center-of-mass kinetic energy of each decay product, and Q is the energy released in the breakup. Many experiments aim to optimize the angular granularity and energy resolution of the employed detector apparatus to reduce uncertainties in the excitation energy calculation. One such experiment utilized double-sided strip detectors (DSSD) to afford the resolution necessary for better constraining the branching ratio between sequential (^{12}C* $\rightarrow$ ^{8}Be g.s. + α) and direct (^{12}C* $\rightarrow 3\alpha$) decay of the Hoyle state as shown in Figure 1.2 [1]. The experiment was designed to significantly suppress the background associated with uncorrelated α-particles, although in many cases the background can be a significant contribution that must be accurately accounted for to extract state properties.

The Hoyle state has long been understood as a dilute, weakly coupled system of three α-particles held together by the Coulomb barrier; from this gas-like description emerges the idea of an s-wave α-particle orbiting an s-wave ^{8}Be. Fully microscopic parameter-free calculations using this description reproduced all known properties of the Hoyle state at the time [29, 30]. This remained the common understanding of near-threshold α-clustering until it was demonstrated that a nuclear liquid can undergo a phase change at sub-saturation density ($\sim\frac{\rho_0}{5}$ - $\frac{\rho_0}{3}$) in which the α-particle bosons all occupy the ground state, giving a nuclear Bose-Einstein condensate [31]. This has led to efforts in expanding the 3-α Hoyle-condensate description in search of heavier N-α analogue states, with a strong focus on discriminating simultaneous N-α emission expected of a clustered condensate state from sequential evaporative emission [32, 33, 34]. Accurately determining the mechanism of α-particle disassembly for heavier N-α systems demands stringent detector requirements to afford the angular granularity, angular resolution, and energy resolution needed. While a

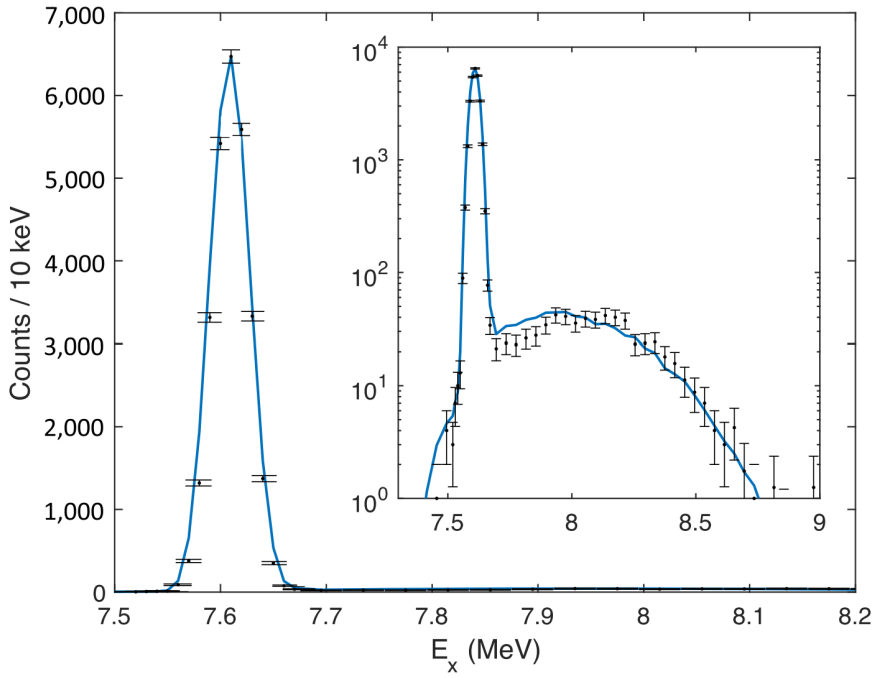

Figure 1.2: ^{12}C excitation energy distribution calculated from 3α decays. The α-particles were measured across six separate double-sided strip detectors to afford the angular granularity needed for the measurement (42 keV FWHM for the Hoyle state). The log-scale inset better shows the small background contribution. A likelihood analysis was performed to give confidence intervals on the sequential-direct branching ratio. Reprinted from [1].

significant focus of condensate state studies is of near-threshold breakups into constituent α-particles, Fermi-energy nuclear collisions provide a unique environment where a wide range of nuclear densities, temperatures, and deformations are accessed [35]. In the early stages of these more violent collisions, α-clustering properties may play a role in determining how nuclear matter arranges itself into clusters, affecting the collision dynamics and reaction exit channels [9]. Additionally, it is possible for exotic clustering states to be produced in such environments; however, isolating experimental observables that are sensitive to this production is difficult [36]. Further study of the interplay between the complex reaction dynamics in Fermi energy collisions and nuclear clustering is needed.

1.2 Toroidal High-Spin Isomers

1.2.1 Theoretical Framework

Ground state stable nuclei typically have spherical geometries. The first evidence of deviation from sphericity emerged when the quadrupole moments of ^{151,153}Eu were more than an order of magnitude greater than that attainable by single nucleon motion, suggesting a collective deformation [37]. This evidence sparked the pioneering work by Bohr, Mottelson, Nilsson, Rainwater, and Wheeler to develop a nuclear model that accounted for the relationship between individual-particle and collective motion consistent with observed phenomena; Bohr, Mottelson, and Rainwater won the Nobel Prize for these efforts in 1975 [38, 39, 40, 41]. Nuclear deformation was required to resolve the existence of rotational bands as collective rotation about a symmetric sphere is quantum mechanically forbidden. With the emergence of the shell model, Nilsson calculated how the single particle potentials changed as a function of quadrupole deformation, giving rise to new shell closures at certain deformation values [42]. A Nilsson diagram illustrating this relationship for ^{24}Mg is shown in Figure 1.3. While most observed phenomena could be explained by rather simple deformations (e.g., prolate, oblate), Wheeler considered the implications and feasibility of a toroidal deformation under certain conditions [43].

Wong, a student of Wheeler, expanded considerably on the idea, performing calculations to predict the stability conditions and structure properties for a range of nuclei using numerous models. In earlier work, Wong predicted toroidal states in the $40 \leq A \leq 70$ and $A \leq 250$ mass range where large shell effects in light nuclei and large Coulomb energies in heavier nuclei are advantageous for toroid stability [44, 45]. Analogous to the Nilsson diagram of Figure 1.3, large energy gaps were observed in the single particle potentials as a function of the toroidal deformation parameter R/d, where R is the major radius and d is the minor radius of the toroid. A modified liquid drop model including rigid body rotation was then used to predict what angular momentum would be necessary to form a stable toroid as a function

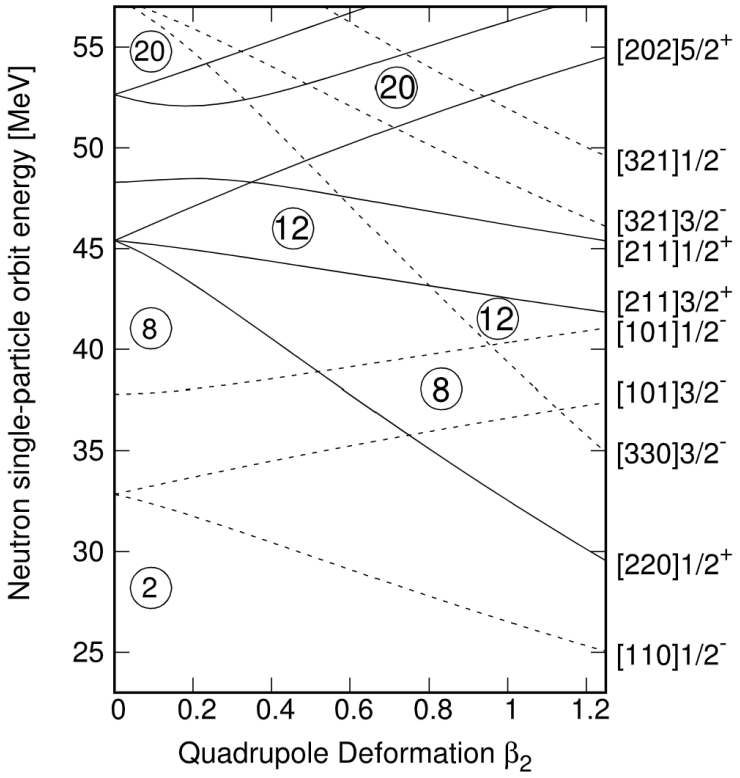

Figure 1.3: Nilsson diagram of neutron single-particle energies as a function of quadrupole deformation parameter β_2 for ^{24}Mg. Shell closures indicating the number of nucleons are given by the circled numbers alongside the negative (dashed) and positive (solid) parity orbitals. Reprinted from [2].

of nuclear mass (Figure 1.4) [3]. While the assumptions made in this calculation are rather stringent, it showed that the basic gross forces relevant to nuclear stability could support the existence of a toroidal nucleus over a large range in nuclear mass if given enough angular momentum. The stability of a nuclear toroid can be intuitively understood by comparison to a liquid toroid, where the rotational energy (and Coulomb energy) tends to expand the toroid and the attractive forces of the liquid (nuclear) bulk tend to contract the toroid. However, as nuclei are quantum mechanical systems, this collective rotation is forbidden. In reality, the total angular momentum of the toroid comes from the alignment of the individual nucleon angular momentum along the symmetry axis, inducing strong circulating currents as shown in panel (b) of Figure 1.5 [46, 5]. While the internal structure of this single-particle

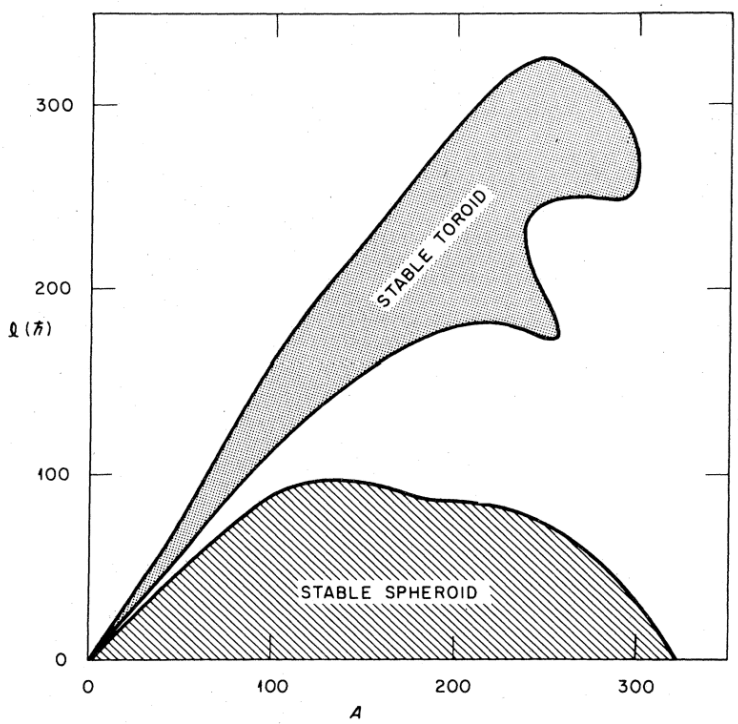

Figure 1.4: Angular momentum as a function of mass number for nuclei along the β-stability line. Regions of stable toroid and spheroid configurations are calculated using a modified liquid drop model with rigid-body rotation and are indicated by the shaded regions. Reprinted from [3].

rotation is significantly different from collective rotation, their behavior is similar [47]. Wong has proposed two ways to populate such states experimentally: having a smaller projectile punch-through a larger target nucleus at small impact parameters, or populating the excitation energy and angular momentum of a toroidal state through deep inelastic heavy-ion collisions as shown in panel (a) of Figure 1.5. The former poses challenges when using charged-particle spectroscopy for such studies, as the low energy target-like toroidal breakup particles are difficult to measure and identify. Consequently, experimental efforts to produce and study toroidal nuclei primarily use the latter method as discussed in Section 1.3.2.

1.2.2 Predictions for Intermediate Mass α-Conjugate Nuclei

In recent years, a number of powerful models have been used to further predict the properties and stability of toroidal nuclei. Staszczak and Wong used a cranked self-consistent

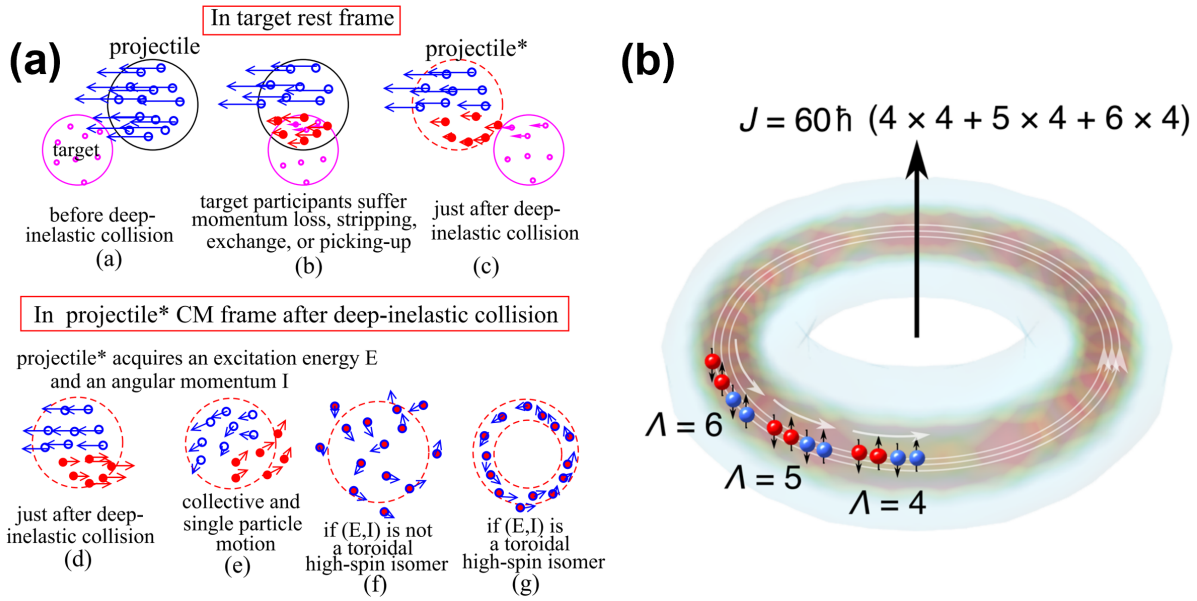

Figure 1.5: Toroidal state production and angular momentum mechanisms. Panel (a): Schematic showing the mechanism for toroid production in deep inelastic heavy-ion collisions. Panel (b): Total angular momentum of an axially-symmetric nuclear toroid. The Λ values correspond to the orbital angular momentum of each individual nucleon, giving a total angular momentum of $60\hbar$. Panel (a) reprinted from [4]. Panel (b) reprinted from [5].

Skyrme-Hartree-Fock calculation to generalize the possible existence of stable toroid configurations in the $28 \leq A \leq 52$ mass region for N=Z nuclei [6]. It was found that for a given quanta of angular momentum, the density configuration of a spherical nucleus would spontaneously take on a toroidal shape as the quadrupole moment constraint was decreased. These toroidal configurations emerge as local minima in the calculated excitation energy as a function of the quadrupole moment as shown for ^{28}Si and ^{32}S in Figure 1.6. This study was even extended to non α-conjugate nuclei in the same mass range, showing similar predicted toroidal isomer properties as their α-conjugate counterparts [48].

In 2018, experimental evidence for toroidal states in the 7-α breakup of ^{28}Si was reported (discussed in Section 1.3.2), fueling interest in being able to predict and replicate the observed properties a priori [49]. Covariant density functional theory (CDFT) using the PC-PK1 and

DD-ME2 density functionals replicated the previous prediction of the $44\hbar$ state in ^{28}Si, as well as finding additional states (local energy minima) for other values of angular momentum [7, 11]. It was also found that the predicted width in the torus geometrical cross section is similar to the width of an α-particle. An α-localization function was used to confirm the minimum necessary conditions for α-clustering in the predicted high spin states as shown in Figure 1.7. The roughly linear correlation between the angular momentum and excitation energy is consistent with the picture of single-particle angular momentum alignment behaving similarly to collective rotation [50]. A separate phenomenological mean field calculation studied the validity of stabilized exotic deformations in the intermediate mass region, suggesting stability of toroidal geometries for both ^{28}Si and ^{32}S [51]. Using a different approach, Zheng and Bonasera developed and employed a semi-classical α-cluster model to predict experimental signatures of spin-induced toroidal α-breakup of ^{28}Si [16]. Unlike the static nature of CDFT, the time evolution of toroidal breakup and the effect of classical fluctuations was explored

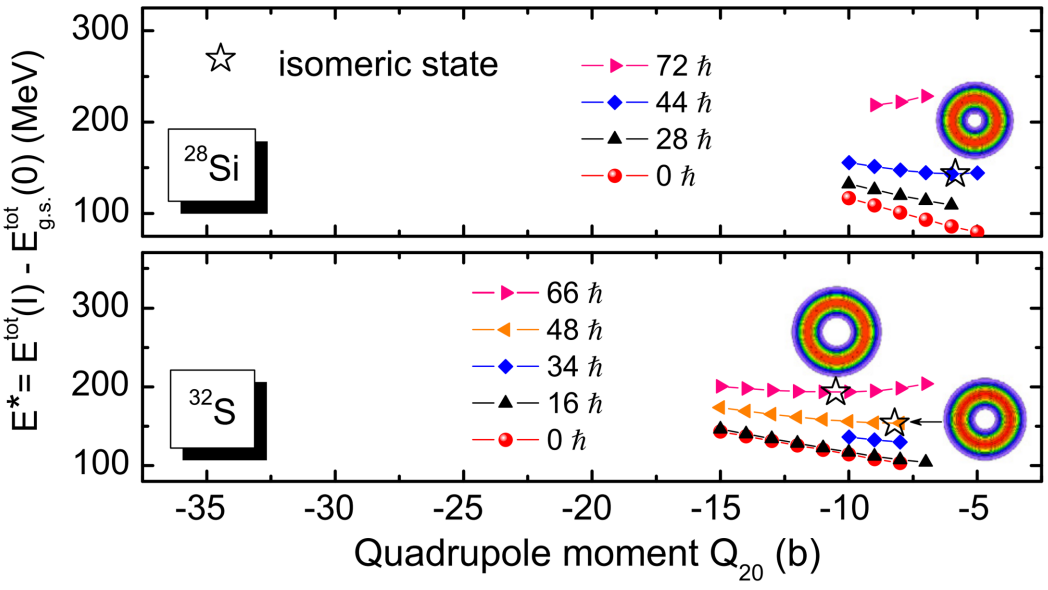

Figure 1.6: Toroidal state predictions in ^{28}Si and ^{32}S using cranked Skyrme-Hartree-Fock model calculations. Excitation energy is given as a function of the quadrupole deformation for different quanta of angular momentum. Minima in the excitation energy curves correspond to toroidal states. Modified and reprinted from [6].

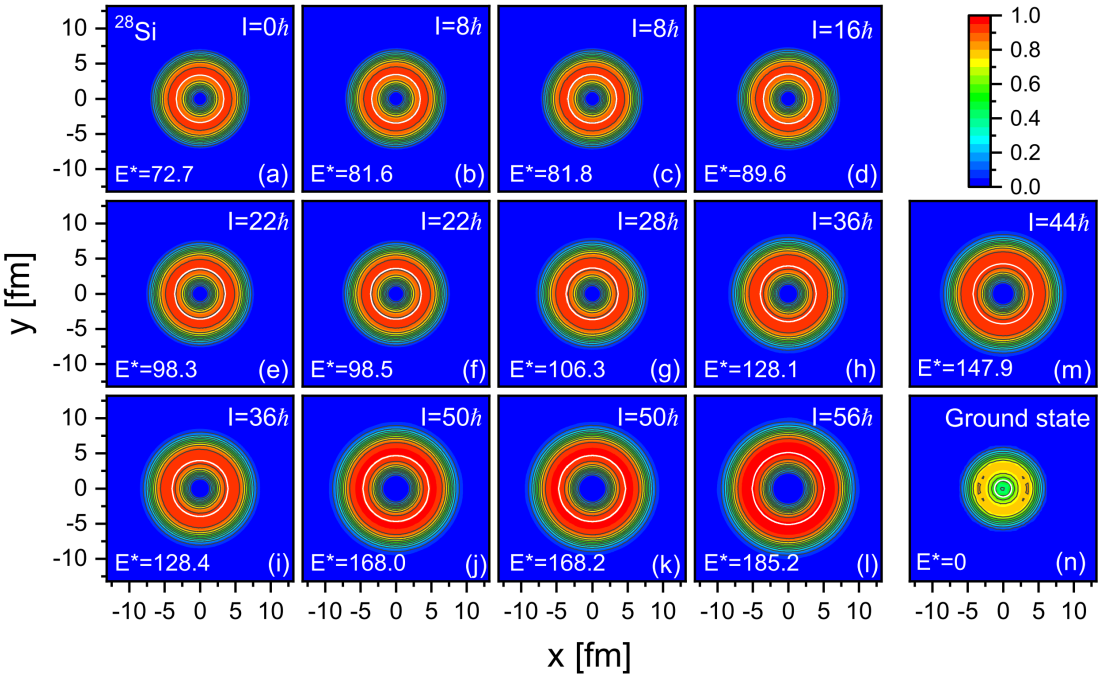

Figure 1.7: Toroidal state predictions in ^{28}Si using covariant density functional theory. α-localization distributions in the toroidal plane are given for predicted states in the spin range of $0\hbar$ to $56\hbar$. Reprinted from [7].

in this work. It is important to note that this work differed from previous calculations in that it did not inherently predict static toroid stability, instead averaging over many 7-α decay channel simulations to observe toroidal breakup geometries under set angular momentum conditions. These model calculations resulted in increased broadening of the excitation energy distributions with increasing angular momentum due to event averaging and classical fluctuations, suggesting that states can only be resolved in the lower spin (and lower excitation energy) regime where distributions do not significantly overlap.

While these predictions suggest that toroidal nuclear geometries are possible under the right conditions, it is important to consider which de-excitation pathways are probable. Experiments designed to search for toroidal nuclei using charged particle spectroscopy must be designed to efficiently and accurately measure such decay pathways. Given the success of the liquid drop model in reproducing many general properties of nuclear matter, it is natural

to look at macroscopic fluid toroid behavior to gain insight to nuclear toroid behavior [52]. It is known that fluid toroids experience Plateau-Rayleigh instabilities that can cause symmetric breakup into smaller fragments of similar size [53, 54]. The number of breakup fragments and finer details of the breakup mode time evolution depends on the rotational energy and aspect ratio [55]. However, properties unique to nuclear matter not accounted for in the macroscopic fluid analogue cannot be ignored; these include shell effects, Coulomb forces, clustering, decay fragment binding energies, and the discrete nature of nucleons. For example, Wong found that the liquid-drop type instabilities predicted for some toroidal nuclei are counteracted by large shell effects, giving toroidal shell closures [45]. Another study found that the theorized shell structure of hyperheavy (Z $\approx$ 130-180) nuclei may stabilize the toroidal configuration to breathing and sausage deformations [56]. Of course, further theoretical support is needed to better understand dominant breakup modes for lighter nuclei. Given the very high excitation energies ($\sim$150 - 200 MeV) of predicted states in the intermediate mass regime of Figure 1.6 and the predicted aspect ratio and density providing an environment conducive to α-clustering, complete α-particle disassembly is a promising exit channel to search for such states. The existence of these high-spin toroidal isomers would be the first occurrence of a distinct nuclear resonant state this high in excitation energy as this region is well described as a continuum of states.

1.3 Experimental Efforts

Experimental efforts to better understand high multiplicity breakups of excited nuclei are challenging due to the strict angular coverage, resolution, and granularity requirements of the detector apparatus for measuring all reaction products accurately. The high granularity and angular coverage requirements necessitate a large number of detector active areas covering a large solid angle. When aiming to optimize both the resolution and granularity, the cost and complexity of such setups can be prohibitive. While some arrays use many single-pad silicon detectors [57, 58, 59, 60], others utilize DSSDs [61, 62] to afford the granularity and angular resolution necessary for such measurements. As a result, only a handful of detector

arrays are suited for studying the α-particle disassembly of intermediate mass nuclei. Section 1.3.1 discusses some work in further characterizing the nature of high multiplicity α-conjugate decay channels of α-conjugate systems, while Section 1.3.2 is focused on the effort to measure and identify the toroidal breakup of nuclei.

1.3.1 α-Conjugate Disassembly in α-Conjugate Systems

Using the CHIMERA detector array, collisions of ^{40}Ca + ^{12}C at 25 MeV/nucleon were studied to gain a deeper understanding of both α-disassembling decay mechanisms and the temperature and density conditions necessary for α-clustering [8, 58]. In this work, focus was placed on analyzing measured exit channels containing the total mass of the projectile (A = 40) consisting of only α-particles and a heavier α-conjugate residue. The α-particles present in each event were treated as if coming from the same α-disassembling source. In doing so, the center-of-mass frame kinetic energy spectra showed thermal characteristics as shown for N-α = 7 on the right of Figure 1.8. Determining the mechanism for these α-disassembly events is challenging, as information about the time evolution of the decay

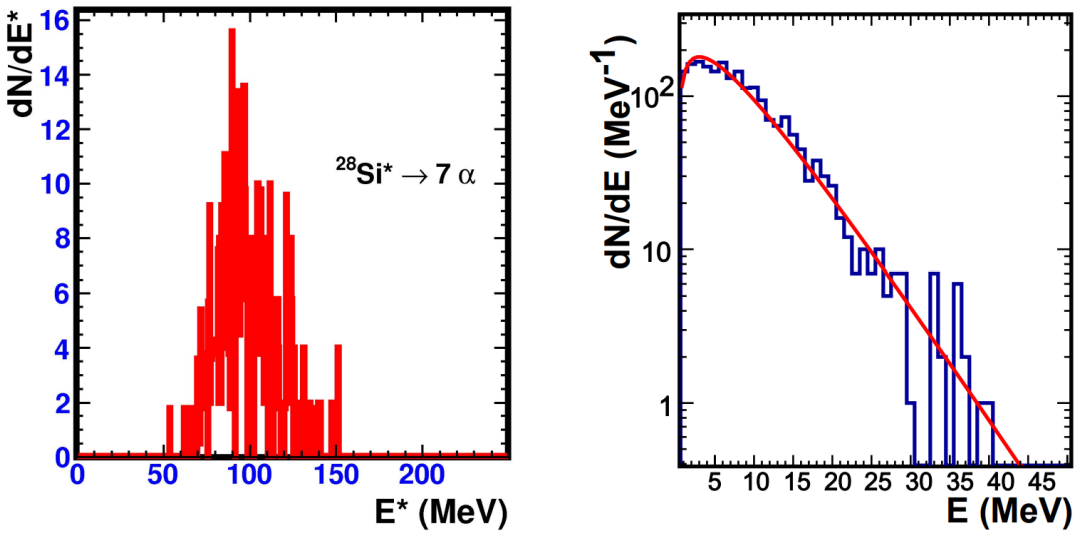

Figure 1.8: Excitation energy distribution (left) and center-of-mass α-particle kinetic energy spectra (right) for events with seven measured α-particles in collisions of ^{40}Ca + ^{12}C at 25 MeV/nucleon. A Maxwell-Boltzmann is fit to the data on the right. Reprinted from [8].

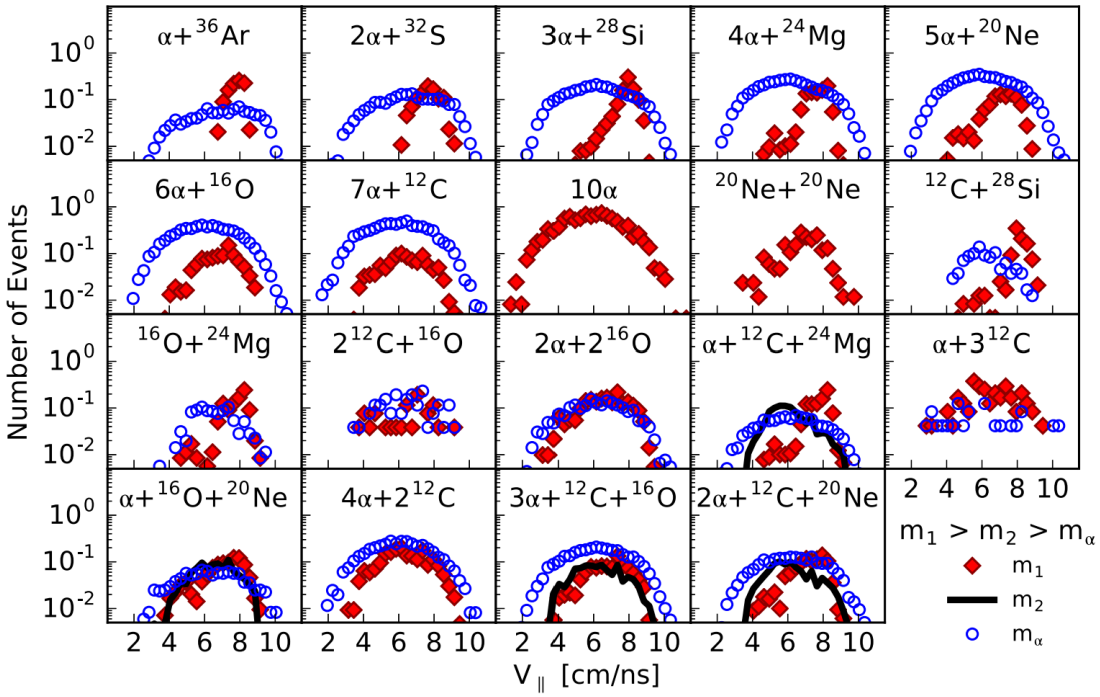

Figure 1.9: Parallel velocity distributions for α-conjugate exit channels in ^{40}Ca + ^{40}Ca at 35 MeV/nucleon. The hierarchy effect, where the heavier fragment parallel velocity is greater than the lighter fragments, is seen in each channel. Reprinted from [9].

must be ascertained from the final state momenta of the decay particles. In this work, two methods were used for distinguishing between simultaneous and sequential decay mechanisms. First, two models were employed that simulated the two extreme decay mechanisms and compared to experimental results. Model-dependent avenues must be interpreted with caution, as the input parameters can greatly influence the resulting signature. Nevertheless, better agreement was found with the simultaneous decay code. To further support the claim, Maxwell-Boltzmann distributions using two different pre-exponential factors (said to be sensitive to the mechanism of decay) were fit to the center-of-mass frame kinetic energy spectra as in Figure 1.8. While other work indicates that this observable is likely not sensitive to the pre-exponential factor, a fully simultaneous decay mechanism was claimed [63]. These conclusions highlight the need for further characterization and study of such decays.

In a separate study, collisions of ^{40}Ca + ^{40}Ca at 35 MeV/nucleon using the NIMROD

array were studied to consider how collision dynamics influence α-conjugate reaction channel yields and properties [9, 60]. The velocity distributions of measured α-conjugate channels with total event mass equal to the projectile revealed that such exit channels are heavily influenced by fragments produced in the early stages of the collision. It was proposed that the low density neck formed between the projectile and target provides a favorable environment for α-clustering. As a result, the α-particle parallel velocity distributions show a hierarchical effect, where lighter α-conjugate fragments are slower than heavier fragments as shown in Figure 1.9. This may indicate that, even for the qualitatively symmetric 10-α disassembly events in this work, there may be two distinct sources of production for some fraction of events. It is important to be mindful that such events may contaminate the background when attempting to select clean projectile decay samples in the search for toroidal breakups.

1.3.2 Toroidal Breakup of Nuclei

While the idea of a toroidal nucleus dates back as far as 1950, experimental evidence for their existence spans a more recent history. A systematic study in 1997 of central ^{86}Kr + ^{93}Nb collisions from 35 to 95 MeV/nucleon revealed macroscopic observables consistent with toroidal breakups. The presented evidence relied heavily on the liquid-drop description

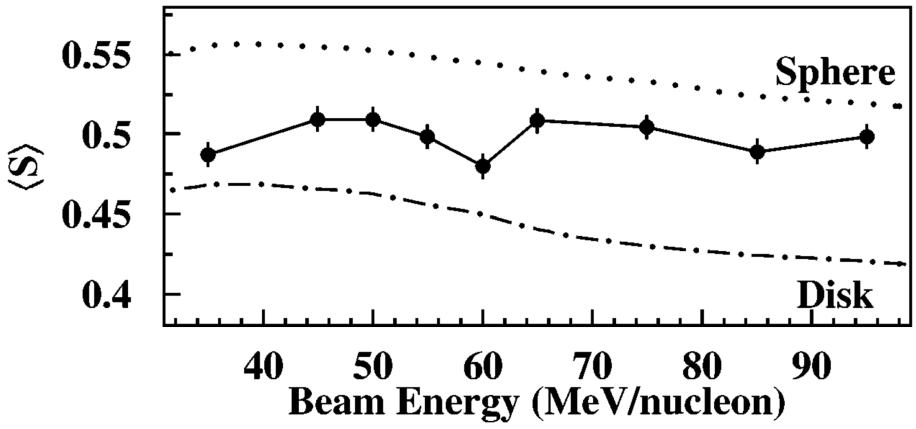

Figure 1.10: Mean sphericity as a function of incident beam energy in collisions of ^{86}Kr + ^{93}Nb from 35 to 95 MeV/nucleon. Reprinted from [10].

of a toroidal nucleus in which instabilities will favor fragmentation into many small, similarly massed sub-units in a disk-like geometry. There was an increase in the light charged particle multiplicity and particle mass similarity starting at 60 MeV/nucleon. Additionally, momentum shape analysis showed a moderate increase in the disk-like nature of breakups as seen in Figure 1.10. While these observables suggest a possible enhancement of toroidal breakup geometries, this measurement lacked the angular resolution necessary for studying the excitation energy of such breakups in detail.

The first experimental evidence for toroidal high-spin isomers consistent with the work of Staszczak and Wong – and the primary motivation for this work – came from an experiment

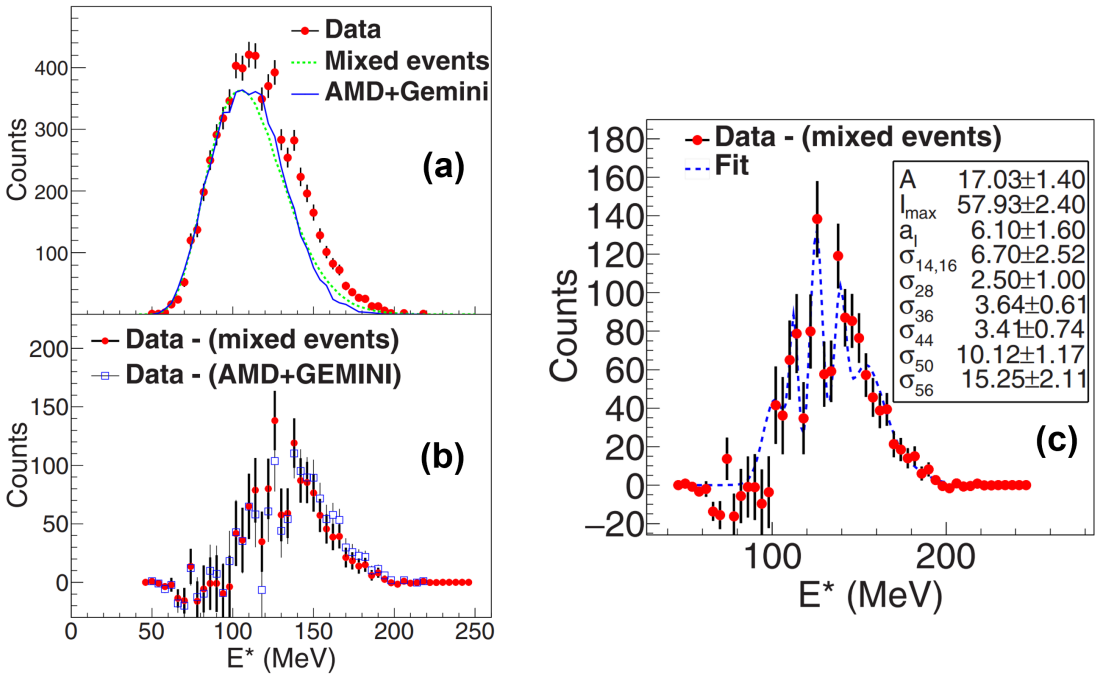

Figure 1.11: Experimental evidence suggestive of toroidal high-spin isomer breakup. Panel (a): Experimentally measured 7-α event excitation energy distribution with proposed backgrounds. Event mixing technique (red dashed) and AMD + GEMINI++ distribution (blue) are shown as possible background descriptions. The AMD + GEMINI++ distribution was shifted in E* to reasonably match the experiment. Panel (b): Residual obtained by subtracting the data in panel (a) from the mixed event distribution (red circles) and the shifted AMD + GEMINI++ distribution (open squares). Panel (c): Phenomenological toroidal state fit to the residual data in panel (b) for the extraction of state properties. Reprinted from [11].

in 2009 where collisions of ^{28}Si + ^{12}C at 35 MeV/nucleon were measured using the NIMROD detector array [60, 11, 6]. This experiment was not designed with the intent of searching for such states; however, when examining the excitation energy distribution for events with seven measured projectile-like α-particles, structure in the form of peaks was observed at very high excitation energy as shown in panel (a) of Figure 1.11. To isolate the possible excited state contributions from the total spectrum, the event mixing technique was used to produce an uncorrelated excitation energy distribution to serve as a background. For this, seven α-particles were selected from seven randomly chosen 7-α events to construct a mixed event. By repeating this procedure many times, a smooth distribution with negligible statistical error is created as shown in blue in panel (a). A residual spectrum is produced by subtracting the experimental data from the normalized mixed event background as seen in panel (b). A semi-empirical model constrained by the general predicted spacing of neighboring angular momentum states was created to fit the residual spectrum as shown in panel (c) of Figure 1.11. The extracted properties indicated that the three most statistically significant peaks may correspond to states with angular momentum of 28$\hbar$, 36$\hbar$, and 44$\hbar$. The width extracted from the fit ranged from 5-9 MeV (FWHM) for the highest yielding peaks, although the angular resolution of NIMROD suggests that states with infinitely narrow intrinsic widths (δ-resonances) at this excitation energy would give measured widths of similar magnitude. In the determination of the cross section for each state, all yield in the residual was assumed to

E* (MeV)	Ang. Mom. ($\hbar$)	Stat. Sig. (σ)	Measured Width (FWHM)	σ (μb)
114	28	5.0	5.88 ± 2.36	—
126	36	7.9	8.57 ± 1.44	51 ± 13
138	44	7.1	8.03 ± 1.75	28 ± 7

Table 1.1: Experimentally determined properties of the potential toroidal high-spin isomer states observed in Ref. [11]. Angular momentum is assigned by comparing to theory predictions. Statistical significance is determined by the yield above the normalized mixed event background. Cross section is estimated using AMD + GEMINI++ simulation data.

originate from broad overlapping contributions from toroidal high-spin breakups. The cross section was estimated by interpolating the systematic calculations of Wilcke to obtain a total reaction cross section [64]. The total number of collisions measured (where at least one particle was detected) was scaled by the detection efficiency of NIMROD determined by using filtered AMD + GEMINI++ simulation data. A similar procedure was then performed to obtain the detection efficiency for the 7-α channel. This allowed for the yield within each peak in the residual spectrum to be scaled to a cross section, albeit with large systematic errors. A summary of the observed peak locations and extracted properties are shown in Table 1.1. Given the limitations of the NIMROD detector array for making such measurements, the authors suggested that an experiment with improved angular resolution is necessary to further identify and characterize these states.

Additional experimental observables sensitive to a toroidal breakup would provide a stronger link between the observed peaks and nuclear toroid predictions. Momentum shape analysis, for example, employs a tensor constructed using the seven α-particle center-of-mass frame momenta to characterize the shape of breakup; once diagonalized, the ordered and normalized eigenvalues of the tensor $(\lambda_1, \lambda_2, \lambda_3)$ provide information about the degree of breakup sphericity ($S = \frac{3}{2}(1 - \lambda_3)$) and coplanarity ($C = \frac{\sqrt{3}}{2}(\lambda_2 - \lambda_1)$). In cases of simultaneous breakup, this momentum shape can provide key insight of the de-exciting nucleus

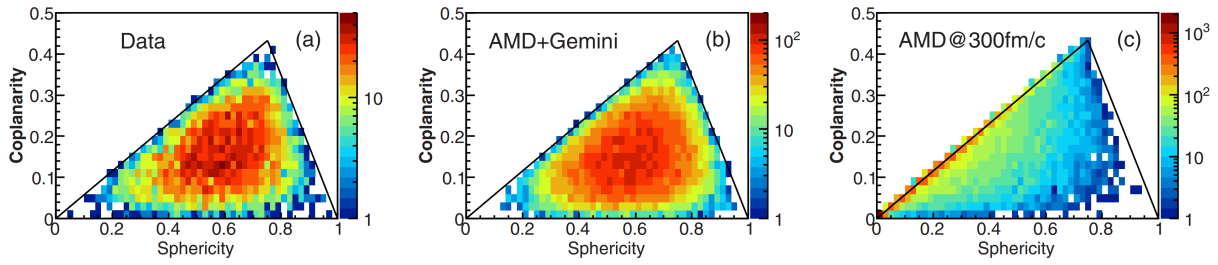

Figure 1.12: Shape analysis for 7-α events in the de-excitation of ^{28}Si in collisions of ^{28}Si + ^{12}C at 35 MeV/nucleon. Experimental results are shown on the left. NIMROD filtered AMD + GEMINI++(labelled GEMINI) events are shown in the middle. The primary AMD fragments fed to GEMINI++ that yield seven filtered α-particles is shown on the right. Reprinted from [11].

geometric configuration. A toroidal ^{28}Si with high angular momentum promptly disassembling into 7-α particles should give enhanced coplanarity over statistical de-excitations. The momentum shape distribution was compared between the measured 7-α data, filtered AMD + GEMINI++ simulation data, and primary AMD fragments that fed GEMINI++ at t = 300 fm/c as shown in Figure 1.12. The three momentum shape vertices seen here correspond to each shape extreme ($(0,0)$: rod, $(3/4, \sqrt{3}/4)$: disk, and $(1,0)$: sphere). It was found that the experimental data was well described by the AMD + GEMINI++ simulation, with the yield centered between each extreme. AMD models the dynamic, early stages of the collision. As evidenced by the bulk of yield lying along the rod-disk axis in panel (c), there were typically only a few primary excited fragments fed to GEMINI++ from AMD. While this may indicate that the experimental data is consistent with a sequential decay picture, further investigation of the collision dynamics and decay mechanism that lead to seven projectile-like α-particles in the exit channel is needed.

The goal of this work is to perform a high angular resolution measurement with a significant increase in the number of measured 7-α events to reduce both the statistical and systematic uncertainties of previous measurement. If these states exist, such a measurement could better determine their intrinsic widths, providing information about their lifetime and stability.

2. EXPERIMENTAL DETAILS

A summary of the collision systems measured and details of the experimental setup are outlined in this chapter. Section 2.1 gives an overview of the reactions measured with the Forward Array Using Silicon Technology (FAUST). Details of FAUST are discussed in Section 2.2, with the individual Si-CsI(Tl) telescopes introduced in Section 2.2.1 and the supporting structure and configuration of the array discussed in Section 2.2.2. The electronics chain and acquisition used for processing the detector signals is discussed in Section 2.3, with details of silicon signal processing in Section 2.3.1 and cesium iodide signal processing in Section 2.3.2. Details of the multi-event readout implementation in the data acquisition over previously used single-event readout can be found in Section 2.3.3.

2.1 Beams and Targets

The primary reaction studied in this experiment was ^{28}Si at 35 MeV/nucleon impinged on a ^{12}C target in inverse kinematics. Additional reaction systems of ^{28}Si at 35 MeV/nucleon impinged on ^{28}Si,^{27}Al targets were also measured to explore the effect of target size and α-conjugation on potential toroidal state production. Additionally, normal kinematic collisions of ^{12}C at 35 MeV/nucleon impinged on a ^{28}Si target were measured to potentially provide information about the unmeasured target-like fragments in the inverse kinematic measurement. Due to the large grazing angle of this normal kinematic reaction, the forward-most ring (ring A) was removed to protect the silicon detectors from radiation damage. The experiment took place in June of 2021; all beams were accelerated using the K500 cyclotron at the Cyclotron Institute at Texas A&M University. Details of the measured collision systems are shown in Table 2.1.

Calibration beams are used to provide energy calibration points at silicon energies above that achievable with radioactive sources. To this end, beams of ^{28}Si and ^{12}C at 35 MeV/u and ^{1}H^{4}He at 10 MeV/u were elastically scattered off of a ^{197}Au target. To access lower inci-

Beam Species	Beam Energy (MeV/nucleon)	Target Material	Target Thickness (mg/cm^2)	Data Collection Duration	Events with PID
^{28}Si	35	^{12}C	0.930	∼6 days	3.35×10^8
^{28}Si	35	^{27}Al	1.0	∼1 day	4.25×10^7
^{28}Si	35	^{28}Si	1.0	∼1 day	3.09×10^7
^{12}C	35	^{28}Si	1.0	∼1 day	6.71×10^7
^{28}Si	35	^{197}Au	1.7	∼2 hours	
^{12}C	35	^{197}Au	1.7	∼2 hours	
^{1}H^{4}He	10	^{197}Au	1.7	∼4 hours	

Table 2.1: Details for each collision system. Calibration beams are separated from the physics beams by the horizontal bar. The number of recorded collision events with identified charged particles are shown in the right column.

dent beam energies that provide larger silicon energy calibration points, aluminum degraders upstream of the ^{197}Au target were used. For the ^{12}C beam, 0.0218" and 0.0470" aluminum degraders were used to provide additional incident beam energies of 25.8 MeV/nucleon and 20.4 MeV/nucleon, respectively. For the molecular ^{1}H^{4}He beam, a 0.0043" aluminum degrader was used to provide an additional incident ^{1}H and ^{4}He beam energy of ∼8.9 MeV/nucleon.

2.2 Forward Array Using Silicon Technology (FAUST)

The Forward Array Using Silicon Technology (FAUST) is a detector array designed to measure charged particle reaction products in intermediate energy heavy-ion collisions. The array consists of 68 Si/CsI(Tl) ΔE-E telescopes arranged in five concentric square rings and covers an angular range of 1.6° - 45.5° [65]. The spatial orientation of the square detectors and rings is designed to minimize "dead space" between the individual detectors, affording excellent geometric coverage. The forward-most ring in laboratory θ is situated furthest from the target position and is referred to as "Ring A". The remaining rings (B-E) are located sequentially closer to the target position and cover larger laboratory θ on average.

2.2.1 FAUST Telescopes

The ΔE detectors of FAUST are nominally 300 µm thick edge-mounted dual-axis duo-lateral (DADL) silicon detectors with an active area of 20 mm x 20 mm. These detectors provide information about the position of particle incidence by measuring resistively-split charge on the top and bottom(left and right) of the front(back) face. Additionally, the detectors have a front and back guard ring providing a low-potential barrier between the silicon active area and the detector surroundings. A single FAUST telescope is shown in Figure 2.1, with the printed circuit board (PCB)-mounted DADL detector seen in front. The four signals and the two guard ring bias connections for the DADL detector can be seen as the six colored wires coming off of the bottom of the green PCB. Details of the DADL detector design, charge-splitting mechanism, and signal analysis procedure are discussed at length in Chapter 3.

Situated behind each DADL detector is a CsI(Tl) inorganic scintillator as shown by the

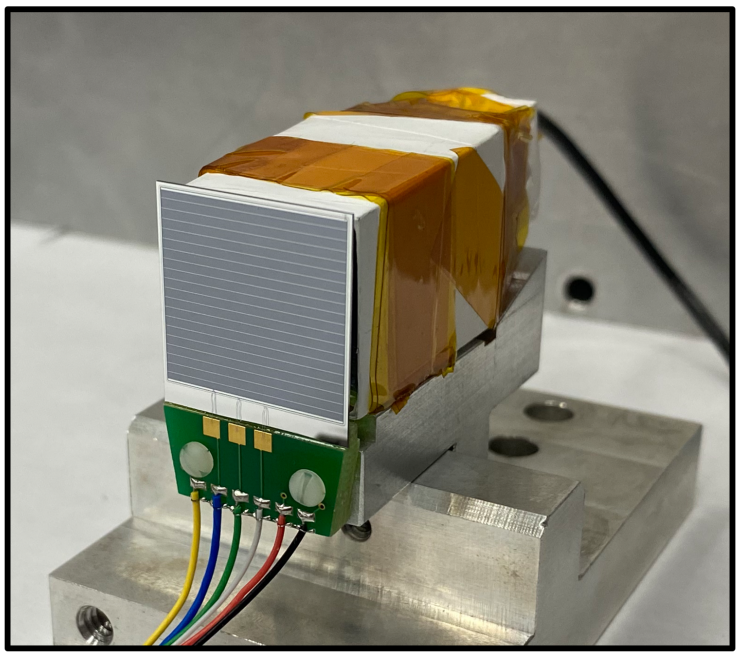

Figure 2.1: Picture of a single FAUST telescope. The 2 x 2 cm DADL detector is mounted on the front with the CsI(Tl) crystal, Lucite light guide, and photodiode mounted behind.

Teflon-wrapped crystal in Figure 2.1. The CsI(Tl) crystals are 3 cm in length in Rings A-D and 2.64 cm in Ring E. Many charged particle detector arrays equipped with CsI(Tl) stopping detectors use photomultiplier tubes for light collection which afford excellent energy resolution, low thresholds, and pulse-shape discrimination capabilities for light charged-particle identification [66, 60]. However, the CsI(Tl) stopping detectors of FAUST are instead optically coupled to Hammamatsu S5107 photodiodes through a Lucite light-guide due to the stringent geometric constraints necessitating the smaller form factor [67]. Additionally, photodiodes are more robust, requiring lower bias voltages and being less susceptible to temperature-dependent gain drifts [68]. It is important to note that pulse-shape discrimination — while typically of lesser quality than that achievable with a photomultiplier tube — is possible with photodiodes if proper preamplification and pulse-processing is performed [69, 70]. This can be beneficial for performing particle identification on high energy light charged-particles (predominantly Z = 1) that deposit too little energy in the ΔE detector for detection. It was not necessary to optimize detection of Z = 1 particles for this experiment, although an upgrade to the preamplification and pulse-processing of the CsI(Tl) could in principle be implemented for FAUST if needed.

2.2.2 FAUST Configuration

In previous experiments, the rings of FAUST were housed in a cylindrical mounting chamber that sat within a larger cylindrical vacuum chamber [71, 72, 73]. A picture of FAUST housed in the cylindrical mounting chamber with rings D and E visible is shown in Figure 2.2 panel (a). In this configuration, accessing the detectors and cables without perturbing the entire array was difficult (e.g., resolving significant noise or a missing signal in ring A required removing rings B-E). As such, it was common to have some detectors not fully functioning for the duration of an experiment. The goal of the present study is to measure high multiplicity decays where the detection efficiency can be severely impacted by the number of offline detectors. To improve the ability of effectively troubleshooting the connectivity and quality of each detector signal, new mounting structures were fabricated to

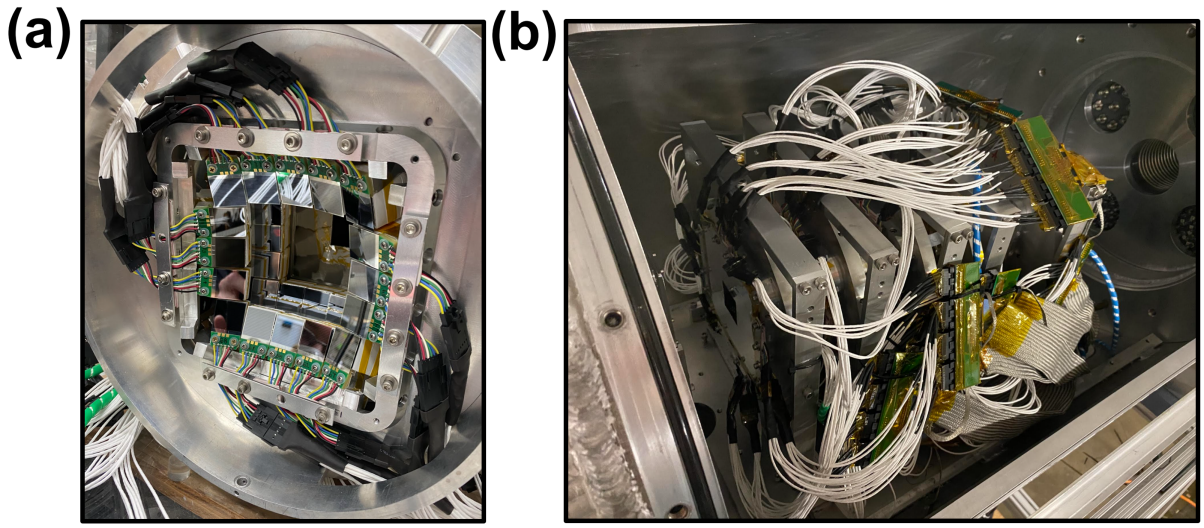

Figure 2.2: Pictures of FAUST. Panel (a): Picture of FAUST housed in the previously used chamber with the telescopes of rings D and E visible. Panel (b): Picture of fully cabled FAUST with rings housed in the newly constructed ring mounts for use in the larger chamber.

house FAUST within a more spacious and accessible vacuum chamber as shown in Figure 2.2 panel (b). The five independent ring-mounts are affixed to a bottom plate that has translational and rotational degrees of freedom for beam axis-array alignment purposes. This adjustable bottom plate rests on a stationary plate in the bottom of the vacuum chamber. This new configuration for FAUST was instrumental in having all 68 detector telescopes fully operational in this experiment.

To maximize angular coverage, the geometric design and spacing of each ring of FAUST is such that the inactive area of each ring (mounting structure, DADL PCB) is blocked by the active area of the ring in front. This gives near complete solid angular coverage ($\sim$ 90%) from 2.3° - 33.6° in laboratory θ, with varying lesser coverage in the 1.6° - 2.3° and 33.6° - 45.5° ranges [65]. There is a front plate between the target position and Ring A to protect the detectors during beam tuning. This front plate has a bevelled opening to allow reaction products produced in the target to reach the detectors of FAUST. Aluminized Mylar foils are used to shield the silicon detectors from electrons that are ejected from the target

ID	Ring	Th.(μm)	D_t(cm)	θ_{cent}	ϕ_{cent}	ID	Ring	Th.(μm)	D_t(cm)	θ_{cent}	ϕ_{cent}
0	A	316	40.0	4.3	45	34	C	316	21.8	11.5	90
1	A	319	40.0	3.1	0	35	C	316	21.8	12.8	63.7
2	A	324	40.0	4.3	315	36	D	314	14.2	25.1	45
3	A	322	40.0	3.1	270	37	D	315	14.2	20.2	26
4	A	324	40.0	4.3	225	38	D	325	14.2	18.3	0
5	A	328	40.0	3.1	180	39	D	314	14.2	20.2	334
6	A	310	40.0	4.3	135	40	D	314	14.2	25.1	315
7	A	319	40.0	3.1	90	41	D	321	14.2	20.2	296
8	B	314	27.9	9.4	45	42	D	317	14.2	18.3	270
9	B	324	27.9	7	18.4	43	D	321	14.2	20.2	244
10	B	325	27.9	7	341.6	44	D	325	14.2	25.1	225
11	B	320	27.9	9.4	315	45	D	310	14.2	20.2	206
12	B	324	27.9	7	288.4	46	D	311	14.2	18.3	180
13	B	324	27.9	7	251.6	47	D	324	14.2	20.2	154
14	B	324	27.9	9.4	225	48	D	322	14.2	25.1	135
15	B	317	27.9	7	198.4	49	D	314	14.2	20.2	116
16	B	324	27.9	7	161.6	50	D	314	14.2	18.3	90
17	B	324	27.9	9.4	135	51	D	314	14.2	20.2	64
18	B	310	27.9	7	108.4	52	E	316	10.0	37.4	45
19	B	310	27.9	7	71.6	53	E	317	10.0	30.8	25.2
20	C	317	21.8	16	45	54	E	311	10.0	28.4	0
21	C	316	21.8	12.8	26.3	55	E	322	10.0	30.8	334.8
22	C	321	21.8	11.5	0	56	E	320	10.0	37.4	315
23	C	324	21.8	12.8	333.7	57	E	316	10.0	30.8	295.2
24	C	324	21.8	16	315	58	E	322	10.0	28.4	270
25	C	314	21.8	12.8	296.3	59	E	306	10.0	30.8	244.8
26	C	324	21.8	11.5	270	60	E	317	10.0	37.4	225
27	C	320	21.8	12.8	243.7	61	E	306	10.0	30.8	205.2
28	C	314	21.8	16	225	62	E	314	10.0	28.4	180
29	C	320	21.8	12.8	206.3	63	E	317	10.0	30.8	154.8
30	C	317	21.8	11.5	180	64	E	320	10.0	37.4	135
31	C	315	21.8	12.8	153.7	65	E	324	10.0	30.8	115.2
32	C	322	21.8	16	135	66	E	314	10.0	28.4	90
33	C	322	21.8	12.8	116.3	67	E	316	10.0	30.8	64.8

Table 2.2: FAUST detector numbering, ring locations, thicknesses, and spatial location details. The thickness of each DADL detector as reported by Micron Semiconductor is labelled as Th.(μm) [17]. The distance between the center of each detector face to the target position is labelled as D_t(cm). The laboratory theta and phi of each detector center is labelled as θ_{cent} and ϕ_{cent} respectively.

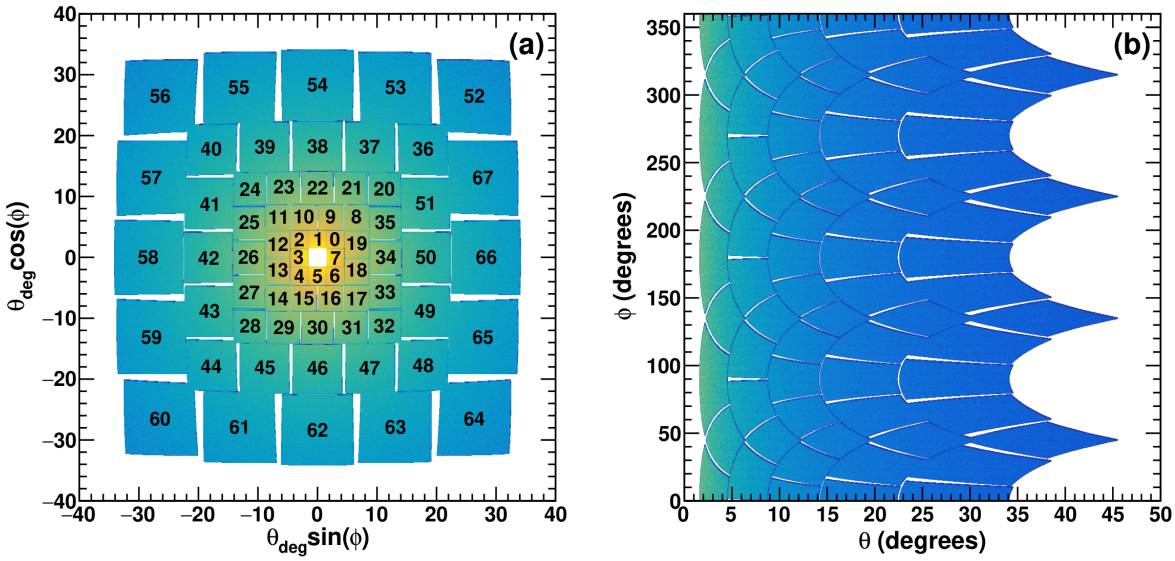

Figure 2.3: Geometry of FAUST. Panel (a): Projection of the FAUST global position showing detector coverage. FAUST telescope numbering scheme used in this work is indicated by the black numbers at each detector position. Panel (b): ϕ_{lab} as a function of θ_{lab} for the detectors of FAUST. Color is only for visual purposes.

during beam bombardment. The foils are fabricated with open squares in the center as to not obstruct the beam path; additionally, the dimensions of the openings are such that a measured charged particle only passes through a single layer. There are three separate foils for this purpose: a 4.788 mg/cm^2 foil mounted to the front of Ring A, a 2.535 mg/cm^2 foil mounted to the front of Ring C (shielding both Rings B and C), and a 0.833 mg/cm^2 foil mounted to the front of Ring E (shielding both Rings D and E). The foil mounted to Ring E can be seen at the front of the array in Figure 2.2 panel (b). The increasing foil thickness for rings that cover smaller laboratory θ accounts for the higher electron yield and energy that these detectors receive. The laboratory θ and ϕ angular coverage of the FAUST detectors is shown in Figure 2.3 panel (b), where the colored area indicates the angular regions sensitive to charged-particle detection. A global projection of the angular coverage with the detector telescope numbering scheme used in this work is shown in panel (a), showing that the solid angle coverage of the detectors in each ring increases from Ring A (detector 0 - 7) to Ring

E (detectors 52 - 67). The details of each detector telescope number, ring, nominal DADL thickness, distance between DADL to target, and laboratory θ and ϕ of the DADL center are shown in Table 2.2. Due to the 45° ϕ rotational symmetry of each FAUST ring, there are a total of 13 unique detector locations which contain detectors that cover the same solid angle.

2.3 Electronics and Signal Processing

Treatment of the DADL signals to give optimal position and energy resolution discussed in Chapter 3 necessitated the use of 16-channel Struck Innovative Systeme SIS3316 VME fast-sampling digitizers [74]. The SIS3316 is capable of performing operations of many common analog pulse-processing electronics (i.e. ADCs, QDSc, TDCs, CFDs, shaping amplifiers, integrators, and signal logic units). For this experiment, the eight integrators of the SIS3316 were essential for processing the DADL signals (see Section 3.2.1). The 272 DADL signals of FAUST required the use of 17 SIS3316 modules across two VME crates. Consistent internal timing between each SIS3316 module is essential for event building (discussed in Section 2.3.3). A common clock for all SIS3316s was provided by a 12.5 MHz clock sample from a Struck SIS36/38xx external clock module. This clock sample was sent to the first SIS3316 in each VME crate and subsequently sent to the remaining SIS3316s through an LVDS front panel bus cable. The clock sample was then multiplied internally to the native sampling speed of the digitizer (250 MHz, 4ns resolution). Despite the use of the external clock, there was still found to be a small drift in the relative timing between the digitizers in the two VME crates. To compensate, a strobe signal from the SIS36/38xx was used to reset the clock of all SIS3316s every 10 seconds, mitigating the effect of the long timescale drift. The external clock and strobe was also sent to the three Mesytec MADC-32 peak-sensing digitizers used for the digital conversion of the CsI(Tl) signals [75]. The raw 12.5 MHz (80ns resolution) clock sample was used for the MADC-32s as their maximum native sampling speed is 75 MHz and do not have the ability to internally multiply the external clock sample.

When a particle incident on a DADL detector produces a charge above threshold, it is

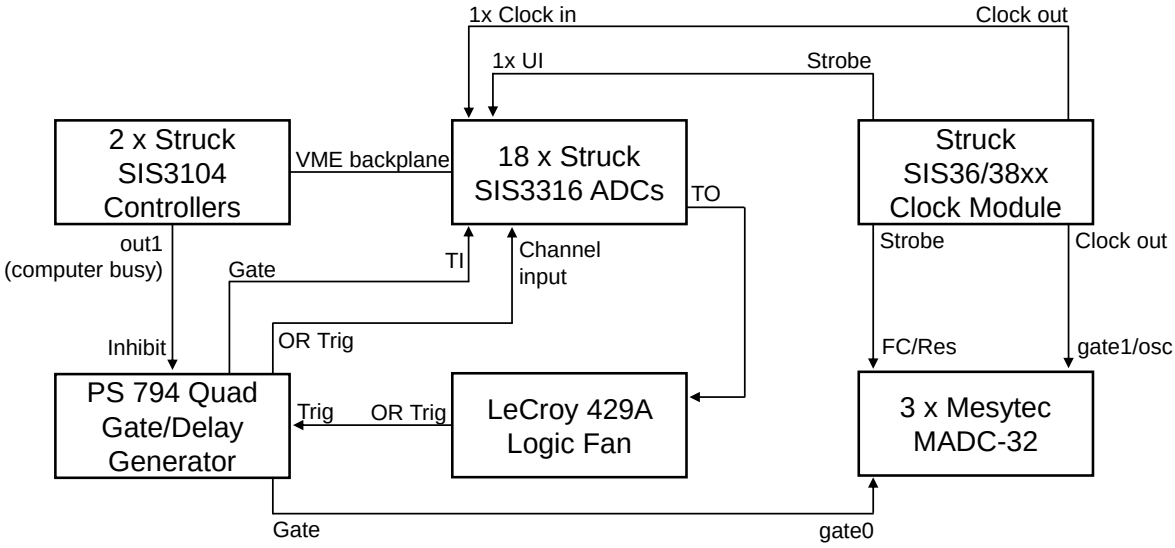

Figure 2.4: Trigger logic and external clock diagram for the FAUST experiment. Boxes indicate modules, arrows indicate connectivity, and text on each arrow indicate the input/output for each module.

internally triggered on in the SIS3316. The OR trigger from all DADL silicon signals was used to determine when to digitize a collision event. To achieve this, the OR trigger from each SIS3316 was summed using LeCroy 429A logic fans and sent to a Phillips Scientific 794 quad gate/delay generator to produce a sum OR gate and trigger; gate/trigger generation was inhibited by a computer busy signal sent from the Struck SIS3104 VME controller modules. A 7 µs gate was sent to the trigger input of each SIS3316 and MADC-32 to instruct the modules to digitize present signals. Additionally, a sum OR trigger was sent to a channel input of an additional SIS3316 for event-building purposes (discussed in Section 2.3.3). A diagram detailing the connectivity for the trigger logic and external clock setup is shown in Figure 2.4. A picture of the FAUST chamber, signal processing chain, triggering electronics, and ADCs is shown in Figure 2.5.

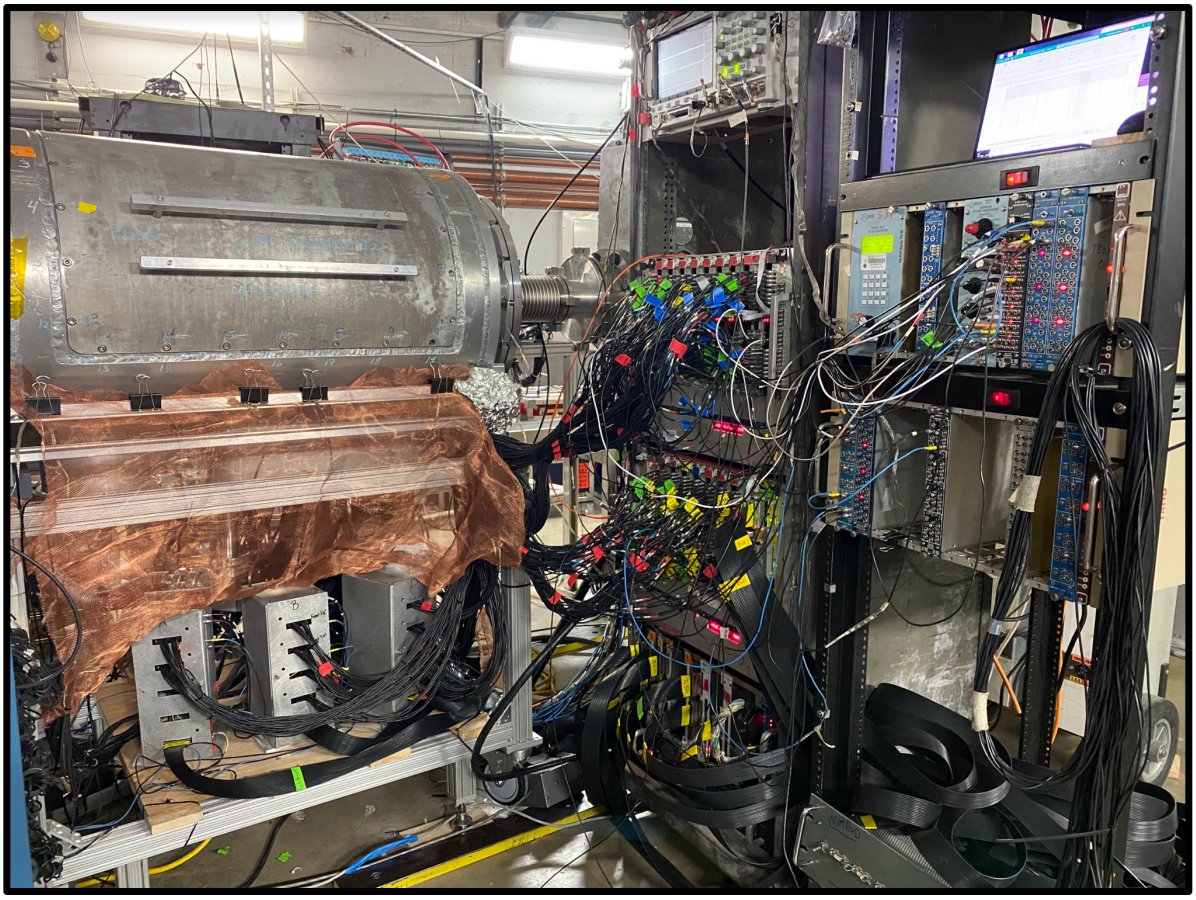

Figure 2.5: Picture of FAUST signal processing electronics and vacuum chamber. Copper mesh enclosing the FAUST chamber supporting structure serves as a Faraday cage for the cables carrying raw signals from the chamber to the tower boards.

2.3.1 DADL Signal Processing

A diagram showing the signal processing pathway for the DADL signals is shown in Figure 2.6. The DADL silicon signals are first brought outside of the chamber using low capacitance cables shielded by tin-plated copper braids. Prior to preamplification, the signal-to-noise ratio of the DADL signals is extremely susceptible to electromagnetic interference. The coaxial cables that transport the signals from the chamber feedthroughs to the preamplifier motherboards are surrounded with copper mesh to act as a Faraday cage as seen in Figure 2.5. The preamplifier motherboards are housed in an aluminum chassis referred to as a "tower board" (seen below the copper mesh underneath the FAUST vacuum chamber in

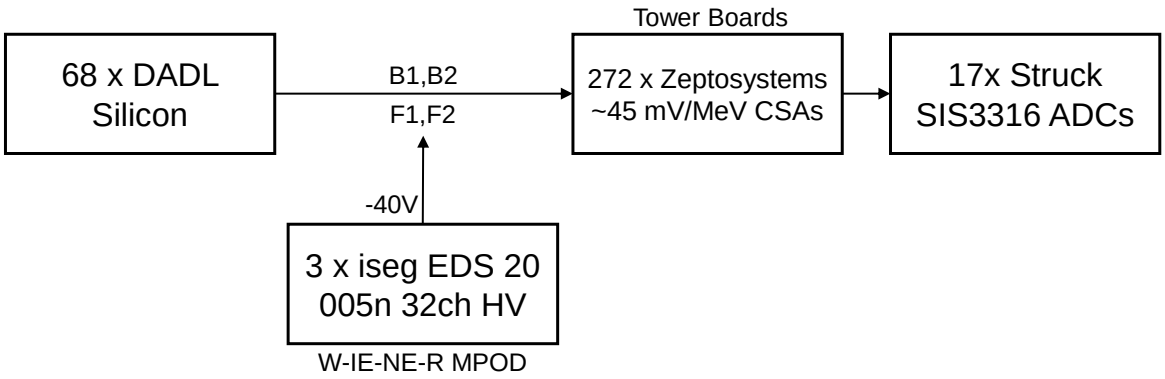

Figure 2.6: Pulse processing and biasing diagram for the DADL detectors in the FAUST experiment. Bias from the MPOD is supplied to the front of the DADL detectors through contacts F1 and F2.

Figure 2.5). Each tower board houses all preamplifier motherboards for an entire ring of FAUST. Details of the connectivity and circuit design within each tower board can be found in Ref. [71].

While FAUST was previously equipped with ultra high-gain ∼110 mV/MeV preamplifiers to improve the measurement of high energy light charged particles, it was found that the signal-to-noise ratio is comparable for lower gain preamplifiers as the largest relative contribution of electronic noise occurs prior to preamplification. Selecting preamplifiers of a certain gain is a balance between maximizing the amplification (to both improve the ability of triggering on small signals due to the discretized thresholds in the SIS3316s, as well as incur less resolution penalty when digitizing the analog signal) and having an appropriate dynamic range for the signals of interest (dictated by the preamplifier saturation voltage). The primary goal of this experiment is to maximize the quality of α-particle measurement, although measuring the full range of isotopes produced in the collision is advantageous for related (and additional) studies. As such, FAUST was equipped with Zeptosystems ∼45 mV/MeV charge-sensitive preamplifiers, providing full-range measurement up to ∼oxygen (Z = 8) isotopes (above which preamplifier saturation begins to occur) without significantly

EnableFrontPanel(Control/StatusLines)	Module 1: On, Module 2+: Off
EnableInternalClockToFrontPanel	Module 1: On, Module 2+: Off
UseFrontPanelTimeStampClear	On
ClockSource	FrontPanelBusSample
FpClockSource	External
ClockFrequency	250
ClockMultiplier	12.5To250
ExternalTriggerNimIn	Off
EnableExternalGate	Module 1: Off, Module 2+: On
ExternalVeto(TI/UI)	Off
UseFpBusTrigger	Off
UseFpBusSampleControl	On
UseFpBusVeto	Off
UseExternalTimeStampClear	On
PreTriggerDelay	1500
SampleSize	0
TriggerGateWindowLength	2500
NumMultiEvents	50
SuppressHitsAboveEventThreshold	On
Threshold	35
InputRange	F1,F2: kMinus5To0, B1,B2: k0To5
InputImpedance	k50Ohm
TriggerPeak	40
TriggerGap	60
InternalTriggerDelay	255
LemoOutTriggerMask	On
InternalTriggerEnableMask	On
ExternalTriggerEnableMask	Off
External(Veto/Gate)EnableMask	Off
EnableAccumulator(1Through6/7Through8)	On
EnableTriggerMawParameters	On
Accumulator1Start, Width	0, 500
Accumulator2Start, Width	1492, 500
Accumulator3Start, Width	1470, 500
Accumulator4Start, Width	1448, 500
Accumulator5Start, Width	1426, 500
Accumulator6Start, Width	1404, 500
Accumulator7Start, Width	1382, 500
Accumulator8Start, Width	1360, 500

Table 2.3: SIS3316 ADC configuration settings used in the FAUST experiment for processing the DADL signals.

impacting the quality of helium (Z = 2) isotope measurement. After preamplification, coaxial cables carry the signals to the input of the SIS3316s for digitization. The SIS3316 settings for the DADL signals are shown in Table 2.3. The accumulator (integrator) settings are essential for performing the "closest integrator" method outlined in Section 3.2.1. The settings used for the collection of all collision data in this work correspond to an integration delay of 2.6 µs and an integrator spacing of 88 ns in the closest integrator method.

To reverse bias the DADL detectors, a negative bias voltage is supplied to the front (p-type) face of each DADL using 32-channel bias modules housed in a multi-channel low voltage (LV) and high voltage (HV) computer-controlled power supply system (W-IE-NE-R MPOD) [76]. The bias cables are connected to the tower boards where voltage is applied to the front-face channels (F1 and F2) prior to preamplification. The leakage current as a function of bias voltage relationship for each detector indicated that supplying −40 V aptly depleted each detector without causing breakdown. The computer-controlled bias system allowed the leakage current of each DADL detector (which can indicate radiation damage) to be monitored for the duration of the experiment. The back face (B1 and B2) of the DADL is held at ground. The front guard rings were biased at −36.4 V using resistive voltage dividers and the back guard rings were held at ground [77, 71].

2.3.2 CsI(Tl) Signal Processing

A diagram showing the signal processing pathway for the CsI(Tl) signals is given in Figure 2.6. Like the DADL signals, the CsI(Tl) signals are transported from the chamber feedthroughs to the preamplifier motherboards using coaxial cables and amplified using Zeptosystems ∼45 mV/MeV charge-sensitive preamplifiers. To help facilitate measurement of the pulse amplitude and reduce the impact of high frequency noise, the signals are then shaped using Pico Systems shaping amplifiers [78, 79]. The shaped signals are then digitized using peak-sensing Mesytec MADC32s [75]. The photodiodes used for CsI(Tl) light collection are biased by supplying 9 V from an ORTEC 710 quad bias supply [80]. Three bias channels supplied the bias voltage to all 68 CsI(Tl) detectors of FAUST.

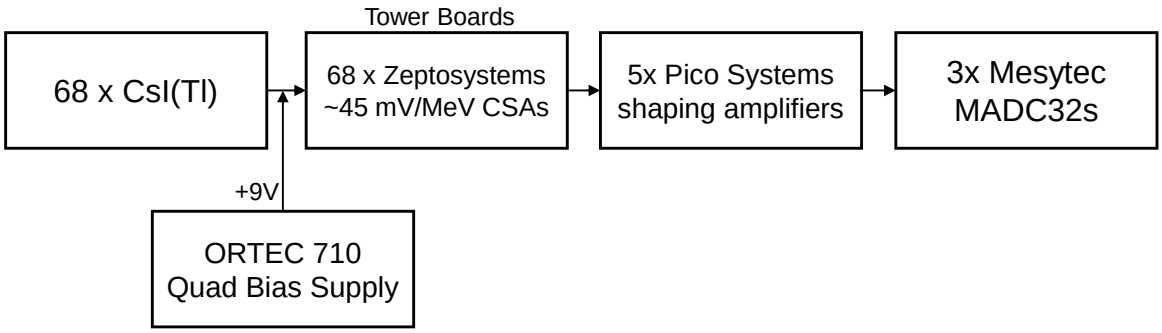

Figure 2.7: Pulse processing and biasing diagram for the CsI(Tl) detectors in the FAUST experiment.

2.3.3 Multievent Readout and Event Building

Experiments at the Texas A&M Cyclotron Institute have typically used single-event readout where each collision event is read out to the computer prior to acquiring the next event. For experimental setups with many channels of electronics (340 for FAUST), this can lead to large dead-times (due to the inability of the data acquisition system acquiring new events during readout) with correspondingly low maximum event rates ($\sim$200 events/second for FAUST). Maximizing data collection rates with FAUST was essential, as the reaction channel of interest is rare ($\sim$1/2000 measured collision events) and the amount of collected data impacts the ability to resolve potential excited states. To accommodate these needs, multievent readout was implemented into the data acquisition system [81].

For multievent readout, all channels are read when any single channel in the SIS3316 is above threshold. The number of stored events before multievent readout occurs is set by the SIS3316 configuration settings (50 for this experiment). Each channel that triggered has a timestamp associated with it in the data stream. To associate channel triggers across all detectors of FAUST as originating from the same collision event, timestamps must be compared in the backend analysis. To simplify the timestamp-matching algorithm, an OR trigger signal from all DADL signals of FAUST was sent into an input channel of a SIS3316. The trigger timestamp between each DADL and CsI(Tl) signal was compared to the times-

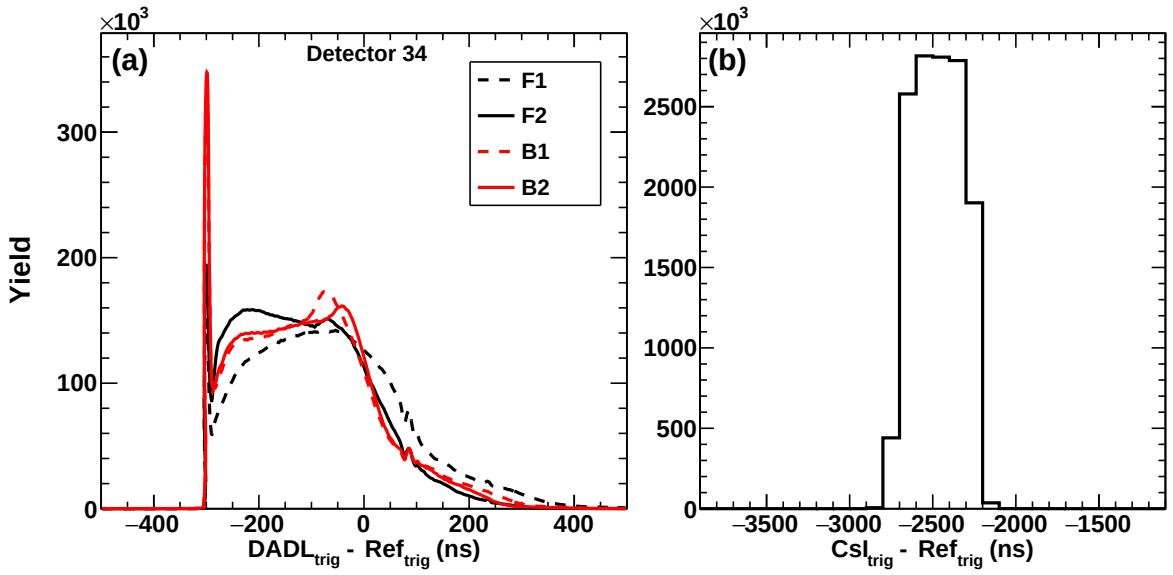

Figure 2.8: Trigger time difference distribution windows for event building. Panel (a): Difference between the DADL signal timestamp (4 ns resolution) and the reference trigger timestamp (4 ns resolution). Panel (b): Difference between the CsI trigger timestamp (80 ns resolution) and the reference trigger timestamp (4 ns resolution). The x-axis ranges shown here are the time difference windows applied for event building.

tamp of the OR trigger signal. The time difference gates used to correlate triggers from the same collision event are shown in Figure 2.8. The sharp peak for the four DADL signals in panel (a) at -300 ns corresponds to that channel triggering the earliest and producing the OR trigger signal. The -300 ns offset of the peak location is caused by differing trigger settings between the DADL silicon signals and the OR trigger pulse. The yield to the right of this peak originates from the distribution in relative trigger times of the DADL detector signals due to differing pulse shapes (discussed in Section 3.1.2). Due to the slower readout speed of the MADC32s, it was essential to search for correlated triggers over two neighboring multievents, as roughly half of all CsI(Tl) triggers within this time difference gate occurred in the multievent following that which contained the DADL OR reference trigger.

The implementation of multievent readout permits near zero dead time data acquisition in FAUST. In this experiment, the event rate was kept around 2000 events per second to prevent beam rate fluctuations from causing excessive radiation damage to the DADL silicon

detectors; however, event rates up to 8000 events per second have been achieved.

3. DADL DETECTOR CHARGE DETERMINATION AND FAUST RESOLUTION*

The characteristics of the measured charge after preamplification from particles incident on the DADL detector, the development of a technique to accurately determine the position and energy of incident particles that minimizes position-dependent distortions, and the characterization of the DADL position and energy resolution attained in this experiment are outlined in this chapter. Section 3.1 discusses the DADL detector characteristics and outlines how energy and position of measured particles are determined. Position and energy distortions previously seen when using these detectors is discussed in Section 3.1.1, with the origin of these distortions explored in Section 3.1.2. Section 3.2 is dedicated to the development of a charge integration technique that minimizes these distortions without sacrificing data collection rates; the technique is outlined in Section 3.2.1 and the event rate attainable with this technique is discussed in Section 3.2.2. With an improved understanding of the factors that affect DADL signal charge determination uncertainty, the position resolution of FAUST is characterized in Section 3.3. For this purpose, Section 3.3.1 outlines a simple model of the DADL detector created to reproduce experimental features, with the resulting position and angular resolution of FAUST reported in Section 3.3.2. The results of this chapter have been reported in refs. [12, 13] .

3.1 Dual-Axis Duo-Lateral Position Sensitive Silicon Detectors

The dual-axis duo-lateral (DADL) silicon detectors of FAUST are silicon diodes fabricated by Micron Semiconductor with a nominal thickness of 300 µm and a 20 mm x 20 mm active area [17]. The detector is reverse-biased by applying a negative voltage to the front (p-type) face. When exposed to ionizing radiation, the liberated "holes" are attracted to the front face

Parts of this chapter are adapted or reprinted with permission from "A new waveform analysis technique to extract good energy and position resolution from a dual-axis duo-lateral position-sensitive detector" by A. Aslin, A. Hannaman et al., 2021. *Nucl. Instr. and Meth. A*, 985, 164674, 2023 by Elsevier and "High event rate analysis technique for the dual-axis duo-lateral position-sensitive silicon detectors of FAUST" by A. Hannaman et al., 2023. *Nucl. Instr. and Meth. A*, 1050, 168130, 2023 by Elsevier [12, 13].

while the liberated electrons are attracted to the back face. The front face of the detector has a resistance of $R_{Front} \approx 2\,k\Omega$ and collects holes on contacts at the bottom (F1) and top (F2). The back face of the detector has a resistance of $R_{Back} \approx 4\,k\Omega$ and collects electrons on the left (B1) and right (B2). The differing $R_{Front,Back}$ result from the differing p-type (front) and n-type (back) dopant concentrations set during the manufacturing process. The relative resistance of each charge-carrier path from the position of particle incidence to each of the two contacts on a single face determines the fraction of charge that migrates to each contact. This allows for the particle position to be determined through the relative difference of charge collected on each contact for the front (vertical position) and back (horizontal position) face. To ensure the charge split asymmetry is not too extreme for particles incident on the very edge of the detector, an external resistor of $R_{ext} = 261\,\Omega$ is used. To improve the breakdown voltage and reduce the leakage current, conductive guard rings surround each detector face [82]. A schematic diagram of the DADL detector is shown in Figure 3.1. Particle positions can be calculated from the charges measured on each contact (Q_{F1}, Q_{F2}, Q_{B1} and Q_{B2}) according to Equations 3.1 and 3.2. Due to the external resistor and the delay before integration (discussed further in Sections 3.2 and 3.2.1), the raw calculated position is compressed, so scaling parameters c_x and c_y are included to compensate. Further, due to variations in preamplifier response, the offset parameters s_x and s_y are included to ensure that the position distribution is centered about the origin prior to scaling.

$$X = c_x \cdot \left(\frac{Q_{B2} - Q_{B1}}{Q_{B2} + Q_{B1}} + s_x\right) \tag{3.1}$$

$$Y = c_y \cdot \left(\frac{Q_{F2} - Q_{F1}}{Q_{F2} + Q_{F1}} + s_y\right) \tag{3.2}$$

The charge collected on each face is proportional to the energy deposited by a particle, and so the charge collected by the two contacts for each face are summed to determine E_F and E_B as shown in Equations 3.3 and 3.4. However, due to slight variations in preamplifier

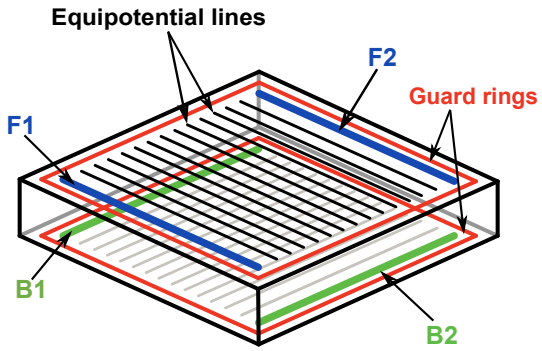

Figure 3.1: Schematic diagram of a DADL detector. The four contacts that collect charge are indicated by F1 and F2 on the front face and B1 and B2 on the back face. Equipotential conductive lines facilitate the spreading of charge across the face of the detector followed by lateral movement to the contacts. Detector thickness and relative component sizes are not drawn to scale. Reprinted with permission from [12].

gain and offset between each contact, a correction must be applied to the calculated energy. Details of this gain-matching process are outlined in Section 4.1.3.

$$E_F \propto Q_{\text{Bottom}} + Q_{\text{Top}} \tag{3.3}$$

$$E_B \propto Q_{\text{Left}} + Q_{\text{Right}} \tag{3.4}$$

3.1.1 Position and Energy Distortions

To demonstrate the type of distortions that can arise with simplified treatment of the DADL detector signals, a simple integration procedure was performed. While the DADL was designed to minimize pin-cushion distortions typical of tetra-lateral resistive detectors [83, 84], position and position-dependent energy distortions were still found when using conventional pulse-processing electronics; these were corrected for empirically [71, 77]. To study the characteristics of the waveforms that may contribute to position and position-dependent energy distortions seen in previous work, waveforms from a 7.22 MeV/nucleon α-particle beam impinged directly on a DADL detector were recorded. In this experiment, a brass mask was constructed and placed in front of the DADL detector to better assess the

degree of distortion in the calculated position for different waveform integration procedures. The layout of the holes and slots in the brass mask are shown in Figure 3.2. The full 32 µs of baseline-adjusted waveforms recorded for a single event are shown in panel (a) of Figure 3.3. Baseline-adjustment is performed by calculating the average waveform value over the first 2 µs and subtracting this from the total waveform. Panel (b) shows these same waveforms around where they deviate from baseline; each begins its motion from baseline at a different point in time. This is due to each channel being individually triggered, causing different waveform shapes to result in various acquisition trigger times. The various waveform characteristics seen here are discussed further in Section 3.1.2.

As a simple integration procedure, each waveform is integrated for 0.25 µs starting where each waveform reaches 300 channels above baseline, giving $Q_{\mathrm{Top(F2)}}$, $Q_{\mathrm{Bottom(F1)}}$, $Q_{\mathrm{Left(B1)}}$, and $Q_{\mathrm{Right(B2)}}$. The sum of $Q_{\mathrm{Top(F2)}} + Q_{\mathrm{Bottom(F1)}}$ as a function of the difference between

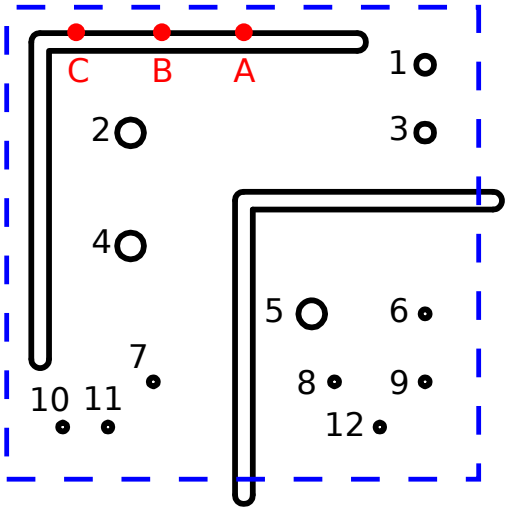

Figure 3.2: Layout of the holes and slots of the brass mask (black solid) placed in front of the DADL detector (blue dashed square). Lettered positions along the top horizontal slit indicate positions for waveforms in Figure 3.5. Reprinted with permission from [12].

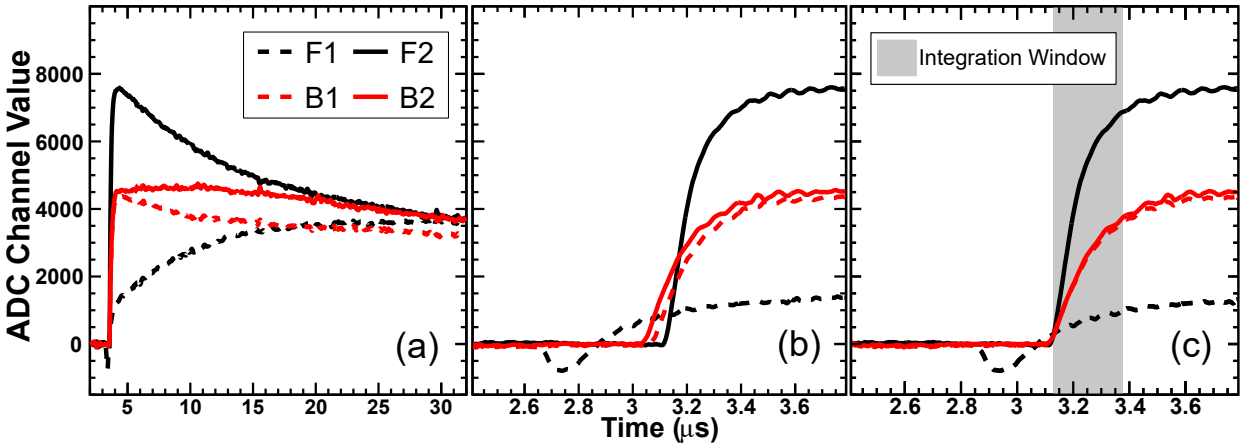

Figure 3.3: Individual trigger analysis method for waveforms collected by all four contacts for a single incident particle. Waveforms in black correspond to charge collected by the front face of the detector, while waveforms in red (gray) correspond to charge collected by the back face of the detector. Panel (a): Full 32 µs length of baseline-corrected waveforms. Panel (b): Baseline-corrected waveforms over the time the waveforms begins to rise. Panel (c): Individual trigger analysis method: each waveform is shifted in time such that each reaches threshold at the same time and is then integrated over 0.25 µs, as indicated by the gray box. Reprinted with permission from [12].

$Q_{Top(F2)}$ and $Q_{Bottom(F1)}$ for ^{228}Th data are shown in panel (a) of Figure 3.4. Obvious position-dependence of the measured energy is seen by an approximately hyperbolic curvature and an understandably poor energy resolution as evidenced by panel (b) (vertical projection of panel (a)). Additionally, the calculated particle positions for the 7.22 MeV/nucleon α-particle mask data in panel (c) shows position distortions as evidenced by the compressed calculated positions near the center edges of the detector and stretched positions near the corners, resulting in a curved "pin cushion" appearance. The distortions seen here are more severe than those obtained from conventional pulse-processing electronics of previous work due to the lack of shaping electronics and the short integration window. These results serve only to demonstrate the types of distortions that can occur.

3.1.2 Waveform Characteristics

It is clear that the shape of the DADL waveforms are inconsistent, and that these waveform distortions can severely impact the position and energy calculated if not treated prop-

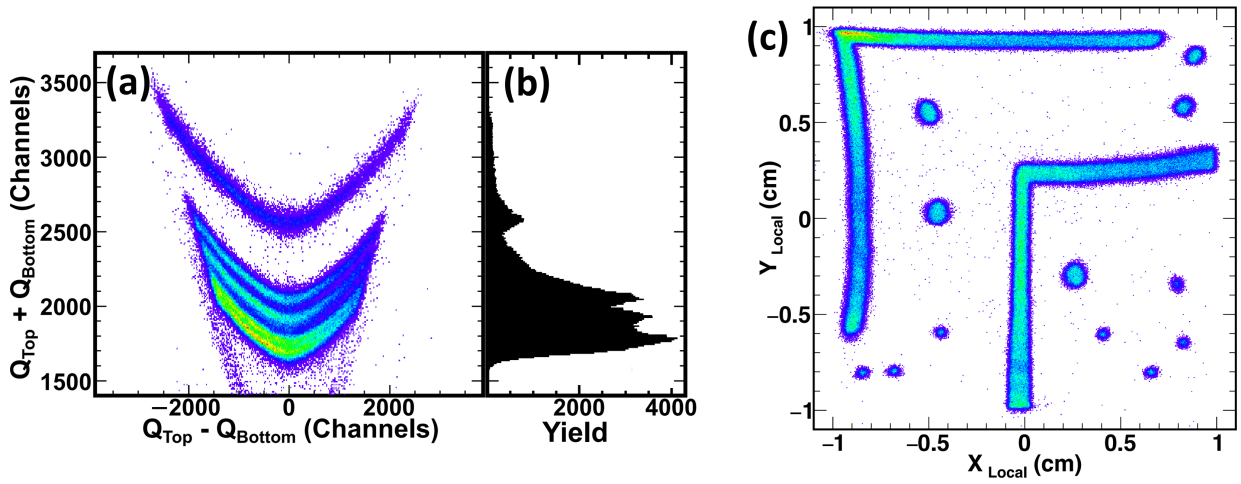

Figure 3.4: Raw energy versus position spectrum using the individual trigger analysis. Data are from a ^{228}Th alpha source exposed to the full DADL detector surface. Panel (a): The vertical axis is proportional to the total energy deposited. The horizontal axis is related to the vertical position of incidence. Panel (b): Projection of the left panel onto the vertical axis providing an energy spectrum. Panel (c): Position plot calculated using the individual trigger analysis method. Reprinted with permission from [12].

erly. Panel (d) of Figure 3.5 shows all four waveforms from the 7.22 MeV/nucleon α-particle data aligned based on the ADC trigger for a particle incident near the top vertically (close to contact F1) and in the middle horizontally (between B1 and B2) of the DADL. While the waveforms collected on F1, B1, and B2 exhibit typical characteristics of a silicon detector signal with a sharp monotonic rise, the waveform collected on F2 (the contact furthest from the position of particle incidence) has an anomalous shape. Here, the waveform is bimodal, initially dipping below the baseline before rising. Due to the capacitive coupling between the front and back face of the detector, capacitively induced currents cause such distortions [85]. The duration of this effect is determined by the capacitance of the detector and the resistances relevant for any particular position. The time that each waveform triggers is recorded, so the four waveforms can be shifted to have the same relative timing to the time of particle incidence as shown in panel (a). All waveforms are shifted relative to the waveform with the earliest trigger time (in this case, F1). The amount that each waveform shifts

depends on the rise time and degree of the bimodal distortion present, as the trigger occurs later in such waveforms. The same treatment for the four waveforms recorded for particles incident with a similar vertical position, but a horizontal position approaching the left side of the DADL (contact B1) are shown in panels (b,e) and (c,f). As the distance between the particle position and B1 approaches the distance between the particle position and F1, the B1 waveform increasingly resembles the F1 waveform. The same is true for the B2 and F2 waveforms. It is important to note the increasing trigger time difference between B2 and B1

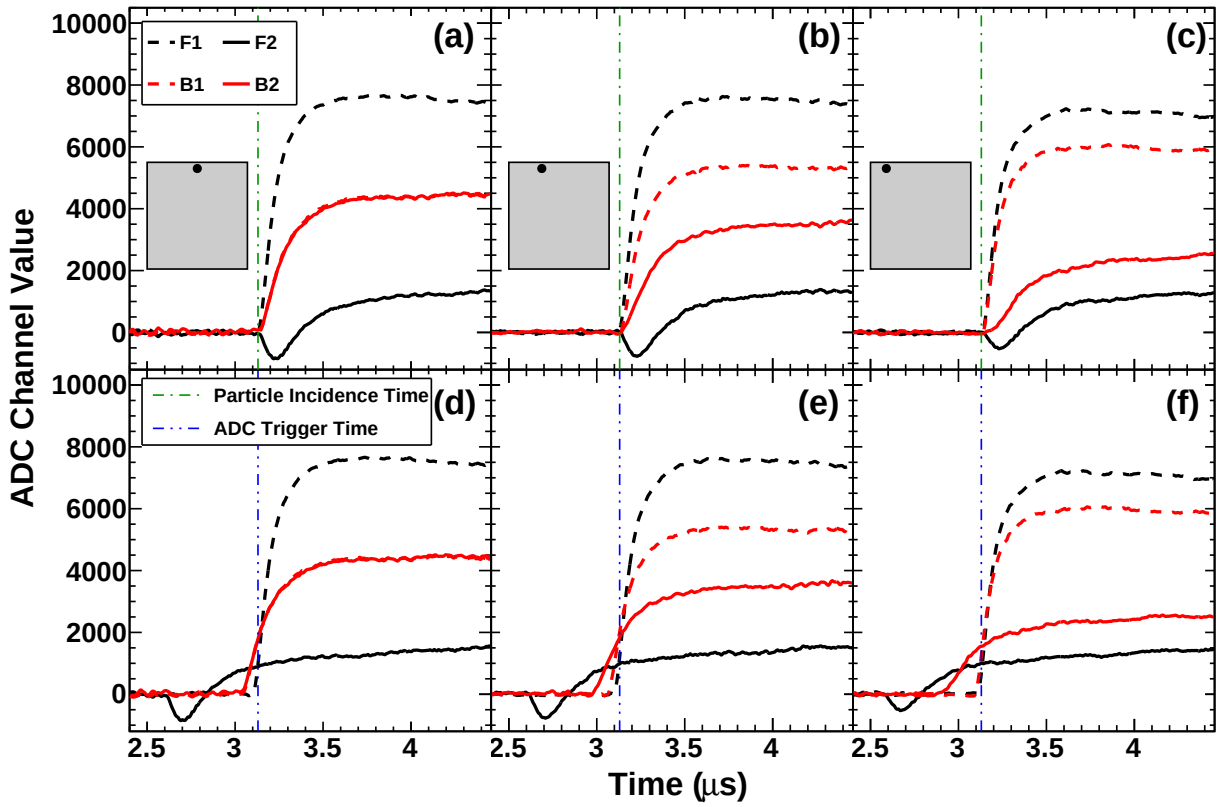

Figure 3.5: Sample waveforms recorded from a beam of 7.22 MeV/nucleon α-particles impinged directly on a DADL detector. Panels (a-c) have the waveforms aligned based on the time of charge collection, while panels (d-f) have the waveforms aligned based on the ADC trigger. The green dot-dashed line in panels (a-c) indicate the approximate time of particle incidence on the detector. The blue double dot-dashed line in panels (d-f) indicate the ADC trigger time of the signals. The gray box-diagrams and black markers indicate the approximate location of the particle incident on the DADL. The waveforms for each pair of vertical panels (e.g., panels (a) and (d)) are from the same event and are only shifted in time.

as the distance between the particle and the B2 contact increases.

Waveforms from ^{228}Th source data were also recorded to assess the energy resolution obtained for different integration techniques. Baseline adjustment of each waveform is performed as previously stated. All recorded waveforms from each contact are overlaid in panels (a,b,d,e) of Figure 3.6 where the color indicates the yield of waveform channel values at each given time. It is clear that the inconsistencies in waveform shape persist for these smaller energy deposits, as evidenced by the bimodal feature where some waveforms dip below baseline before rising at 3 µs. All waveforms, independent of amplitude, approach equilibration at long times, and the difference in amplitude between the smallest and largest waveforms

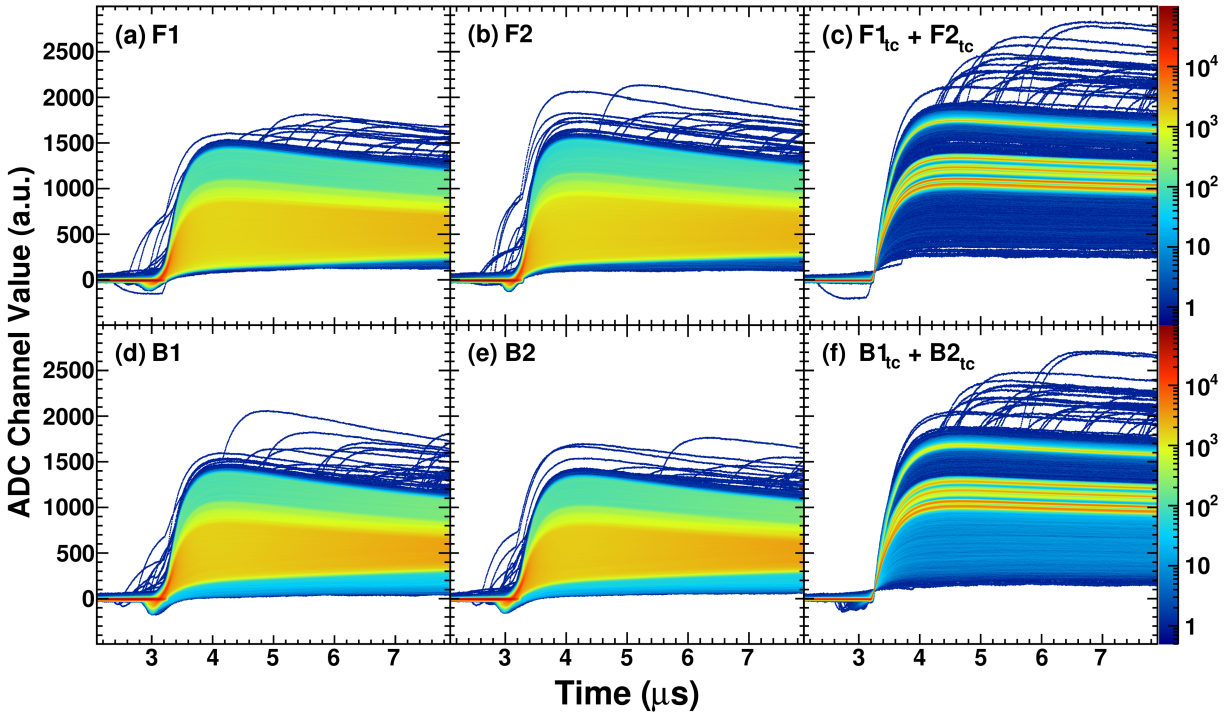

Figure 3.6: Density plot of baseline-adjusted waveforms recorded from ^{228}Th source on a single DADL detector. Panels (a,b): Waveforms from the F1 and F2 contacts, respectively, aligned based on the ADC trigger. Panels (d,e): Waveforms from the B1 and B2 contacts, respectively, aligned based on the ADC trigger. Panels (c,f): Time-corrected sum waveforms for F1 + F2 and B1 + B2 respectively; these waveforms are aligned based on a software leading-edge discriminator with a threshold of 100 channels. Reprinted with permission from [13].

for F1 and F2 is greater than that for B1 and B2 due to the differing $R_{ext}/R_{Front(Back)}$.

We have previously shown that integrating all waveforms relative to their respective ADC trigger causes distortions in position and energy, which motivated the development of the waveform method [12]. In this method, the waveform with a later trigger timestamp for a given face (e.g., F1) is shifted in time relative to the other (e.g., F2) based on the difference in their trigger timestamps. This difference in trigger times arises due to the position-dependence of the waveform shape; as the distance between the contact and the particle position increases, the rise-time is lengthened and the bipolar feature becomes more severe. With the waveforms now aligned based on the time of charge collection, they are summed together to give $F1_{tc}$ + $F2_{tc}$ ($B1_{tc}$ + $B2_{tc}$) as shown in panels (c,f) of Figure 3.6. These sum waveforms are plotted so that each reaches 100 channels above baseline at 3.3 µs. The discrete α-particle energies expected from a ^{228}Th source are clearly seen by the sharp bands that begin around 4 µs, suggesting that waveform integration in this region will yield values that well represent the energy deposited in the detector. Integrating these waveforms for 0.25 µs starting at 3.9 µs (0.6 µs delay after 100-channel departure from baseline) replicates the waveform analysis method we previously developed to circumvent effects of the capacitively induced currents. The waveforms that rise well above the bulk of the data are from double-hits, where two α-particles are incident on the detector close in time due to the high activity and close proximity of the source. Additionally, the small yield present in panels (c,f) below the smallest expected α energy is from protons being ejected from the Mylar film covering the source to prevent contamination of the detector face. The enhancement of yield in this region for panel (f) compared to panel (c) is due to a larger fraction of incomplete charge collection occurring on the back signals from charge being lost to the grounded back guard ring for particles incident near the edge of the detector.

The 35 MeV/nucleon ^{28}Si + ^{12}C collision data measured with FAUST was used to observe how the trigger time difference distribution relates to the energy deposited in the detector as shown in Figure 3.7. For this detector, the bulk of the data spans ±0.4 µs for both the

front and back signals. This region contains all measured isotopes, with many depositing large amounts of energy in the DADL as evidenced by the ∼6 MeV plateau in the mean DADL energy shown in red. This value is well above the mean energy deposited by H and He isotopes, which make up a significant portion of the charged particles produced in these collisions. On the other hand, the tails of the yield distribution largely correspond to high-energy protons that deposit very little energy in the detector, as shown by the corresponding sharp reduction in the mean energy. The amplitude of these signals is near the trigger threshold, giving large trigger time uncertainties due to low signal-to-noise ratios. It is important for the new technique to account for the difference in trigger times (and, by extension, difference in waveform shapes) for the data contained in this plateau, but it is less important to fully capture this distribution, as the trigger times in the tails are largely inaccurate. The curved nature of the plateau in the mean DADL energy is caused both by

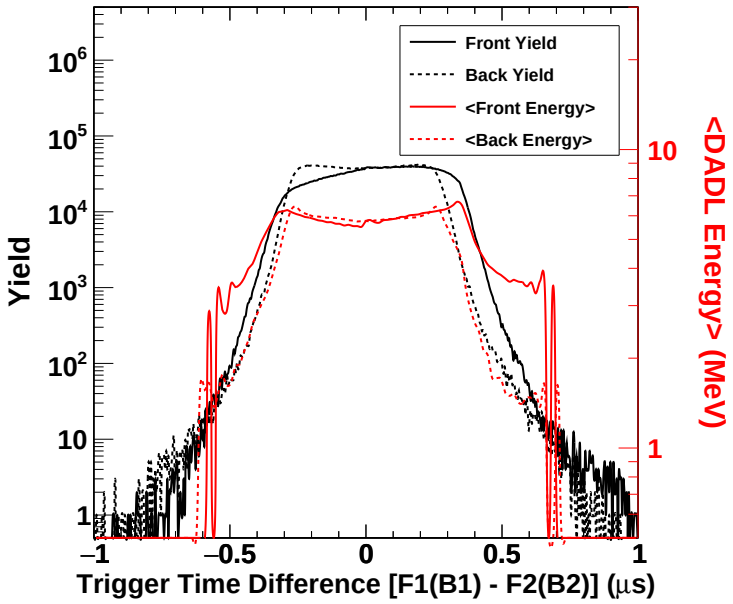

Figure 3.7: ADC trigger time difference distribution between F1 and F2 (black solid) and B1 and B2 (black dashed) of a single DADL detector in FAUST for 35 MeV/nucleon ^{28}Si + ^{12}C data. The corresponding mean energy deposited in the detector as a function of the trigger time difference is shown in red for the front (solid) and back (dashed) signals. Reprinted with permission from [13].

the trigger time difference having a non-linear relationship to particle position and how the solid angle of the selected detector in FAUST spans θ and ϕ.

3.2 DADL Charge Determination

While the waveform analysis technique mentioned in Section 3.1.2 greatly minimizes position and position-dependent energy distortions, the requirement of recording every waveform can significantly reduce maximum data collection rates. This prohibits its application to the present experiment which aims to study rare reaction channels [12]. This section presents a new method that retains the principles and benefits of the waveform analysis technique using only eight waveform integrator values.

3.2.1 Closest Integrator Method

A technique has been developed that harnesses the benefits of the waveform method using only the eight integrators available to the SIS3316 digitizer and will be referred to as the "closest integrator method". For each channel of the digitizer, the integration length for each integrator can be defined and the integration start times can be set relative to the internal trigger. One of the integrators is used to integrate the first 2 µs of the waveform to obtain the baseline, leaving seven available integrators. A schematic of the closest integrator method and the placement of the remaining integrators is shown in panel (a) of Figure 3.8. The start time of integrator 1 is set after the internal trigger (red dashed line) by some delay (green dashed arrow); this is similar to the delay imposed in the waveform method. Integrators 2-7 are then placed to be staggered earlier in time relative to integrator 1 as indicated by the horizontal bars corresponding to each waveform. The spacing between these integrators should be set so that the time difference between integrator 1 and integrator 7 spans the trigger time difference distribution of Figure 3.7. In this case, a spacing of 88 ns was chosen to span a time difference range of ± 0.52 µs. This range is slightly larger than the bulk of the data in Figure 3.7 to give room for slight variations in detector response across the array. The waveform with an earlier trigger time (e.g., F2) always has a sharper rise than that with

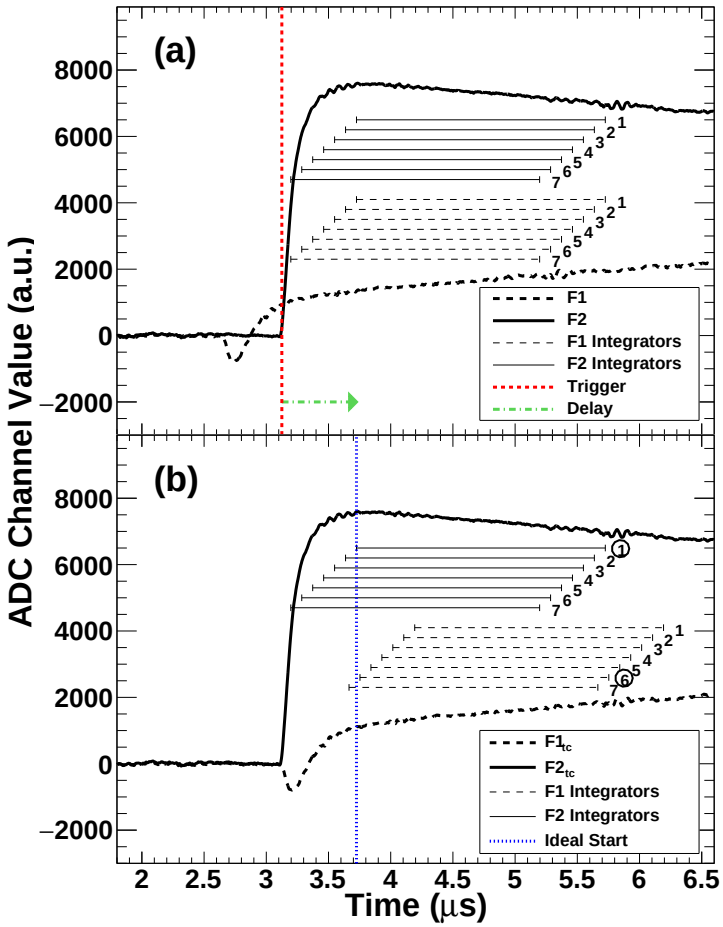

Figure 3.8: Closest integrator method. Panel (a): Sample baseline-adjusted F1 (black solid) and F2 (black dashed) waveforms from an α-particle depositing $\sim$24 MeV in the DADL aligned based on the ADC trigger (vertical red dashed). The 7 integrators are shown by the horizontal bars for both F1 (black, solid) and F2 (black, dashed). The delay applied from the ADC trigger for the placement of the first integrator is shown by the green dot-dashed arrow. Panel (b): The waveforms are now displayed in the same time of charge collection (time-corrected), where the F1 waveform and integrators are shifted relative to F2. The ideal integration start time (vertical blue dashed) lies where the first integrator begins for the reference waveform (in this case, F2). The chosen integrator for each are shown by the black circled integrator numbers. Reprinted with permission from [13].

the later trigger time (e.g., F1), as the more severe the waveform distortions become, the later in the waveform the trigger occurs. As such, the earlier trigger time well approximates the summed waveform trigger time used in the waveform method. Integrator 1 is used for this waveform as it is located at a precise delay after the initial sharp rise of the waveform,

replicating the waveform method. The waveform with the later trigger time (e.g., F1) is then shifted in time relative to that with the earlier trigger time (e.g., F2) to set them at the correct relative timing. The integrator chosen for the shifted waveform (e.g., $F1_{tc}$) is that which has a start time closest to integrator 1 for the reference waveform (e.g., $F2_{tc}$). This is shown by the proximity of the vertical blue dashed line to the left edge of integrator 6 in panel (b) of Figure 3.8. The baseline integrator value is then subtracted from these chosen integrator values to obtain Q_{F1}, Q_{F2}, Q_{B1} and Q_{B2}.

It has been explored whether the performance of the closest integrator method can be improved by using linear interpolation for selecting the integral value of the waveform with the later trigger time. An example of this procedure is shown in Figure 3.9. For this event, F2 and B1 are the reference waveforms with the earlier trigger times than F1 and B2 respectively. In the closest integrator method, the integral value for integrator 6 would be chosen for F1 and and the integral value for integrator 2 would be used for B2. Instead, the integral value chosen can be linearly interpolated between the two neighboring integrators (i.e. integrator 6 and 7 for F1). For events where the ideal start time is earlier than the integrator 7 start time, the integral value for integrator 7 is used instead. The shape of the integral - integrator curves shown here depend on integration delay and length. The integrator spacing of 88 ns used in this work leaves a maximum error in the waveform alignment of 44 ns.

For all integration delays and lengths explored in this work, the linear interpolation procedure was also tested; however, no statistically significant improvement to the energy resolutions was obtained. As an example, the ^{228}Th source spectra both with (black solid) and without (red dashed) linear interpolation is shown in Figure 3.10, where it is clear that there is not a significant difference between the two results. A significant difference between the energy resolution of the closest integrator method and waveform method was only observed for short integration lengths with a delay of 0.6 µs. As such, it is likely that the uncertainty that leads to this discrepancy is not caused by the integrator spacing.

The other uncertainty present in the closest integrator method comes from how the

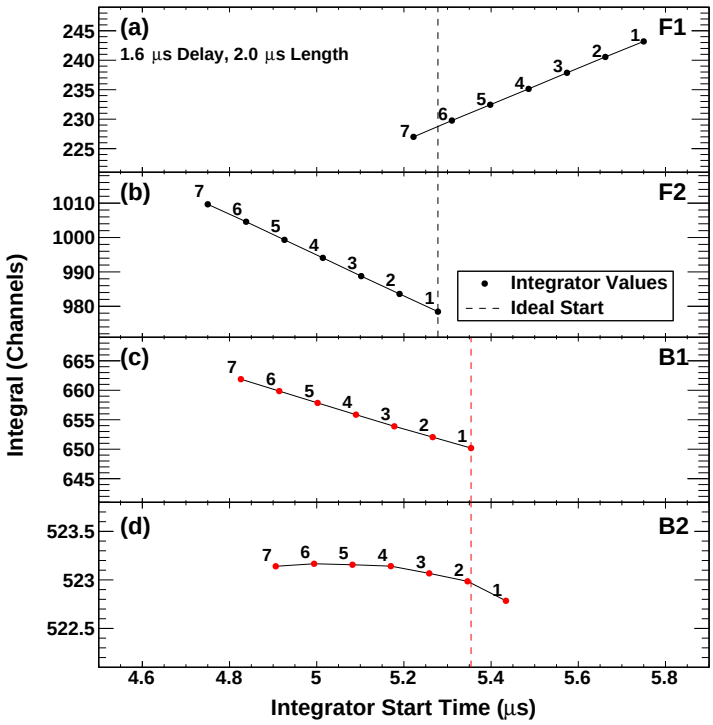

Figure 3.9: Procedure for closest integrator method linear interpolation. Baseline-adjusted integral for each integrator is shown as a function of the integrator start time for F1 (panel (a)), F2 (panel (b)), B1 (panel (c)), and B2 (panel (d)) for a single event. Integrator numbers are shown next to each point. This example event has a delay of 1.6 µs and an integration length of 2.0 µs. Reprinted with permission from [13].

integration reference time is determined. In the waveform method, a consistent reference time is determined by summing the time-corrected waveforms from each face and finding where this sum waveform reaches threshold (in this case, 100 channels above baseline); this allows for all waveforms to be integrated in a region with the same relative timing to the time of particle incidence. The shape of this sum waveform is consistent for any particle position as evidenced by panels (c,f) of Figure 3.6 which contains data across the entire face of the DADL detector. For the closest integrator method, the integrators can only be placed relative to the ADC trigger for each individual signal; the approximation that must be made is that the ADC trigger time relative to the time of particle incidence for the contact closest to the particle position changes minimally with particle position. In Figure 3.12 panel (a),

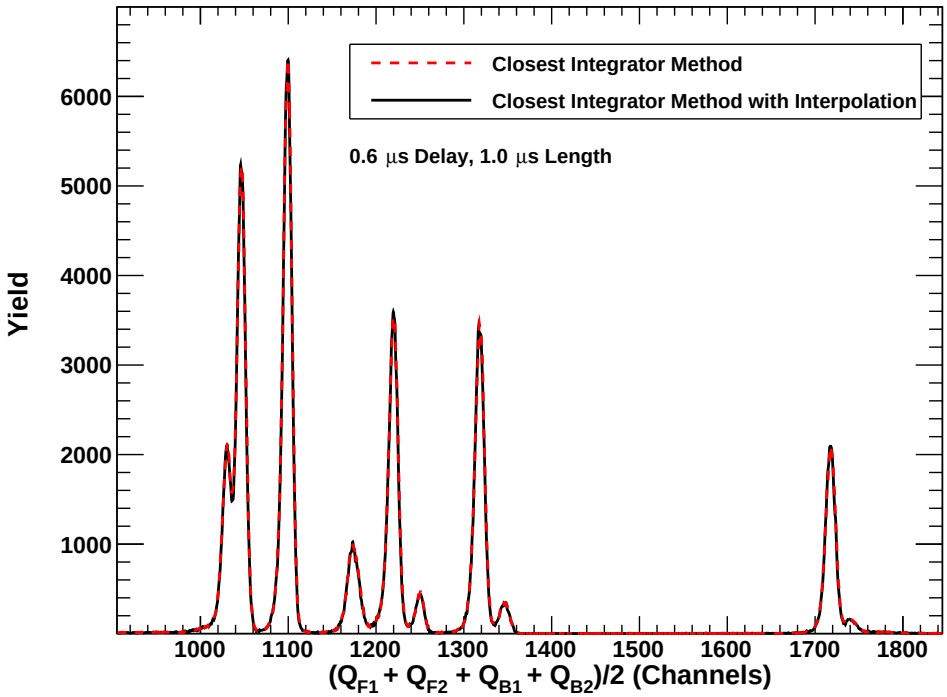

Figure 3.10: Linear interpolation result. Yield as a function of the measured charge of ^{228}Th source spectra using the closest integrator method with (black solid) and without (red dashed) linear interpolation using a delay of 0.6 µs and an integration length of 1.0 µs. Reprinted with permission from [13].

the rise time for charge collected on the nearest contact for a particle incident near the edge of the face (black solid) is similar, but not the same as the rise time for a particle incident near the center of the detector (red solid). The difference between the reference time obtained using the waveform method and closest integrator method as a function of the difference in measured charge for B1 and B2 is shown in Figure 3.11. $Q_{B2} - Q_{B1}$ is proportional to the particle position. For particles near the left and right edge of the detector, the reference time difference is minimal, but for particles near the center, the reference time deviates by ∼100 ns. This error is over twice the maximum associated with the integrator spacing and systematically depends on the particle position. For short integration lengths and delays, this is the dominant source of error from the integration windows including larger fractions of the waveform rise, deprecating energy resolution; this effect becomes insignificant with

larger integration lengths and delays. It was also explored whether using the waveform with the earliest trigger time of all four DADL signals (rather than for the front and back face separately) could improve resolution by reducing this reference time uncertainty. In this case, the integrator start time for F2 would be used to select the integrator (or interpolated value) of the three remaining signals in Figure 3.9. Again, there was no improvement in the obtained resolution as the magnitude of the reference time uncertainty remains (i.e. particles incident in the center of the detector). Additionally, it is advantageous to perform the integrator method independently on the front and back face of the detector, as events that are missing a signal (either below threshold or above saturation) can be recalculated while still using the integrator method for the DADL face that measured both signals. This procedure is discussed further in Section 4.1.2. It is possible that the reference time uncertainty can be reduced by improving the ADC triggering parameters used for the DADL signals.

In previous work, a representation of the energy deposited in the detector was obtained by using either $Q_{F1} + Q_{F2}$ or $Q_{B1} + Q_{B2}$ [71, 12, 77]. Panel (a) of Figure 3.12 shows all four time-corrected waveforms for a single event. Despite the varying amplitudes and waveform shapes present, upon summation of each pair, the two sum waveforms agree well as shown in panel (b). Upon closer inspection of these summed waveforms, it is clear that a significant portion of the noise present in each have opposite polarity, shown most clearly in the inset. This feature arises due to each face collecting opposite charge-carriers. After amplification with the inverting preamplifiers, the negative polarity front face waveforms are flipped upon digitization so that all recorded waveforms have the same positive polarity. Therefore, noise that affects all four channels similarly can be cancelled by taking the average of the two waveforms as seen by the pink dashed waveform. Given this, $(Q_{F1} + Q_{F2} + Q_{B1} + Q_{B2})/2$ is used as a representation of the energy measured in the DADL for the remainder of this work.

The closest integrator method contains three free parameters: the integration length, the delay before the placement of the first integrator, and the integrator spacing. The

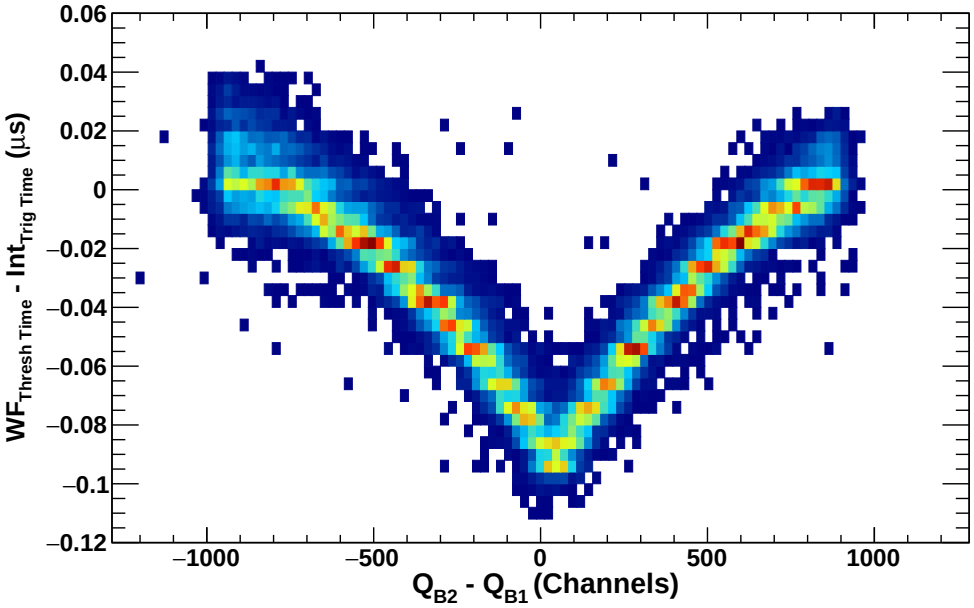

Figure 3.11: Trigger time uncertainty. Difference between the reference time obtained using the 100-channel threshold on the time-corrected sum waveform in the waveform method and the ADC trigger time of the earlier triggering waveform in the closest integrator method as a function of the difference between the two measured horizontal charges (B2 and B1). The data shown here is gated on the 8.78 MeV peak in the ^{228}Th source data. Reprinted with permission from [13].

integrator spacing is well constrained by the trigger time difference distributions. The two remaining parameters were explored to find optimal values for maximizing position and energy resolution. In the interest of benchmarking the improvement between choosing the closest integrator over the same delayed integrator, a third charge determination method (single integrator method) was implemented; this method uses only integrator 1 to integrate all waveforms. ^{228}Th source data was used for this study to simultaneously obtain the energy and position resolution of each method over a range of parameter values. For the energy resolution assessment, a multi-Gaussian fit was performed. The fit procedure constrains the energy spacing for the seven highest yielding α-decays while allowing the gain, offset, the common peak width, and the individual peak amplitudes to vary freely. A representative distribution and fit result are shown for the single integrator and closest integrator method

for two pairs of parameter values in Figure 3.13. The resolution for the closest integrator method in panel (b) is noticeably better than the single integrator method in panel (a), evidenced by the clearer separation in neighboring peaks at ∼1000 and ∼1200 channels. Whether the integration method or the method parameters are more responsible for this improvement will be studied further in this section. The three small peaks not included in

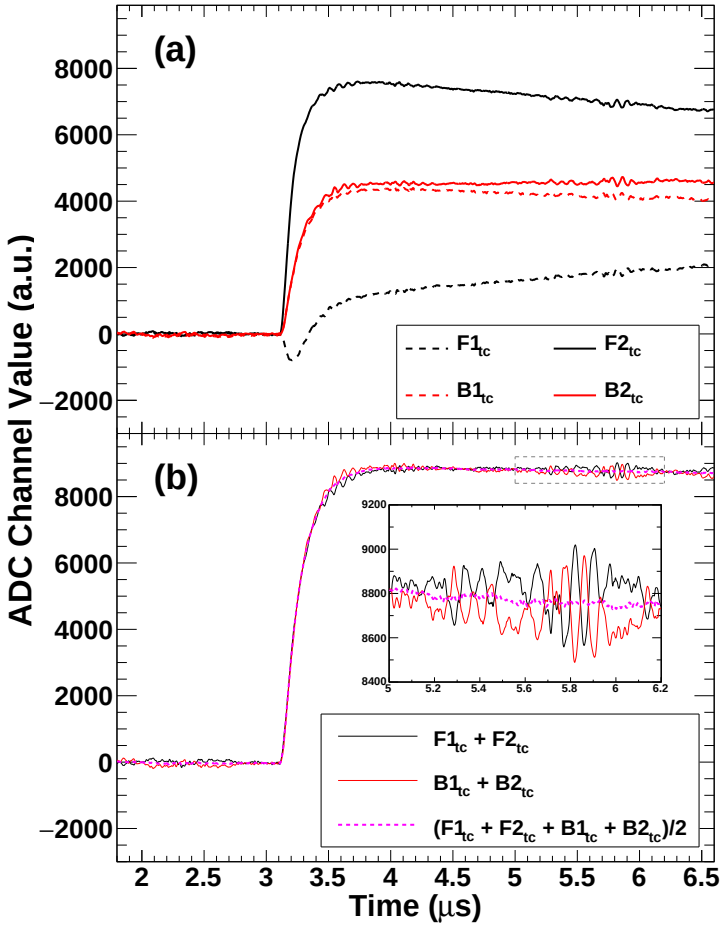

Figure 3.12: Noise cancellation. (a): Baseline-adjusted and time-corrected waveforms for F1 (black dashed), F2 (black solid), B1 (red dashed), and B2 (red solid) for the same event as Figure 3.8. (b): The time-corrected front sum (F1 + F2) (black) and back sum (B1 + B2) (red) waveforms are shown alongside the result of averaging (pink dashed). Noise is significantly reduced in the averaged waveform due to the opposite noise polarity between the front and back sum waveforms. The inset corresponds to the region indicated by the gray dashed box. Reprinted with permission from [13].

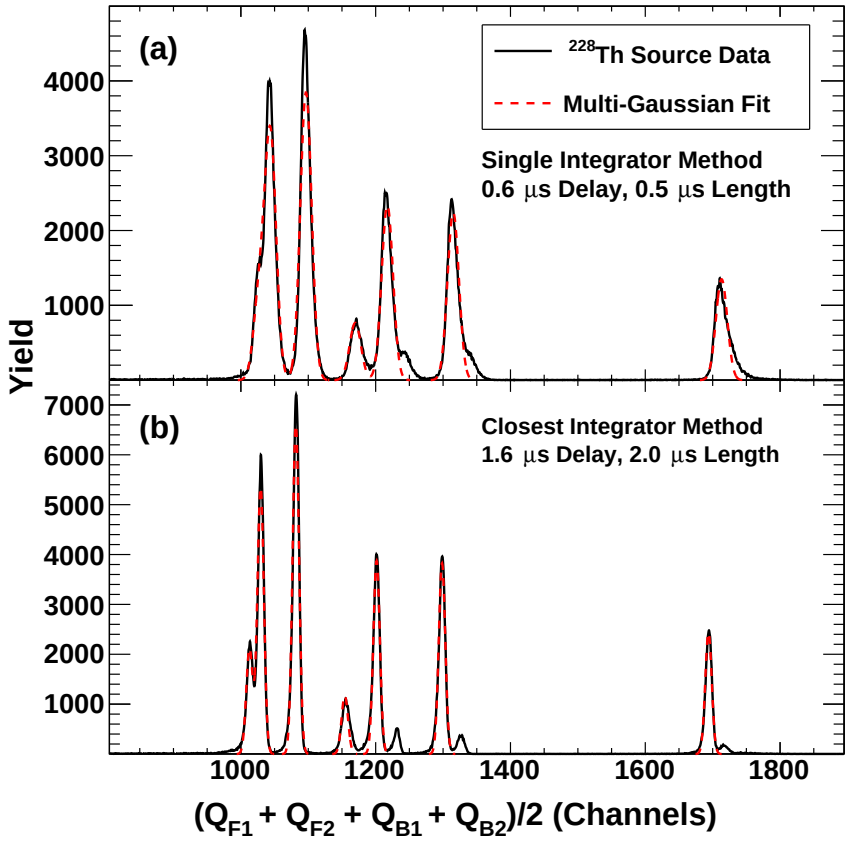

Figure 3.13: Energy resolution determination. Panel (a): Yield as a function of the measured charge for ^{228}Th source data using the single integrator method (black solid). The result of a constrained multi-Gaussian fit to the data to obtain the energy resolution is shown by the red dashed line. Panel (b): Same as panel (a) but using the closest integrator method with adjusted integration parameters. Integration parameters are displayed on the right side of each panel. Reprinted with permission from [13].

the fit (seen most clearly in panel (b)) are due to gaseous ^{220}Rn isotopes in the decay chain escaping the Mylar-covered source material. Measured α-decays that originate from escaped ^{220}Rn and subsequent decay chain isotopes do not lose energy in the Mylar covering.

To determine and compare the position resolution between methods and parameters, the raw x and y position distribution gated on the ^{228}Th 8.78 MeV α-particle was produced. To simultaneously obtain stretching parameters $c_{x,y}$ and offset parameters $s_{x,y}$, the distributions were fit with the sigmoid functional form (eq. 3.5) to determine the detector edges,

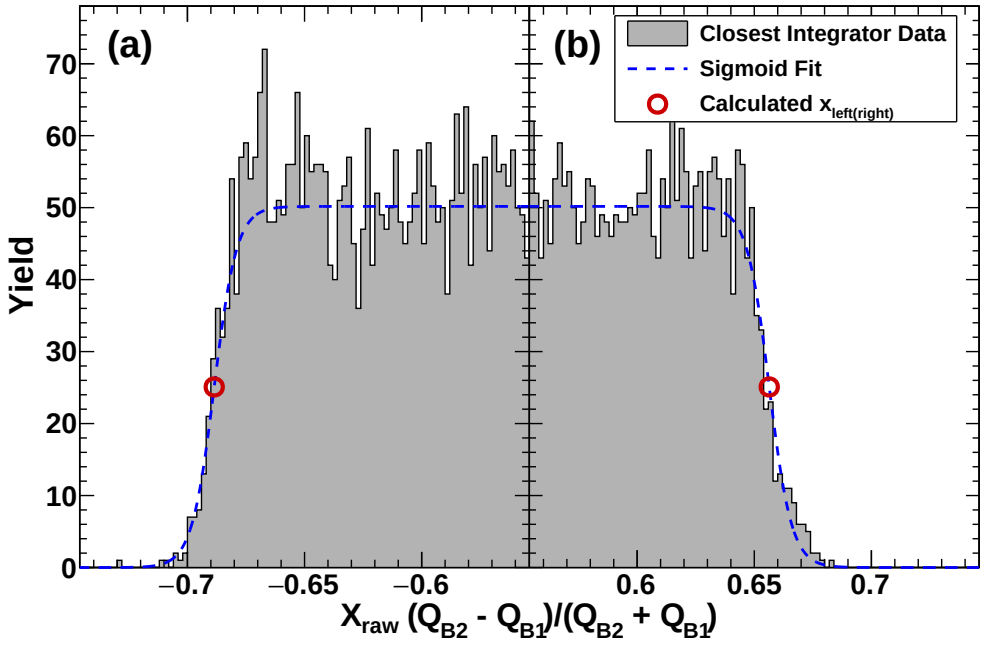

Figure 3.14: Position resolution determination. Raw position distribution (gray shaded region) gated on the 8.78 MeV α from ^{228}Th source data using the closest integrator method. The distribution is fit with Eq. 3.5 (blue dashed line). Panel (a): Position data near the left side of the detector where x_{left} (red open circle) is determined by the fit. Panel (b): Same as panel (a) but for x_{right}. Reprinted with permission from [13].

$x(y)_{left(right)}$, and the sigmoid width, σ.

$$f(x) = \frac{a}{1 + e^{(x - x_{\text{right}})/\sigma}} + \frac{a}{1 + e^{-(x - x_{\text{left}})/\sigma}} - a. \tag{3.5}$$

A representative distribution and fit to obtain the X-position resolution are shown in Figure 3.14. The resulting fit parameters are used to shift and scale both the position distribution and fit so that $x(y)_{left(right)}$ are at the physical dimensions of the DADL detector of -1 cm and 1 cm, respectively. The position resolution (σ_{Gaussian}) is defined as the Gaussian-distributed uncertainty to the measured particle position, and is linearly related to the scaled sigmoid width parameter σ_{sigmoid}. To determine the relationship between σ_{sigmoid} to σ_{Gaussian}, a simple model was developed. First, positions were randomly and uniformly sampled between -1 cm and 1 cm. A Gaussian distribution with a defined σ_{Gaussian} centered about 0 was randomly

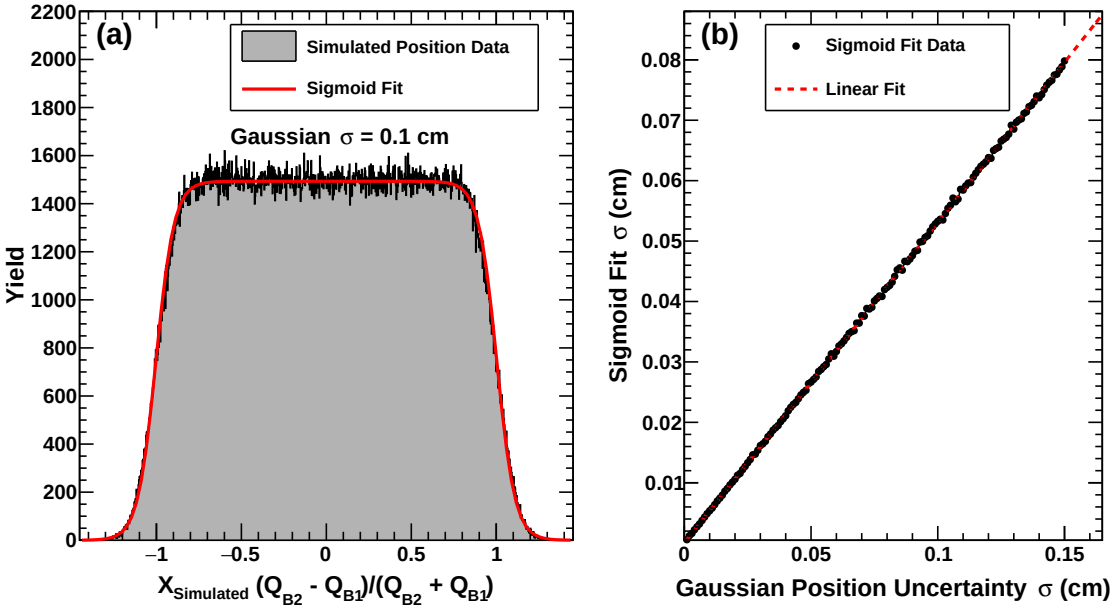

Figure 3.15: Panel (a): Simulated position distribution (grey-filled black) using a Gaussian-distributed uncertainty of 0.1 cm. A sigmoid fit using Eq. 3.5 is shown in red. Panel (b): Sigmoid fit parameter σ as a function of the input Gaussian position uncertainty. A linear fit of this relationship is shown as the red dashed line. Reprinted with permission from [13].

sampled and added to the position. This process was repeated many times to produce simulated position distributions over a range of σ_{Gaussian} values. A representative distribution for $\sigma_{\text{Gaussian}} = 0.1$ cm is shown in Figure 3.15 panel (a). The sigmoid function of Eq. 3.5 was fit to these distributions and the resulting σ_{sigmoid} was plotted as a function of the input σ_{Gaussian} as shown in Figure 3.15 panel (b). A linear fit was performed, giving $\sigma_{\text{sigmoid}} = 0.5300(\pm 0.0002)\cdot\sigma_{\text{Gaussian}}$.

Figure 3.16 shows the position and energy resolutions obtained for the three methods using integration lengths ranging from 0.5 µs to 5.5 µs in 0.5 µs increments with delays of 0.6 µs, 1.6 µs, and 2.6 µs. For the energy resolutions shown in panels (a,b,c), the waveform method unsurprisingly gives the best energy resolution with a minimum occurring near an integration length of 2.5 µs for the 0.6 µs delay. The shorter delay places the beginning of the integration window near the peak of the summed waveforms shown in panels (c,f) of Figure

3.6, where the charge measured reflects the energy deposited in the detector most accurately. The worsening energy resolution at short integration lengths is caused by noise features that fail to be integrated out due to their timescale. Because the data was taken under very well controlled laboratory conditions of low noise, the degradation in energy resolution with decreasing integrator length will typically be greater in accelerator experiments. For long integration lengths, energy resolution worsens as a larger fraction of the waveform tail is

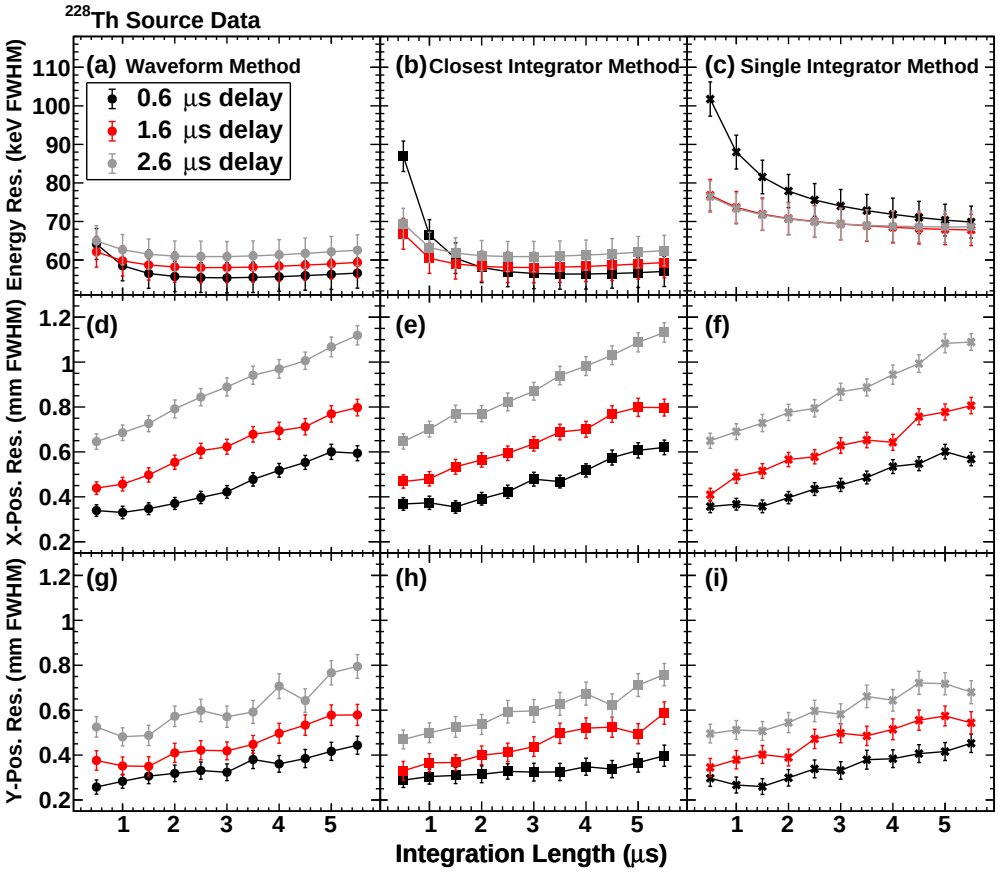

Figure 3.16: Integration parameter optimization using ^{228}Th data. Energy resolution (a,b,c), x-position resolution (d,e,f), and y-position resolution (g,h,i) as a function of integration length for the waveform method (a,d,g), closest integrator method (b,e,h), and single integrator method (c,f,i). Three separate delay values were tested for each and are distinguished by the marker color. The energy resolution was determined using the 7 major α-decays of the ^{228}Th decay chain while the position resolution was determined using only the 8.78 MeV α. Error bars are obtained from error in the fitting routines (multi-Gaussian fit, sigmoid fit). Reprinted with permission from [13].

included. These trends remain for the closest integrator method in panel (b), in addition to a notable effect for the 0.6 µs delay. While the closest integrator method is designed to integrate the waveforms at the same time of charge collection as done in the waveform method, the two approximations of the closest integrator method introduces uncertainty to how well the waveforms are aligned. The first approximation is the discretization of the waveform alignment dictated by the integrator spacing. The second approximation is that the waveform with the earlier trigger time (and by extension, faster rise-time) approximates well the time-corrected sum waveform trigger time of the waveform method. For the 0.6 µs delay, this misalignment can cause the integration window to include the rise of some waveforms; this is of particular concern for short integration lengths, as a larger fraction of the total integration contains this rise, yielding poorer energy resolution. As such, it is important to use a larger delay for the closest integrator method than the waveform method would suggest. For the 1.6 µs and 2.6 µs delays, the waveform alignment uncertainties do not contribute significantly to the integration result. The single integrator results in panel (c) clearly demonstrates that integrating the waveforms with similar relative timing is essential, as the resolutions here are notably worse than the other two methods across the entire range of integration lengths and delays. It is important to note that the poor performance of the single integrator method originates from position-dependent energy distortions similar in character to those seen in refs. [12, 77].

The trends in the position resolution between the three methods shown in panels (d-i) of Figure 3.16 are fairly consistent. Two waveforms for a given face approach unity at long times as seen in panel (a) of Figure 3.12. It is unfavorable to include portions of the waveforms where their amplitude difference is small, as the amplitude of electronic noise remains constant on average. Usage of a shorter delay leads to integration in a region with the largest difference in amplitude, giving improved resolution. Shorter integration lengths show a similar trend due to this effect. The position resolutions in panels (g-i) are, on average, better than the position resolutions in panels (d-f) due to the front signals having a

larger difference in amplitude than the back signals from its larger $R_{ext}/R_{Front(Back)}$. Again, it is important to note that the position resolution determination does not fully capture the position distortions present in the single integrator method. Nevertheless, choosing the optimal parameter set for the closest integrator method is a balance between energy and position resolution. A delay of 1.6 µs and an integration length of 2.0 µs gives the best energy resolution, with only a marginally worse position resolution than could otherwise be obtained with a shorter integration length. Appropriate parameters can be selected to meet the needs of a given experiment.

3.2.2 Impact on Data Rate

Data collection rates in an experiment are largely dictated by disk-writing, network, and ADC speeds. Holding these factors constant, the overall event rate can be increased by reducing the total amount of data collected for each event. The closest integrator method reduces the amount of data written per event by a factor of 250 over the waveform method (eight integration values compared to 2000 waveform bins) while providing comparable position and energy resolution. Even with multievent readout, the writing of all DADL waveforms for FAUST limited data rates on the order of ∼50 events per second. By reducing the amount of data written per event, the closest integrator method has allowed data collection rates up to ∼8,000 events per second.

3.3 FAUST Resolution

The closest integrator method was used in the collection of all collision data outlined in Table 2.1. For this experiment, it is essential to understand and characterize the position and energy resolution performance of FAUST to predict the uncertainty in the calculated excitation energy of high-multiplicity decays (e.g. 7-α disassembly events).

3.3.1 DADL Detector Model

The position resolution of the DADL detector depends on both the degree of charge-splitting that occurs, dictated by $R_{Front(Back)}/R_{ext}$, and the signal-to-noise ratio of each signal.

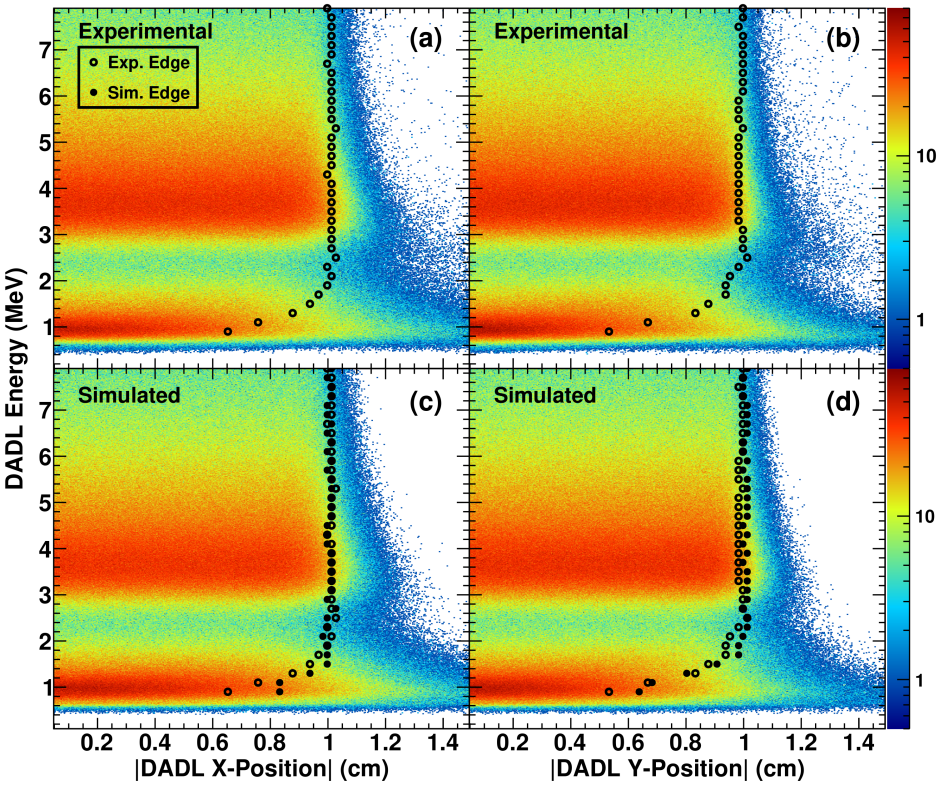

Figure 3.17: DADL detector model. Yield as a function of the energy (MeV) deposited in the DADL and the x-position (a) and y-position (b) in a single FAUST detector for 35 MeV/nucleon ^{28}Si + ^{12}C data. Panels (c) and (d) are analogous to (a) and (b), respectively, but for data produced using the DADL detector model as discussed in the text. For small slices in the DADL energy, the position where the yield is one-half that in the center of the detector (position = 0) is shown for the experimental data (black open circles) in all panels, and the simulated data (black solid circles) in the bottom panels. Reprinted with permission from [13].

Consequently, the position resolution depends on the energy deposited in the DADL detector, which depends on the particle type, incident energy, and detector thickness. This dependence for the X and Y position of a single DADL detector in FAUST is shown in panels (a,b) of Figure 3.17. The physical edge of the detector is located at ± 1 cm; however, calculated particle positions extend well past this region, especially for smaller energy deposits which have larger relative uncertainty in position. As the deposited energy decreases, it becomes increasingly difficult to trigger on the small signals that reach the contact farther from the

particle position, decreasing the effective active area of the detector. The open black circles in panels (a,b) of Figure 3.17 are a rough determination of x,y_{right} cut on the DADL energy to show this effect. While this effect does not impact the energy region corresponding to α-particles at 3.5 MeV, it does significantly impact the energy region corresponding to ^{1,2,3}H at 1 MeV. To reproduce these features of the DADL detector, a simple model was developed. For any given particle position, the charge that is collected on each contact was calculated according to the degree of resistive charge splitting that occurs. Then, Gaussian distributed noise was applied to each signal. This noise was designed to emulate the fast correlated electronic noise that has opposite polarity between the signals collected on the front and back face of the detector as seen in panel (b) of Figure 3.12. This noise is ultimately integrated out, so it serves only to aid in triggering on signals that would otherwise be below threshold, and was set to be a positive contribution to the signals. An additional Gaussian distributed noise was then applied to each signal, replicating the uncorrelated noise that contributes to uncertainty in charge determination. A threshold was then set to trigger on the four modeled charges. The energy distribution that is sampled is a slightly modified version of the experimentally measured energy distribution, so that after filtering it resembles the measured distribution once more. It is modified by scaling the yield below 2 MeV by a rough determination of $1/x,y_{right}$ indicated by the open (experimental) and solid (simulated) circles in Figure 3.17 to account for the missing yield in this region. To account for the high energy ^{1}H that produce signals well below threshold, exponentially decaying yield was added below $\sim$0.6 MeV. The position of the simulated particle was randomized and the procedure described above was performed as shown in panels (c,d) of Figure 3.17. The threshold and noise parameters were adjusted so that the experimental and simulated energy-position plots shown in Figure 3.17 showed reasonable agreement. Exceptional reproduction of the experimental features was obtained.

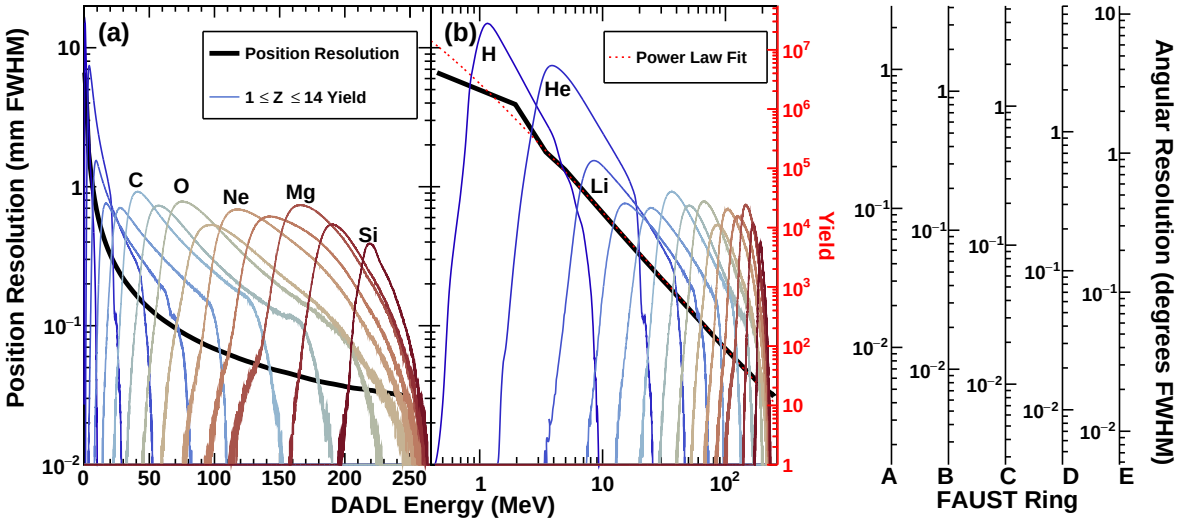

Figure 3.18: Position and angular resolution of the DADL detectors of FAUST. Panel (a): DADL detector position resolution (black line) as a function of the energy deposited in the detector. The experimental DADL energy distribution for each element measured in the ^{28}Si + ^{12}C collision data are labelled and overlaid to indicate the resolutions achievable for each. Panel (b): Same as panel (a), but with log-scale DADL energy to better show light charged particles. The red yield axis on the right side corresponds to the yield of the $1 \leq Z \leq 14$ distributions. The additional black axes to the right correspond to the angular resolution obtained for each ring of FAUST and corresponds to the black position resolution line. A power law is fit to the data in panel (b) as shown by the gray dashed line, giving Equation 3.6.

3.3.2 Position and Angular Resolution

The DADL detector model makes it possible to predict and calculate the DADL position resolution as a function of the energy deposited in the DADL detector as shown in Figure 3.18, which depends both on the particle type and particle energy. Moreover, it is capable of reproducing position- and energy-dependent threshold effects that exist for resistive silicon detectors. The position resolution of the DADL detectors depends strongly on the energy deposition. For lighter elements like hydrogen that deposit little energy (∼1 MeV on average for this experiment), the position resolution is on the order of 5 mm as seen in panel (b). The corresponding angular resolution in FAUST depends on which ring the particle was detected in due to the differing solid angle coverage of the DADL detectors. This DADL position

resolution translates to an angular uncertainty of ∼0.6° in ring A and ∼3° in ring E. For heavier particles of higher charge that deposit more energy, the position resolution quickly improves; for example, oxygen isotopes have an average position resolution of ∼60 µm as seen in panel (a). For the α-particles measured in FAUST, the position resolution spans ∼0.4 mm - 2.5 mm depending on the particle energy. The linear relationship between DADL energy and position resolution in log-log space as seen in panel (b) allows the dependence to be well described by a power law. By fitting the data (red dashed line in panel (b)), the position resolution can be calculated from the energy deposited in the DADL using:

$$\sigma_{FWHM} = 6.44(E_{DADL} - 0.98)^{0.17} \tag{3.6}$$

where σ_{FWHM} is the position resolution in mm, and E_{DADL} is the energy deposited in the DADL in MeV. Given the degree of sensitivity in the constraints to the noise parameters of the DADL detector model in Section 3.3, the calculated position resolution using Equation 3.6 has an approximate uncertainty of $\sim \pm 10\%$.

4. CALIBRATIONS

The numerous calibrations performed in this experiment to accurately determine the measured particle types, energies, and angles are outlined in this chapter. The calibrations associated with obtaining the energies deposited and particle locations in the DADL detectors is outlined in Section 4.1. The ΔE-E technique for particle identification used in this work is discussed in Section 4.2. Section 4.3 outlines the technique used for the light output to energy conversion for each element measured in the CsI(Tl) detectors. Various diagnostics used to assess and improve the quality of the calibrations are shown in Section 4.4. Characterization of the FAUST detector response and resolution are included in the detector filter, as discussed in Section 4.5.

4.1 Silicon Calibrations

The resistive DADL silicon detectors of FAUST require careful treatment and calibration to give accurate energy and position information. Due to the charge splitting mechanism of the DADL detectors, it is possible to miss measurement of some number of the four DADL signals for certain charged particles due to the signals being below threshold or above saturation (Section 4.1.1). Depending on the number and location of signals missing, information about the particle position and energy can still be obtained (Section 4.1.2). Additionally, due to the energy assessment of incident particles depending on the sum of multiple signals, the slight gain and offset variations between preamplifiers must be accounted for (Section 4.1.3). An accurate energy calibration of the DADL detectors is then obtained by using a mixture of radioactive sources and beam scatter data (Section 4.1.4). The raw measured position must also be scaled to reflect the physical location of particle incidence on the detector (Section 4.1.5).

4.1.1 Thresholds

It is important to ensure that the signals measured from the four contacts on each DADL detector reflect the charge liberated from incident charged particles and is unaffected by preamplifier saturation. To trigger on the smallest signals possible given the noise level of each channel, the trigger thresholds on each DADL channel were set to give ∼10 noise triggers per second. To exclude such noise triggers from further analysis, a noise threshold is placed on each channel as shown by the red dot-dashed lines in Figure 4.1. The location of this noise threshold was placed at the minima between the distribution associated with noise triggers that is centered about 0 channels, and the neighboring distribution centered about ∼40 channels that is largely associated with Z = 1 particles.

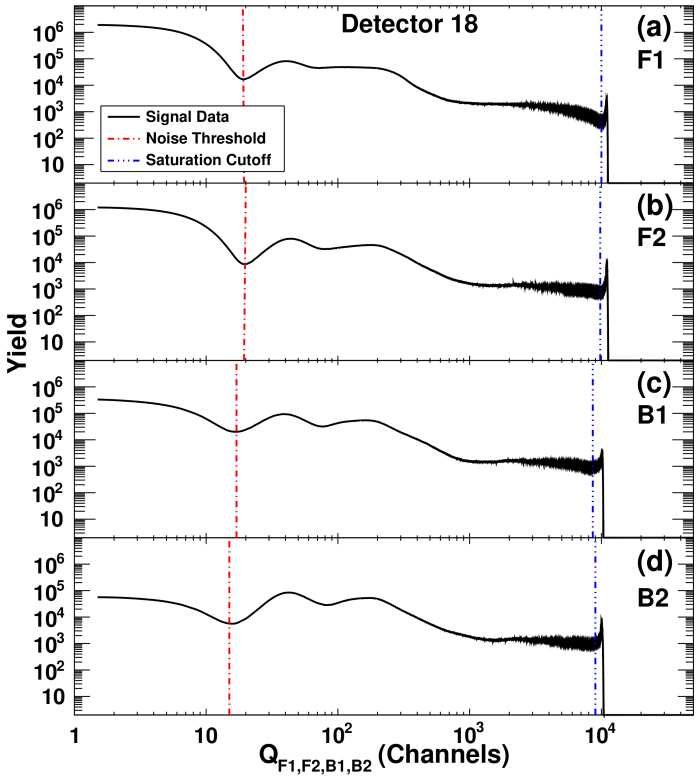

Figure 4.1: Noise threshold and saturation cutoff procedure for detector 18. Panels (a-d): Raw yield of $Q_{F1,F2,B1,B2}$ for all ^{28}Si + ^{12}C data obtained using only integrator 1 for each signal. Noise thresholds and saturation cutoffs determined for this detector are shown by the red dot-dashed lines and blue double dot-dashed lines respectively.

The output pulse from charge-sensitive preamplifiers begins to saturate when the preamplifier capacitor becomes fully charged. For the ∼45 mV/MeV preamplifiers used for the DADL signals, this occurs at ∼4 V. This saturation causes the signals to have a flat top once they reach this saturation voltage; the signal integrals contain varying degrees of saturation for large enough signals that depends on the amount of charge at the preamplifier input. To exclude signals affected by saturation from further analysis, a saturation cutoff is placed before the peak associated with saturated signals for each channel as seen by the blue double dot-dashed lines in Figure 4.1.

4.1.2 Missing Signal Calculations

All four DADL signals (above noise and below saturation) are measured for most charged particles in this experiment (measured 2F + 2B). However, high-energy light charged particles that deposit little energy (< 2 MeV) in the DADL can result in some signals being below threshold. Similarly, heavier ions (Z > 7) that deposit large amounts of energy (> 150 MeV) begin to cause some signals to saturate. The number of signals missing depends on both the energy deposited in the detector and the position of particle incidence (due to the position-dependent degree of charge splitting).

As previously discussed in Section 3.2.1, the energy deposited in the DADL detector is determined by averaging the sum of the two front and two back signals. However, the sum of either the two front or two back signals is also proportional to the energy deposited. Further, there is a tight correlation between the front sum ($Q_{F1} + Q_{F2}$) and back sum ($Q_{B1} + Q_{B2}$) for each DADL detector. As such, for particles where the measurement of only one signal was missed (measured 2F + 1B or 1F + 2B), the missing signal can be recalculated using the measured charges and the relationship between the front and back sum. The back sum as a function of the front sum for one of the DADL detectors is shown in Figure 4.2 panel (a). While there is some yield associated with incomplete charge collection (charge lost to the grounded back guard ring) below the main locus of data, a tight linear correlation between the two sums is seen. To accurately fit this correlation, an initial linear fit is performed

on the data in panel (a). A gate is then placed around this initial fit (±150 channels) to exclude incomplete charge collection measurements. A linear fit is then performed on this gated data shown in panel (b) to give the slope (m) and offset (b) of the front sum to back sum relationship. In the case of an event missing measurement of Q_{F1}, the equation to calculate Q_{F1} given the measurement of Q_{F2}, Q_{B1}, and Q_{B2} is:

$$Q_{\mathrm{F1}} = \frac{Q_{B1} + Q_{B2} - b}{m} - Q_{F2} \tag{4.1}$$

With this procedure, the x-position, y-position, and energy of three signal events is retained. To show which particle types and energies this procedure recovers, the light output measured in the CsI(Tl) detector as a function of the energy deposited in the DADL silicon detector for three signal events is shown in panel (b) and panel (f) of Figure 4.3. The three loci of data in panel (b) where the missing signal is below threshold correspond to ^{1}H, ^{2}H, and ^{3}H

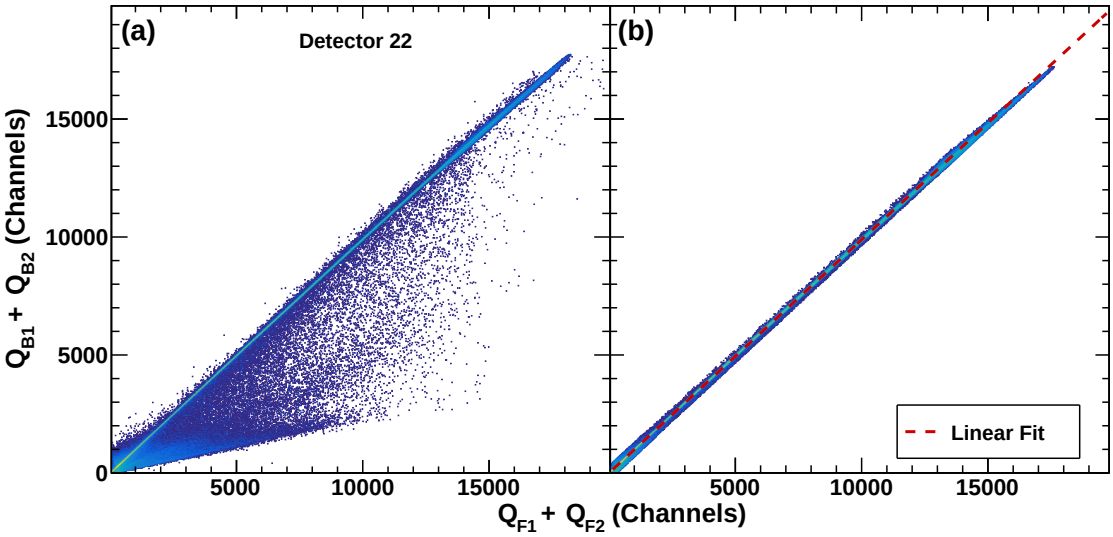

Figure 4.2: Back vs. front calibration for the DADL detectors. Panel (a): Sum of charge measured on the back face of the DADL (channels) as a function of the sum of charge measured on the front face of the DADL (channels) for events where all all four charges passed the noise and threshold cutoffs. Panel (b): Same as panel (a), but including a gate around the bulk of the data to exclude events where charge is lost to the back guard ring. A linear fit is performed on this gated data as shown by the red dashed line.

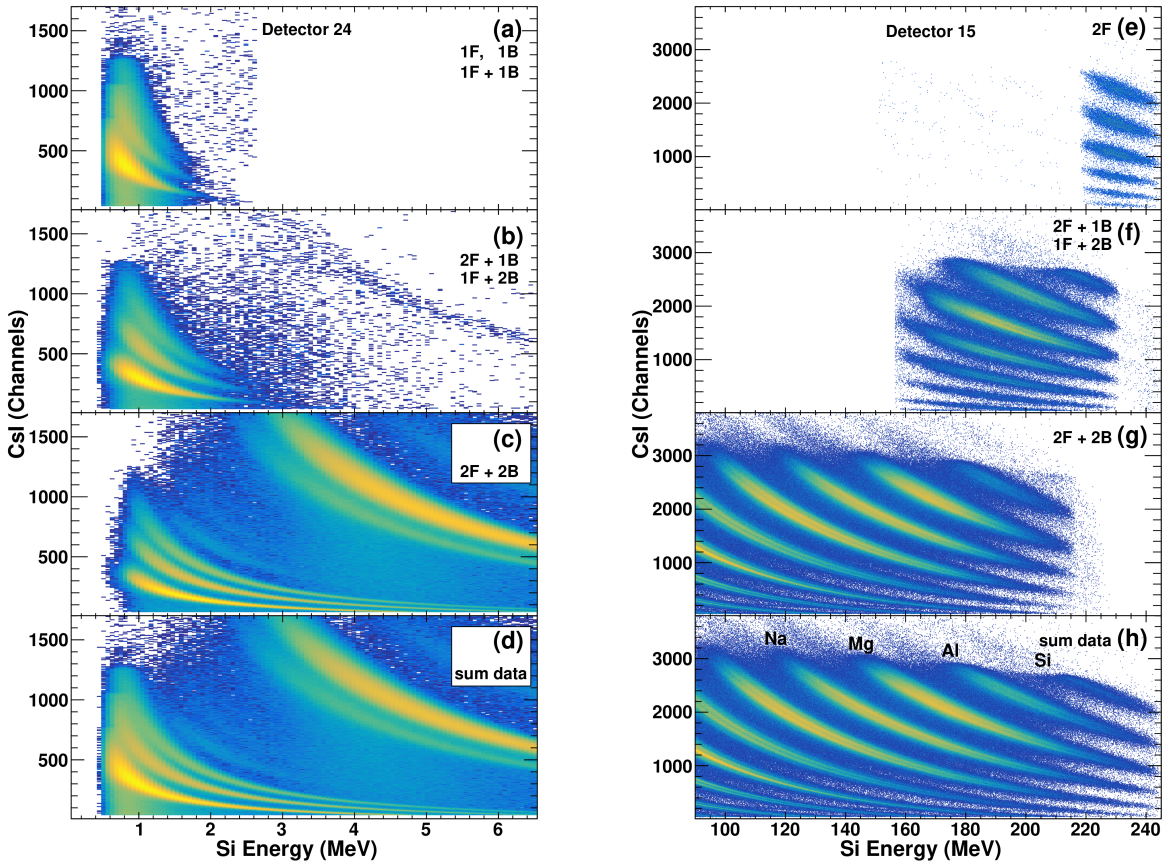

Figure 4.3: Missing signal recalculation scenarios. Panels (a-h) show the CsI light output as a function of silicon energy for recovered events with different configurations of measured signals. Panels (a-d): Recovered events for when the missing signals were below threshold for detector 24. Panels (e-h): Recovered events for when the missing signals were above saturation for detector 15. Panels (d,h) are the sum of all data contained in the panels above each, respectively.

particles. The details of why different particle types populate certain regions of this plot is discussed in Section 4.2. The loci of data in panel (f) where the missing signal is above saturation contains particles from oxygen (Z = 8) up through silicon (Z = 14).

A similar procedure can be performed for the other missing signal scenarios. In the case of only measuring two signals from the same face of the detector (measured 2F or 2B), the energy can still be calculated using the front sum to back sum relationship. However, there is no position information for the face with missing signals. While this scenario does not occur often for events where the missing signals are below threshold, it does occur significantly for

those with saturation. Due to the back signals saturating earlier than the front signals as seen in Figure 4.1, there are many heavy ions that fall into this category (Figure 4.3 panel (e)).

In the case of only measuring one signal on the front or back of the detector, or one signal on the front and one signal on the back (measured 1F, 1B, or 1F + 1B), there is no clear way to recover any energy or position information, as the total charge liberated on either face is not measured. However, if the single measured charge is assumed to be the total charge for that face when the missing signals are below threshold, the three loci corresponding to ^{1}H, ^{2}H, and ^{3}H particles can be seen (albeit with worse resolution) in Figure 4.3 panel (a). It is important to note that an offset value was added to the single charge values to reasonably align these events with the rest of the data as evidenced by the continuous distributions for the sum data in panel (d). Because particle identification can be performed for these events, the total energy can still be assessed using the residual energy measurement in the CsI(Tl) and calculating the expected energy loss in the DADL silicon on an event-by-event basis. While it is reasonable to assume that the particle position is closest to the contact that had measured charge, the particles were assigned a position in the center of the detector to not introduce any biased uncertainties. The consistency between the energy measured for four signal events and the energy calculated for the different missing signal scenarios is evidenced by the continuous nature of the particle type distributions in the sum data shown in panels (d,h).

4.1.3 Gain-Matching Correction

Due to the slight variations in preamplifier gain (k_i) and offset (j_i) between the two contacts on a given DADL face, there exists a dynamic linear position-dependence to the measured energy. When using the sum of all four contacts to determine the energy deposited in the detector as in Figure 3.12, if considering the ideal charge that is not affected by gain

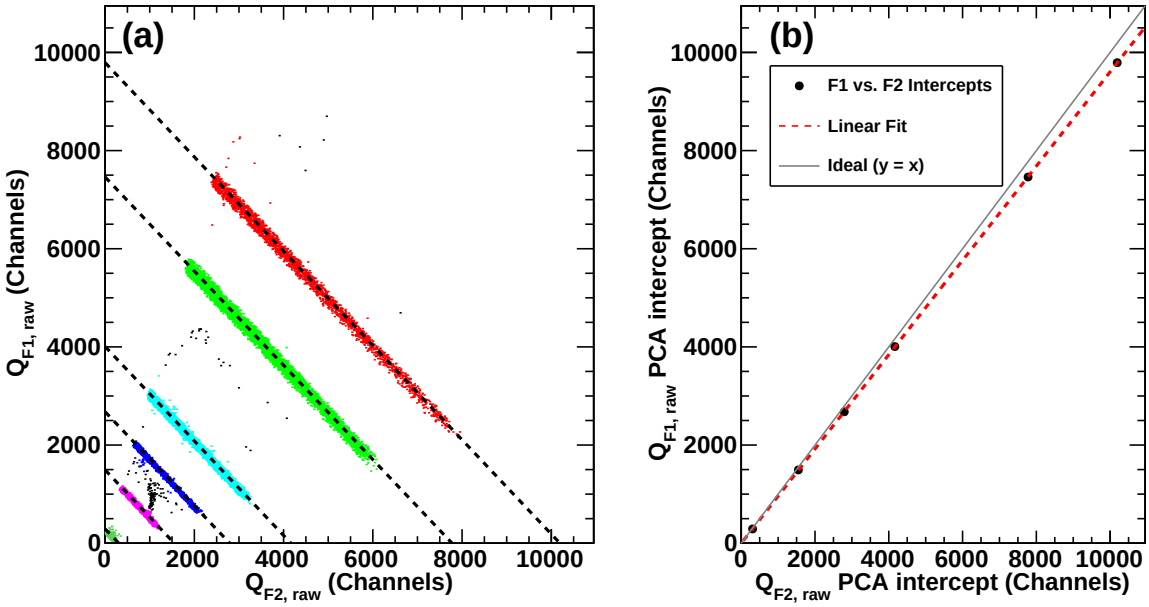

Figure 4.4: Panel (a): Raw measured charge for F1 as a function of raw measured charge for F2 for clustered bands (colored) of mono-energetic particles. These clusters are then fit using PCA (black dashed lines). Panel (b): Principal component analysis fit intercepts (from panel (a)) when $Q_{F2} = 0$ as a function of PCA fit intercepts when $Q_{F1} = 0$. A linear fit is applied to these data points (red dashed line). Deviation from ideal can be seen when comparing the fit results to a y = x line (gray solid line).

and offset differences (i.e., Q^*_{F1}), this can be expressed as:

$$E_{\text{measured}} = \frac{(k_{F1}Q^*_{F1} + j_{F1}) + (k_{F2}Q^*_{F2} + j_{F2}) + (k_{B1}Q^*_{B1} + j_{B1}) + (k_{B2}Q^*_{B2} + j_{B2})}{2} \tag{4.2}$$

A charge measured on the nearby contact for a particle incident on the edge of the detector (e.g., F1) should be the same for a particle incident on the opposite edge (e.g., F2). To characterize the degree of deviation from ideal across the DADL energy range relevant for the ^{28}Si + ^{12}C dataset, it is important to observe the relationship between measured $Q_{F1(B1)}$ and $Q_{F2(B2)}$ for discrete particle energies that will deposit similar energies across the entire face of the detector. To isolate such particles, a narrow gate was placed on the measured CsI(Tl) energy for various identified particle types as shown in Figure 4.4. The particle

identification procedure is discussed in Section 4.2. Each band of data points corresponding to mono-energetic particles of the same type were clustered using the Hierarchical Density-Based Clustering for Applications with Noise (HDBSCAN) algorithm [86]. These clusters, shown as different colors of data points, were then fit using principal component analysis (PCA) to determine the major axis as shown by the black dashed lines. The effect of the differing preamplifier gains and offsets is evidenced by the difference in the Q_{F1} and Q_{F2} PCA intercepts for each band. The relationship between the $Q_{F1}(Q_{F2} = 0)$ PCA intercepts and the $Q_{F2}(Q_{F1} = 0)$ PCA intercepts gives a clear linear relationship as shown by the fit (red dashed line) in Figure 4.4 panel (b). If there is no offset or gain difference between the two preamplifiers, this line would have a slope of $\alpha = 1$ and an intercept of $\beta = 0$ as shown by the gray line. Empirically for this detector $\alpha = 0.9605 \pm 0.0008$ and $\beta = -0.8 \pm 4.5$.

The gain correction can theoretically be applied in an infinite number of ways, but the transformation chosen for this work preserves the measured position while modifying both $Q_{F1(B1)}$ and $Q_{F2(B2)}$. In other words, the measured energy is adjusted to be independent of position, while the measured position is unchanged. It is important to note that possible dependence of the position on the preamplifier gains and offsets is later accounted for in the position-scaling using the sigmoid fitting (Section 4.1.5).

The α and β parameters obtained from performing the fit described above on each DADL detector of FAUST are used to calculate the corrected DADL front face energy ($EF_{meas,corr}$) as shown in Eq. 4.3. The raw y-position (Y_r) calculation is unchanged and is shown in Eq. 4.4 for completeness. The corrected energy and raw position can be used to calculate corrected charges, $Q^{corr}_{F1(F2)}$, as shown in Eqs. 4.5 and 4.6; these charges should be proportional to the ideal charges unaffected by gain and offset differences, $Q^{*}_{F1(F2)}$. Given the constraints of this transformation, the relative difference between Q^{corr}_{F1} and Q^{corr}_{F2} is identical to the relative difference between Q_{F1} and Q_{F2}. The process for obtaining the corrected DADL back face energy, $EB_{meas,corr}$, and corrected charges, $Q^{corr}_{B1(B2)}$, is analogous.

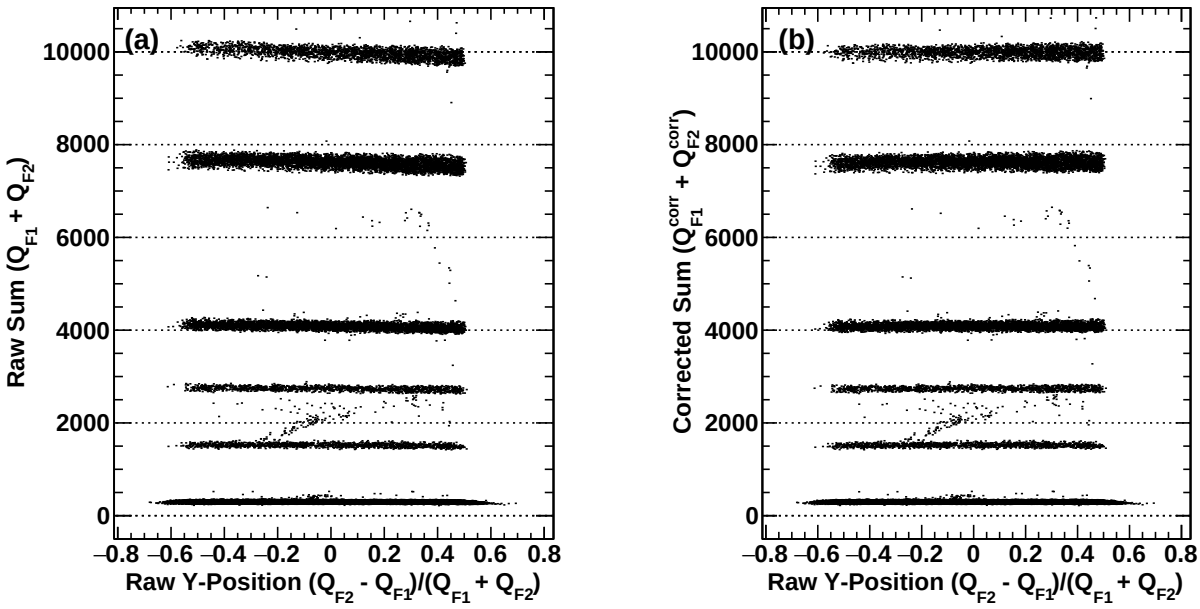

Figure 4.5: Panel (a): Raw measured DADL front sum ($Q_{F1} + Q_{F2}$) as a function of the raw measured y-position for the same clusters of data as in Figure 4.4 panel (a). Panel (b): Same as panel (a), but with the corrected front sum ($Q^{corr}_{F1} + Q^{corr}_{F2}$).

$$EF_{\text{meas,corr}} \propto \left(Q_{F1} + \frac{\beta}{2\alpha}\frac{Q_{F1}}{Q_{F1}+Q_{F2}}\right)\left(\frac{\alpha+1}{2}\right) + \left(Q_{F2} + \frac{\beta}{2}\frac{Q_{F2}}{Q_{F1}+Q_{F2}}\right)\left(\frac{\alpha+1}{2\alpha}\right) \quad (4.3)$$

$$Y_r = \frac{Q_{\text{F2}} - Q_{\text{F1}}}{Q_{\text{F2}} + Q_{\text{F1}}} \quad (4.4)$$

$$Q^{corr}_{F1} = EF_{\text{meas,corr}}\left(\frac{Y_r+1}{2}\right) \quad (4.5)$$

$$Q^{corr}_{F2} = EF_{\text{meas,corr}}\left(\frac{1-Y_r}{2}\right) \quad (4.6)$$

Figure 4.5 panel (a) shows the uncorrected energy as a function of position for the same clusters of data as used in Figure 4.4 panel (a). As the energy increases, the bands are

increasingly more skewed from horizontal due to the gain differences. Applying the transformation causes a small change in the orientation of these bands as shown in Figure 4.5 panel (b), where these bands are now more horizontal. While the correction here is somewhat subtle, it is essential for minimizing systematic error in the assessment of the particle energy.

4.1.4 Energy Calibration

To obtain the measured charge-to-energy calibration of each DADL detector, particles of discrete and known energies were measured over a broad range. A ^{229}Th radioactive source provides five discrete α-particle energies ranging from 4.8 to 8.4 MeV, but as the charged particles measured in this experiment deposit as much as 220 MeV in the DADL detector (with yield of heavier ions that deposit large amounts of energy increasing with decreasing laboratory θ), data from various beams scattered off a ^{197}Au target were also used to ensure an accurate calibration and to reduce the degree of extrapolation necessary.

For the ^{229}Th source data, it is important to take into account any α-particle energy loss that occurs between the source material and the detector active volume. For this purpose, a C++ implementation of the SRIM (Stopping and Range of Ions in Matter) energy loss tables was used for all energy loss calculations [87, 88, 89]. Before reaching the detectors, the α-particles pass through a 0.026 µm thick gold layer that coats the radioactive source, an aluminized Mylar foil (thickness depends on the ring and is quoted in Section 2.2.2), and the dead layer of the silicon detector (approximated as 0.1 µm). Because the gold layer and Mylar foils are perpendicular to the beam axis, the effective thickness that each particle passes through depends on the laboratory θ of the particle ($1/\cos\theta$ dependence). The effective thickness was calculated assuming the particle hit the center of each detector. The energy loss through the Mylar foils is most significant; for Ring A, the Mylar is thick enough to completely stop the three α-decays of lowest energy from the source. A multi-Gaussian fit was performed on the ^{229}Th source data for each detector (as in Figure 3.13), and the mean of each α-decay peak in channels was plotted as a function of the calculated energy

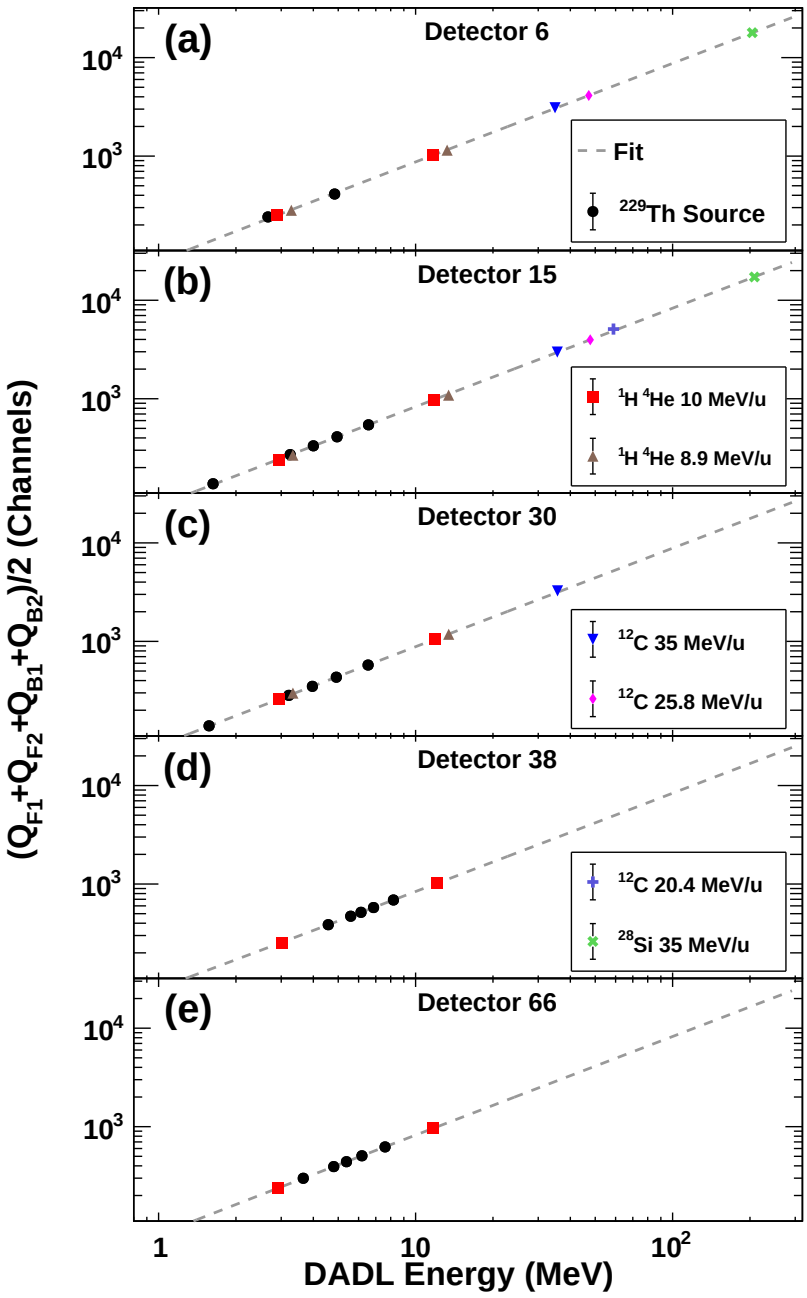

Figure 4.6: DADL Si energy calibration. Panels (a-e): Mean charge (Gaussian fit) measured from ^{229}Th source and beam scatter data as a function of the calculated DADL energy for a detector in each ring of FAUST. The color and style of each data-point corresponds to the data used as indicated by the legends. The series of data-points for each detector is fit with a linear equation to obtain the energy calibration.

as shown by the black data points in Figure 4.6. Detectors in separate rings that share the same Mylar foil show similar calculated DADL energy deposits for the ^{229}Th source α-decays (e.g. panel (b, c)). The average energy resolution (FWHM) for the 8.4 MeV α-decay peak is 1.3% for all DADL detectors, with some as good as 0.8%.

The beam scatter data used for energy calibration requires additional considerations for calculating the energy deposited in the DADL detectors. For the beam data that used an aluminum degrader to access lower incident beam energies, the energy loss of the beam particles through the degrader was calculated. Next, the energy loss through half of the ^{197}Au target thickness was calculated (to assume that the scattering occured in the middle of the target). The elastically scattered beam particle energy at the laboratory θ of each detector center was calculated using:

$$E(\theta) = E_p \left(\cos\theta + \sqrt{\frac{A_t^2}{A_p^2} - \sin^2\theta} \right)^2 \left(\frac{A_p}{A_p + A_t} \right)^2 \tag{4.7}$$

where $E(\theta)$ is the scattered particle energy at the measured angle, E_p is particle energy before scattering, A_p is the mass of the beam particle, A_t is the mass of the target, and θ is the laboratory angle of the detector that measured the scattered particle. This equation conserves the total momentum and kinetic energy for two-body scattering. The energy loss through the remaining half of the ^{197}Au target thickness, the Mylar foil, and the silicon dead layer was calculated as described previously. The remaining scattered particle energy in each case is large enough to pass entirely through each DADL detector. The energy deposited in each DADL was calculated using the detector thicknesses reported by Micron semiconductor (Table 2.2). The distribution of measured charge for each elastic scatter data set for all detectors with sufficient yield was fit with a Gaussian distribution, and the mean was plotted as a function of the calculated DADL energy deposition as shown in Figure 4.6.

As the laboratory θ of the detectors increase, there is less yield of scattered events, decreasing the number of useful calibration points; however, the mass distribution (and DADL

energy distribution) of measured particles also decreases with θ. Collinearity was found between the ^{229}Th and beam scatter calibration points for all detectors. The calibration points were fit with a linear equation to obtain the measured charge to energy conversion for the DADL detectors.

4.1.5 Position Calibration

As discussed in Section 3.1, the calculated raw particle x- and y-positions in the DADL detector (the relative difference between the two measured charges for each detector face) are both compressed and shifted as shown in panel (a) of Figure 4.7. To scale the raw position data to span the physical dimensions of the DADL detector, the raw position distributions are fit with Equation 3.5 to determine the sigmoid inflection point of each edge as shown by the black dashed lines. To ensure significant yield in the raw position plots for this procedure, a mixture of ^{28}Si + ^{12}C collision data (for Rings A, B, and C) and ^{229}Th source data (for Rings D and E) was used. The edges are then used to calculate the scaling parameters,

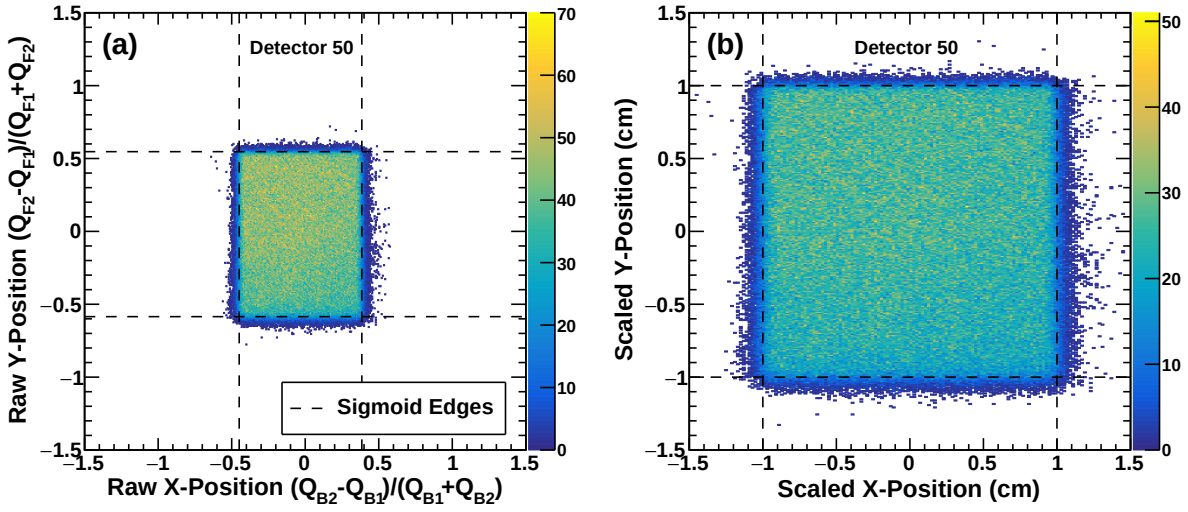

Figure 4.7: DADL position scaling procedure. Panel (a): Raw unscaled position plot of ^{229}Th source data for DADL detector 50. Black dashed lines indicate the edges calculated from performing sigmoid fitting (Eq. 3.5) of projected position data. Panel (b): Same data as panel (a), but scaled using Eqs. 3.1 and 3.2 to span the physical dimensions of the DADL detector.

$c_{x,y}$, and offset parameters, $s_{x,y}$ for each DADL. The calibrated x- and y-positions can then be calculated using Equations 3.1 and 3.2 as shown by the scaled position data in panel (b). The geometric design specifications of the FAUST detectors is used to transform the calibrated local DADL position to the global FAUST angle for each measured particle.

4.2 Particle Identification

The charged particles measured in FAUST lose some amount of energy in the thin DADL silicon (ΔE) detectors, and deposit the remaining energy in the thick CsI(Tl) (E) detectors. In the energy regime for charged particle reaction products produced and measured in this experiment ($>$ 1 MeV), the mechanism for energy loss in matter is dominated by electronic stopping. With this, charged particle energy loss through matter is well described by the Bethe-Bloch equation [90, 91]. The dependencies in this equation pertinent to the relationship between the energy deposited between the ΔE and E detector is:

$$\frac{dE}{dx} \propto \frac{Z^2 A}{E} \tag{4.8}$$

where Z and A are the charge (proton number) and mass (nucleon number) of the charged particle accordingly. The ΔE-E technique for particle identification makes use of this relationship where plotting the remaining energy in the E detector as a function of the energy lost in the ΔE detector reveals distinct clusters of data corresponding to different elements and isotopes as shown for a detector in each ring of FAUST in Figure 4.8. Each elemental cluster has similar spacing when viewing this relationship in square-root space (as in Figure 4.8) due to the Z^2 dependence of energy loss in Equation 4.8. The finer structure within these clusters corresponds to different isotopes of each element. This is most clearly seen for the three isotopes of hydrogen (Z = 1) on the left-most side of each panel.

While there have been some efforts to automate the labelling of the charge and mass of each measured particle in ΔE-E space, applicability to any given experiment remains difficult due to the shape and characteristics of the clusters depending heavily on the detector

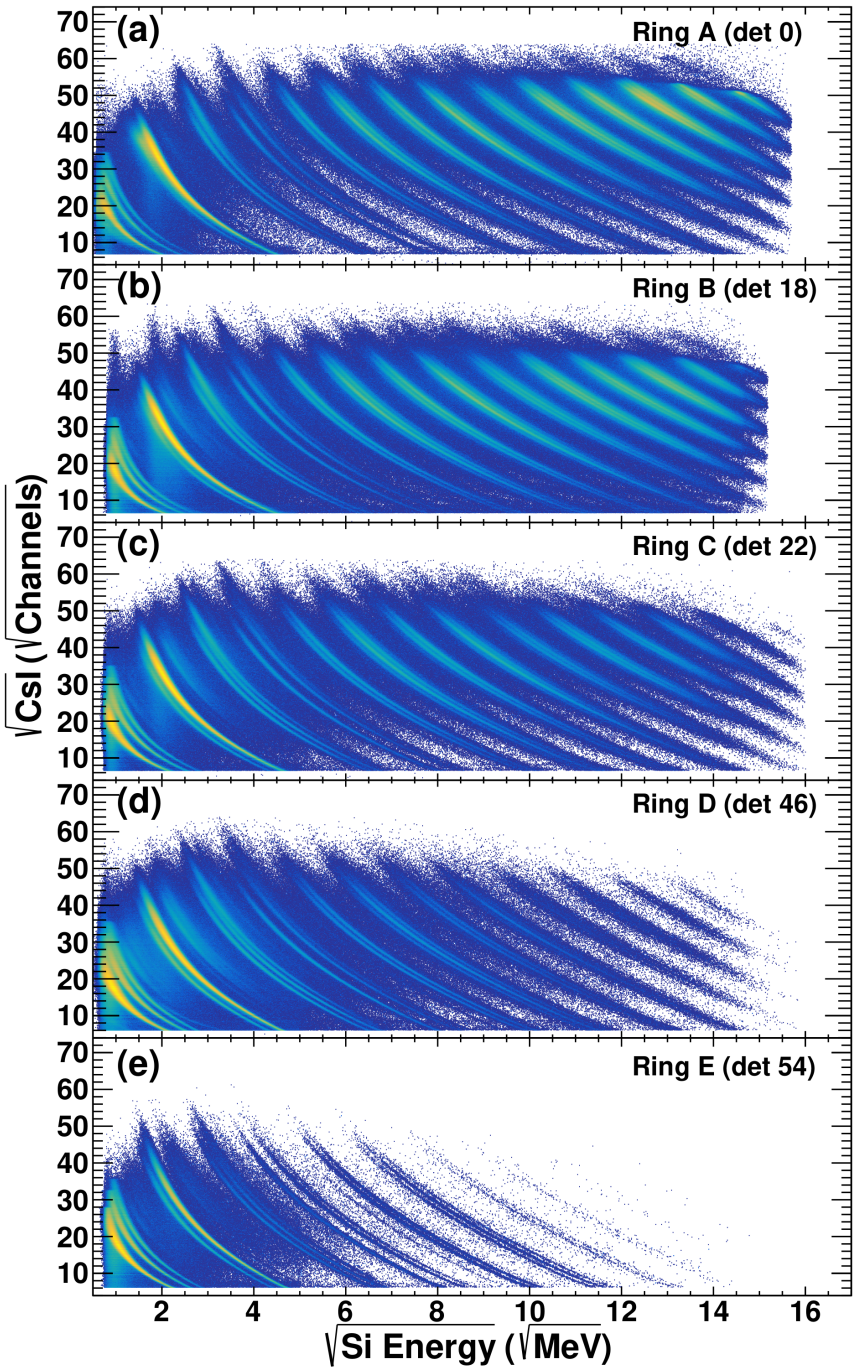

Figure 4.8: ΔE-E for a detector in each ring of FAUST. Panels (a-e): CsI(Tl) light output as a function of DADL silicon energy in square-root space and with logarithmic color scale to better see the full range of particle types for rings A-E respectively. Elemental separation is seen by the separate larger clusters of data (Z = 1 up to Z = 14 for panels (a,b) (rings A and B)), while isotopic separation is seen by the finer structure within each elemental band.

apparatus and collision parameters [92]. For this experiment, the linearization technique was used for elemental and isotopic identification [93]. First, points are hand-picked along each elemental cluster for every detector of FAUST as shown by the red stars in panel (a) of Figure 4.9; multiple series of points are picked for lighter elements to improve the linearization

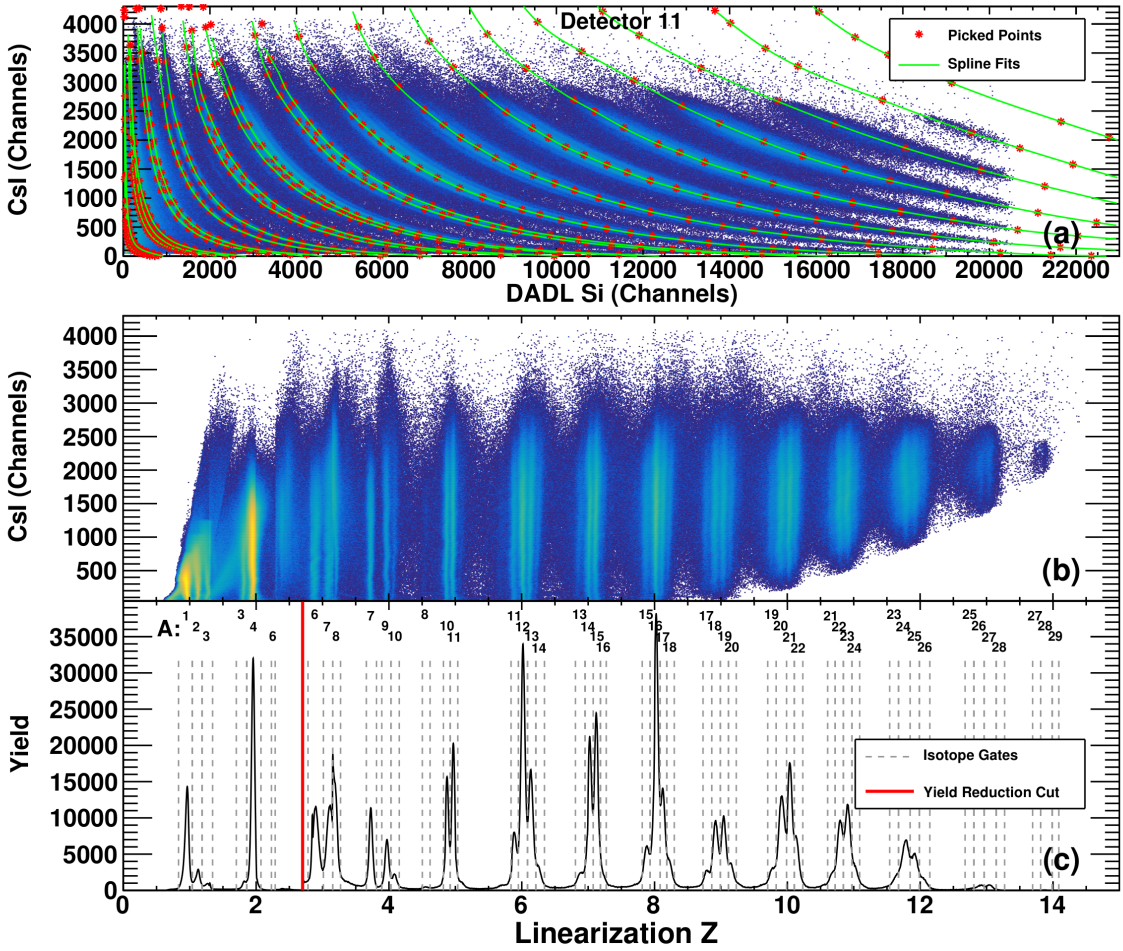

Figure 4.9: Linearization procedure for particle identification for a detector telescope in ring B. Panel (a): ΔE-E (channels) including missing signal recalculations. Points picked by hand along elemental and isotopic clusters of data are shown by the red stars. Spline fits performed on the picked points are shown by the green lines. Panel (b): The data from panel (a) is transformed so that the spline fits are now vertical and linear. Panel (c): The data from panel (b) is projected to the x-axis. Gates are placed around each isotope to give particle identities. The particle charge (Z) of each gate is shown by the x-axis units, while the particle mass (A) of each gate is indicated above the gates. The yield for Z = 1,2 particles is reduced by a factor of 25 to better show the yield distributions for heavier isotopes.

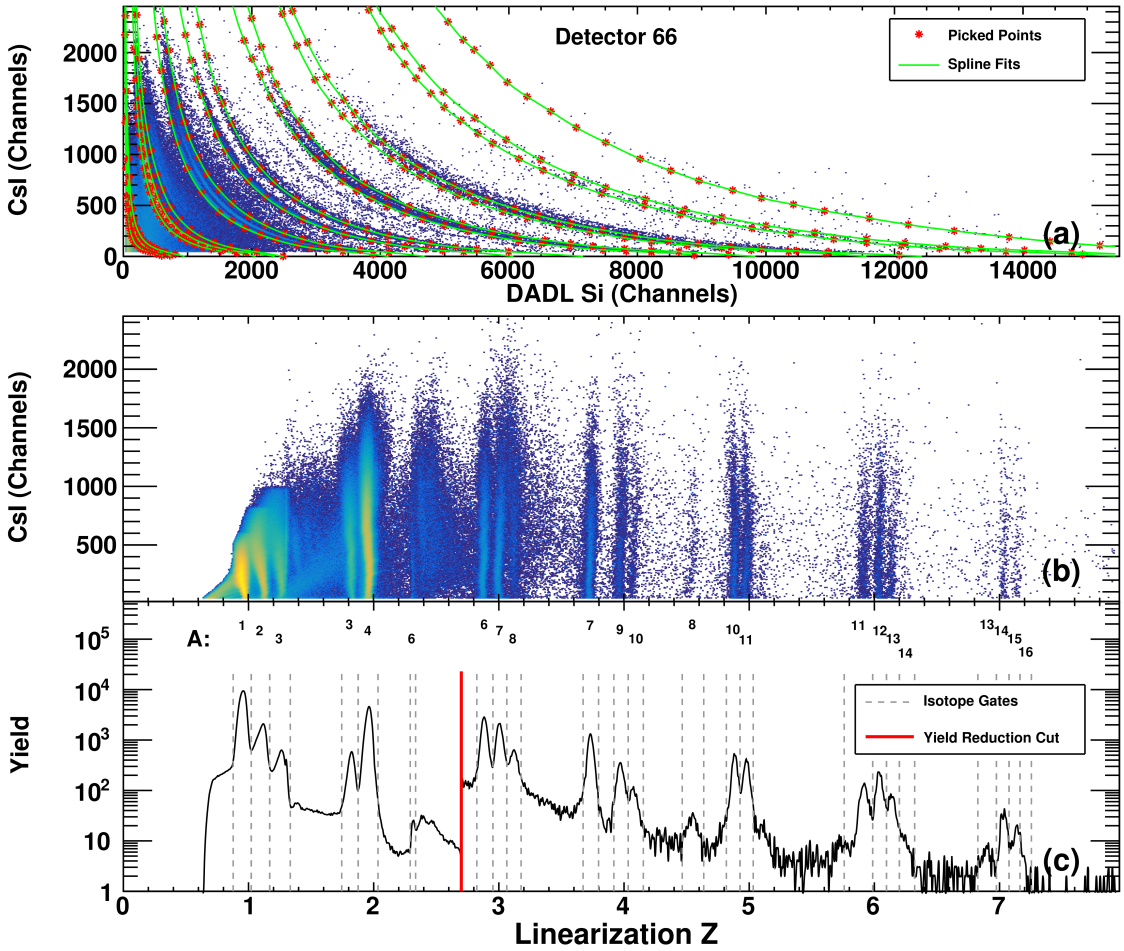

Figure 4.10: Linearization procedure as in Figure 4.9 but for a detector telescope in ring E.

quality in this region. The series of points are then fit with third order polynomial spline functions as shown by the green lines in panel (a). A spline-spline interpolation algorithm then linearizes the data so that each spline function is now vertical in panel (b). The projection of this data to the x-axis reveals distinct distributions associated with each isotope measured in this experiment (panel(c)). Gates are then placed around each isotope to label the particles with their mass and charge as shown by the vertical gray dashed lines. The location of each gate is placed to intersect the minimum between neighboring isotope distributions. While the isotopic resolution degrades as the mass and charge increases (increasing contamination of neighboring isotopes within the gates), the resolution of the FAUST detectors allowed for mass and charge identification over the entire range of measured particles.

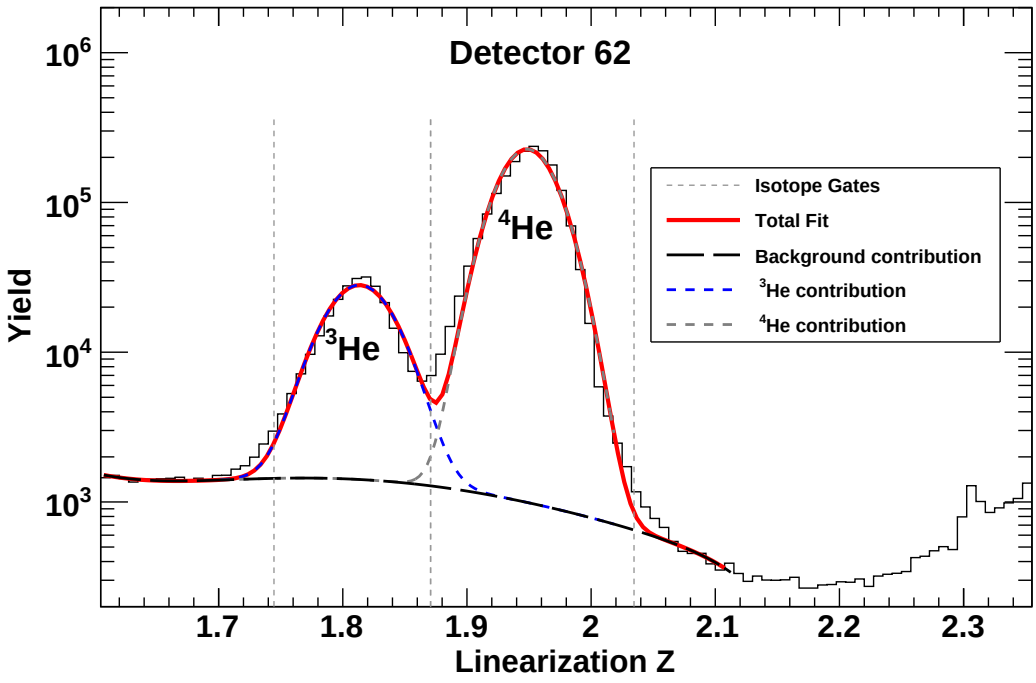

Figure 4.11: Determination of ^{3}He and background contamination for particles identified as ^{4}He for a detector in Ring E of FAUST.

The sharp-peaked artifact for the lithium (Z = 3) isotope distributions is caused by heavy contamination of α-α double hits (two α-particles incident on the same detector telescope), as they populate the same region in ΔE-E space; it is not possible to separate these double hit events from lithium isotopes for this experiment. However, other common double-hit scenarios populate regions between elemental clusters and do not significantly contaminate the isotope gates. For instance, ^{1}H + ^{1}H, ^{1}H + ^{2}H, and ^{1}H + ^{3}H populates the region between the hydrogen and helium isotopes and can be seen in panel (d) of Figure 4.8 ($\sim$2 MeV$^{1/2}$ Si, $\sim$20 channels$^{1/2}$ CsI(Tl)). Additionally, ^{4}He + ^{1,2,3}H populates the region between the helium and lithium isotopes ($\sim$3 MeV$^{1/2}$ Si, $\sim$30 channels$^{1/2}$ CsI(Tl)). The broad, featureless, and low-yielding background seen in all ΔE-E distributions largely originates from events where one or more neutrons are coincident on the same detector telescope as a charged particle; CsI(Tl) detectors have some sensitivity to neutron detection [94]. The linearization procedure for a FAUST detector at larger laboratory θ that receives and measures particles of lighter

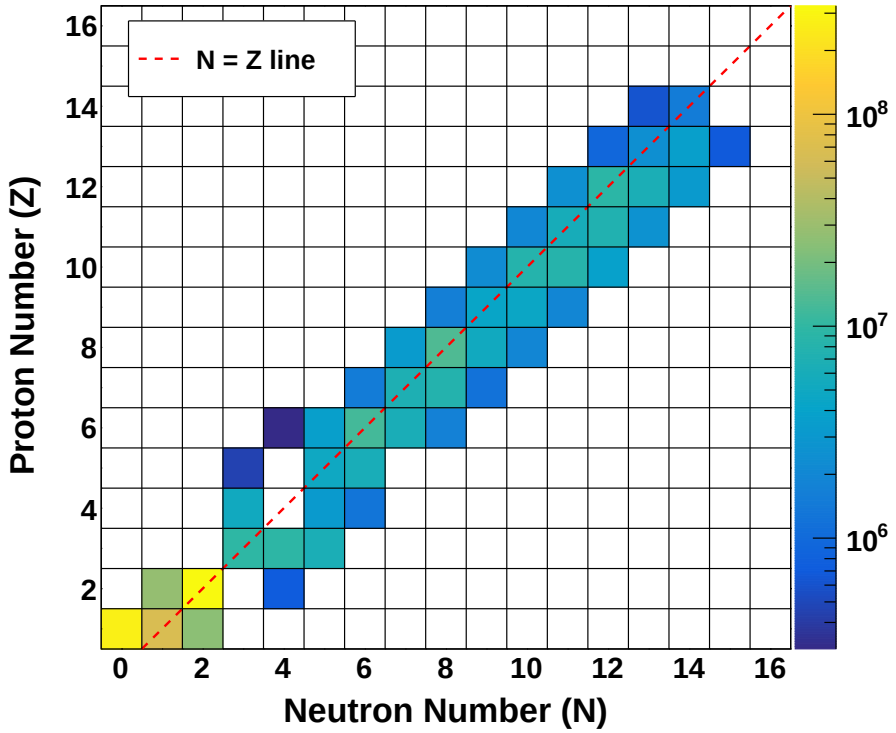

Figure 4.12: Yield of all isotopes identified in the ^{28}Si + ^{12}C collision system using the technique outlined in Figure 4.9. A red dashed line corresponding to N = Z is shown for reference.

mass and charge on average is shown in Figure 4.10. The linearization procedure is very sensitive to any changes in the gain of the DADL silicon and CsI(Tl) detectors. The quality of the linearized distributions was monitored in one hour increments to ensure robustness of the FAUST telescopes to gain drifts; the linearization parameters gave the same quality of particle identification for the duration of the experiment.

With the measurement of complete α-particle disassembly events being the focus of this work, it is important to characterize the level of ^{3}He and background contamination for ^{4}He-identified particles. The projected ^{3,4}He isotope distributions for one FAUST detector are shown in Figure 4.11. A double-Gaussian (^{3,4}He) with a fifth order polynomial (background) is fit to the distribution to assess each contribution. The fit contributions were integrated within the ^{4}He gate, giving a ^{3}He contamination of 0.2% and a background contamination

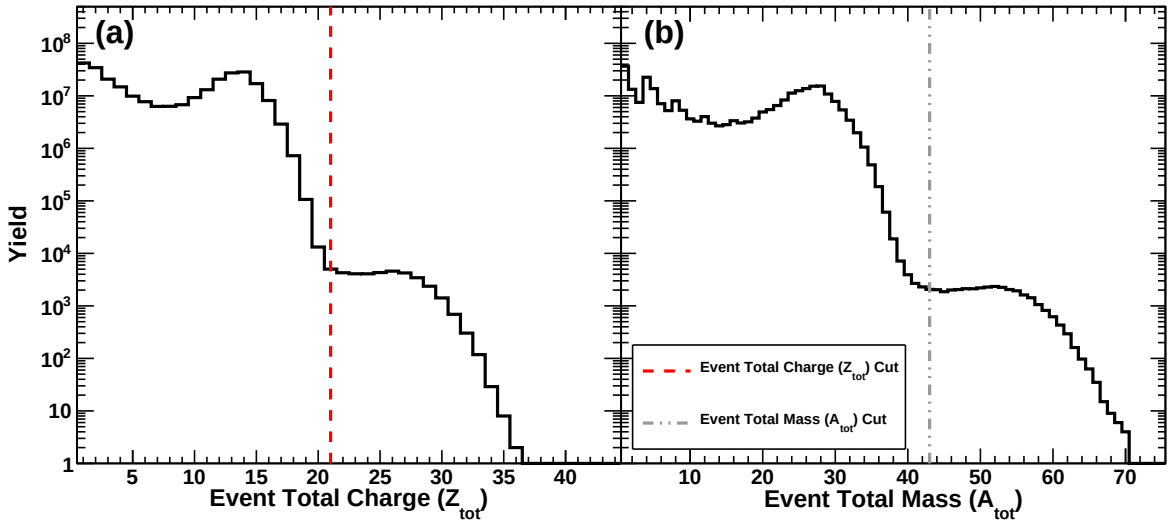

Figure 4.13: Total charge (Z_{tot}) and mass (A_{tot}) measured in all ^{28}Si + ^{12}C events. Panel (a): Yield distribution for the total charge measured in all events. The yield to the right of $Z_{tot} = 20$ is from two collisions occurring in the same beam burst. A cut is placed to exclude events with $Z_{tot} > 21$ as shown by the red dashed line. Panel (b): Same as panel (a), but for the event total mass, where the $A_{tot} > 43$ cut is shown by the gray double dot dashed line.

of 1.2% for this detector telescope. This procedure was repeated across many FAUST detectors to determine the consistency of this result. The background contamination of 1.2% is consistent across FAUST, however the ^{3}He contamination varies between 0.1% and 1.1%.

The yield of all measured and identified isotopes in the ^{28}Si + ^{12}C system is shown in Figure 4.12. The isotope distributions are roughly centered around the N = Z line due to the collision system having an equal number of protons and neutrons. The slight enhancement of neutron-rich isotopes over their proton-rich counterparts is due to proton-rich instability associated with the Coulomb force [52].

The yield of the total mass and charge measured in each event for the ^{28}Si + ^{12}C system is shown in Figure 4.13. The yield past the total charge ($Z_{tot} = 20$) and mass ($A_{tot} = 40$) of the collision comes from two collisions occurring close enough in time to where the measured reaction products from both collisions pass the event-building time gate (Section 2.3.3). It is possible for two beam particles to collide with two target nuclei close enough in time to pass the same event-building time window gate (Section 2.3.3). To exclude such events from

further analysis, a total charge and mass cut were applied as shown by the vertical dashed lines. The contamination of double beam burst events below these cutoffs is on the order of 0.01%. The cuts were made slightly above the theoretical total mass and charge limit to allow for single-collision events with contamination-caused particle misidentification to not be excluded.

4.3 Cesium Iodide Energy Calibration

The relationship between the light output produced in a CsI(Tl) scintillator and the energy deposited in the crystal depends on the charged particle energy, mass, and charge. Generally, higher particle energies exhibit a linear relationship; however, a reduction in the light output is observed at lower energies due to quenching [95]. The linear relationship and quenching contribution to the calibration curve depends largely on the charge of the particle. The light output to energy conversion in CsI(Tl) scintillators can be well described by:

$$L.O. = q \ln \left(E_{CsI} + b \right) + m E_{CsI} + d \tag{4.9}$$

where L.O. is the measured light output, E_{CsI} is the energy deposited in the scintillator, q accounts for the degree of quenching near the Bragg peak, m is the slope of the linear relationship, and b and d are offset parameters.

The charge dependence of the CsI(Tl) light output necessitates an independent CsI(Tl) light output to energy calibration for each element. First, the calibrated silicon energy as a function of the measured light output for the most abundant isotope of each element was plotted as shown for ^{4}He and ^{12}C in panels (a,b) of Figure 4.14. Given the particle type, silicon energy loss, and silicon detector thickness, the residual particle energy that is deposited in the CsI(Tl) detectors can be calculated using SRIM. The CsI(Tl) energies calculated use the mean silicon energy for small slices of the light output as shown by the black data points in panels (c,d). Equation 4.9 is then fit to these data to give the light output to energy conversion for each element measured in every FAUST CsI(Tl) detector.

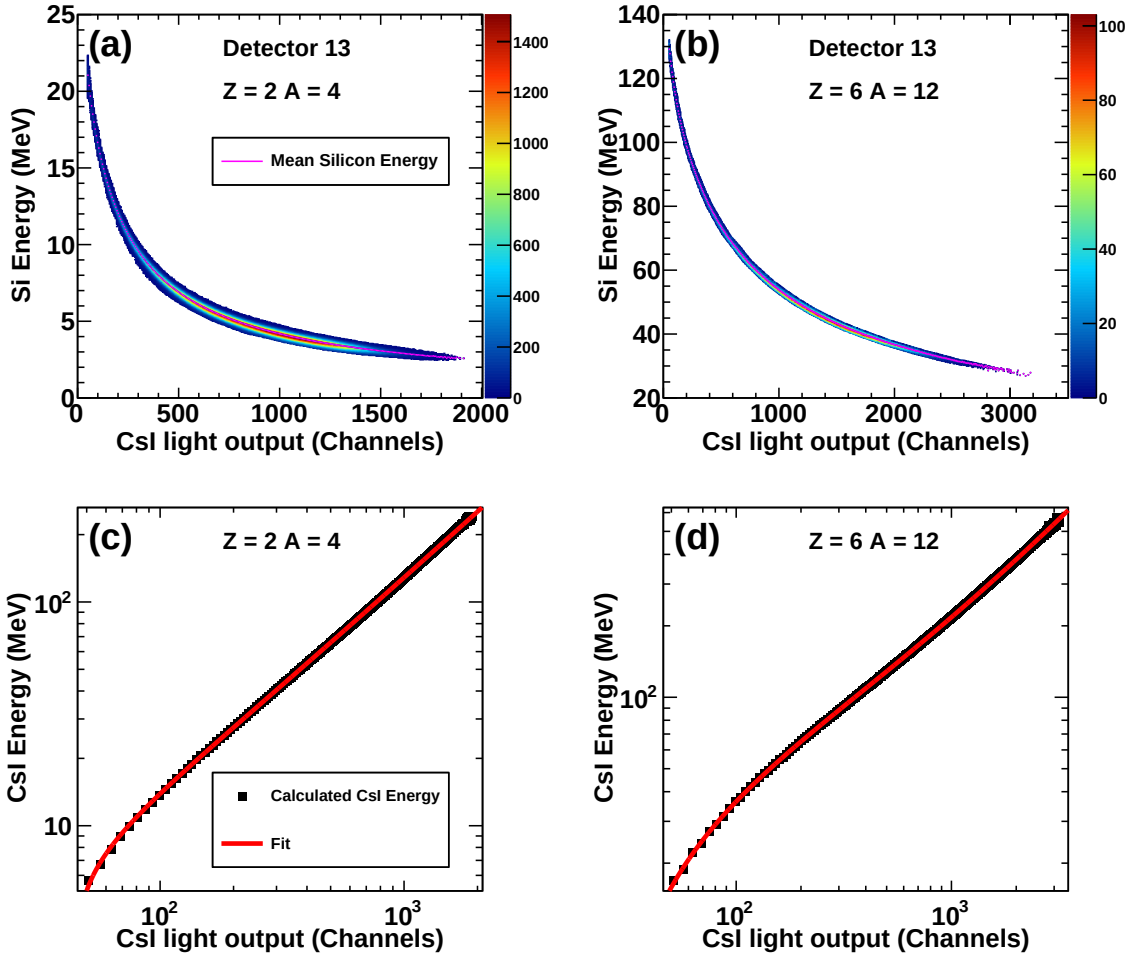

Figure 4.14: CsI(Tl) energy calibration. Panels (a,b): Calibrated silicon energy as a function of the CsI light output for ^{4}He and ^{12}C respectively. The mean silicon energy cut on small slices of the CsI light output is shown in pink. Panels (c,d): The mean silicon energy for each value of the CsI light output is used to calculate the expected residual energy deposited in the CsI using SRIM. This series of data are then fit with a Equation 4.9 to obtain the CsI light output to CsI energy relationship.

The expected increase in the degree of quenching for ^{12}C over ^{4}He is seen here as evidenced by the much larger ^{12}C energy (as compared to ^{4}He) spanning a very similar range in light output. After the CsI(Tl) energy calibration, the total energy of measured particles is assessed by summing the energy measurement in the DADL and CsI(Tl) detectors, and adding the energy loss through the mylar shields and half of the target thickness. An energy cutoff is placed to exclude supposed particles with greater energy than the punch-through

energy for the CsI(Tl) detector.

4.4 Quality Assessment of Calibrations

The resolution of the measured excitation energy for high α-multiplicity decays depends heavily on having accurate and consistent calibrations across all FAUST detector telescopes. Significant effort has been placed on assessing and improving the quality of α-particle energy assessment. Given the energy and α-conjugation of the collision system, a significant amount of ^{8}Be is produced in the collisions. The ^{8}Be ground state is unbound and promptly decays into two α-particles with a relative energy of 92 keV [96]. The width in the α-α relative energy distribution associated with this decay that is measured in charged particle spectroscopy experiments is dominated by the energy and angular resolution of the detector apparatus due to the very narrow intrinsic width of the state (6 eV). Further, with the two α-particles being measured in separate detectors, the resolution of the ^{8}Be ground state measurement depends on consistent relative calibrations for each detector pair of FAUST. Due to the beam energy being much larger than the relative energy of the decay, the two α-particles from the ^{8}Be ground state are typically measured in nearby detectors; however, the relationship between the detection efficiency and spatial proximity of detectors does vary across FAUST due to the range of detector solid angles and distances from the target.

α-α relative energy distributions were produced and examined for all detector pairs of FAUST. For a large majority of the detector pairs with significant yield, the measured ^{8}Be ground state width is $\sim$50 keV. However, some detector pairs exhibited significantly worse resolution (on the order of $\sim$110 keV); nearly all Ring A to Ring B detector pairs showed this deviation. It was found that these worse resolutions were caused by an inaccurate energy calibration for 13 detectors — these detectors had poor detector pair resolutions with all of their neighbors. It is possible that this is due to these DADL silicon detector thicknesses deviating from the the thickness reported by the manufacturer, affecting the CsI(Tl) energy calibration. Given the ubiquitous presence of this discrepancy for all Ring A detectors, it is also possible that the thick Mylar shield caused inaccuracies in the ^{229}Th calibration points

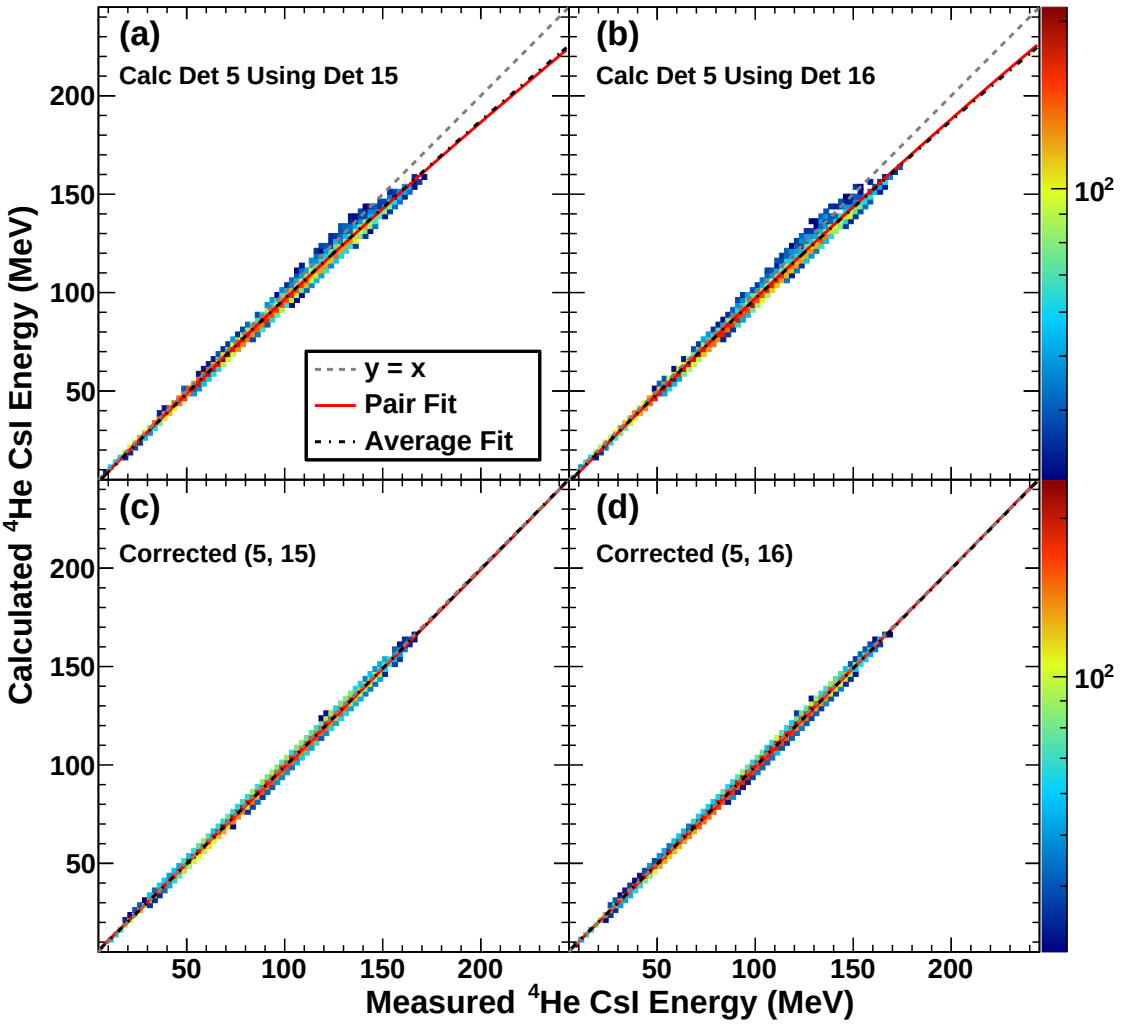

Figure 4.15: Ring A α-particle CsI(Tl) energy calibration correction using the ^{8}Be ground state. Panel (a): α-α pairs measured between detector 5 and 15 with a relative energy < 0.5 MeV. Calculated CsI(Tl) energy for detector 5 assuming the detector 15 energy measurement is accurate and that the two α-particles originated from a ^{8}Be ground state decay. A second order polynomial is fit to the data shown by the black dot dashed curve. A gray dashed line shows the ideal y=x relationship. Panel (b): Same as panel (a) but for detector pair (5,16). The red solid curves show the average between the two fits performed in panels (a) and (b). Panels (c,d): Same as panels (a,b) respectively after the calibration correction is applied.

which help constrain the same DADL energy region as higher energy particles. To correct for these discrepancies, the ^{8}Be ground state can be used as in internal standard. First, α-α pairs with a measured relative energy less than 0.5 MeV for a detector pair where one of the detectors has an inaccurate energy calibration (e.g. Det 5) were gated on (as even with the

energy calibration discrepancy, ^{8}Be ground state measurement falls in this range). Then, the angle and energy measured in the detector with an accurate calibration (e.g. Det 15) is used to calculate what CsI(Tl) energy in the other would give an α-α relative energy of 92 keV. The relative energy is calculated using the vector difference of both measured α-particle velocity vectors. The angle of the inaccurate detector velocity vector is known, while the magnitude of the vector is treated as unknown. The unknown magnitude is found by finding the intersection point of the unknown magnitude vector with a relative velocity sphere centered on the known α-particle measurement with a radius of 0.01 c (which corresponds to 92 keV α-α relative energy). Given that there are two intersection points of a vector with a sphere, the intersection point that gives a calculated velocity magnitude closest to the original measured magnitude is used. The measured α-particle energy as a function of the energy calculated using this procedure where detector 5 has inaccurate energy and detector 15 is used as reference is shown in panel (a) of Figure 4.15. Ideally the data

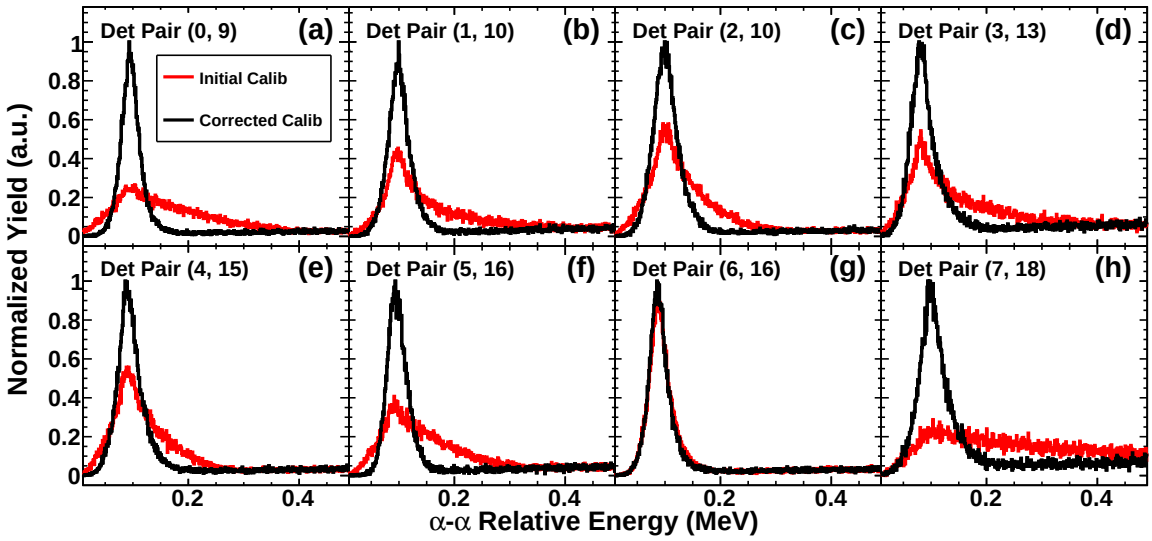

Figure 4.16: ^{8}Be ground state measurement between Ring A and Ring B detectors before and after applying the correction procedure shown in Figure 4.15. Panels (a-h): α-α relative energy measurement showing the ^{8}Be ground state using the initial CsI(Tl) calibration (red) and after applying the correction (black) for a Ring A-B detector telescope pair for each Ring A detector telescope.

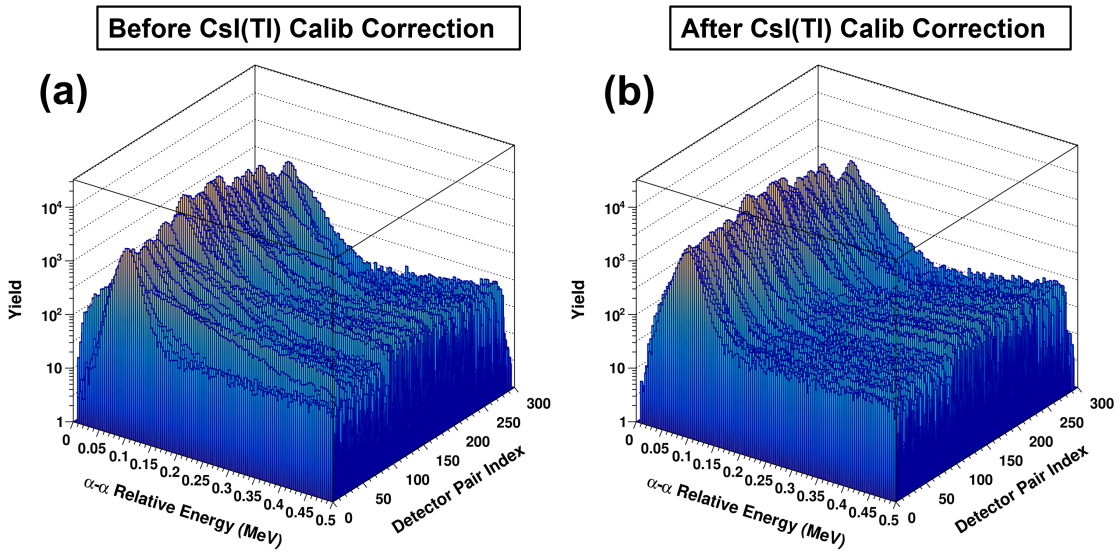

Figure 4.17: ^{8}Be ground state measurement for all detector pairs with sufficient yield (> 250 counts less than 0.5 MeV) before and after performing the CsI(Tl) calibration correction for α-particles. Increasing detector pair indices correspond to increasing detector numbers for one of the detector telescopes in the pair. Detector pairs of significant yield typically correspond to adjacent detectors.

would lie along the y = x line; however, curvature away from this line is seen at higher α-particle energy. The data is fit with a second order polynomial to provide a CsI(Tl) energy calibration correction. To ensure that the correction does not solely rely on one reference detector, the procedure is repeated for another neighboring detector as shown in panel (b). The average of the two fits is then used to correct the CsI(Tl) α-particle energy as shown in panel (c,d). The improvement in the ^{8}Be ground state measurement for all Ring A detectors when implementing this procedure is shown in Figure 4.16. The asymmetric and broad distributions before correction (red) now have sharp peaks centered at 92 keV with widths that are consistent with the rest of FAUST (black). The α-α relative energy distributions shown here are equivalent to the ^{8}Be excitation energy after subtraction of the Q-value.

The ^{8}Be ground state measurement for all detector pairs of FAUST with significant yield both before and after applying this correction are shown in Figure 4.17. The logarithmic yield scale used here is sensitive to any poor relative energy distributions; after correction,

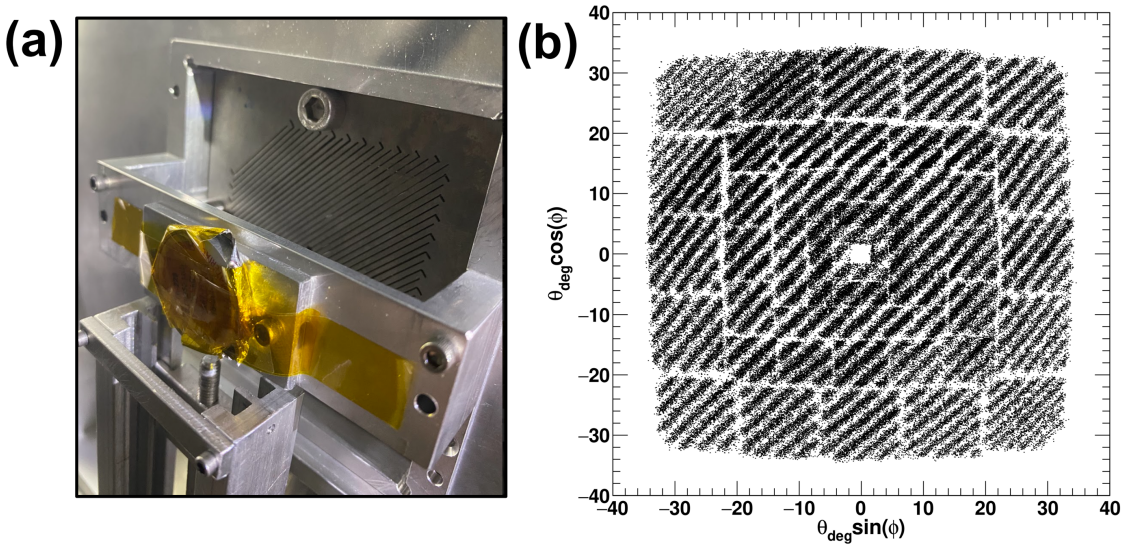

Figure 4.18: Global FAUST position assessment using the slotted tungsten mask. Panel (a): Picture showing the ^{229}Th source mounted at the FAUST target position and situated behind the slotted tungsten mask. Panel (b): Global FAUST position for ^{229}Th source data through the tungsten mask.

all detector pairs show good quality of ^{8}Be ground state measurement.

Particle angles are determined by transforming the local DADL positions to the global FAUST angle using the geometric design specifications of FAUST. A ^{229}Th source mounted at the target position and situated behind a striped tungsten mask was used to verify correct mapping of the electronic channels to their corresponding detector locations, to confirm the detector orientations, and to ensure the absence of any significant detector location uncertainties due to the mounting structures of FAUST. A picture of the source-mask setup can be seen in panel (a) of Figure 4.18 and the design details of this mask can be found in ref. [71]. The global position of measured particles in FAUST that pass through this mask is shown in panel (b), where continuous stripes can be seen across the entire array. While small uncertainties in the detector locations do exist, the mask data is not sensitive enough to provide any reasonable corrections.

The quality in particle identification, energy calibration, and FAUST position calibration can be simultaneously assessed by examining the quality of particle-unbound excited state

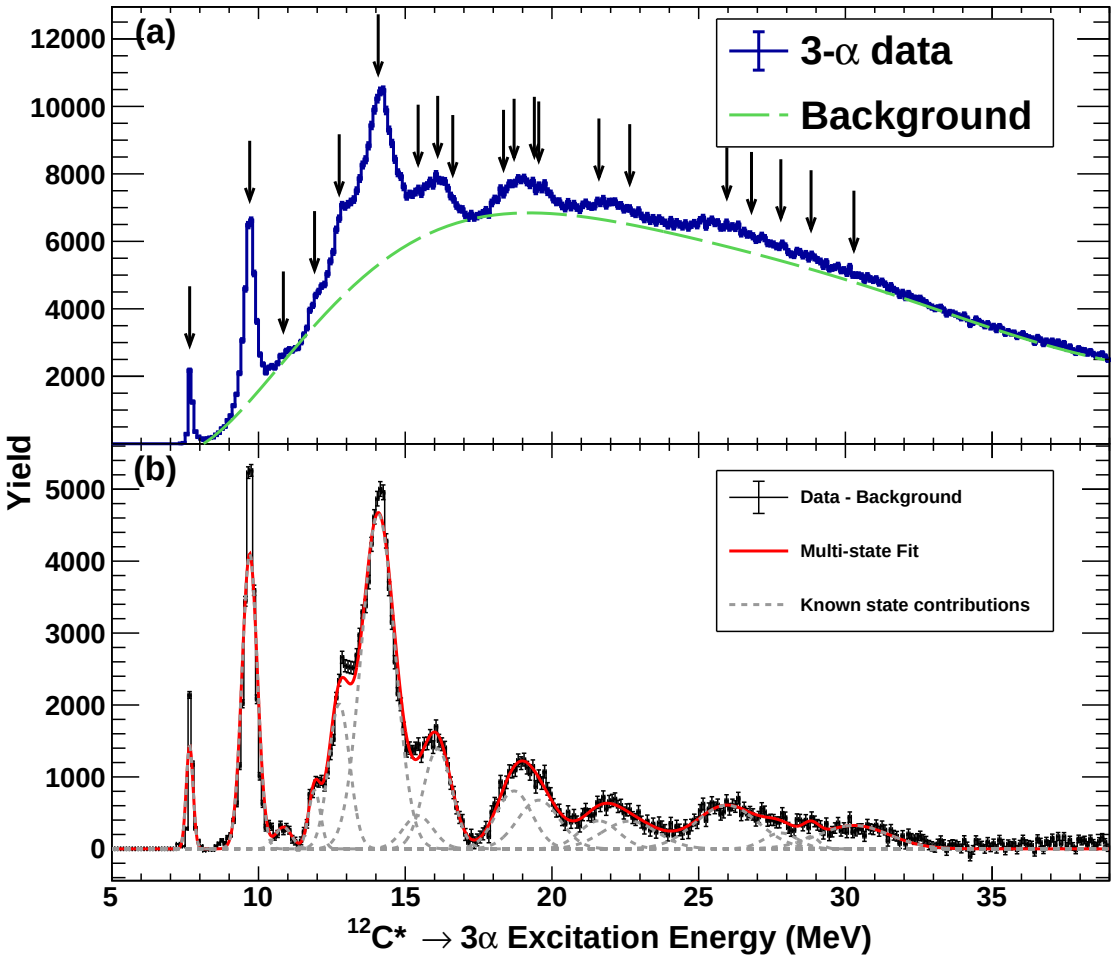

Figure 4.19: 3-α decay excited state measurement of ^{12}C* for the ^{12}C + ^{28}Si collision data. Panel (a): 3-α excitation energy distribution (blue) for all events with three or more measured α-particles. A rough background was produced using a 7th order polynomial (green dashed line). The means of known states are indicated by the black arrows [14]. Panel (b): The background is subtracted from the data in panel (a) and a multi-Gaussian function is fit to the data (red line). The individual Gaussian distributions (gray dashed lines) have means fixed to known excited state levels.

measurement. While the quality of the ^{8}Be ground state measurement across FAUST has already been demonstrated, a more sensitive probe of FAUST calibration accuracy is to inspect the measurement of known ^{12}C excited states that decay into 3 α-particles (e.g., the Hoyle state) [28]. α-decaying excited states of ^{12}C that are produced in the ^{28}Si + ^{12}C data set will have significant background due to the projectile having an equivalent mass of seven

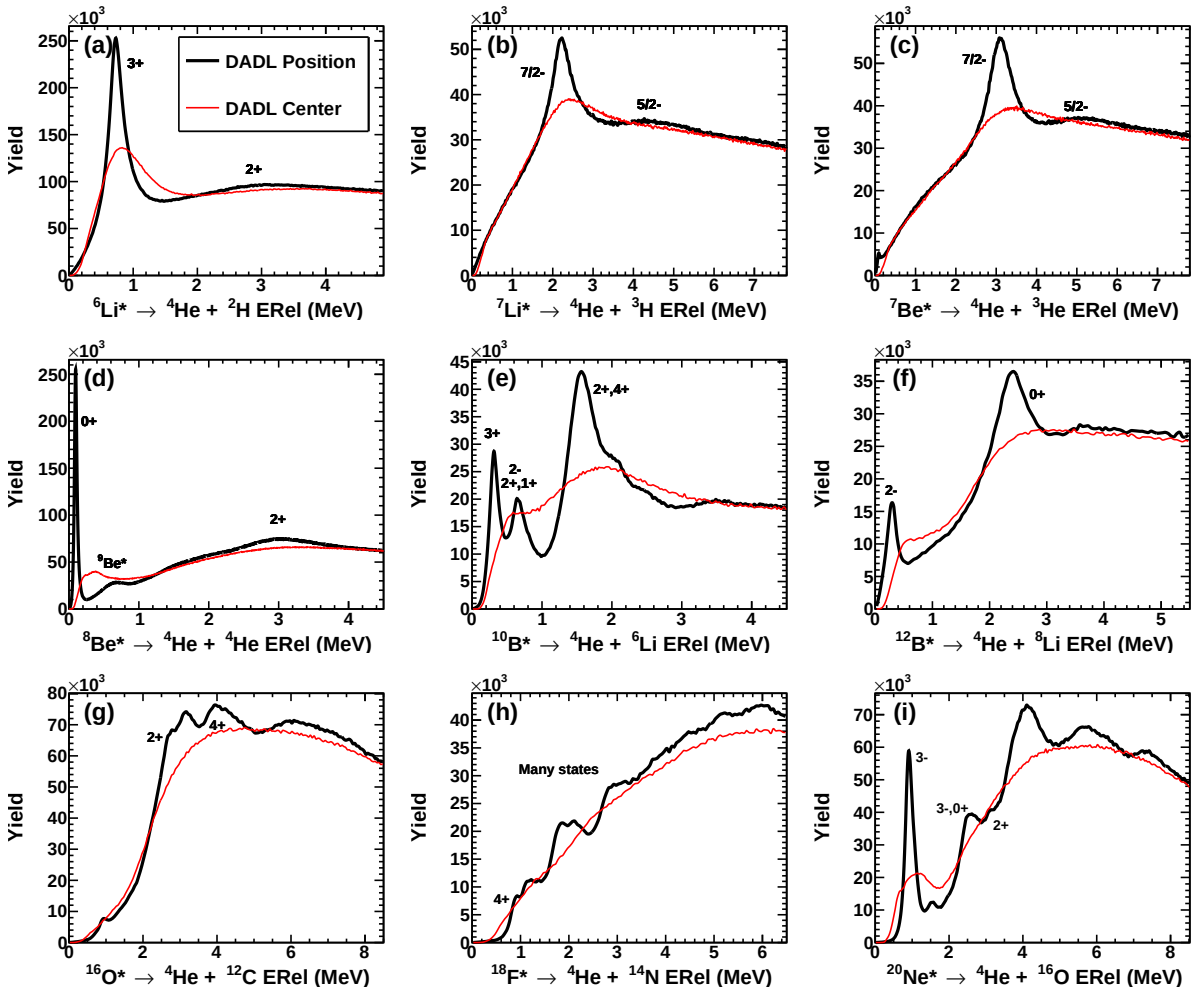

Figure 4.20: Importance of DADL position information for measuring particle-unbound excited states. Panels (a-i): Two particle relative energy distributions to observe α-unbound excited states of the parent nucleus (e.g. panel (a) shows the ^{4}He + ^{2}H relative energy distribution for all measured events, showing excited states of ^{6}Li). The distributions obtained using the measured DADL positions are shown in black, while the distributions obtained when assuming the particles hit the center of the DADL are shown in red. The overlaid spin-parity assignments are made by comparing the mean of some measured states to literature values [15].

α-particles. To improve the state to background ratio, the 3-α excitation energy distribution for the normal kinematic ^{12}C + ^{28}Si collision data is shown in panel (a) of Figure 4.19. The means of known excited states are indicated by the black arrows and well describe the locations of peaks in the spectrum. The lowest energy peak in the spectrum that contains

negligible background contribution (Hoyle state) was fit with a Gaussian distribution to compare the measurement to reported literature values. The measured mean of the Hoyle state (7.67 MeV) is well within the literature value uncertainty (7.65 MeV$\pm$0.19), while the measured width (FWHM) is 0.104 MeV (9 eV intrinsic width) [14]. A rough determination of the background using a 7th order polynomial was subtracted from the spectrum to better isolate the individual state contributions. To see how well all features in the spectrum can be described by known state properties, a multi-Gaussian fit was performed with the mean of each individual Gaussian fixed at the literature energies of known states. The width of each state is allowed to fit freely. While this fitting procedure of the excitation energy distribution is somewhat crude and does not account for the convolution of intrinsic state widths with the detector resolution, all gross features of the subtracted spectrum are well described by the fit, indicating the quality of the α-particle calibrations. While it is possible that this excitation energy distribution may be able to provide additional constraints to the properties of α-decaying ^{12}C states, a more detailed analysis would be necessary and is outside the scope of this work.

Ensuring consistent and accurate calibrations across a broader range of isotopes that are measured in the ^{28}Si + ^{12}C collision data can be achieved by examining the quality in the measurement of additional particle-unbound excited states. The measurement of excited states for decay channels containing an α-particle for various parent nuclei are shown in black in Figure 4.20. The spin and parity for some of the states are indicated above the corresponding peaks [15]. The ability to accurately measure these resonant state decays through particle correlations requires quality calibrations across all of FAUST, as these decays are measured between many detector pairs. Additionally, to demonstrate the importance of the position sensitivity of the DADL detectors, the distributions were produced when assuming each particle hit the center of the detector as shown in red (as this is the assumption that is typically invoked for single-pad silicon arrays). Under this assumption, most states are no longer resolved.

4.5 FAUST Filter

The particles that are measured in each collision event are impacted by the acceptance conditions of FAUST. Further, the energy and angle that is measured contains uncertainty that is largely dictated by the position (DADL) and energy (DADL + CsI(Tl)) resolution of the detectors. Many important analyses depend on an accurate modelling of the detector array response; examples include filtering simulated data to compare to experimental data, predicting excited state measurement resolution, determining the detection efficiency for specific reaction channels, and ensuring that features in the data do not originate from detection biases. The pre-existing FAUST filter accounted for geometric acceptance, detector energy resolution, exclusion of double-hit scenarios, and threshold energies for punching through the DADL detectors. Position- and energy-dependent cutoffs for each detector were added to account for preamplifier saturation. For a given energy, saturation can cause particles incident in the center of the detector (where equal charge-splitting occurs) to be measured while particles closer to the edge (significant charge-split asymmetry) to give saturated signals. For this work, all FAUST filter parameters were constrained to reflect the acceptance of 3- and 4-signal events, as both the x- and y-position is retained. Nearly all α-particles fall into the 4-signal category. To further improve the accuracy of the filter, the energy-dependent position resolution and threshold effects from the DADL detector model (Section 3.3.1) were incorporated. To evaluate how well the DADL detector model replicates experimentally measured results, the ^{8}Be ground state was again used as a reference.

As a consequence of the position resolution energy dependence, the uncertainty in measured particle angles is correlated to the particle velocity. Higher particle velocities give lower energies deposited in the DADL, which in turn gives worse angular resolution. Therefore, there is a velocity dependence to the resolution on the measurement of excited states that undergo charged particle decay. To observe this effect for the ^{8}Be ground state, the relative energy between every pair of α-particles is calculated in events with two or more measured α-particles and is cut on the laboratory-frame velocity of the α-α center-of-mass as shown in

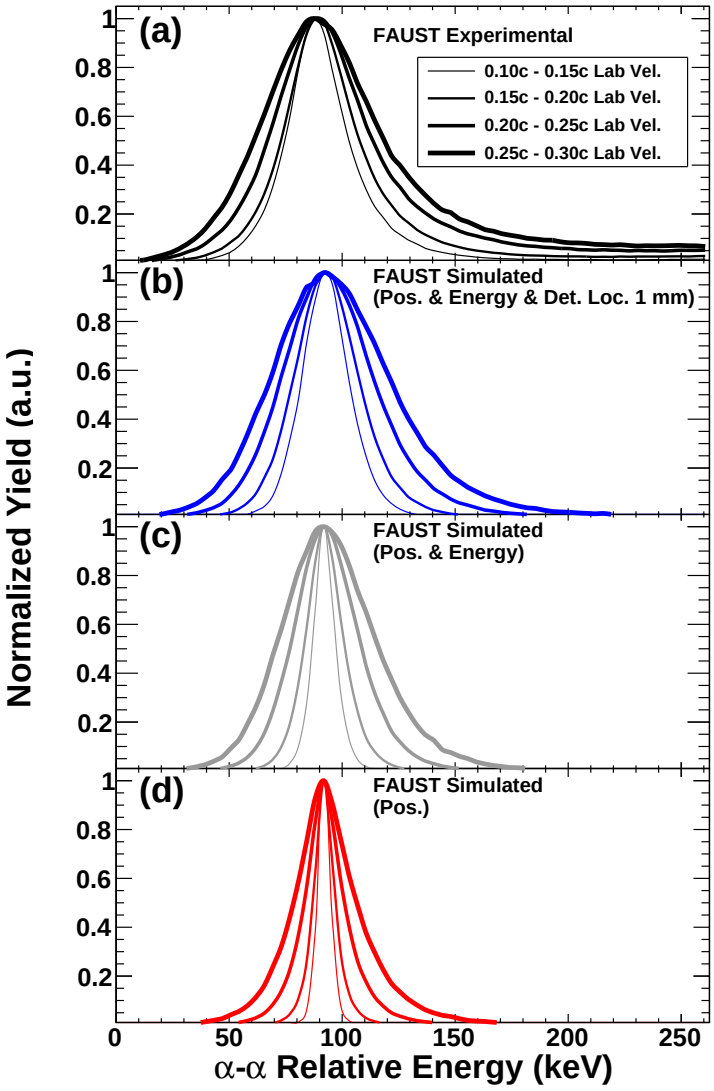

Figure 4.21: ^{8}Be ground state α-α relative energy distributions cut on ranges of α-α center-of-mass velocity in the laboratory frame for experimental data (a), simulated data with position smearing using the DADL detector model (d), simulated data with position and energy smearing (1% Si, 1.5% CsI(Tl) FWHM) (c), and simulated data with position, energy and detector location smearing ($\pm$1 mm in x and y, $\pm$5 degrees in the plane of the detector) (b).

panel (a) of Figure 4.21. As the ^{8}Be velocity increases, the measured decay width increases accordingly. Given the target thickness and energy of measured α-particles, any effect of α-particle energy loss and angular straggling when traversing through the target material is

well below the dependence seen here. The high energy tails observed on the right side of the distributions are due to uncorrelated α-particles that do not originate from ^{8}Be ground state decays.

To investigate how well the FAUST filter (with the DADL detector model incorporated) reproduces these results, ^{8}Be ground state decays were simulated. To set reasonable initial kinematic conditions for each simulated ^{8}Be, the experimental ^{7}Be energy and angular yield distributions were sampled to avoid any double-filtering biases that may be introduced if otherwise using the reconstructed α-α center-of-mass (^{8}Be) kinematics. The decay orientation was then randomized prior to filtering. The result of only filtering by geometric acceptance and smearing the position of each particle is shown in panel (d). While the same trend is observed here as in the experimental data, the filter under-predicts the measured widths on average. The experimental and simulated ^{8}Be ground state widths cut on narrower ranges in the ^{8}Be laboratory frame velocity were obtained by performing Gaussian fits on the distributions and are shown in Figure 4.22. To see if this discrepancy can be explained by the energy resolution of the detectors, a reasonable energy smearing of 1% for the Si and 1.5% for the CsI(Tl) (FWHM) was included and the result is shown in Figure 4.21 panel (c) (gray diagonal crosses in Figure 4.22). There is only a modest widening of the decay energy distributions compared to panel (d). It is evident that the position resolution smearing of the DADL detector model describes the experimental trend very well, but, even with energy smearing, under-predicts the experimentally obtained widths. It is possible that this discrepancy can be explained by uncertainties in the global detector positions. Currently, the detectors are assumed to be located based on the designed geometry of FAUST. While there are many potential sources of error for the detector locations, the error associated with the screw-holes that mount the detectors to the ring frames is well constrained. To model how this uncertainty effects the ^{8}Be ground state measurement, detector location smearing that approximates this uncertainty was also included. First, each detector location was translated in x and y (in the plane of each detector) by uniformly and randomly sampling

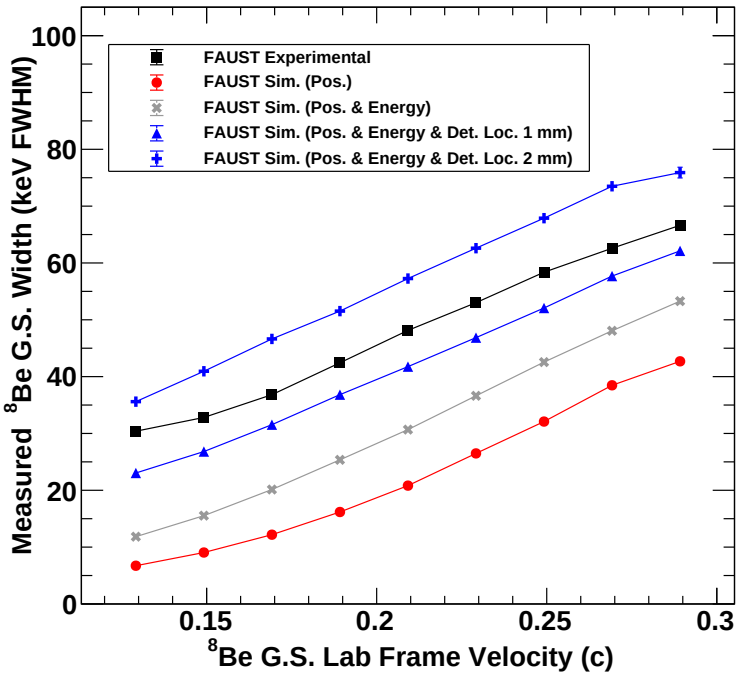

Figure 4.22: Width obtained for the ^{8}Be ground state as a function of the ^{8}Be (α-α center-of-mass) velocity in the laboratory frame for experimental data (black squares), simulated data with position smearing using the DADL detector model (red circles), simulated data with position and energy smearing (gray diagonal crosses), and simulated data with position, energy, and detector location smearing ($\pm$1 mm blue triangles, $\pm$2 mm blue vertical crosses). Error bars are obtained from errors in the fits and are smaller than the markers.

between -1 and 1 mm. Then, the angle of each detector (in this same plane) was adjusted by uniformly and randomly sampling between -5 and 5 degrees. This detector location smearing was performed at the beginning of the simulation. While a modest under-prediction of the experimental widths persists, including the detector location uncertainty in the simulation improves agreement between the simulated results (blue triangles) and experimental results (black squares) as shown in Figure 4.22. To ensure that this discrepancy can be explained by a reasonable detector location uncertainty, this procedure was repeated using a translational uncertainty of $\pm$2 mm as shown by the blue vertical crosses in Figure 4.22. The experimental results are bracketed by the two simulated series. These simulations assume the same energy, position, and location uncertainties for each detector in the array. The subtle differ-

ences in the shape of the experimental and simulated results can likely be attributed to the finer details of the individual detector performances and location uncertainties that exist in FAUST. For the remainder of this work, a detector location uncertainty of 1.3 mm is used in the FAUST filter to account for the general level of global uncertainty that exists.

5. RESULTS AND ANALYSIS

The formal analysis of the experimental data begins by introducing a transport model used for comparisons to the experimental data in Section 5.1. Considerations and requirements for preferentially selecting projectile-like α-disassembly events in experimental data are outlined in Section 5.2. The main excitation energy analysis is presented in Section 5.3, including determination of the detection efficiency and resolution (Section 5.3.1), comparison to the prior measurement (Section 5.3.2), and discussion regarding the description of the background (Section 5.3.3). Partitioning of the experimental α-disassembly events into those more consistent with simultaneous or sequential decay is shown in Section 5.4. Momentum shape analysis is used to further assess the characteristics of such decays in Section 5.5. A brief investigation into target mass and α-conjugation effects on toroidal state production is performed in Section 5.6. A detailed statistical significance analysis and associated determination of the upper limit for toroidal state cross section consistent with the present work is reported in Section 5.7.

5.1 Anti-Symmetrized Molecular Dynamics Simulations

The anti-symmetrized molecular dynamics (AMD) model was developed to simulate heavy-ion collisions in the intermediate energy regime [97, 98]. This microscopic simulation framework treats each individual nucleon as a Gaussian wave packet and solves a single Slater determinant to ensure the Pauli exclusion principle is satisfied. Comparison of collision properties and observables between AMD and experimental data give excellent agreement [99, 100]. AMD is a powerful tool for studying the details of primary collision dynamics that lead to certain exit channels and observables. Although AMD models the complex dynamics of nuclear collisions with exceptional detail, it does not possess either particle-particle correlations emergent from discrete nuclear excited states or the proper ingredients for populating high-spin toroidal isomer states. As such, AMD simulation results can provide an accurate

background signature for comparison to experimental observables that may be sensitive to toroidal state decays. The anti-symmetrization conditions of AMD result in great computational expense that scales as $\sim A^3$ of the collision system. Given the relatively small mass of the $^{28}Si + {}^{12}C$ collision system, reasonable calculation time yielded 1,600,000 AMD collisions at 35 MeV/nucleon simulated out to 300 fm/c.

The nuclear fragments produced in AMD collisions contain excitation energy and must undergo de-excitation according to available pathways. For this purpose, a statistical decay code (GEMINI++) is paired with AMD to produce the final state reaction products for each collision [101]. For light charged particle ($1 \leq Z \leq 3$) emission, GEMINI++ uses a Monte-Carlo technique of selecting the decay pathway according to Hauser-Feshbach decay widths. Heavier fragment emission and fission is treated using the Moretto and Bohr-Wheeler formalism, respectively [102, 103]. Gamma-ray decay pathways are considered once the gamma decay branch competes with charged particle emission, although this occurs only near thermal excitation energies when particle decay widths approach zero. GEMINI++ assumes input fragments are spherical and are at nuclear saturation density (ρ_0=0.16 fm^{-3}); however, many AMD fragments will exhibit strong deformations and be at sub-saturation densities. These limitations are important to consider when interpreting simulation results. Each AMD collision was coupled to GEMINI++ once (some other work runs GEMINI++ many times per AMD collision to bolster limited AMD statistics). For the remainder of this work, figures labeled with "AMD" refers to the pairing of AMD and GEMINI++.

To assess both the predictive power of AMD and the agreement between FAUST-filtered simulation data and experimental data, the energy distributions for various isotopes are shown in Figure 5.1. After filtering of simulation data, agreement with experimentally measured distributions is excellent. The unfiltered AMD distributions in gray show low energy target-like particle yield for isotopes of $Z \leq 6$ as seen in panels (a-e). The saddle-point between yield associated with primarily target-like particles and projectile-like particles (seen at $\sim$10 MeV/nucleon for ^{12}C in panel (e)) occurs very close to the DADL punch-through

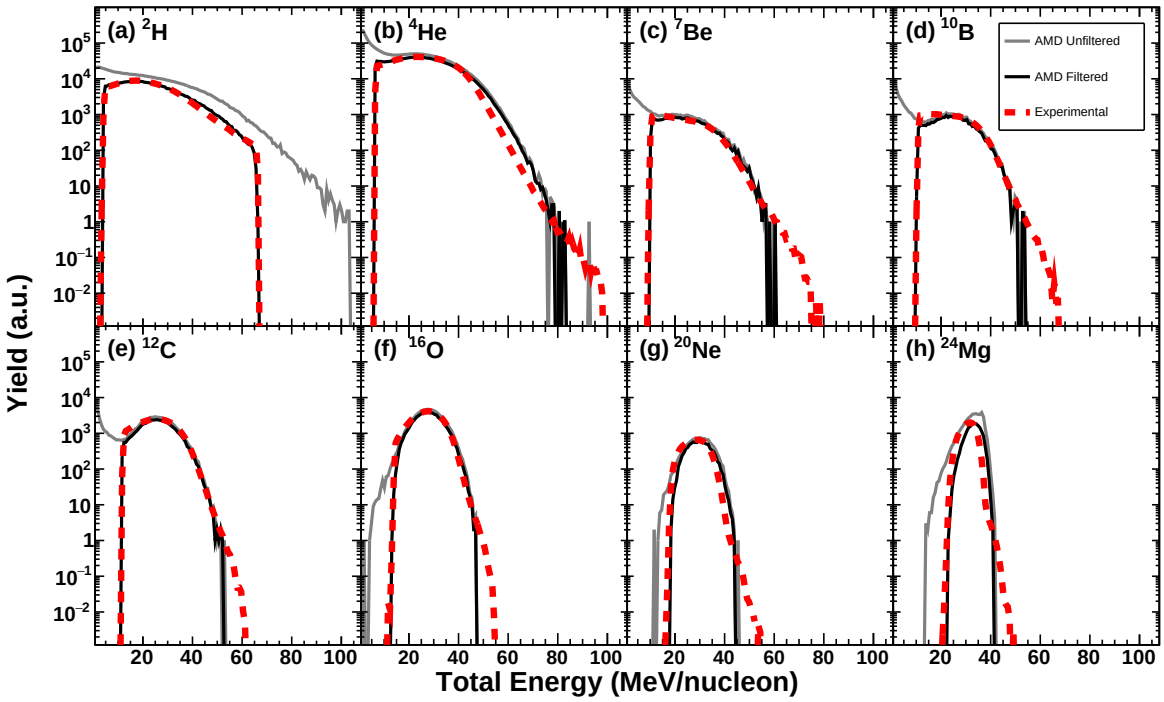

Figure 5.1: Experimental and AMD + GEMINI++ (FAUST filtered and unfiltered) energy spectra for N=Z isotopes (excluding ^{8}Be) produced in collisions of ^{28}Si + ^{12}C at 35 MeV/nucleon. Panels (a-h): Unfiltered AMD energy distributions are shown in gray. Experimental distributions (red dashed) are normalized to the filtered AMD distributions (black) in each panel.

energy for each isotope, indicating that the thickness of the DADL detectors is well suited for preferentially measuring projectile-like fragment decays at this collision energy. Accurate modeling of the position- and energy-dependent threshold effects in the FAUST filter are most notably seen by the increasing yield reduction between unfiltered and filtered ^{2}H distributions with increasing particle energy, as a larger portion of DADL particle positions give signals below threshold. The shape of the ^{2}H distributions impacted by this are well matched between experiment and simulation. The hard cutoff seen around 65 MeV/nucleon accounts for ^{2}H particles that have enough energy to punch through the CsI(Tl) crystal.

The experimental yield of α-particle multiplicities is shown by the red dashed line in Figure 5.2. The high event rate, duration of data collection, and adequate FAUST acceptance

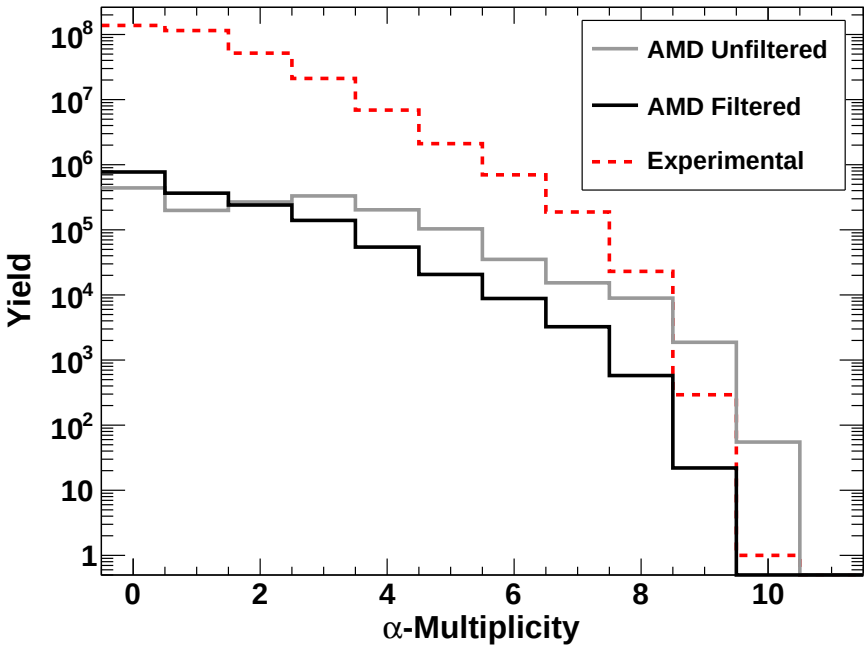

Figure 5.2: Experimental and AMD + GEMINI++ (FAUST filtered and unfiltered) α-particle multiplicity distributions.

has yielded over an order of magnitude increase in measured 7-α event compared to previous work (186,097 FAUST events compared to 6,467 NIMROD events) [11]. Additionally, a total of 22,602 8-α events have been measured, allowing the α-disassembly of ^{32}S to be examined for possible toroidal states. For unfiltered AMD (gray), a peak in yield for an α-multiplicity of three arises from the 3-α makeup of the ^{12}C target; filtering AMD removes this feature as target-like particles are usually below detection thresholds, resulting in a distribution (black) with similar shape to that of experiment (red dashed). The increased yield reduction between the unfiltered and filtered 8-α yield compared to the 7-α yield comes from 8-α detection requiring an α-particle from the target to have projectile-like character. Further, the requirement of measuring each α-particle in separate detectors reduces detection efficiency with increasing α-multiplicity.

5.2 Event Selection

Judicious choice of the experimental reaction exit channel is important for maximizing the likelihood of observing toroidal states. There is experimental suggestion and theoretical support for toroidal state breakup proceeding through complete α-disassembly [11, 7]. Heavy-ion collisions at this energy can have various reaction mechanisms which can depend on the impact parameter, including multifragmentation, nucleon transfer, incomplete fusion, and binary excited decay [104, 105, 106, 107]. Binary reaction mechanisms that give a highly excited projectile-like fragment are promising candidates for toroidal state production, as excitation energies up to ∼6 MeV/nucleon and angular momenta up to $96\hbar$ may be reached in this collision energy regime [64, 105].

To gate on such events, it is important to exclude 7,8-α events that contain signatures of

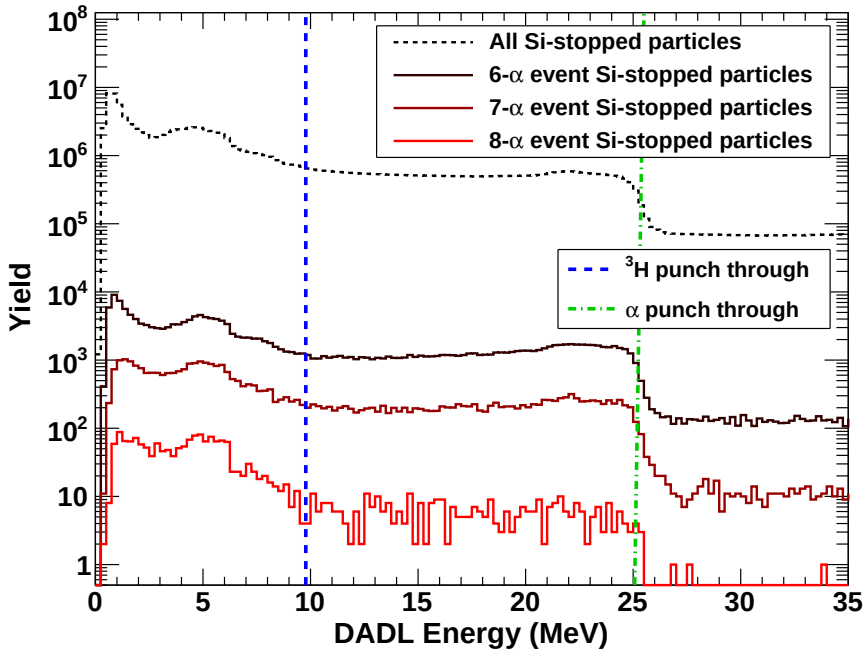

Figure 5.3: Measured DADL energy for particles that stop in the DADL detector. The distribution is shown for all measured particles (black dashed), gated on measured 6-α events (black), 7-α events (maroon), and 8-α events (red). The energy where ^{3}H isotopes and α-particles punch through the DADL detector are shown by the blue dashed and green dot dashed lines respectively.

pre-equilibrium emission and target-like α-particles. While the DADL detector thicknesses are well tuned to measure projectile-like particles, there is no discrete cutoff between target-like and projectile-like contributions; it is possible that α-particles stopped in the DADL detector may have properties consistent with projectile-like fragment decay and punch-throughs with target-like properties. Charged particle isotopic identification is performed on particles that punch through the DADL detector; however, because the DADL was used as the experimental trigger, the energy of particles that stopped is still measured. The energy distribution of particles measured in the DADL detector where no energy was measured in the CsI(Tl) detector for all events and individually gated on 6-,7-, and 8-α events is shown in Figure 5.3. In all cases, the low energy target-like particles cause significant yield increase with decreasing energy. The sharp reduction in yield at $\sim$25 MeV corresponds to the punch-through energy for α-particles through $\sim$315 µm of silicon indicated by the vertical green dot dashed line. The punch-through point for ^{3}H isotopes is at $\sim$9.7 MeV, where energies greater than this will give energy measurement in the CsI(Tl) and permit particle identification. Particles between these two punch-through energies are primarily comprised of α-particles, although ^{3}He and Z $>$ 2 particles will contaminate. The isotopic yield ratio between ^{3}He and α-particles for all data indicates an approximate ^{3}He contamination of 7.8%. To estimate the level of contamination from Z $>$ 2 particles, the roughly constant yield to the right of the α-particle punch-through energy can be extrapolated. As the number of α-particles measured in the event increases, there is less remaining mass in the collision system to contaminate. The total contamination when identifying particles within this re-

α-Mult	Q-value (MeV)	Yield	Si-Stop α-Yield	Contam. (%)
6	-28.48	699172	79381	17.0
7	-38.46	187893	13244	11.5
8	-45.41	23004	364	8.7

Table 5.1: Experimental α-particle multiplicity yield, Q-value, and yield of events containing at least one silicon-stopped α-particle with associated approximate contamination.

gion as α-particles for 6,7,8-α events is shown in Table 5.1. If the stopped α-particles are consistent with originating from a projectile-like decay, it would be sensible to recategorize such events to the correct α-multiplicity. Given the $\sim$17% contamination level of 6-α events, only recategorization of 7,8-α events is considered.

Inclusion of silicon-stopped α-particles lowers the energy threshold for detection as evidenced by the identified (DADL + CsI(Tl) measurement) α-particle transverse and parallel velocity distributions overlaid with silicon-stopped α-particle yield contours shown in panel (a) of Figure 5.4. The phase space of these stopped α-particles is consistent between all measured events, 7-α events, and 8-α events as seen between panels (a-c). The good angular resolution of FAUST afforded by the position sensitivity of the DADL detectors is evidenced by continuous nature of the identified α-particle distributions. The mean α-particle velocity is mildly damped for 7-α events compared to all data and slightly more so in the 8-α case. This damping can likely be attributed to both energy sharing to target-like particles during the violent collisions that lead to high multiplicity exit channels and the associated Q-value for each N-α decay (Table 5.1).

α-particle velocities in the calculated 7,8-α event center-of-mass (source) frame are shown in panels (d,e). These distributions are largely symmetric about the center-of-mass, although a slight asymmetry is observed due to the acceptance of FAUST. The silicon-stopped α-particle yield contours overlaid in each panel correspond to the velocity space that these particles inhabit in the corresponding source frame (e.g., for a 7-α measured event with an eighth stopped α-particle, what region of velocity space does the stopped particle inhabit in the 7-α source frame as in panel (d)). The velocity cut shown by the black double dot dashed circles corresponds to the 40 MeV source frame energy cut used in Refs. [11, 8] to exclude pre-equilibrium and target-like α-particles. While some of the stopped particle distributions extend past this region, a significant portion is contained within the velocity cut, indicating that a portion of these particles may be consistent with a projectile-like decay. To better assess the validity in N-α event recategorization, the 8-α source frame α-

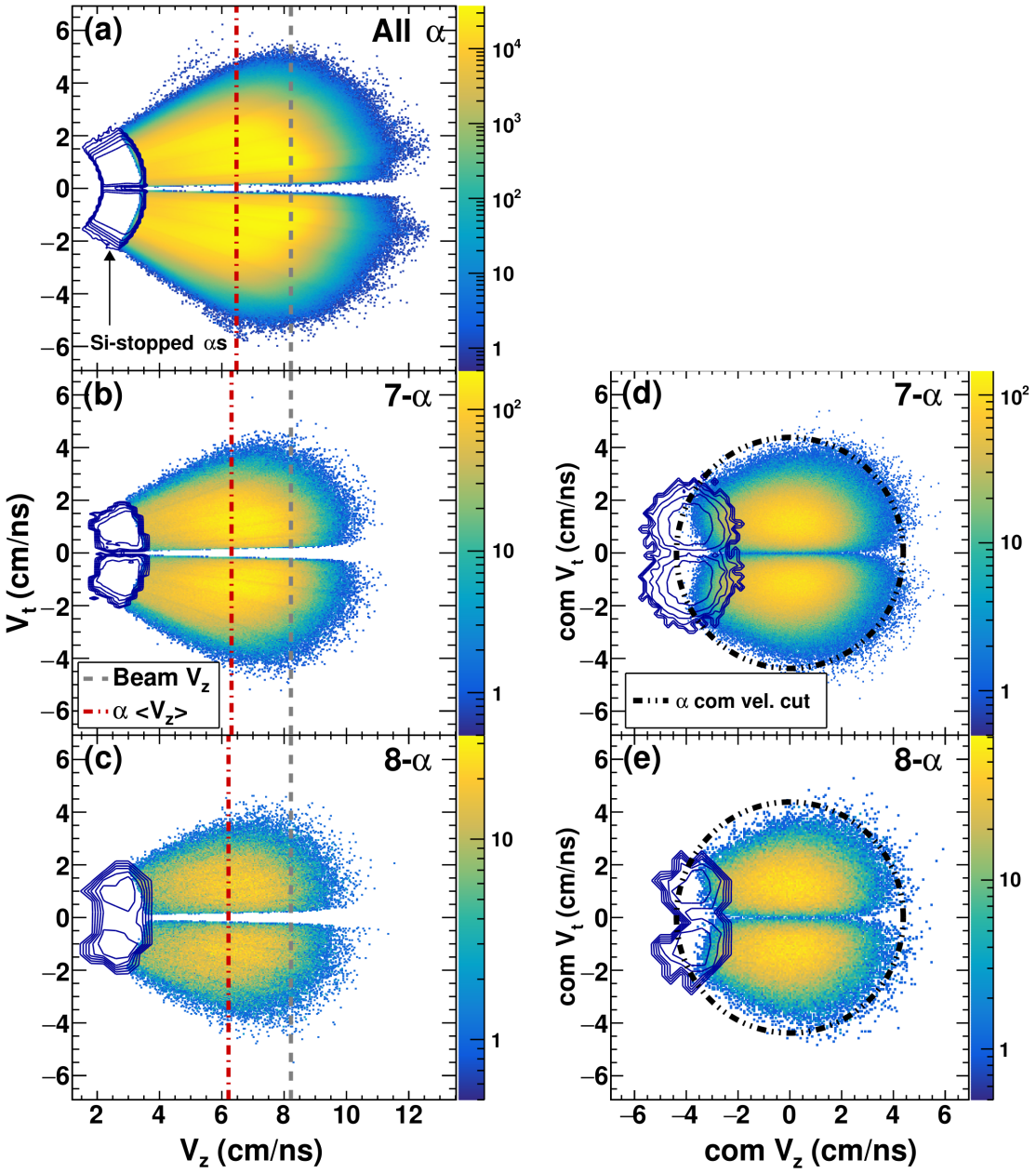

Figure 5.4: Experimental α-particle parallel velocity (V_z) vs transverse velocity (V_t) distributions for ^{28}Si + ^{12}C. Contour lines showing region of silicon-stopped α-particle yields are overlaid in each panel. Panels (a-c): Laboratory frame distributions for all events (a), 7-α events (b), and 8-α events (c). Lines indicating the beam velocity (gray dashed) and the mean α-particle velocity excluding stopped α-particles (red dot dashed) are overlaid. Particles in the upper hemisphere of FAUST are given a positive V_t, with the lower hemisphere a negative V_t. Panel (d,e): Source frame distributions for 7-α events (d) and 8-α events (e). Velocity cut applied in Refs. [11, 8] is shown by the black double dot dashed circle.

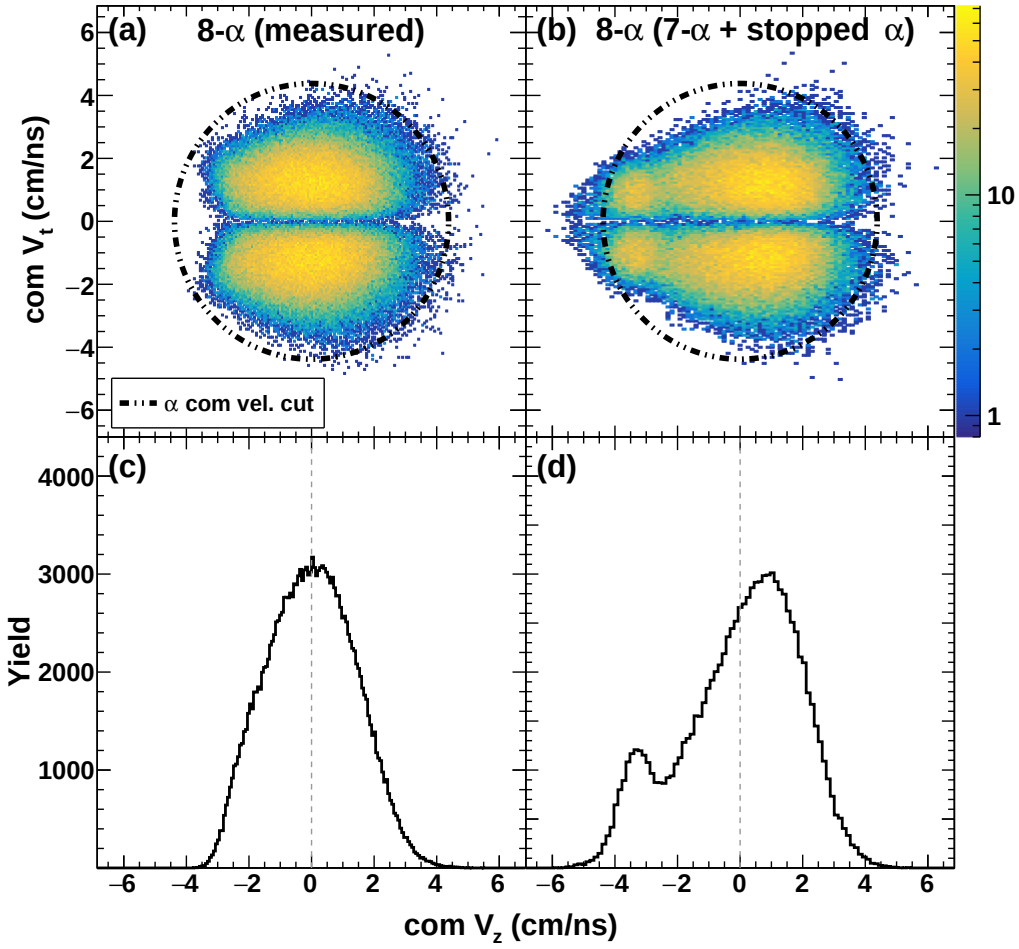

Figure 5.5: Source frame α-particle V_t vs V_z distributions for 8-α events. Panels (a,b): Events with all eight α-particles identified with DADL and CsI(Tl) measurement (a) and events with seven identified α-particles and one silicon-stopped α-particle. The velocity cut as in Figure 5.4 is overlaid. Panels (c,d): Projection of panels (a,b) to the V_z axis respectively. Gray dashed line centered at $V_z = 0$ is shown for reference.

particle velocity distributions are compared between events with eight identified α-particles and events containing seven identified α-particles and one silicon-stopped α-particle as shown in panels (a,b) of Figure 5.5. While the silicon-stopped distribution in panel (b) is fairly well contained within the velocity cut, there is obvious deviation in the overall shape compared to panel (a). The locus of data centered at $\sim$-3.5 cm/ns V_z (seen clearly in the projection) indicates that a large portion of these stopped α-particles are target-like in nature. Further, the inclusion of stopped α-particles shifts the mean of the main locus of data off of $V_z = 0$ as

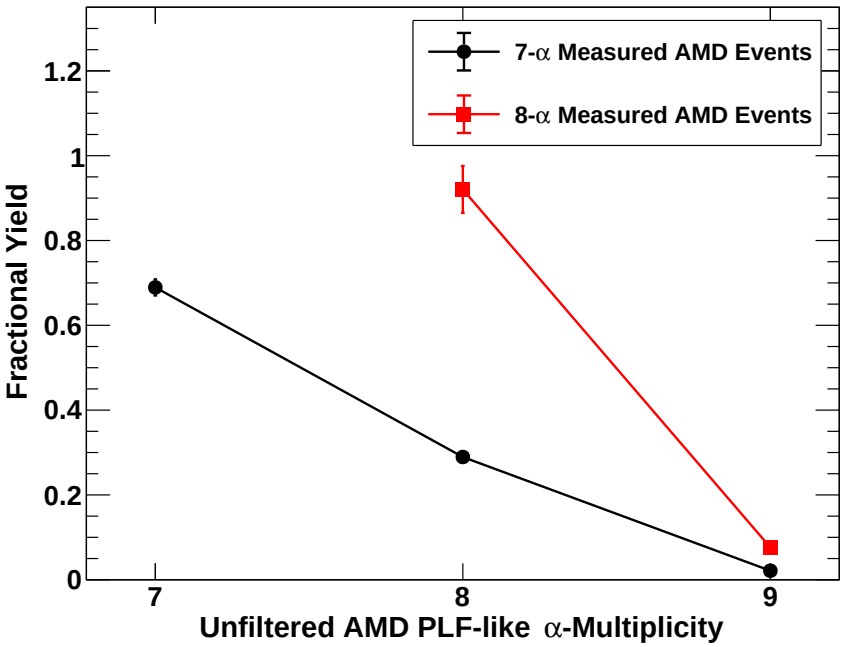

Figure 5.6: AMD + GEMINI++ N-α breakup discrimination. Fractional yield of measured (FAUST filtered) 7-α (black circle) and 8-α (red square) AMD events as a function of the unfiltered AMD projectile-like α-multiplicity. Projectile-like character determination is discussed in the text.

seen in panel (d). To ensure that each class of N-α events best contains properties consistent with N-α breakups, recategorization of events using stopped α-particles is avoided (i.e., 7,8-α events for the remainder of this work refers to events where all seven or eight α-particles were measured in both the DADL and CsI(Tl) detectors). In this analysis, 7- and 8-α events containing additionally measured Z = 1 particles are included, but the excitation energy is calculated excluding such particles (7-α: 56% contain at least one measured Z = 1 particle. 8-α: 45%). The 40 MeV source frame velocity cut is applied to measured 7,8-α events to remain consistent with prior work; the small number of events containing any α-particles outside of this region are excluded from the corresponding analysis.

Whenever an N-α event is measured in FAUST, it is difficult to know a priori whether additional projectile-like α-particles were present that missed detection due to double-hits or geometric acceptance. AMD simulation data can be used to help characterize the overall

contribution of these scenarios. To this end, FAUST-filtered AMD collisions with measured 7,8-α events were considered. For these events, particles that missed FAUST detection were examined to see if any were projectile-like α-particles. An α-particle was determined to be projectile-like if it was within the general forward-focused angular acceptance of FAUST ($\theta_{lab} \leq 45^{\circ}$) and if it had enough energy to punch through a DADL detector ($E_{lab} \geq 25$ MeV); these requirements closely replicate the projectile-like α-particle FAUST measurement requirements previously discussed. Missed detection is primarily due to double-hits (e.g., α-particle + proton incident on the same detector) or the α-particle travelling between the narrow gaps that exist between detectors. The fractional yield of the AMD unfiltered N-α projectile-like breakup for events where 7- or 8-α-particles are measured after filtering is shown in Figure 5.6. In the 7-α measured case, $\sim$30% of events had additional α-particles with projectile-like character whereas for the 8-α measured case, only $\sim$7%. The cleaner discrimination for 8-α events likely comes from there being less additional mass in the collision system to contaminate and that this lower yield class of events already requires a more rare reaction mechanism of mass pickup from the target.

5.3 Excitation Energy Analysis

A clear experimental observable for identifying charged-particle-decaying excited states is to look for correlations in the form of peaks in the excitation energy distribution for the decay channel of interest [108]. The excitation energy of the ^{28}Si(^{32}S) that leads to 7-(8-)α decay can be calculated by summing the center-of-mass kinetic energy of each α-particle and subtracting the decomposition Q-value (as in Equation 1.1). The experimental excitation energy resolution and detection efficiency of FAUST is characterized in Section 5.3.1. The experimental excitation energy distributions for the 7,8-α decay channels with comparisons to prior experimental results and theoretical predictions are shown in Section 5.3.2. Challenges in accurately describing the background contribution for these channels and a proposed alternative are discussed in Section 5.3.3.

5.3.1 Efficiency and Resolution

When interpreting experimental excitation energy distributions for the study of nuclear excited states, it is important to understand the detector apparatus bias and efficiency. Given that toroidal high-spin isomer state excitation energies, widths, and possible existence is not well constrained, it is crucial to ensure that the FAUST detector energy thresholds, geometric acceptance, double-hit bias, and energy-dependent angular resolution does not produce artifacts in the excitation energy distribution that could be falsely interpreted as excited states. For this purpose, 7,8-α breakups were simulated and FAUST-filtered to obtain the detection efficiency as a function of the excitation energy as shown in panels (c,d) of Figure 5.7. To simulate breakups, the experimental laboratory velocity and θ distributions of the 7,8-α center-of-mass were sampled; the laboratory ϕ of the source was randomized. α-particles were emitted from the source with randomized θ and ϕ at a velocity sampled from the experimental α-particle source frame distribution. Breakups produced using this procedure that exceeded the total momentum of the collision were excluded ($<$0.01% of the data). Despite this treatment simplifying many nuances and underlying correlations of high multiplicity breakups, it was expected to adequately sample a broad region of phase space for this class of events. The resulting ratio between the excitation energy distribution of simulated breakups before and after filtering exhibit no sharp features in regions of considerable yield for both 7- and 8-α events. Variance in the tails of the distributions arose from limited counts. Having all detector telescopes of FAUST fully operational for this experiment was essential for maximizing detection efficiency; "turning off" only four detectors (among Rings B and C) for both this simulation and the experimental data reduced the number of 7-α events by roughly half.

The width in the energy of a nuclear excited state decay is related to the lifetime of that state; thus, the ability to accurately measure decay energy widths provides key insight to the stability of the excited state [109]. Characterizing the expected resolution for an excited state decay measurement is necessary for untangling the convolution of the intrinsic state

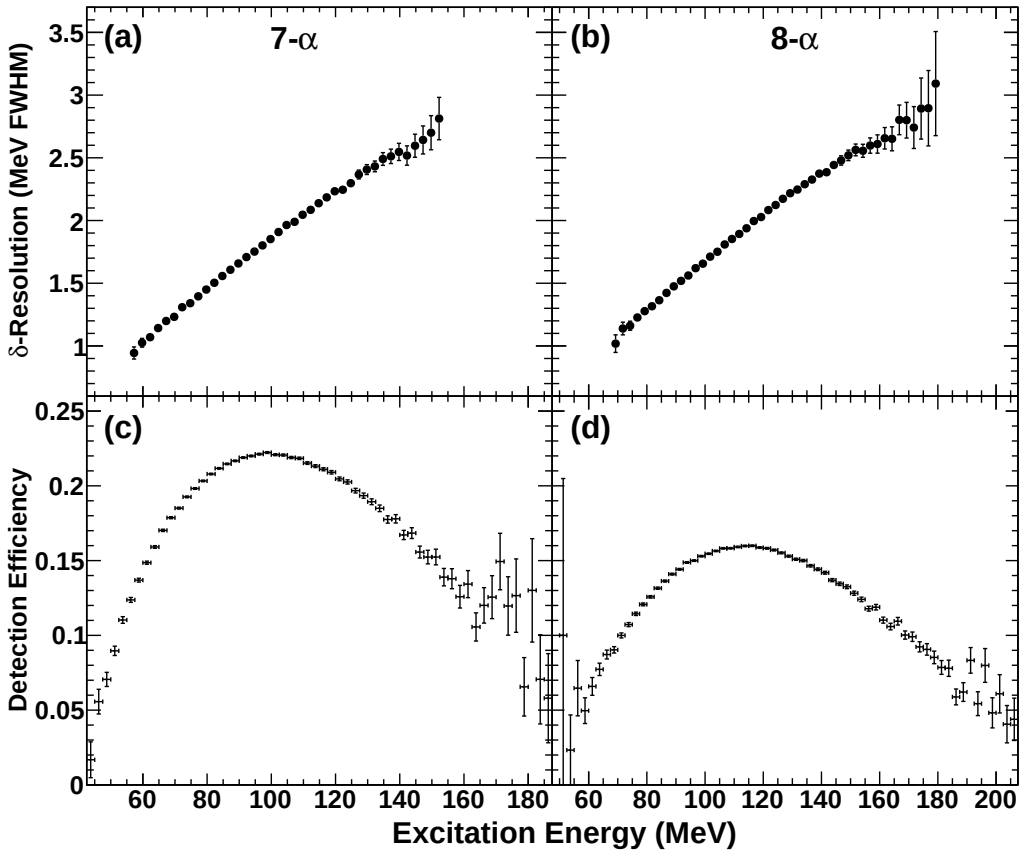

Figure 5.7: Monte Carlo simulation results for determining the resolution and detection efficiency of FAUST as a function of the excitation energy. Panels (a,b): Width (MeV FWHM) of the excitation energy distribution measured in FAUST for an infinitely narrow state for 7-α events (a) and 8-α events (b). These values indicate the Gaussian uncertainty to the excitation energy measurement. Error bars are obtained from the error in the Gaussian fits to the smeared distributions. Panels (c,d): Detection efficiency for simulated 7-α breakups (c) and 8-α breakups (d). The technique used for breakup simulation is described in the text.

width and the detection resolution. The uncertainty of the excitation energy measurement for 7,8-α decays depends heavily on the energy and angular resolution measurement of each individual α-particle. To determine the expected resolution for such decays, excitation energy distributions can be generated after filtering decays of discrete excitation energy through the FAUST filter, which models the energy resolution, detector location uncertainty, and energy- and ring-dependent angular resolution of the array (as discussed in Sections 3.3.2 and 4.5).

To sample 7,8-α decays of discrete excitation energy where the individual α-particles retain similar laboratory energy and angular distributions, an event mixing procedure was used. To create a 7-α mixed event, an α-particle is randomly chosen in seven separate, randomly chosen experimental 7-α events. Mixed events containing two particles in the same detector telescope of FAUST were rejected. The measured energies and angles of each α-particle in the mixed event are then treated as the true values. The excitation energy of this mixed event is then calculated before (true) and after (smeared) filtering. This process is repeated for a large number of iterations. Gaussian fits are then performed on the smeared distributions for small regions of the true excitation energy and the resulting uncertainty (FWHM) is plotted as a function of the true excitation energy as shown in panel (a) of Figure 5.7. The mean of each smeared distribution matches the true excitation energy. The same procedure was repeated for 8-α events as shown in panel (b). In both cases, a roughly linear, positive correlation is established between the excitation energy and the resolution, which results from larger excitation energy breakups containing α-particles with greater energies; as the energy of the α-particle increases, the energy deposited in the DADL detectors decreases, and the position (angular) resolution worsens. These higher energy α-particles will also have a larger absolute uncertainty on the energy measurement. Additionally, as the excitation energy increases, a larger fraction of α-particles will be measured at larger θ_{lab} angles where the FAUST detectors cover a larger solid angle, giving worse angular resolution. For a simulated narrow resonance at 140 MeV excitation energy, the work of ref. [11] reported that the observed experimental width in NIMROD would be $\sim$9.5 MeV FWHM; in comparison, an equivalent FAUST measurement is expected to have a $\sim$2.5 MeV FWHM.

5.3.2 Excitation Energy Distributions

The excitation energy for each measured 7,8-α event is calculated using Equation 1.1 and the distributions are shown in panels (a,b) of Figure 5.8. The excitation energy range of the measured 7-α distribution is consistent with that measured in ref. [11]; however, a slight difference in the overall shape is observed due to detection efficiency differences between

NIMROD and FAUST. Yield associated with any appreciably produced resonances would show up as finer peak-structures above the smooth continuum. Qualitatively, there are no discernible strong resonances in the 7-α spectrum; in comparison, the 8-α spectrum shows minor fluctuations that could possibly indicate correlated yield, although this spectrum has significantly lower counts and requires closer quantitative analysis to determine if these are statistically significant. To produce a background distribution that well-describes non-resonant contributions to the spectrum, many works (including the NIMROD 7-α work of ref. [11]) invoke the event mixing technique [110, 111]. This method provides a potential avenue for producing uncorrelated background spectra a priori while retaining experimentally

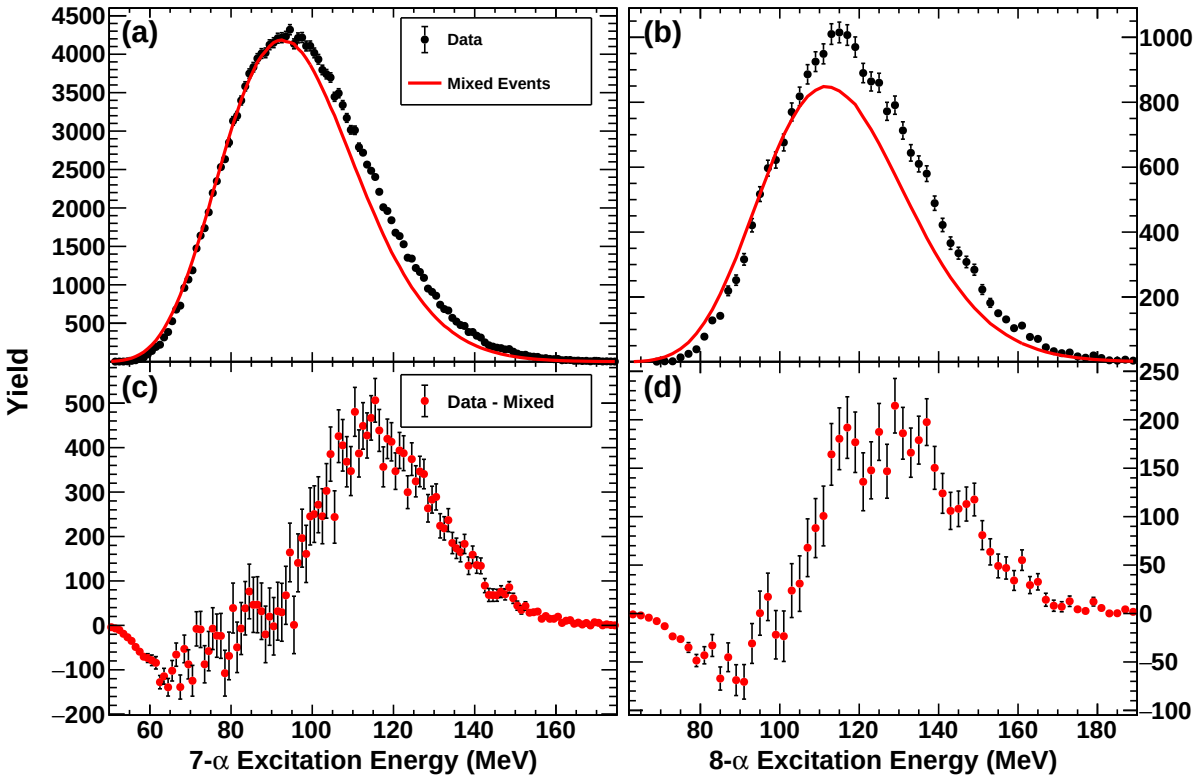

Figure 5.8: Excitation energy distributions and mixed event subtraction for measured 7,8-α events. Panel (a,b): Experimental 7-α (a) and 8-α excitation energy distribution with 1 MeV and 2 MeV bin widths, respectively. The mixed event background (red line) is normalized to the experimental distribution as described in the text. Panels (c,d): Residual spectrum after subtracting the mixed event distribution from the experimentally measured distribution.

measured single particle energy and angular distributions.

For this analysis, the event mixing technique as described in Section 5.3.1 was performed 200 times per measured event to ensure that the resultant background distribution is largely free of statistical fluctuations. It is important to keep in mind that mixed events do not contain Coulomb repulsion effects that exist in the experimental data, giving a higher probability for producing events with lower excitation energy than exists for experimental data. Normalization of the mixed event distribution to the experimental distribution should ideally not be performed in a region significantly impacted by this Coulomb discrepancy or where resonant contributions are expected to occur. Given this, the normalization was performed from 70 to 96 MeV for 7-α events and from 91 to 107 MeV for 8-α events. Subtraction of the normalized mixed event distribution from the experimental distribution for 7-α events as seen in panel (c) shows similar gross features to previous work, including a Coulomb-caused yield deficit at low excitation energy ($\sim$70 MeV) and a broad yield excess at higher excitation energy ($\sim$115 MeV). The broad excess was previously interpreted to originate entirely from multiple toroidal states [11]. While the same general features are seen for the subtracted 8-α spectrum in panel (d), the normalized mixed events fail to describe the data in the normalization region. It is possible this arises from the Coulomb contribution being more significant due to the additional α-particle, affecting a larger range of excitation energy. Further discussion about the validity of the mixed event technique in this framework is given in Section 5.3.3.

The residual spectrum from panel (c) of Figure 5.8 is reproduced in Figure 5.9 and overlaid with both the data from ref. [11] and all predicted toroidal state means of various calculations to compare results. By comparing the current data with the locations of states reported in the NIMROD experiment, no strong signature for states at these energies is present in the current data set, despite significantly improved statistics and resolution of measurement. If the mixed event background description is assumed to be accurate, the presence of broad overlapping state contributions to explain the yield excess cannot be ruled

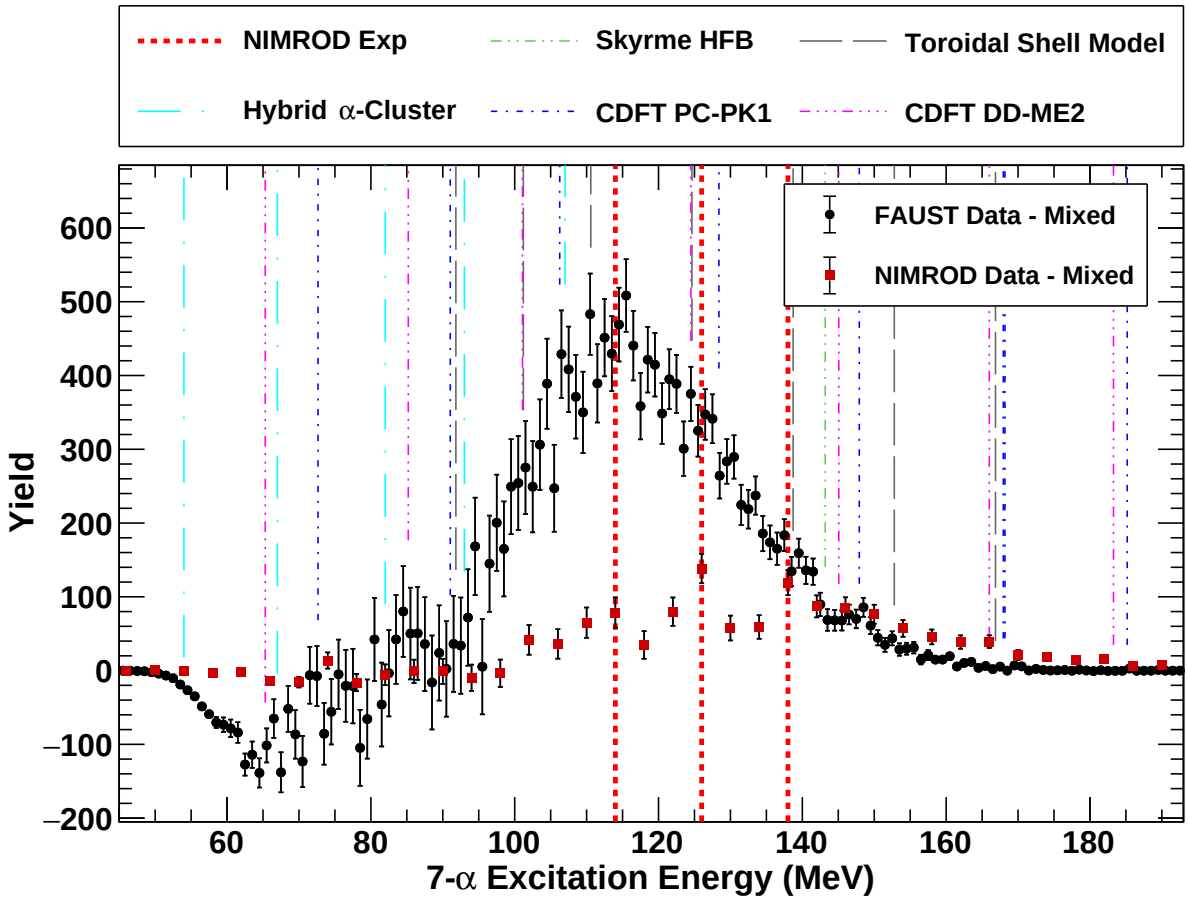

Figure 5.9: Subtracted 7-α excitation energy distribution from the current work (black circles) compared to previous work (red squares, red dashed vertical lines) and theoretical predictions of toroidal high-spin isomers in ^{28}Si (vertical lines) [16, 11, 7, 6]. States from ref. [16] with significant broadening and overlap are not reproduced in this figure, as experimental sensitivity is not expected.

out, although the width of such states would be too large to be consistent with the NIMROD measurement. While the presence of finer peak structure may be seen in a few regions (e.g., ∼87 and ∼148 MeV), lack of predictive power in the various theoretical calculations — as evidenced by the various vertical lines spanning the entire distribution — makes attributing such subtle features to a toroidal state exceptionally challenging [16, 11, 7, 6]. A potential peak nearly anywhere in the distribution could be reasonably attributed to a predicted state, highlighting the importance of exercising caution when using such predictions as guidance.

As an aside, all α-conjugate exit channels of ^{28}Si and ^{32}S were examined for possible resonant yield contributions at high excitation energy as shown in Appendix A, although no obvious peaks are seen.

5.3.3 Background Description

The event mixing technique, sometimes referred to as the "combinatorial background", is used extensively for producing uncorrelated background descriptions in the high energy regime of nuclear particle physics [112]. This technique has also been used in a number of intermediate energy heavy-ion collision analyses [113, 110]. Under ideal circumstances, event mixing carries the benefit of allowing broad and overlapping state contributions to be extracted from the total measured spectrum. However, it has been found that careful requirements and constraints to mixed event kinematic properties can be important for producing an accurate background [114, 110]. The broad excess of yield seen in panel (c) of Figure 5.8 motivated the addition of kinematic requirements to the event mixing procedure to see if reasonable constraints could produce a background description that captures the entire experimental distribution. To this end, various mixing constraints were attempted, including only mixing between events of similar reconstructed source velocity, only mixing between events of similar excitation energy, or both constraints simultaneously. Further, using the center-of-mass frame velocity vectors calculated in each of the randomly chosen α-particles real measured event center-of-mass frame rather than using the laboratory frame velocities was attempted. For this treatment, constraints to the center-of-mass angles between α-particles in the mixed events were included to prevent choosing multiple α-particles emitted at similar angles. In every case, the produced mixed event background description was shifted to lower mean excitation energies than the unconstrained procedure, failing to agree with the experimental distribution in any region; after subtraction, there is even greater enhanced yield deficits at lower excitation energies and yield excesses at higher excitation energies.

The inability to reasonably produce a mixed event background that well describes the

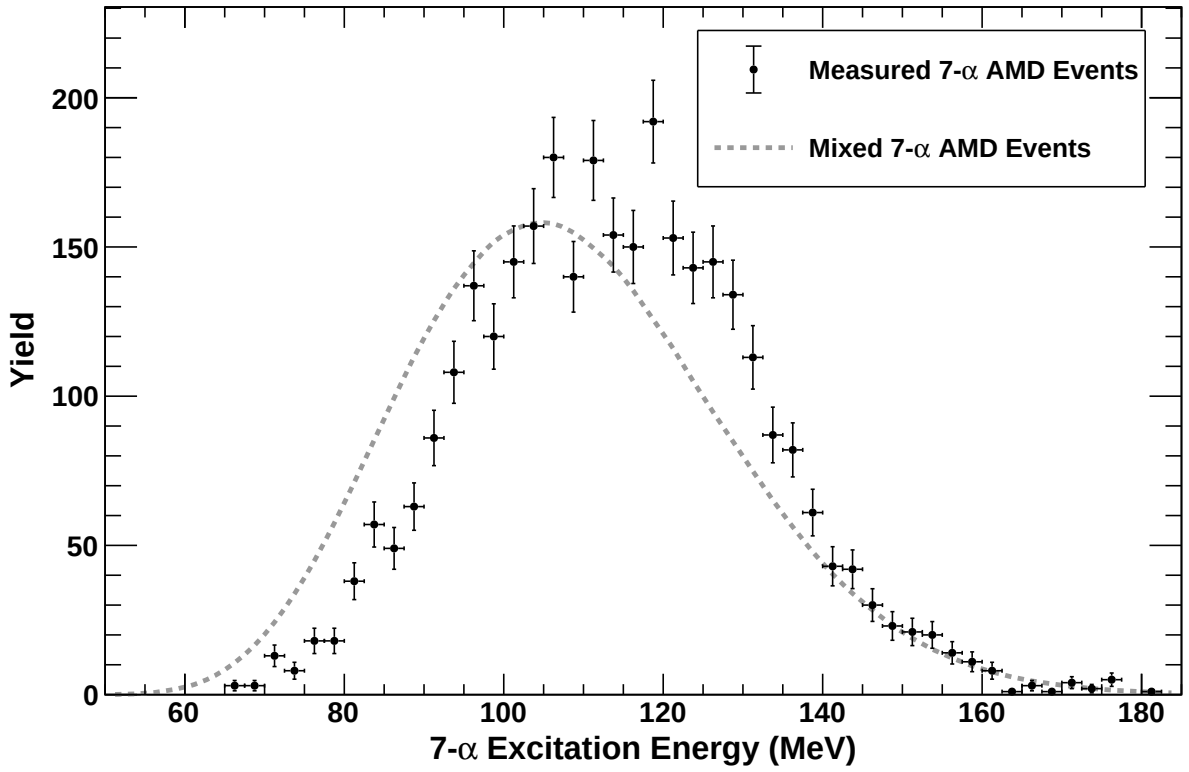

Figure 5.10: Filtered AMD + GEMINI++ simulated excitation energy distribution for 7-α events (black circles). The distribution obtained after performing the event mixing technique is shown by the gray dashed curve. The mixed event distribution is normalized to the measured distribution to give equal total integrals.

grossly smooth, single-peaked experimental 7-α distribution raises concern for the applicability of this technique to this class of events. The AMD + GEMINI++ simulation does not contain particle-particle correlations, and so the excitation energy distribution for 7-α events produced in the simulation is expected not to contain any resonant yield contributions. The 7-α excitation energy distribution for filtered AMD + GEMINI++ events is shown in Figure 5.10. The shape of this distribution is qualitatively similar to the experimental data; however, the mean is $\sim$15 MeV greater. This similar discrepancy was observed in ref. [11] where the AMD + GEMINI++ distribution was shifted down in excitation energy to agree with experiment. Nevertheless, if the mixed event procedure is a valid way to produce a background description for these 7-α events, event mixing of the simulated data

should agree with the event-by-event excitation energy distribution. Comparison between the filtered simulation excitation energy distribution and the distribution obtained through filtered event mixing is shown in Figure 5.10. For this study, no energy or angular smearing was performed by the filter. Nevertheless, the distribution obtained from event mixing does not match the measured distribution. If this mixed event distribution was normalized to the measured distribution in an analogous range as Figure 5.8 and subtracted, a similar deficit and excess of yield would be obtained. While the Coulomb interaction likely plays a role in this discrepancy, it is unlikely to explain the deviation in shape at higher excitation energies (> 100 MeV). Typically, event mixing is applied to particle correlations that are a relatively small subset of the total collision system and thus there is little precedent for applying such a technique for describing background contributions where the correlation of interest contains most of the mass of the system. These observations raise concern in the application of the mixed event technique for this class of events, casting doubt on the significance of broad yield excesses previously observed.

Given the observed shortcomings of the mixed event technique in this context, an alternative approach for assessing the statistical significance of any fluctuations is essential. For many experimental resonant state studies, there is significant yield, narrow measured width, and confidence in the predicted decay energy. In this case, the error introduced in roughly describing the background with a smooth polynomial does not impede the extraction of state properties [115, 116]. Using this treatment for the current data is not justifiable due to the absence of high yielding, obvious peaks. Locating yield associated with excited state resonant decay relies on determining whether any features of the experimental distributions deviate from expected fluctuations of a smooth continuum. To phenomenologically produce a continuum that well describes the entire range of the excitation energy distribution, the experimental 7-α data is fit with a 9^{th} order polynomial, producing a smooth, single-peaked background as shown in panel (a) of Figure 5.11. The order of the polynomial was chosen by finding a minimum in the χ^2/ν for polynomials of order 4 through 11 and ensuring that the

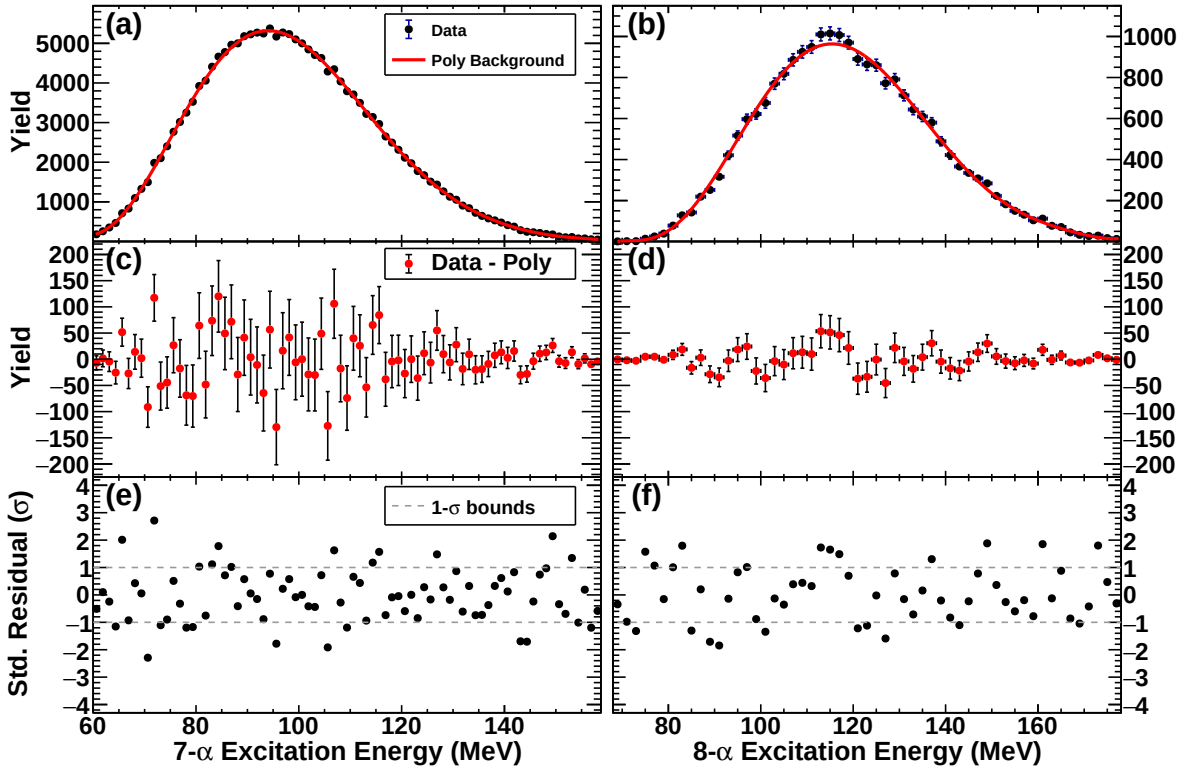

Figure 5.11: Excitation energy distributions and background continuum descriptions using polynomial fits. Panel (a,b): Experimental 7-α (a) and 8-α excitation energy distributions in 1.25 MeV and 2 MeV wide bins respectively. A polynomial of 9^{th} (a) and 7^{th} (b) order are fit to the data as shown by the red curves. Panels (c,d): Residual spectra after subtracting the polynomial fits from the experimentally measured distributions. Panels (e,f): Standardized residual plots obtained by dividing the data in panels (c,d) by the square root of the expected count error of the fits. Horizontal dashed lines are drawn to indicate the 1-σ region.

resulting fit was unimodal and described the gross shape of the experimental data. Just as in Figure 5.8, the polynomial background was subtracted from the experimental data, leaving the residuals in panel (c). As the count error scales with the square root of the number of counts, larger error bars in the residual correspond to larger absolute yield in the data. One way to account for the changing relative error across the distribution is to instead plot the standardized residual as shown in panel (e), where the residual values in panel (c) are divided by the expected count error of the fit. If the data is well described by the produced background, the standardized residual data is expected to obey Gaussian populations, with

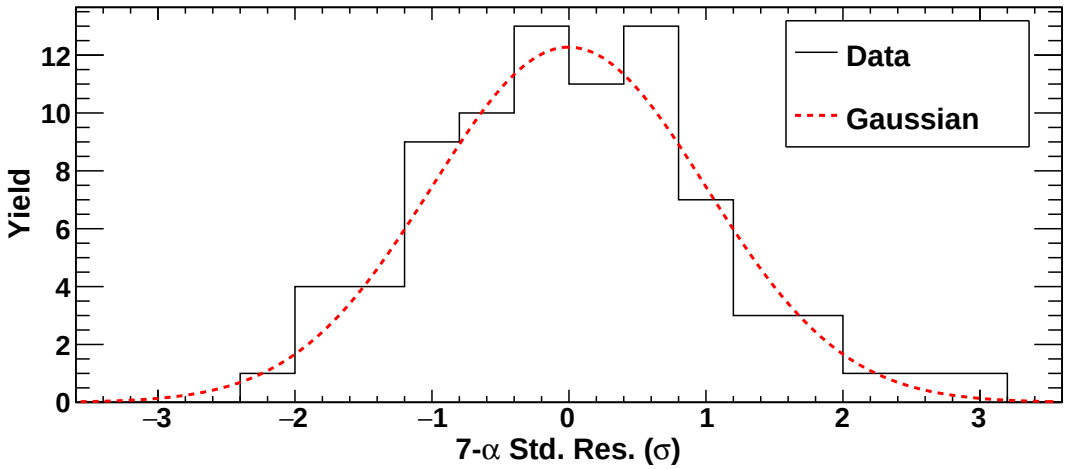

Figure 5.12: Projected 7-α standardized residuals from panel (e) of Figure 5.11 (black) compared to a Gaussian with a mean of 0 and standard deviation of 1σ (red dashed).

$\sim$68.2% of the data lying between -1σ and 1σ, $\sim$27.2% of data lying between $\pm$(2σ and 3σ), $\sim$4.2% of data lying between $\pm$(3σ and 4σ), and so on. In other words, the data in panel (e) projected to the y-axis will give a Gaussian distribution centered at 0 with a standard deviation of 1σ if the background well describes the underlying distribution; a comparison between the projected standardized residuals for the 7-α event data and such a Gaussian is shown in Figure 5.12. The χ^2/ν of the fit indicates the width of this projected distribution and has a value of 1.01 for the 7-α data. The calculated χ^2/ν can be compared to the corresponding χ^2 distribution (which depends on the number of degrees of freedom, ν). Integration of this distribution to the right of the measured χ^2/ν yields a p-value, indicating the probability that the measured distribution with the given fluctuations would happen by chance (p = 0.44 for the experimental 7-α distribution with this assumed background). The ubiquitously used standard for a statistically significant p-value is p = 0.05, well below what is seen here. The standardized residuals also show a qualitatively random deviation from the mean with no apparent structure. It is important to note that this statistical analysis loses sensitivity as the width of possible states increases and the yield decreases, as at some limit such features will drive the fit to describe them. The main takeaway is that there is no

evidence for statistically significant, relatively narrow ($\sigma \lesssim 5$ MeV) states in the measured spectrum under the assumption of a smooth, unimodal background. The same procedure was performed using a 7$^{\text{th}}$ order polynomial for 8-α events in panels (b,d,f) of Figure 5.11, giving a χ^2/ν of 1.17 with an associated p-value of 0.22. While the two residual spectra in panels (d,f) may show subtle structure, none of the features deviate substantially from the expected distribution or agree with the ∼154 MeV predicted state in ^{32}S [6]. Further statistical significance analysis and discussion can be found in Section 5.7.

5.4 Sequential vs. Simultaneous: Decay Intermediates

The mechanism of decay for highly excited nuclei can be largely categorized into two extremes: successive binary decays (sequential) and prompt multifragmentation (simultaneous). The simultaneous decay scenario is typically used to describe a fast mechanism where the colliding nuclei "explode" into many fragments [117]. For lower excitation energies ($\lesssim$1

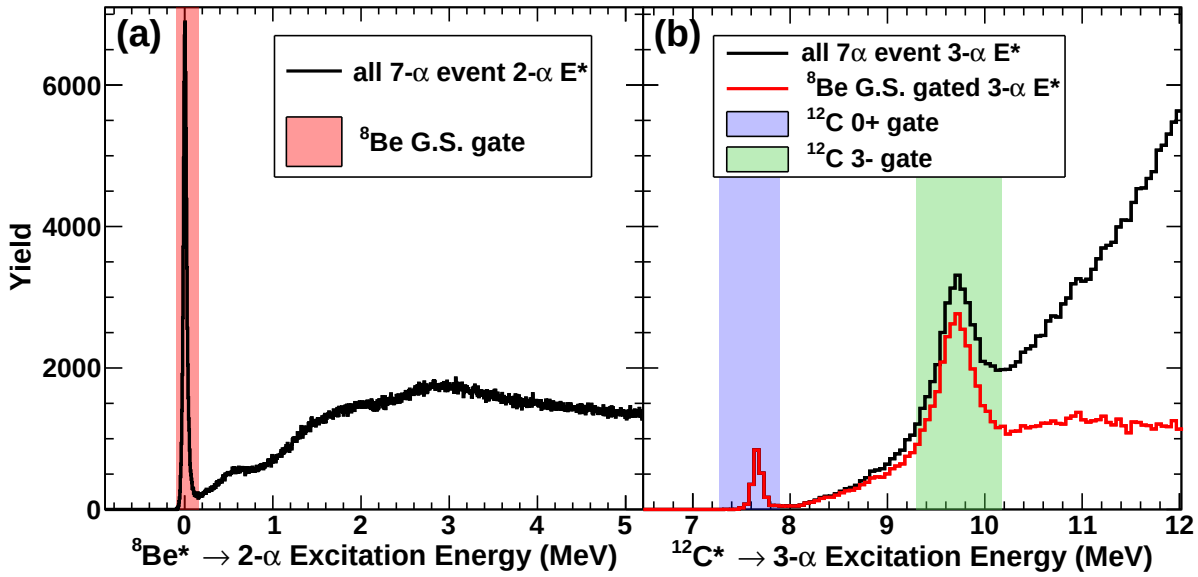

Figure 5.13: 2,3-α particle excitation energy distributions in 7-α events used for determining sequential decay pathway yields. Panel (a): 2-α excitation energy to observe excited states of ^{8}Be. The gate used to determine a ground state decay is shown by the red shaded region. Panel (b): 3-α excitation energy for all events (black) and for events gated on the ^{8}Be ground state (red) to observe excited states of ^{12}C. The 0+ and 3- gates, shown by the blue and green shaded regions respectively, were applied to the ^{8}Be ground state gated distribution.

MeV/nucleon), nuclei are well understood to de-excite by evaporating particles successively [118]. The dominant decay mode has been found to depend largely on the excitation energy of the decaying nucleus, in which the simultaneous mechanism becomes favorable at higher excitation energies (>3 MeV/nucleon) [119]. There is limited theoretical support for the predicted decay timescale (lifetime) and mechanism of a clustered toroidal high-spin isomer. Given the high excitation energy, large angular momentum, ring-like structure, and predicted stability of such states, it is reasonable to consider the possibility of simultaneous decay enhancement even over longer timescales. One way the degree of simultaneity is characterized in experimental data is by simulating each decay mechanism extreme and comparing the model results to various breakup observables (e.g, source frame relative angles and kinetic energy spectra) [8, 120]. A more selective technique involves identifying sequential breakups on an event-by-event basis by observing intermediate unbound excited states [34].

The α-decaying excited states of ^{8}Be and ^{12}C that are produced in 7,8-α disassembly events can be observed by examining the excitation energy distribution for all combinations of two and three α-particles in each event as shown in Figure 5.13. The ^{8}Be ground state seen at $\sim$0 MeV in panel (a) and the ^{12}C 0+ Hoyle state seen at $\sim$7.65 MeV in panel (b) contain negligible background contributions. As a result, gates can be placed around these peaks to determine when these intermediate state breakups occured during the 7-α disassembly. Additionally, the ^{12}C 3- state seen at $\sim$9.64 MeV in panel (b) shows considerable yield; however, for all 3-α pairings as seen in black, there is $\sim$75% background contribution. Like the 0+ Hoyle state, the ^{12}C 3- state is known to decay through the ^{8}Be ground state [121]. By only calculating available 3-α excitation energies when two of the α particles are within the ^{8}Be ground state gate, the background contribution is reduced to $\sim$50%. Accepting this level of contamination, a gate can be placed around this state to identify the presence of these intermediate decays. All possible intermediate decay channels consisting of these three excited states in 7,8-α breakups are shown in Table 5.2. Careful categorization of each 7,8-α event was performed to determine the measured intermediate decay channel. While

there are no high-yielding and low contamination states observed for 4-α pairings (^{16}O* $\rightarrow$ 4-α), some excited states of ^{16}O are known to decay through the ^{8}Be ground state, and thus it is understood that some number of events containing the ^{8}Be ground state may contain sequential decay steps associated with ^{16}O [116].

There is evidence that the ^{8}Be ground state and ^{12}C Hoyle state may be Bose-Einstein condensate states, where each α-particle cluster inhabits the same 0s orbital. There should be equal probability of a condensate state to decay through any of the possible condensate-containing decay channels, with the branching ratios only depending on the Coulomb barrier and allowable phase space for each pathway [122]. There is significant effort to better constrain the branching ratio between simultaneous (^{12}C $\rightarrow$ 3-α) and sequential (^{12}C $\rightarrow$ α + ^{8}Be G.S. $\rightarrow$ 3-α) decay of the Hoyle state [1]. Equal probability of these two pathways would indicate the condensate nature of this state; however, the simultaneous decay pathway has significantly less phase space, making experimental efforts of its precise measurement challenging. There are also some efforts to search for condensate states in heavier N-α systems using the same technique, albeit over a larger number of condensate-containing decay pathways [34]. Given that there is still a lack of agreement within the scientific community on the

Identifier	7(8)-α Decay Channel	Identifier	7(8)-α Decay Channel
1	$(\alpha) + 7\alpha$	10	$(\alpha) + \alpha + {}^{12}C_{3^-} + {}^{12}C_{3^-}$
2	$(\alpha) + 5\alpha + {}^{8}Be_{gs}$	11	$(\alpha) + \alpha + {}^{8}Be_{gs} + {}^{8}Be_{gs} + {}^{8}Be_{gs}$
3	$(\alpha) + 4\alpha + {}^{12}C_{0^+}$	12	$(\alpha) + {}^{8}Be_{gs} + {}^{8}Be_{gs} + {}^{12}C_{0^+}$
4	$(\alpha) + 4\alpha + {}^{12}C_{3^-}$	13	$(\alpha) + {}^{8}Be_{gs} + {}^{8}Be_{gs} + {}^{12}C_{3^-}$
5	$(\alpha) + 3\alpha + {}^{8}Be_{gs} + {}^{8}Be_{gs}$	14	${}^{8}Be_{gs} + {}^{12}C_{0^+} + {}^{12}C_{0^+}$
6	$(\alpha) + 2\alpha + {}^{8}Be_{gs} + {}^{12}C_{0^+}$	15	${}^{8}Be_{gs} + {}^{12}C_{0^+} + {}^{12}C_{3^-}$
7	$(\alpha) + 2\alpha + {}^{8}Be_{gs} + {}^{12}C_{3^-}$	16	${}^{8}Be_{gs} + {}^{12}C_{3^-} + {}^{12}C_{3^-}$
8	$(\alpha) + \alpha + {}^{12}C_{0^+} + {}^{12}C_{0^+}$	17	${}^{8}Be_{gs} + {}^{8}Be_{gs} + {}^{8}Be_{gs} + {}^{8}Be_{gs}$
9	$(\alpha) + \alpha + {}^{12}C_{0^+} + {}^{12}C_{3^-}$		

Table 5.2: Categorization of events with 7- and 8-α-particles in the exit channel into the intermediate decay channels that contain ^{8}Be$_{gs}$, ^{12}C$_{0^+}$, and ^{12}C$_{3^-}$. Decay channels 1 - 13 are similar between the 7- and 8-α events, with the 8-α events containing an additional α-particle. Decay channels 14 - 17 are only for 8-α events.

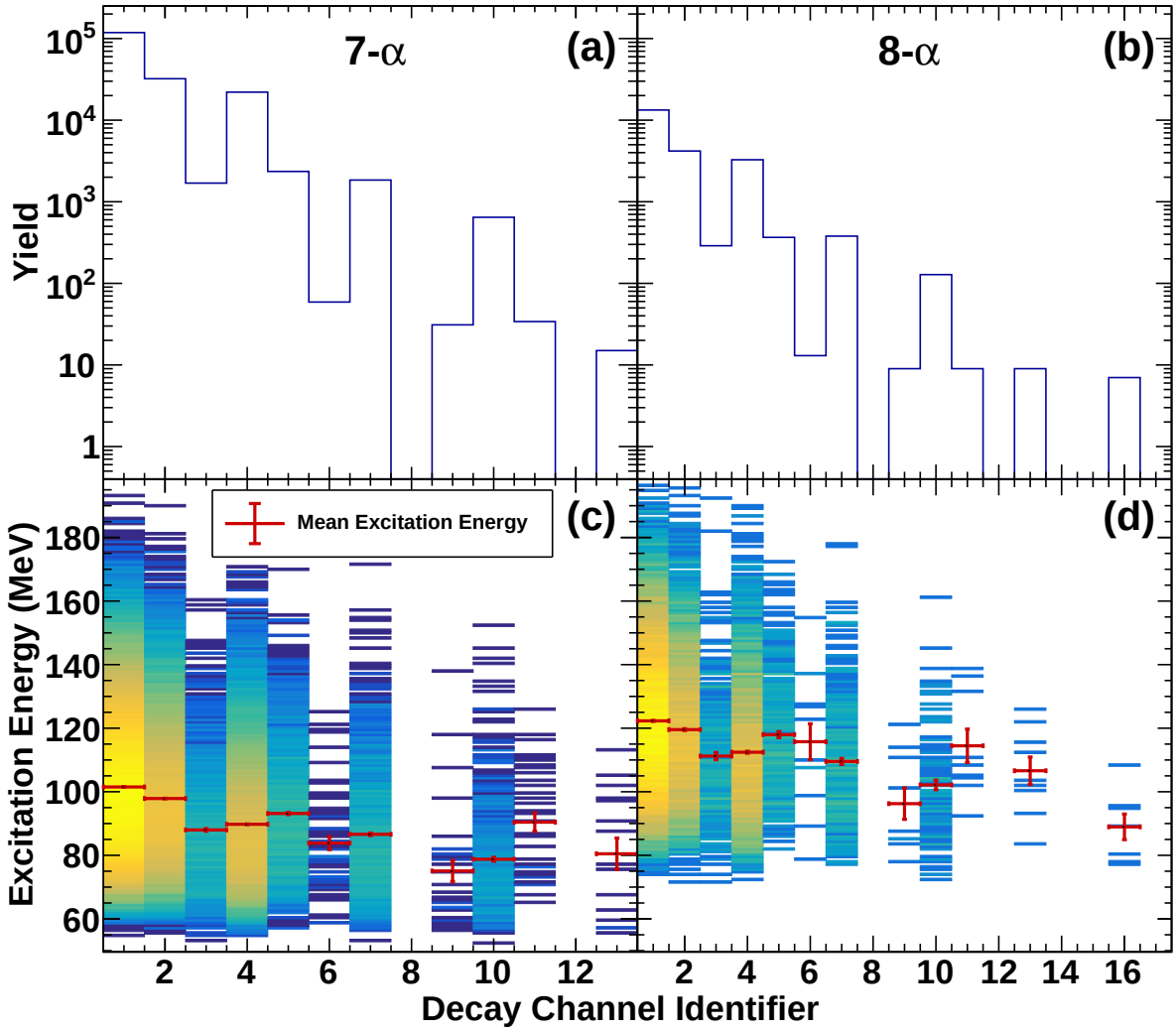

Figure 5.14: Yield and excitation energy of each intermediate decay channel for 7,8-α events. Panels (a,b): Yield of each intermediate decay channel for 7-α (a) and 8-α (b) events. The details of each decay channel identifier can be found in Table 5.2. Panels (c,d): Excitation energy distribution of eac intermediate decay channel for 7-α (c) and 8-α (d) events. The mean excitation energy for each channel is shown by the red data points.

location and existence of the predicted ^{16}O 0^+_6 condensate state, and that heavier N-α condensates are not yet confirmed, the application of this work to such efforts is currently limited [113, 123]. Further, accurately assessing the primary yield distribution of each intermediate decay channel depends heavily on the associated detection efficiency. These difficulties are exacerbated by the low intrinsic detection efficiency of these low energy decays. Even

in isolation (no additional fragments to contribute to double hits), the detection efficiency for the ^{8}Be ground state, ^{12}C Hoyle, and ^{12}C 3- state for this collision system and energy in FAUST is ∼25.53%, 11.4%, and 20.1%, respectively; this was determined via a Monte Carlo technique, where each decay was simulated by sampling the experimental energy and angular (θ_{lab}) distribution of each parent nucleus (e.g., ^{12}C for the Hoyle state), randomizing the azimuthal angle (ϕ_{lab}), performing the decay with a random orientation, and filtering. Nevertheless, if any 7,8-α events proceed through a simultaneous decay mechanism, the ensemble of data that does not include the ^{8}Be ground state (and, by extension, the ^{12}C 0+ Hoyle state and ^{12}C 3- state) will contain a higher fraction of such events.

The yield and excitation energy for each intermediate decay channel measured in 7,8-α events is shown in Figure 5.14. The measured yield of each channel is heavily impacted by the detection efficiency of each intermediate excited state, as seen by the lack of any yield associated with events containing two ^{12}C 0+ Hoyle states (decay channel identifier = 8). Such events would contain two separate 3-α groupings that have very small relative energies between them, resulting in α-particles that often strike the same detector. As expected, the mean excitation energy of all sequential decay channels (decay channel identifier > 1) is less than the ensemble that does not contain intermediates (decay channel identifier = 1), as lower excitation energy favors sequential decays. Inspection of each decay channel excitation energy distribution showed no evidence of strongly populated excited states.

The evolution of primarily sequential decays to prompt multifragmentation is known to depend on both the excitation energy and temperature of the excited nucleus [119]. The kinetic energy spectra of emitted particles in the frame of the source can give information about the temperature of the decaying nucleus [124, 125]. Such spectra can often be well described by a Maxwell-Boltzmann distribution of emitted particle energies, giving information

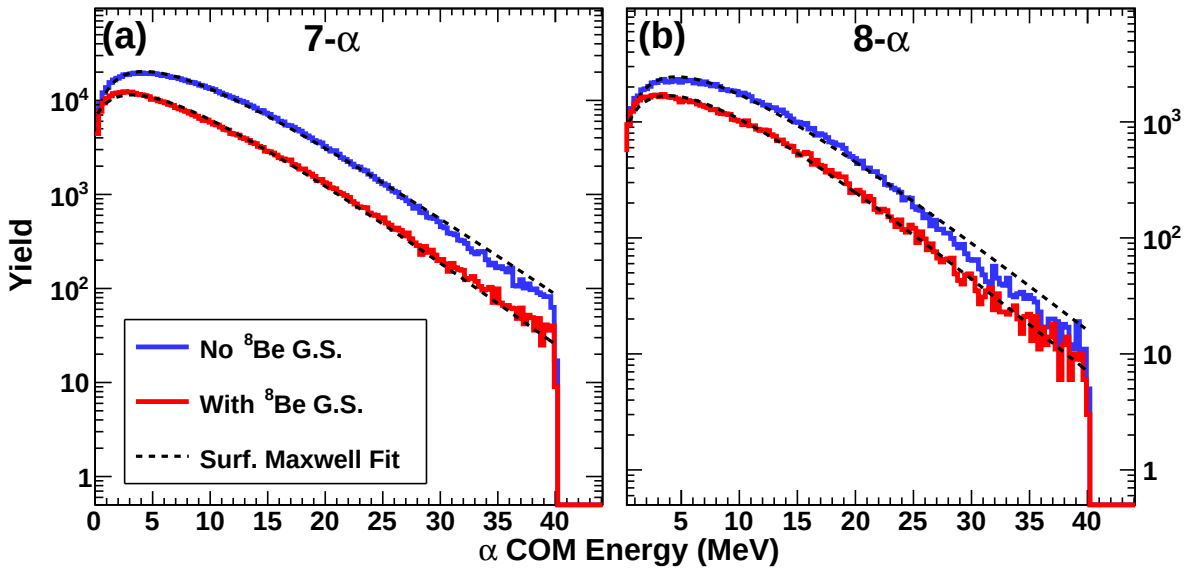

Figure 5.15: α-particle kinetic energy spectra in the frame of the decaying source for 7,8-α events with and without a ^{8}Be ground state intermediate decay. The surface pre-exponential factor Maxwell-Boltzmann fit (Eq. 5.1) is fit to each distribution as shown by the black dashed curves. The cutoff at 40 MeV corresponds to the velocity cut applied in Section 5.2 to exclude pre-equilibrium emission. Panel (a): Data and fits for 7-α events. Panel (b): Data and fits for 8-α events.

about the temperature when fit:

$$dN/dE \propto P_{(surf,vol)} exp[-(E - C_c)/T] \tag{5.1}$$

$$P_{surf} = (E - C_c) \tag{5.2}$$

$$P_{vol} = (E - C_c)^{1/2} \tag{5.3}$$

where dN/dE is the yield as a function of the decay particle center-of-mass kinetic energy, $P_{surf,vol}$ is the corresponding pre-exponential factor, C_c is the Coulomb barrier, and T is the temperature. Some work tries to determine the dominant decay mechanism (sequential vs. simultaneous) by fitting these spectra with two different pre-exponential factors [8]. It has been suggested that sequential decays may be better described using a surface term, P_{surf} (particles emitted from the surface of a decaying nucleus) and that simultaneous decays may

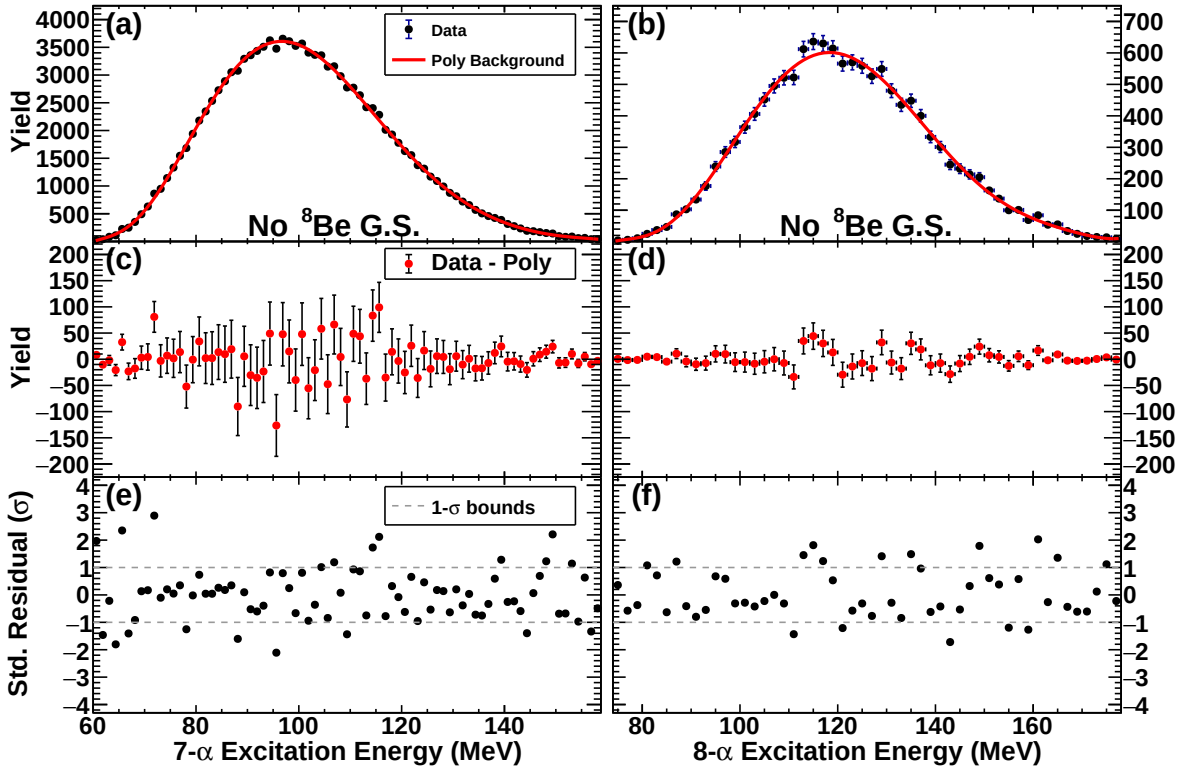

Figure 5.16: Excitation energy distributions for 7,8-$\alpha_{NoG.S.}$ events with background continuum descriptions using polynomial fits. Panel (a,b): Experimental 7-$\alpha_{NoG.S.}$ (a) and 8-$\alpha_{NoG.S.}$ (b) excitation energy distributions in 1.25 MeV and 2 MeV wide bins respectively. A polynomial of 9$^{\text{th}}$ order are fit to both sets of data as shown by the red curves. Panels (c,d): Residual spectra after subtracting the polynomial fits from the experimentally measured distributions. Panels (e,f): Standardized residual plots obtained by dividing the data in panels (c,d) by the square root of the expected count error of the fits. Horizontal dashed lines are drawn to indicate the 1-σ region.

be better described using a volume term, P_{vol} (expanding volume of gas); however, confidently distinguishing between the two via experiment has been posed as unlikely due to the strong energy dependence of the Coulomb barrier [63]. The center-of-mass kinetic energy spectra for α-particles in 7,8-α events that do (7,8-$\alpha_{WithG.S.}$) and do not (7,8-$\alpha_{NoG.S.}$) contain a ^{8}Be ground state are shown in Figure 5.15. Equation 5.1 was fit to the distributions with both pre-exponential factors. It was found that using P_{surf} was necessary for reasonably fitting the 7,8-$\alpha_{NoG.S.}$ data. While this could indicate that such events are better described

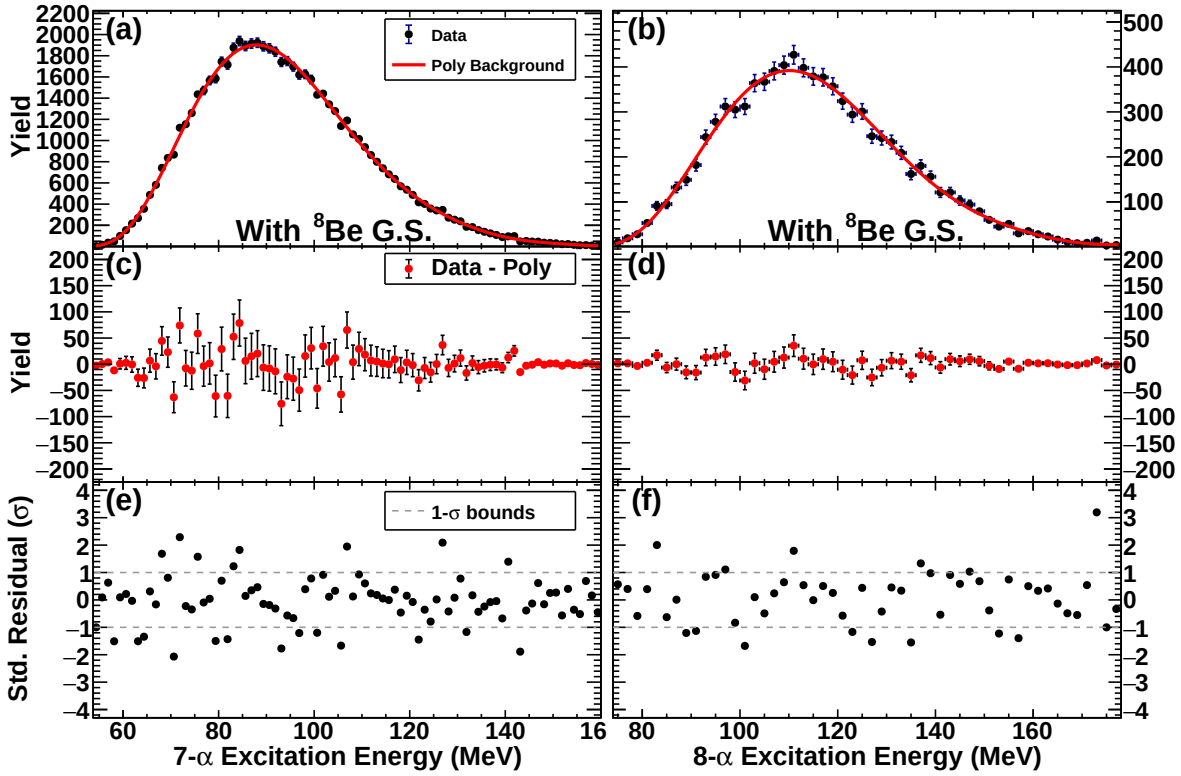

Figure 5.17: Excitation energy distributions for 7,8-$\alpha_{WithG.S.}$ events with background continuum descriptions using polynomial fits. Panel (a,b): Experimental 7-$\alpha_{WithG.S.}$ (a) and 8-$\alpha_{WithG.S.}$ (b) excitation energy distributions in 1.25 MeV and 2 MeV wide bins respectively. A polynomial of 11$^{\text{th}}$ (a) and 9$^{\text{th}}$ (b) order are fit to the data as shown by the red curves. Panels (c,d): Residual spectra after subtracting the polynomial fits from the experimentally measured distributions. Panels (e,f): Standardized residual plots obtained by dividing the data in panels (c,d) by the square root of the expected count error of the fits. Horizontal dashed lines are drawn to indicate the 1-σ region.

by a sequential decay mechanism, these surface fits all give non-physical negative values for the Coulomb barrier. Further, 7,8-$\alpha_{WithG.S.}$ events gave fits of comparable quality using both P_{surf} and P_{vol}, casting doubt on the conclusions of simultaneous α-clustered decay for all 7-α disassembly events that are drawn in ref. [8]. Nevertheless, the fits indicate that 7,8-$\alpha_{NoG.S.}$ breakups ($T_{7\alpha} = 4.69 \pm 0.01$ MeV, $T_{8\alpha} = 4.96 \pm 0.02$ MeV) have a higher temperature than 7,8-$\alpha_{WithG.S.}$ ($T_{7\alpha} = 4.40 \pm 0.01$ MeV, $T_{8\alpha} = 4.70 \pm 0.02$ MeV), in agreement with the understanding that lower temperatures favor sequential decays [119]. The higher tempera-

ture for 8-α events when compared to 7-α events is unsurprising given the higher excitation energies necessary for 8-α breakup. The slight deviation from an exponential tail seen at $\sim$30 MeV for 7,8-$\alpha_{NoG.S.}$ events may suggest the presence of breakup mechanisms not well described by the thermal decay picture, although no strong conclusions can be drawn.

A major goal of partitioning 7,8-α events into 7,8-$\alpha_{WithG.S.}$ and 7,8-$\alpha_{NoG.S.}$ is to increase the possible resonant state yield to background yield ratio. While the work of ref. [11] indicates that the bulk 7-α breakup properties are consistent with a sequential decay mechanism, the mechanism for possible toroidal high-spin state breakup remains an open question which, if present, would only constitute a small fraction of the data. As in Section 5.3.3, the 7,8-α excitation energy distributions can be examined for statistically significant yield enhancements. The same treatment of the data as for Figure 5.11 is performed for 7,8-$\alpha_{NoG.S.}$ events as shown in Figure 5.16. While there is some indication of overfitting, as evidenced by the regions of excitation energy with similar and small standardized residuals in panels (e,f), the polynomial fit is still a unimodal description of the data and does not contain any perceivable fluctuations. There is no indication of resonant state yield outside of expected fluctuations (7-α: p = 0.73, 8-α: p = 0.52). The slight enhancement seen at $\sim$115 MeV in panel (f) does not agree with the predicted $\sim$154 MeV state and is otherwise below the threshold for making any significant claims. The same analysis is performed for 7,8-$\alpha_{WithG.S.}$ events as shown in Figure 5.17. The standardized residual plots in panels (e,f) also do not show any evidence of strong resonant state yield (7-α: p = 0.20, 8-α: p = 0.47).

5.5 Momentum Shape Analysis and Source Properties

Momentum shape analysis is a way to characterize the emission pattern, reveal details of the reaction dynamics, provide insight to decay timescales, and study collective flow for particles produced in heavy-ion collisions at intermediate and relativistic energies [126, 127]. For examining the properties of 7,8-α decays, the two main properties of interest are the sphericity and coplanarity. As previously discussed in Section 1.3.1, if a toroidal high-spin isomer decays through a simultaneous mechanism into fragments of equal mass, the

momentum shape distribution would be directly related to the geometric configuration at breakup and thus such breakups could be expected to have enhanced coplanarity. On the other hand, the relationship between momentum shape and configuration space becomes increasingly indeterminate for sequential decays. The momentum shape analysis uses a tensor constructed from the product of all α-particle momenta and can be written as:

$$T_{i,j} = \Sigma_{\nu=1}^{N} p_i^{\nu} p_j^{\nu} \tag{5.4}$$

where N is the total number of α-particles, p_i^{ν} is the momentum component of the ν^{th} particle in the center-of-mass frame, and i refers to the Cartesian coordinate. Diagonalizing the tensor reduces the overall momentum shape to an ellipsoid. Qualitative shape information about each event is obtained using the normalized and ordered tensor eigenvalues, λ_1, λ_2, and λ_3. The sphericity of the momentum shape is defined as $S = \frac{3}{2}(1 - \lambda_3)$, and the coplanarity is defined as $C = \frac{\sqrt{3}}{2}(\lambda_2 - \lambda_1)$. This defines a sphericity-coplanarity space bound by a triangle with (S, C) vertices of $(0, 0)$, $(3/4, \sqrt{3}/4)$, and $(1, 0)$, corresponding to the extreme shape cases of entirely rod-like, disk-like, or sphere-like, respectively. Momentum shape information

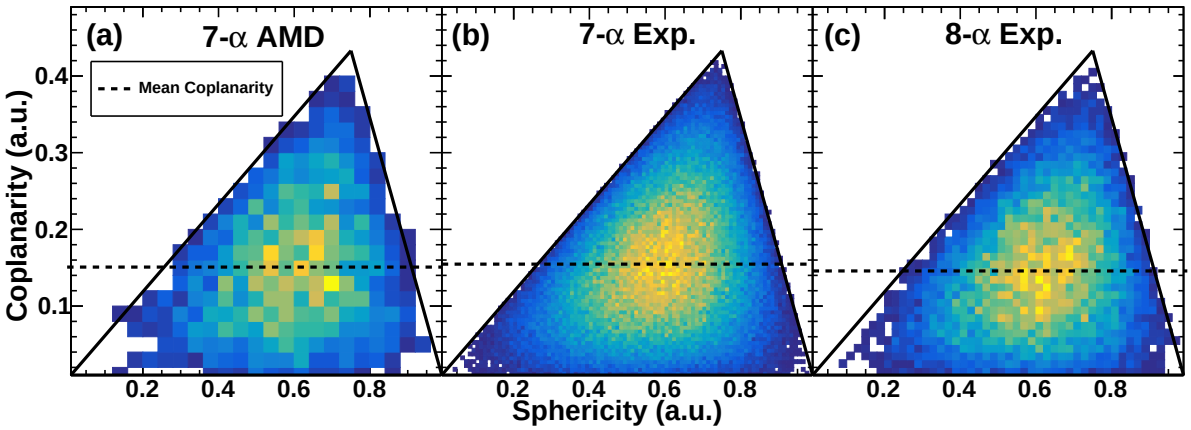

Figure 5.18: Simulated and experimental momentum shape sphericity-coplanarity yield distributions with a linear color scale. The mean coplanarity for each panel is shown by the horizontal black dashed line. Panel (a): Shape distribution for AMD+GEMINI++ filtered 7-α events. Panel (b): Experimental 7-α data. Panel (c): Experimental 8-α data.

becomes increasingly well defined with increasing number of particles in the tensor. In the case of two or three particles, all data will lie along the rod-disk axis. Sphericity-coplanarity distributions for AMD + GEMINI++ filtered 7-α events and experimental 7,8-α events are shown in Figure 5.18. There is qualitative agreement between all three distributions with the peak of the data located between all shape extremes and the mean coplanarity of each distribution being comparable. The same agreement was found in ref. [11] as it was discovered that the characteristics of the AMD + GEMINI++ shape distribution is largely dictated by the GEMINI++ sequential decay code; simulated events that give seven α-particles in the exit channel typically only have a few excited primary fragments fed to GEMINI++ from AMD at $t = 300$ fm/c (as seen in Figure 1.12). Like in this previous work, there is no indication of enhanced coplanar yield in the experimental distributions compared to simulation.

The lack of strong evidence for toroidal high-spin isomers in the excitation energy yield distributions prompts the exploration of other observables potentially sensitive to their existence. The mean sphericity and coplanarity as a function of excitation energy for 7,8-α events is shown in Figure 5.19. For both 7- and 8-α events, the mean sphericity and coplanarity decrease as the excitation energy increases. In other words, as the excitation energy increases, the shape of the α-particle momenta becomes elongated on average. These trends are well reproduced by the AMD + GEMINI++ simulation data for 7-α events (8-α event simulation results are excluded due to poor statistics). This relationship between the momentum shape observables and excitation energy may provide further insight to the nature of α-disassembly in these collisions, as both observables are related to the timescale and mechanism for decay. Model calculations of prompt multifragmentation typically yield significantly higher mean sphericity and modestly higher coplanarity than that obtained using sequential decay models [127, 128, 129]. However, as discussed in Section 5.4, prompt decays are thought to become favored for sources with higher excitation energies. The trends seen in Figure 5.19 show the opposite trend from what would be expected in a scenario of prompt

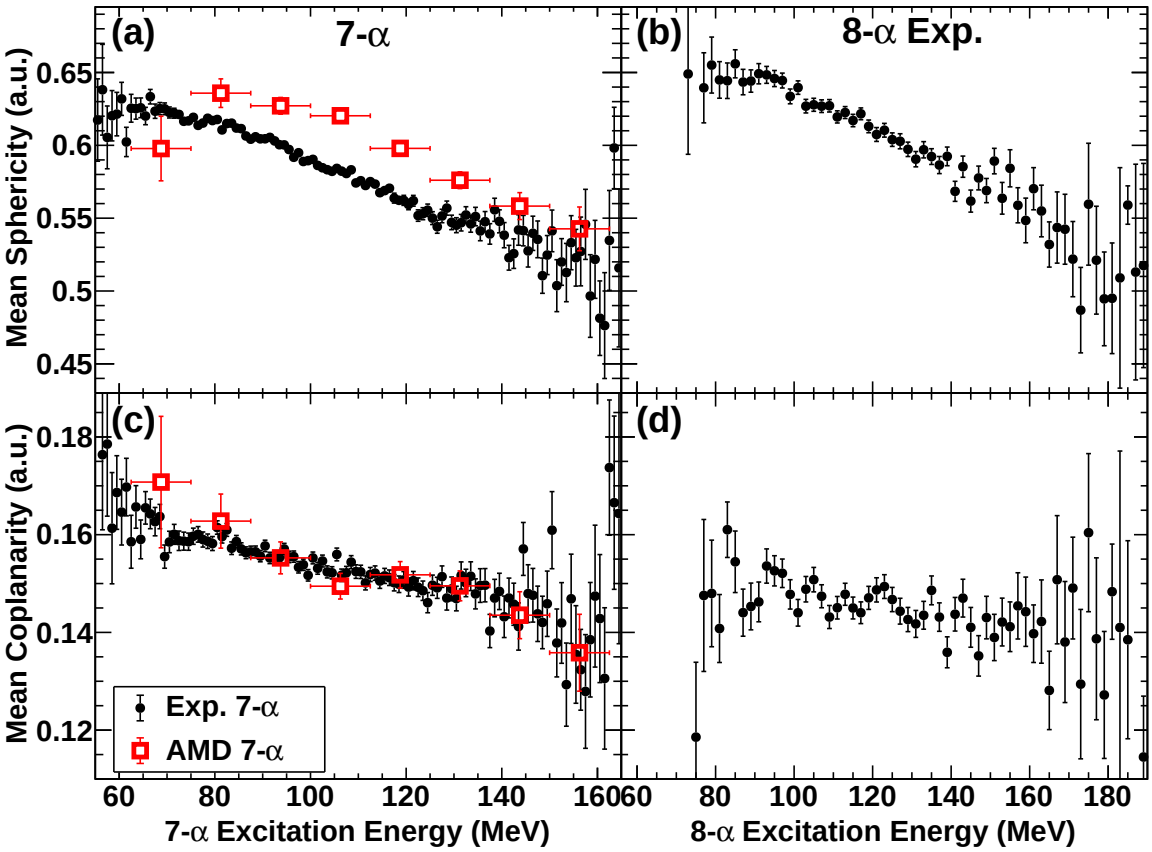

Figure 5.19: Mean sphericity and coplanarity as a function of excitation energy for 7,8-α events. Panels (a,b): Experimental sphericity dependence for 7-α (a) and 8-α (b) events (black circles). Panels (c,d): Same as panels (a,b) but for the mean coplanarity dependence. The filtered AMD + GEMINI++ results (red open squares) are overlaid for 7-α events in panels (a,c).

breakup. Given that the experimental trend is reproduced by simulation and that most simulated 7-α events come from the sequential de-excitation of a few dynamically produced primary fragments, is is unlikely that all the 7-α events come from a de-exciting ^{28}Si source. As previously discussed in Section 1.3, authors of ref. [9] have demonstrated the difficulty in isolating clean projectile decay samples in collisions of ^{40}Ca + ^{40}Ca at 35 MeV/nucleon due to the dynamics at the early stages of the collision leading to detected α-conjugate exit channels. It was found that in these α-conjugate decay channels, a hierarchical effect is seen in the projectile-like decay products; on average, heavier α-conjugate fragments have larger

beam-component velocities than the lighter fragments (as seen in Figure 1.9). This indicates that a significant portion of α-particles in such channels emerge from the low density overlap region in the early stages of the collision [130]. These particles are still projectile-like enough to pass the event selection in this work and are difficult to exclude due to the broad phase space they inhabit; in this previous work, the parallel velocity distributions do not show distinguishable features in α-disassembly events to permit isolation between the two α-particle sources. It is likely that the origin of many 7-α events is best understood as some portion of α-particles originating from dynamical interactions early in the collision and the remaining originating from a heavier, faster α-conjugate source disassembly. In such cases, the misidentified common center-of-mass reference would lie between these two distinct "sources", leading to an artificially higher calculated excitation energy and a seemingly elongated momentum shape of breakup. This proposed interpretation is further supported by the AMD + GEMINI++ simulation agreement with the experimental shape-excitation energy trends. AMD is capable of modelling the complex dynamics of early collision stages. Given that the simulated events that result in seven measured α-particles in the exit channel originate from the sequential de-excitation of a few excited fragments produced in the dynamical stage of the collision, the same common center-of-mass misidentification is likely to occur.

As previously discussed, momentum shape analysis is more sensitive to the geometric configuration of the de-exciting source for prompt decays. The shape distributions between the experimentally partitioned 7,8-α events into those identified as containing sequential decay steps (7,8-$\alpha_{WithG.S.}$), and those without (7,8-$\alpha_{NoG.S.}$) is compared in Figure 5.20. For all 7,8-α events, the mean sphericity decreases as a function of the excitation energy as previously discussed (and seen in Figure 5.19). Despite the 7,8-$\alpha_{WithG.S.}$ events giving lower calculated excitation energies on average (as seen in Figure 5.14), these 7,8-$\alpha_{WithG.S.}$ events show a substantially lower mean sphericity than the 7,8-$\alpha_{NoG.S.}$ events ($< S >$: $7\alpha_{No} : 0.609 \pm 0.001, 7\alpha_{With} : 0.557 \pm 0.001, 8\alpha_{No} : 0.630 \pm 0.001, 8\alpha_{With} : 0.583 \pm 0.001$). These differences

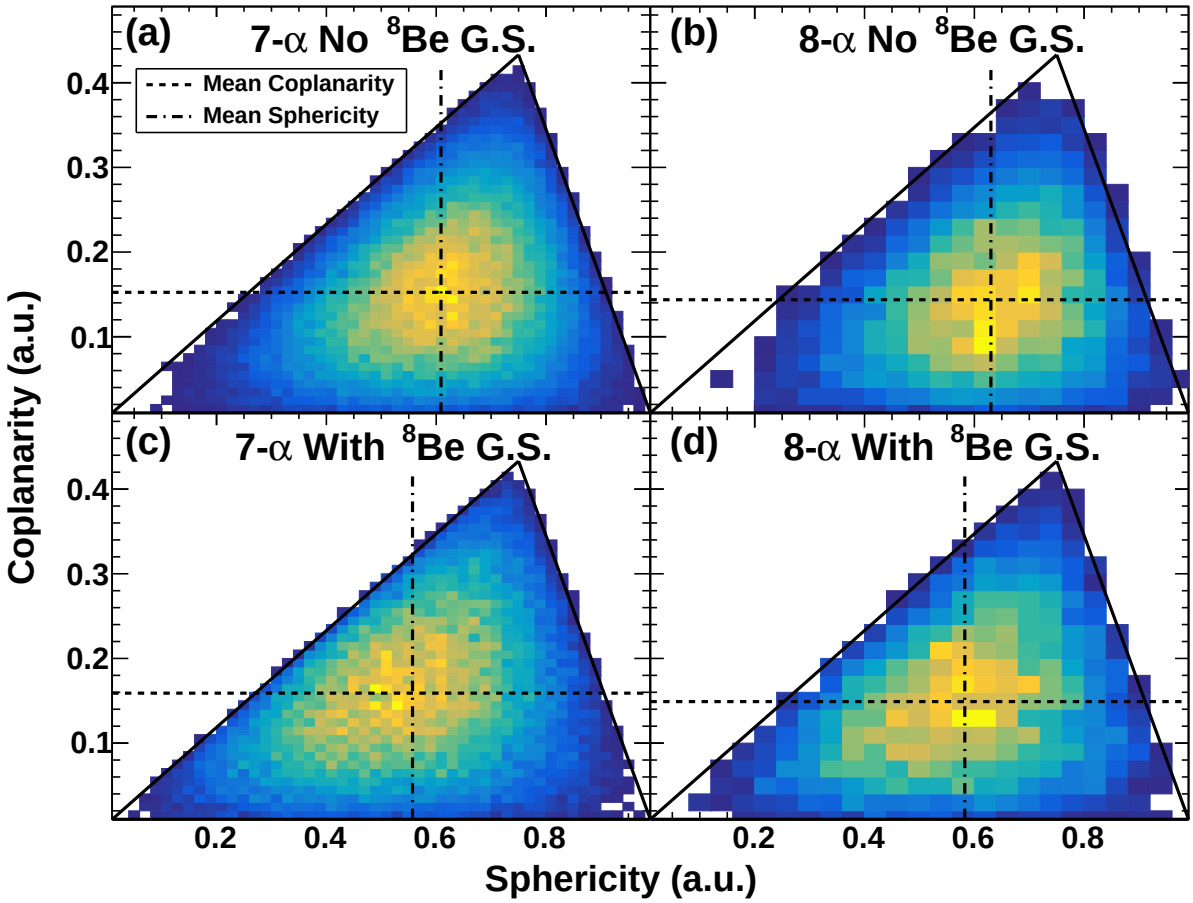

Figure 5.20: Experimental momentum shape sphericity-coplanarity yield distributions for 7,8-$\alpha_{NoG.S.}$ and 7,8-$\alpha_{WithG.S.}$ with a linear color scale. The mean sphericity and coplanarity for each distribution is shown by the vertical dot dashed and horizontal dashed lines, respectively. Panels (a,b): Shape distributions for 7-$\alpha_{WithG.S.}$ (a) and 8-$\alpha_{WithG.S.}$ (b). Panels (c,d): Shape distributions for 7-$\alpha_{NoG.S.}$ (a) and 8-$\alpha_{NoG.S.}$ (b).

between the mean sphericity for each experimental classification of 7,8-α events agree with the model calculations between simultaneous and sequential decays of refs. [127, 128, 129]. This indicates that such events do not follow the mean overall trend and that the intermediate excited state decay identification procedure of Section 5.4 is quite selective. Additionally, the 7,8-$\alpha_{NoG.S.}$ events, which may have enhanced yield of simultaneous decays, show the same general distribution as the AMD + GEMINI++ distribution in panel (a) of Figure 5.18.

Another way to probe the general reaction mechanism that leads to 7- or 8-α particles in the exit channel is to examine the mean center-of-mass (source) frame velocity as a function

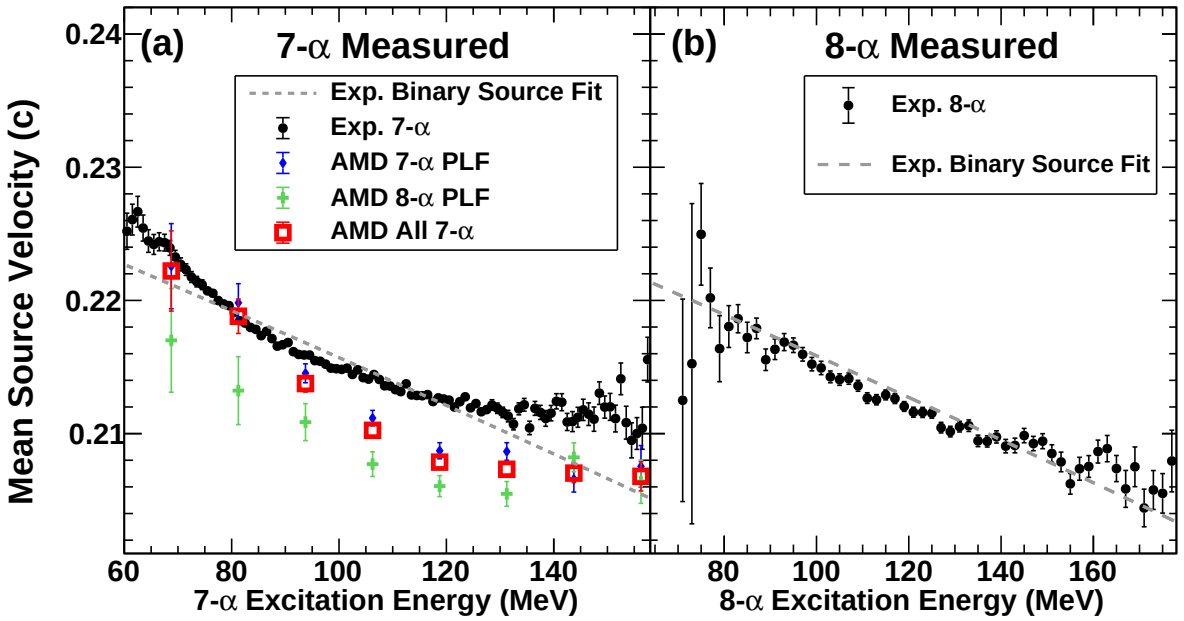

Figure 5.21: Mean source velocity as a function of excitation for 7,8-α events. Equation 5.5 is fit to the experimental data in each panel (gray dashed line). Panel (a): Experimental 7-α data (black circles) is compared to filtered AMD + GEMINI++ simulation data (red open squares). Simulation data originating from a 7-α projectile-like decay (blue diamonds) is compared to that from an 8-α projectile-like decay (green crosses). Panel (b): Experimental 8-α data.

of the excitation energy as shown in Figure 5.21. Assuming an idealized reaction mechanism where the collision leaves an excited ^{28}Si (panel (a)) and ^{32}S (panel(b)) that de-excites through α-disassembly, the excitation energy of each source is unavailable to contribute to its velocity. Additionally, some amount of the initial kinetic energy of the beam projectile will be imparted to the target remnant mass. If this amount of energy left to the target remnant is assumed to be constant as a function of the excitation energy, the relationship between the source velocity and excitation energy can be described by:

$$v_{source}(E^*) = \sqrt{\frac{2(E_{beam} - E_{targ.rem.} - E^*)}{m_0^{source}}} \tag{5.5}$$

where E_{beam} is the total kinetic energy of the beam species (MeV), $E_{targ.rem.}$ is the amount of energy left to the target remnant mass (MeV), E^* is the excitation energy (MeV), and m_0^{source}

is the rest mass of the assumed source in MeV/c^2. If $E_{targ.rem.}$ is left as a free parameter, Eq. 5.5 can be fit to the data as shown in panels (a,b) of Figure 5.21. The overall shape of the fit is defined by the excitation energy, with the fit procedure only involving the $E_{targ.rem.}$ offset. The general trend for both 7- and 8-α events is well described by this simple picture; however, in the case of 7-α events in panel (a), a concave curvature is seen in the mean experimental dependence. This deviation from the simple description indicates that 7-α events are not well described by only a clean source breakup description, in agreement with previous results. There may be evidence of curvature in 8-α events as well, albeit less pronounced. The results of Figure 5.6 indicate that the fraction of 8-α events originating from an 8-α projectile-like breakup is greater than the fraction of 7-α events originating from a 7-α projectile-like breakup. It was investigated if the curvature observed in panel (a) of Figure 5.21 originates from 8-α projectile-like breakups where one α-particle missed detection. In this case, the excitation energy calculation assumes the wrong Q-value, and both the source velocity and excitation energy calculation is missing an α-particle. The mean source velocity to excitation energy relationship for filtered AMD + GEMINI++ events is shown by the three data series in panel (a). The determination of the number of α-particles in the unfiltered breakup is done in the same manner as for Figure 5.6. For all simulated events that give seven measured α-particles, the overall trend is well reproduced. It is also clear that this curvature is not caused by the aforementioned scenario, as both 7-α projectile-like breakups and 8-α projectile-like breakups that give seven measured α-particles exhibit this non-linear dependence. The lower mean source velocities on average for the 8-α projectile-like breakups can likely be attributed to the error introduced when misidentifying the source. Additionally, the mean $E_{targ.rem.}$ per nucleon (of the remaining target) obtained for both fits are in agreement (7-α : 22.7 $\pm$ 0.2 MeV/nucleon, 8-α : 23.2 $\pm$ 0.1 MeV/nucleon), suggesting that on average, the collision mechanism and amount of target interaction that leads to measured 7- and 8-α events are similar.

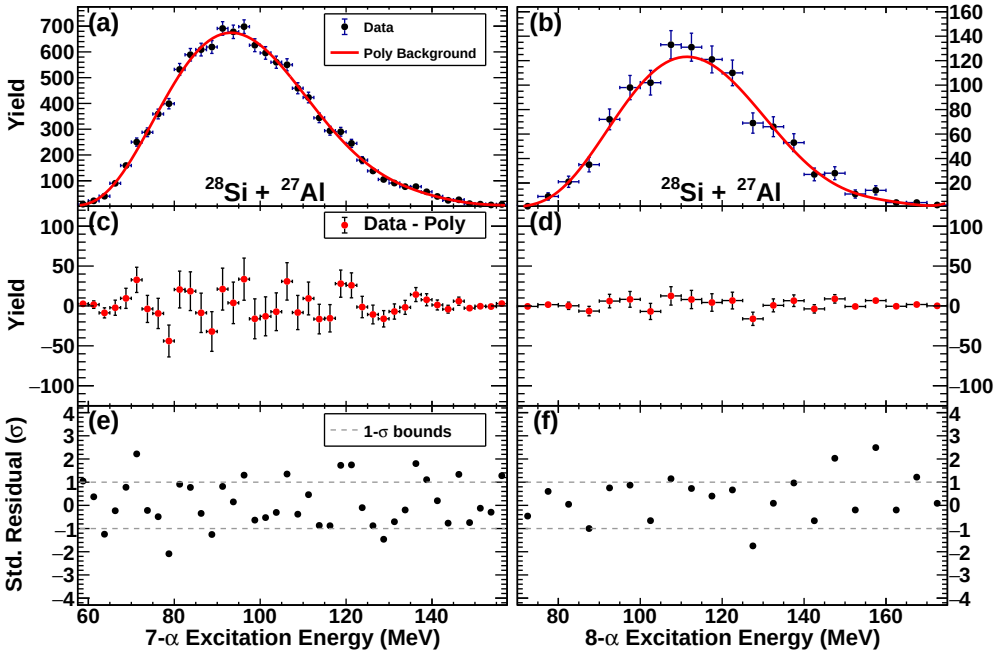

(a) ^{28}Si + ^{27}Al at 35 MeV/nucleon.

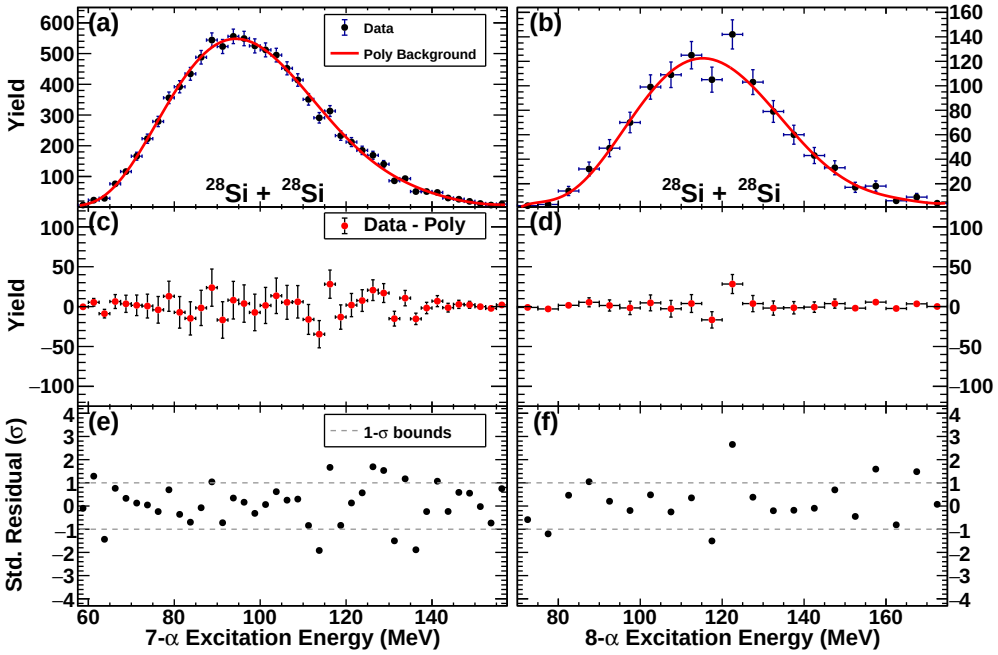

(b) ^{28}Si + ^{28}Si at 35 MeV/nucleon.

Figure 5.22: Analogous excitation energy analysis procedure for 7,8-α events as in Figure 5.11 but for ^{27}Al and ^{28}Si targets.

5.6 Target Size and α-Conjugation

The choice of a ^{12}C target for the collision system was largely to replicate the experimental conditions of ref. [11]. As the role of the target is primarily to provide a means of exciting the projectile during the collision, it is of interest to explore if alternative target species may enhance toroidal high-spin isomer production. The authors of ref. [16] have also proposed that symmetric collisions of ^{28}Si + ^{28}Si may enhance such production, as only even l-values are admitted in the entrance channel. As a direct comparison to the symmetric collision scenario, data was also obtained using a similar mass, non-α-conjugate ^{27}Al target. The same analysis procedure as performed for Figure 5.11 was used with the ^{27}Al and ^{28}Si target data as shown in Figure 5.22. As this study is largely exploratory, less data collection time was devoted to the study of these collision systems. Nevertheless, inspection of the 7,8-α event excitation energy distributions and associated standardized residuals for each collision system reveal similar agreement between the data and a smooth, unimodal continuum description (^{27}Al Target: 7α p = 0.19, 8α p = 0.24. ^{28}Si Target: 7α p = 0.44, 8α p = 0.43).

5.7 Statistical Significance Analysis and Upper Limit on Toroidal Cross Section

Although no obvious peaks are observed in the 7-α excitation energy distribution measured in FAUST, it is not possible to completely rule out the presence of states that are either too low yielding, too broad, or some combination that results in yield enhancement below statistical fluctuations. Confidently claiming the measurement of a resonance in this data depends on the state's cross section (corrected for FAUST detection efficiency), intrinsic width (convolved with FAUST resolution), and yield relative to background (accounting for background determination uncertainty). By reasonably accounting for these factors and assessing a limit of statistical significance, an approximate toroidal high-spin isomer cross section upper limit in the 7-α exit channel can be obtained. The procedure for simulating 7-α excitation energy spectra with resonant yield and the simulation of expected experimental results consistent with previous measurement is discussed in Section 5.7.1. A statistical

likelihood analysis for determining upper limits on toroidal state cross sections that can be compared to previous measurement is discussed in Section 5.7.2.

5.7.1 Simulated FAUST-Measured 7-α Spectra

As discussed in Section 1.3.2, authors of ref. [11] used AMD + GEMINI++ simulations to approximate cross sections of the observed high excitation energy states as seen in Table 1.1. Repeating the same procedure used in the prior experiment allows for a direct comparison between the two results. As neither the NIMROD nor FAUST experiment were designed for accurately measuring cross sections, there exists significant systematic uncertainty in the conversion from measured yield to cross section; however, when using the same procedure, the systematic error should be, to a great extent, the same. To this end, the 7-α decay cross section to measured yield conversion for the FAUST data was obtained by first interpolating the systematic parameterization of heavy-ion collision properties of ref. [64] to estimate a total cross section of 2417 mb for collisions of ^{28}Si + ^{12}C at 35 MeV/nucleon. It is then assumed that the total number of detected events in FAUST, corrected by the detection efficiency for measuring at least one particle, represents this total cross section. This total event detection efficiency was determined from the ratio between all AMD + GEMINI++ simulated collisions and those where at least one particle was measured after filtering; approximately 79% of AMD + GEMINI++ collisions have at least one particle measured in FAUST. The 7-α channel detection efficiency was found in a similar way; for AMD + GEMINI++ events that had at least seven projectile-like α-particles, the yield ratio of unfiltered to filtered events where seven α-particles were measured give a 7-α detection efficiency of $\sim$21%. These efficiency corrections allow for the relative frequency of measured resonant 7-α yield to all 7-α events ($\nu_{res.}$) to correspond to a cross section for the state ($\sigma_{res.}$); for FAUST, this conversion factor is $\sigma_{res.} = 52.0 \cdot \nu_{res.}$, where $\nu_{res.}$ is expressed as a percent.

The results in Section 5.3.3 demonstrated that the experimental 7-α distribution is well described by a smooth, unimodal background description. While the 9$^{\text{th}}$ order polynomial previously used aptly provided a continuum background description for most of the excita-

tion energy range of the data, this functional form struggles to accurately capture the tails of the distribution where the yield approaches zero. To compensate, kernel density estimation (KDE) can be used to effectively smooth the measured 7-α distribution, providing a reasonable underlying probability density function given the finite data sample [131]. A kernel density estimation of a discrete data sample can be expressed as:

$$f_h(x) = \frac{1}{n}\sum_{i=1}^{n} K_h(x - x_i) \tag{5.6}$$

where n is the number of discrete data points, K_h is the kernel function used at each data point with h bandwidth, and x_i is the x-value for each data point. A Gaussian distribution is chosen as the kernel for this work with the bandwidth h representing the standard deviation. A KDE generated using a bandwidth of 2 MeV produces a good description for the experimentally measured 7-α excitation energy distribution as shown by the agreement between the red line and black experimental data in panel (a) of Figure 5.23. By sampling the KDE distribution once for every experimentally measured 7-α event, a simulated distribution with no resonant state yield is produced as shown in panel (b); this "background" distribution contains the same magnitude of statistical fluctuation as is present in the experimental distribution. Resonant states of varying intrinsic widths and cross sections (yields) can be added to the KDE to assess what state properties are necessary for confident identification among the fluctuations of the distribution. While the decay energy of a resonance follows a Breit-Wigner functional form, a Gaussian distribution serves as a good approximation [132]. The measured width of an excited state in FAUST is a convolution between the intrinsic width of the state and the resolution uncertainty in the excitation energy measurement as described by Equation 5.7.

$$\sigma_{measured} = \sqrt{\sigma^2_{intrinsic} + \sigma^2_{resolution}} \tag{5.7}$$

For any given excitation energy and intrinsic width, the measured width in FAUST can be

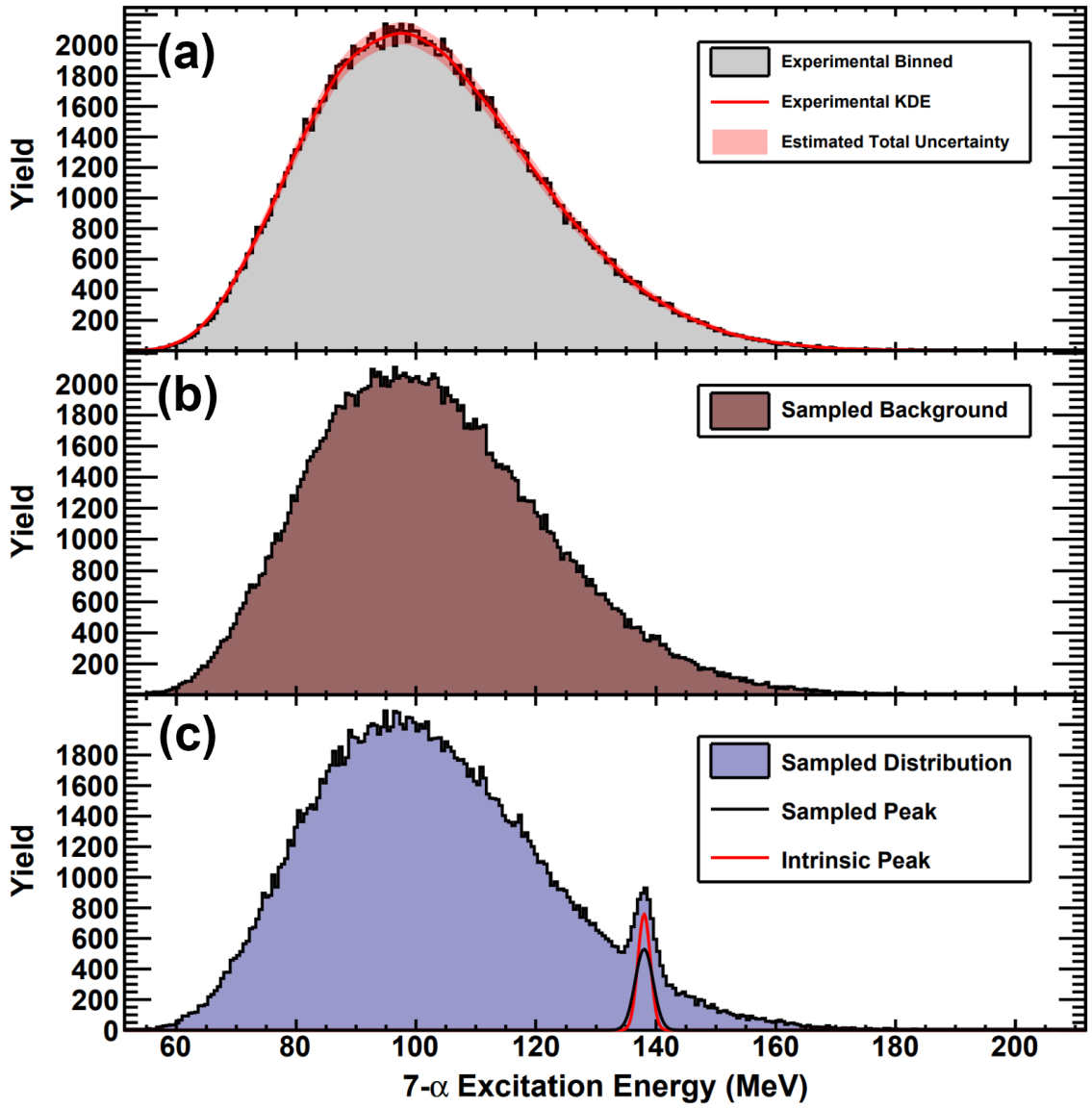

Figure 5.23: FAUST-simulated 7-α excitation energy distributions. Panel (a): Experimentally measured 7-α excitation energy distribution with the associated kernel density estimation (KDE) probability distribution (red line). The motivation and application of the shaded uncertainty region is discussed in the text. Panel (b): Simulated 7-α distribution produced from sampling the KDE in panel (a). Panel (c): A simulated Gaussian resonance (peak) is added to the KDE with a specified intrinsic width (FWHM) and cross section as shown by the red line. The associated experimental width due to FAUST resolution is shown by the black line. The total background + peak distribution is sampled to the same level of counts as in panel (a).

calculated using the excitation energy dependent resolution previously calculated in Figure 5.7. A 138 MeV resonance with $\nu_{res.} = 2.0\%$ ($\sigma_{res.} = 108\,\mu b$) and intrinsic width (FWHM) of

3.1 MeV (giving a measured width of 4.0 MeV) is added to the KDE and sampled, providing a reasonable example of how the experimental distribution would appear if such a state were present as seen in panel (c). The total yield in the sampled background + peak distribution of panel (c) is kept consistent with the experimental 7-α yield (186097 counts).

Using this procedure, a simulated FAUST-measured 7-α excitation energy distribution using the state means and cross sections reported in the NIMROD experiment (Table 1.1) are shown for three intrinsic widths in Figure 5.24. A cross section of 30 µb is given to the 114 MeV state (similar to the reported cross section of the 138 MeV state), as no cross section was explicitly reported. The standardized residuals between the simulated spectra and the KDE background used in the sampling procedure are shown for each case. For this demonstration, the KDE background is assumed to have no associated uncertainty so that the standardized residuals represent the level of sensitivity to possible states given an exact background. For intrinsic widths up to 4 MeV FWHM, there are clear indications of resonant yield contributions in the simulated spectra and residuals. Given the ∼9.4 MeV FWHM 7-α excitation energy resolution of the NIMROD array, the widths and associated errors of the reported states indicate maximum intrinsic widths of ∼3.4 MeV and ∼2.6 MeV for the 126 MeV and 138 MeV states, respectively; the simulated spectrum in panel (b) is an approximate representation of the largest possible state width result consistent with the previous measurement. As an example of the difficulty in identifying resonant yield at the limit of large intrinsic width even with a perfect background description, panel (c) shows the result when this width is set to 9.0 MeV FWHM; while there is some indication of resonant yield in the residual plot of panel (f), identifying these states in practice is challenging due to imperfect background knowledge.

5.7.2 Statistical Likelihood Analysis for Cross Section Upper Limit

While the results of Figure 5.24 give an intuitive and qualitative indication that the state properties reported in ref. [11] would have produced rather obvious features in the 7-α excitation energy distribution of the present work, it is important to quantitatively assess

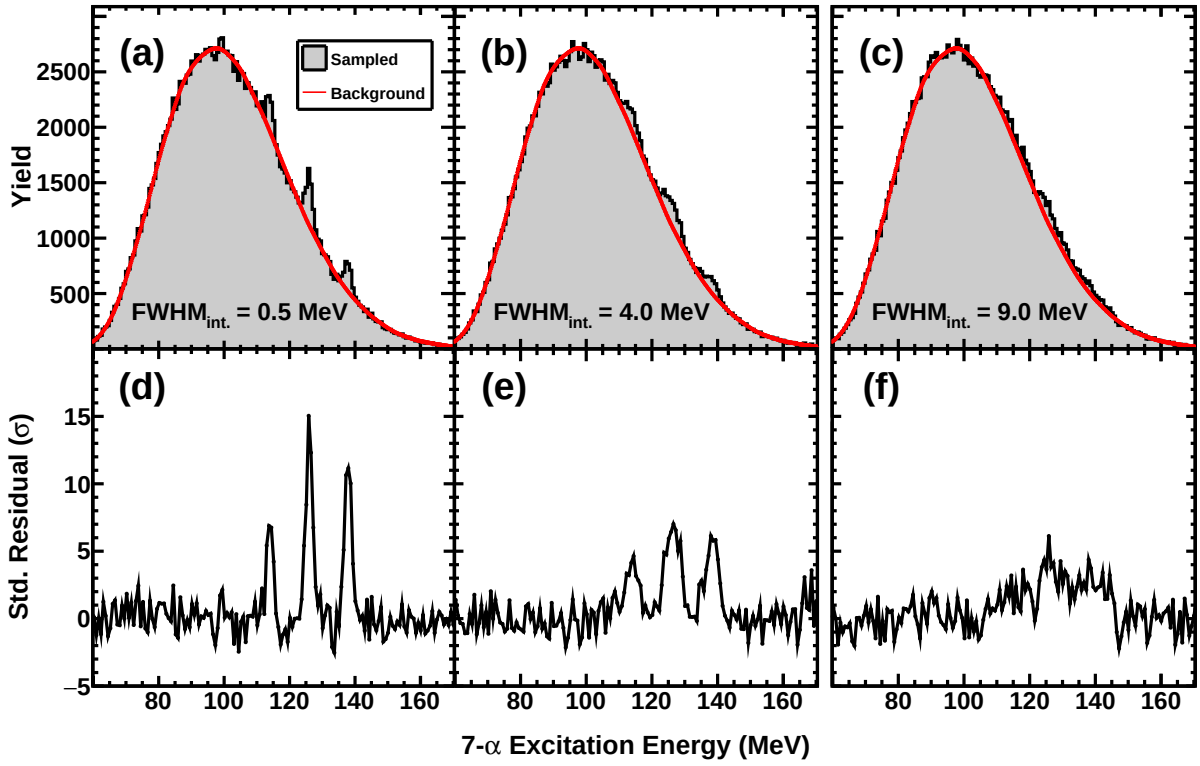

Figure 5.24: Simulated FAUST-measured 7-α distributions using the procedure of Figure 5.23 and the reported state cross sections and means of Table 1.1. A cross section of 30 µb is used for the 114 MeV state. Panels (a,b,c): Intrinsic state widths (FWHM) of 0.5 MeV (a), 4.0 MeV (b), and 9.0 MeV (c) are shown. Panels (d,e,f): Standardized residuals between the simulated spectra and the perfectly known background (KDE).

the limits of toroidal state cross section, mean, and width where statistical significance can be claimed. One method for comparing the likelihood between two models for a given data sample is to compare the χ^2 between the fits. To this end, the procedure shown in Figure 5.23 can be used to create simulated spectra for each toroidal state mean over a broad range of cross sections and widths. Each simulated spectrum is then fit with the KDE background (including a free scaling parameter) and the KDE background (including a free scaling parameter) + a Gaussian peak (three free Gaussian parameters). The χ^2 of each fit is indicative of which model best describes the data. In both cases, there will be near perfect statistical agreement ($\chi^2/\nu = 1$) between the non-resonant portion of the spectrum and the fit. In reality, however, there is uncertainty associated with how well the background can

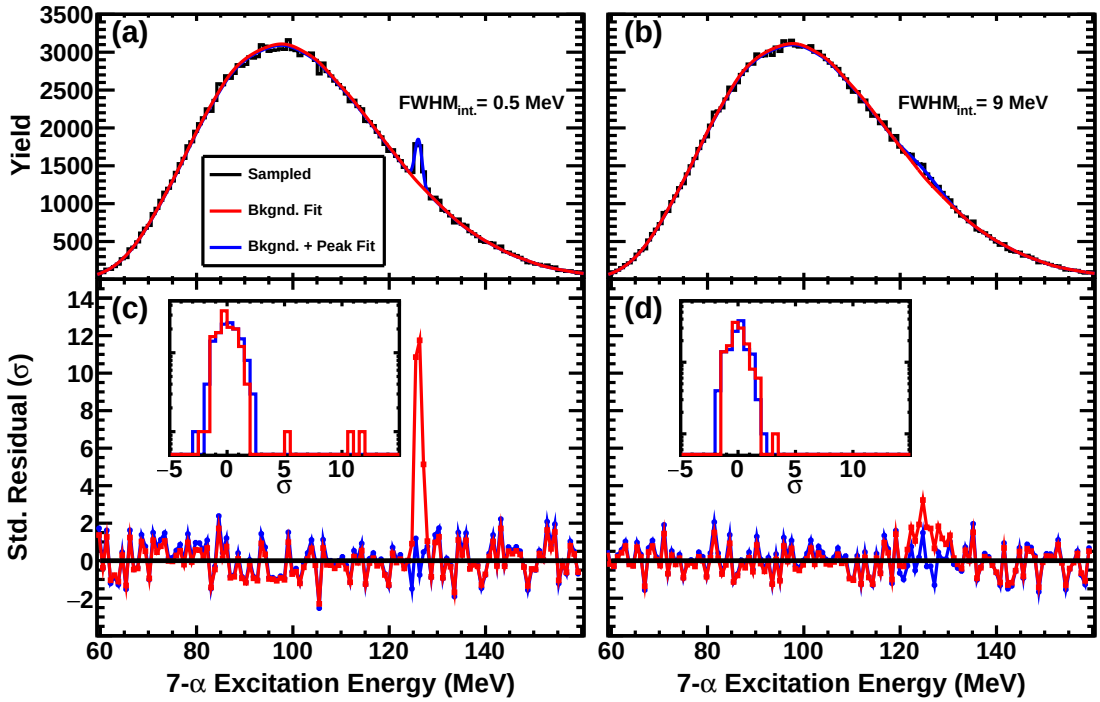

Figure 5.25: Statistical likelihood analysis procedure. Panels (a,b): Simulated FAUST-measured 7-α distributions (black) containing resonant yield peak with intrinsic FWHM of 0.5 MeV (a) and 9.0 MeV (b) using the procedure of Figure 5.23 and fit using the background model (red) and peak model (blue) (as described in the text). Panels (c,d): Standardized residuals obtained from the background model and peak model. Insets show the projection of the standardized residuals for the two models; the uncertainty associated with the background model causes the distribution to generally be narrower than the peak model distribution.

be determined. If this uncertainty is not accounted for, such an analysis would provide an unfairly low estimate on the upper bounds of the cross section.

The details of the uncertainty in the background are difficult to constrain in practice. For the experimental data, inconsistencies in the shape of the produced background when using the event mixing technique for this data (Section 5.3.3) motivated the use of a polynomial background description. While the polynomial treatment should provide a background description capable of extracting resonant yield contributions with sufficiently narrow widths and high cross sections, this method becomes less applicable at the limits of broad widths

and low cross sections as such states will drive the fit to describe them. One way to emulate these features of the background uncertainty is to add an associated error to the KDE background. For this purpose, the error in the KDE background was defined as the KDE statistical error and the KDE statistical error multiplied by a background scaling factor added in quadrature:

$$\sigma_{Tot.} = \sqrt{\sigma_{stat.}^2 + \beta\sigma_{stat.}^2} \tag{5.8}$$

where $\sigma_{Tot.}$ is the total background error, $\sigma_{stat.}$ is the statistical error associated with the KDE ($\sqrt{yield}$), and β is a scaling factor to account for the general uncertainty in the background. The magnitude of this error when using $\beta = 0.5$ is shown by the shaded region in panel (a) of Figure 5.23. In simple terms, this error region allows for the "true" background to be any distribution reasonably contained within these limits, in effect allowing for a shape uncertainty in the background. The fitting procedure previously described is performed on simulated resonance spectra as shown in Figure 5.25 where the KDE background fit (background model) possesses this error and the KDE background + peak fit (peak model) does not. The standardized residuals in panel (c) give a graphical indication of the goodness of each fit. For the background model, the increased error over the peak model emerges as a slight compression of the residuals centered about $\sigma = 0$, giving a reduction in the χ^2 for the non-resonant portions of the spectrum; however, the background model does not fit the resonant yield contribution, giving increased χ^2 over the peak model in this region. The standardized residual projection of each fit is given in the inset showing the slightly narrower distribution for the background model over the peak model for the bulk of the data but possessing a few extreme outliers associated with the peak region. The model that best describes the sampled spectrum is chosen as the one with the smaller χ^2 (for panel (a,c) the peak model is preferred). Panel (b) shows this same procedure for a simulated spectrum for a peak with the same cross section as panel (a) but a much broader width. The slightly compressed residuals for the background model compensate for any enhancement associated with the peak, resulting in preference of the background model for this case.

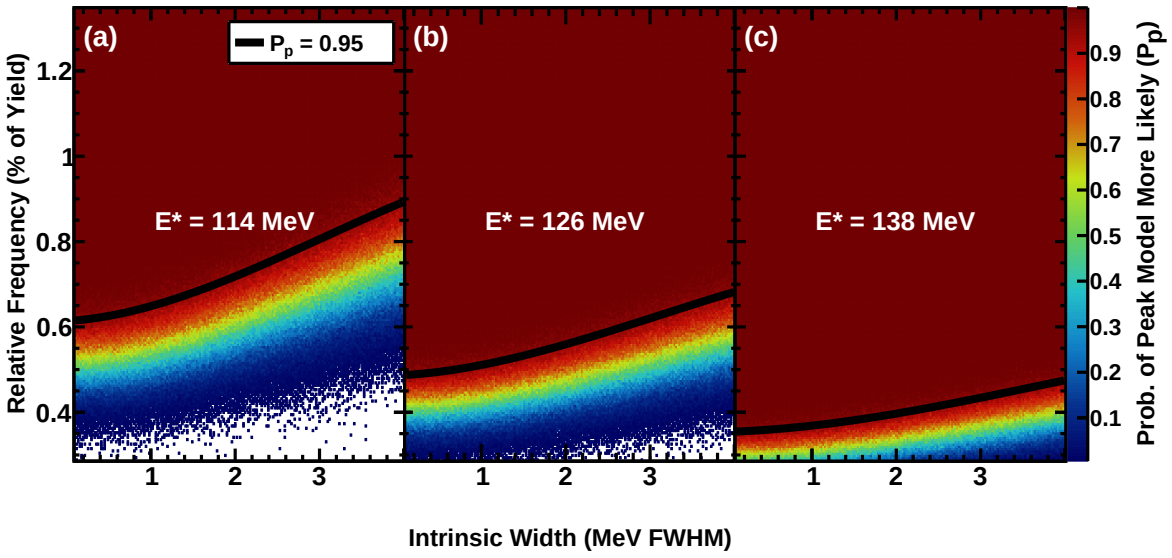

Figure 5.26: Statistical likelihood analysis results between the background and peak model for resonant states simulated at 114 MeV (a), 126 MeV (b), and 138 MeV (c). The ratio of times the peak model is preferred over the background model (p_p) is shown as a function of the intrinsic width (MeV FWHM) and relative frequency (resonant yield to total yield). A 3$^{\text{rd}}$ order polynomial is fit to the $p_p = 0.95$ boundary as shown by the black curves.

This simulated spectra fitting procedure is performed as a function of the intrinsic width and relative frequency (ratio of resonance yield to total sampled yield) for the three reported state means as shown in Figure 5.26. For each pixel in these plots, the distribution sampling and fitting procedure is independently performed 200 times to aptly account for the broad range of statistical fluctuations that can occur during sampling. The color scale corresponds to the ratio of times the peak model fit has a lower χ^2 than the background model, indicating that it is a better description of the data. The boundary where this ratio is equal to 0.95 is shown by the 3$^{\text{rd}}$ order polynomial in each panel. For a given relative frequency (and by extension, cross section) there is greater sensitivity in regions with less background due to the larger signal to background ratio. The background yield from panels (a) to (c) is decreasing, reducing the required resonance yield for peak model preference. The relative frequency axis can be transformed to cross section using the AMD + GEMINI++ procedure previously described; while there will be large systematic uncertainties in the absolute cross section

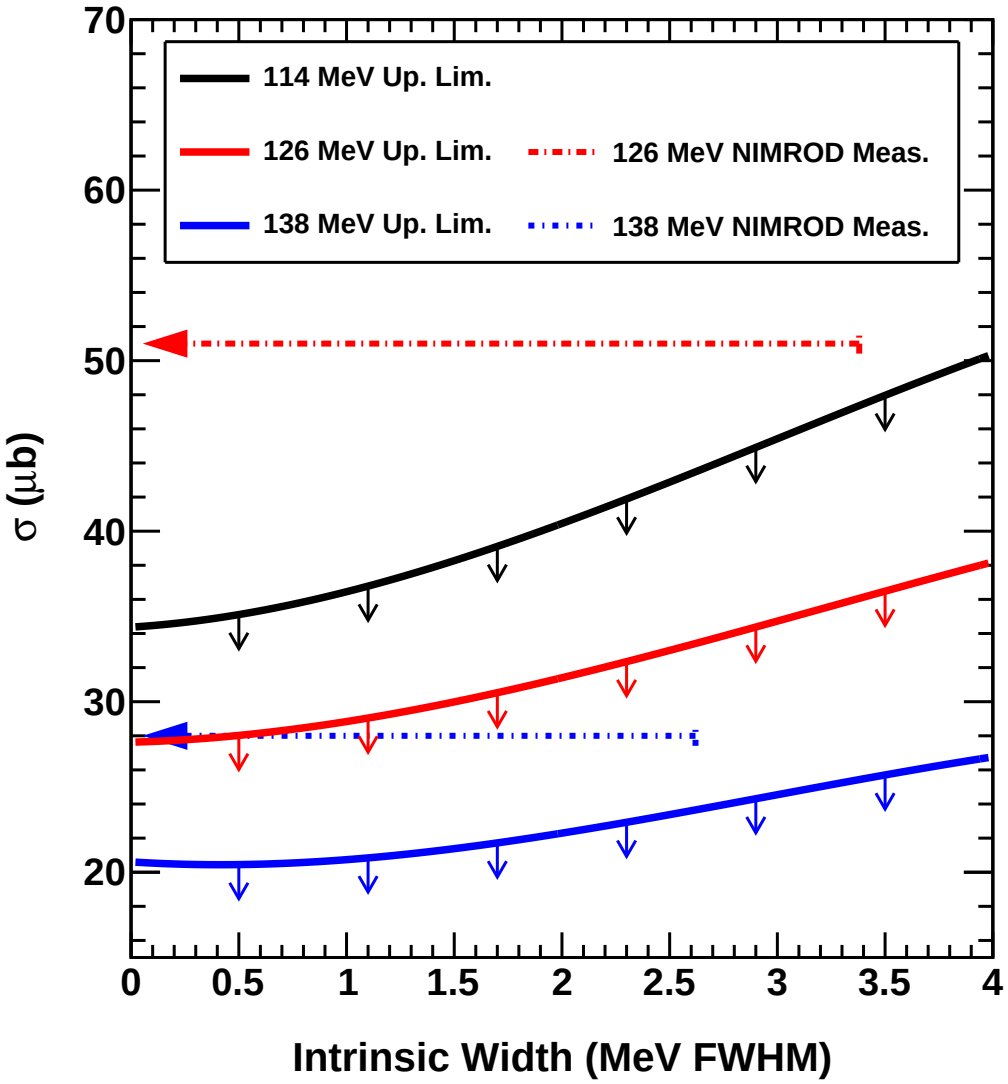

Figure 5.27: Comparison between the FAUST upper limit of toroidal high-spin isomer cross section (solid lines) using a background uncertainty parameter of $\beta = 0.5$ to the cross sections reported in ref. [11] (dashed horizontal arrows). Arrows indicate the range of allowable intrinsic widths of reported states consistent with the experimental resolution.

estimate, the replicated procedure allows for comparison to previous work, as the primary difference between the two experiments is detection efficiency. Figure 5.27 shows the upper limit for statistical significance of the three NIMROD-reported state means as a function of the intrinsic width and cross section. The dashed horizontal lines indicate the allowable intrinsic widths of the states measured in NIMROD according to the detector resolution and

measured widths. Based on the data acquired from experiment and calculations performed in this section, a very approximate but fair comparative upper limit to ref. [11] for toroidal high-spin isomer cross section in this reaction channel is obtained. For the two states that had reported cross sections (126 MeV and 138 MeV), the obtained upper limits fall well below what was reported.

It is important to note that the estimated background error for this analysis is an ansatz and is included to approximate the level of uncertainty that may exist. The selection of the error parameter ($\beta = 0.5$) was guided by inspecting simulated spectra determined to be significant and ensuring that these spectra contained qualitatively distinguishable features. Accurately determining the magnitude and characteristics of the background uncertainty free of bias is a challenging and considerable undertaking; work is ongoing to improve the agreement between the background error used in this calculation and the level of background uncertainty that exists in treatment of experimental data. Nevertheless, the features seen in the FAUST-simulated spectra using the broadest allowable intrinsic width consistent with the NIMROD measurement (panel (b) of Figure 5.24) indicate that such resonances would be readily seen if they possessed properties suggested by previous measurement.

6. CONCLUSIONS

6.1 Summary

Theoretical predictions suggest that angular momentum stabilized toroidal high-spin isomers of intermediate mass α-conjugate nuclei may exist. A prior experiment observed possible evidence of toroidal α-disassembling ^{28}Si states, but due to limited statistics and angular resolution, a confirmation experiment was necessitated. The current experiment was designed to confidently and accurately measure such states if their widths and cross sections were on the order suggested by the prior experiment. To this end, collision data of ^{28}Si + ^{12}C at 35 MeV/nucleon was recorded using position-sensitive FAUST, giving over an order of magnitude increase in the number of measured collisions over the previous experiment. Improvements to the pulse-processing technique and data acquisition allowed for significantly higher event rates and a reduction in position-dependent distortions over past FAUST experiments. Despite the optimized experimental conditions for measuring the proposed states, no strong evidence was found for statistically significant resonant state yield in the seven α-particle channel. Given the large amount of collected collision data, examination of the eight α-particle channel was permitted to search for similar predicted states in ^{32}S; however, a similar lack of resonant state evidence was found. Upon closer inspection of the collision properties of measured 7,8-α events, it was revealed that the observed breakup properties are consistent with a significant fraction of such breakups not originating from clean, excited ^{28}Si* or ^{32}S* breakups. A detailed statistical significance analysis revealed that the sensitivity of the current measurement confidently excludes the reported state properties claimed in the previous experiment.

6.2 Outlook

The results of the current work suggest that if toroidal high-spin isomers exist for intermediate mass α-conjugate nuclei, any future experimental efforts in pursuit of measuring

such states likely requires exploring alternative production pathways or observables which are currently unclear. The lack of predictive power and consistency between theoretical calculations makes these searches exceptionally challenging. A focused theoretical effort to provide clear direction and consistent results between models is needed before additional experimental efforts should be undertaken.

REFERENCES

[1] R. Smith et al., "New Measurement of the Direct 3α Decay from the ^{12}C Hoyle State," *Phys. Rev. Lett.*, vol. 119, p. 132502, 2017.

[2] J.T.H. Dowie et al., "Evidence for shape coexistence and superdeformation in ^{24}Mg," *Phys. Lett. B*, vol. 811, p. 135855, 2020.

[3] C.Y. Wong, "Rotating toroidal nuclei," *Phys. Rev. C*, vol. 17, p. 331, 1978.

[4] C.Y. Wong and A. Staszczak, "Shells in a toroidal nucleus in the intermediate-mass region," *Phys. Rev. C*, vol. 98, p. 034316, 2018.

[5] T. Ichikawa, J.A. Maruhn, N. Itagaki, K. Matsuyanagi, P.-G. Reinhard, and S. Ohkubo, "Existence of an exotic torus configuration in high-spin excited states of ^{40}Ca," *Phys. Rev. Lett.*, vol. 109, p. 232503, 2012.

[6] A. Staszczak and C.Y. Wong, "A region of high-spin toroidal isomers," *Phys. Lett. B*, vol. 738, p. 401, 2014.

[7] Z.X. Ren, P.W. Zhao, S.Q. Zhang, and J. Meng, "Toroidal states in ^{28}Si with covariant density functional theory in 3D lattice space," *Nuc. Phys. A*, vol. 996, p. 121696, 2020.

[8] B. Borderie et al., "Temperature and density conditions for alpha clustering in excited self-conjugate nuclei," *Symmetry*, vol. 13, p. 1562, 2021.

[9] K. Schmidt et al., "Alpha conjugate neck structures in the collisions of 35 MeV/nucleon ^{40}Ca with ^{40}Ca," *Phys. Rev. C*, vol. 95, p. 054618, 2017.

[10] N.T.B. Stone et al., "Evidence for the decay of nuclear matter toroidal geometries in nucleus-nucleus collisions," *Phys. Rev. Lett.*, vol. 78, p. 2084, 1997.

[11] X.G. Cao, E.J. Kim, K. Schmidt, K. Hagel, M. Barbui, J. Gauthier, S. Wuenschel, G. Giuliani, M.R.D. Rodriguez, S. Kowalski, H. Zheng, M. Huang, A. Bonasera, R. Wada,

N. Blando, G.Q. Zhang, C.Y. Wong, A. Staszczak, Z.X. Ren, and J.B. Natowitz, "Examination of evidence for resonances at high excitation energy in the 7α disassembly of ^{28}Si," *Phys. Rev. C*, vol. 99, p. 014606, 2019.

[12] M. Aslin, A. Hannaman et al., "A new waveform analysis technique to extract good energy and position resolution from a dual-axis duo-lateral position-sensitive detector," *Nucl. Instr. and Meth. A*, vol. 985, p. 164674, 2021.

[13] A. Hannaman et al., "High event rate analysis technique for the dual-axis duo-lateral position-sensitive silicon detectors of FAUST," *Nucl. Instr. and Meth. A*, vol. 1050, p. 168130, 2023.

[14] J.H. Kelley, J.E. Purcell, and C.G. Sheu, "Energy levels of light nuclei A = 12," *Nucl. Phys. A*, vol. 968, pp. 71–253, 2017.

[15] "From ENSDF database as of March 28, 2023." Version available at http://www.nndc.bnl.gov/ensarchivals/.

[16] H. Zheng and A. Bonasera, "Spin quantization in heavy ion collision," *Symmetry*, vol. 13, p. 1777, 2021.

[17] 1 Royal Buildings, Lancing, Business Park, West Sussex, BN15 8SJ, UK, "Micron Semiconductor Ltd.." http://www.micronsemiconductor.co.uk, 2020.

[18] G. Gamow, "Mass defect curve and nuclear constitution," *Proc. Roy. Soc. [A]*, vol. 126, p. 632, 1930.

[19] P.E. Hodgson, "Alpha-clustering in nuclei," *Nature*, vol. 257, p. 446, 1975.

[20] J.A. Wheeler, "On the mathematical description of light nuclei by the method of resonating group structure," *Phys. Rev.*, vol. 52, p. 1107, 1937.

[21] L. A. Hafstadt and E. Teller, "The alpha-particle model of the nucleus," *Phys. Rev.*, vol. 54, p. 681, 1938.

[22] L. Pauling, "The close-packed-spheron model of atomic nuclei and its relation to the shell model," *Proc. Natl. Acad. Sci.*, vol. 54, p. 989, 1965.

[23] C. Beck, "Clustering effects induced by light nuclei," *J. Phys.: Conf. Ser.*, vol. 436, pp. , 2013.

[24] K. Ikeda et al., "The systematic structure-change into the molecule-like structures in the self-conjugate 4n nuclei," *Prog. Theor. Phys. Suppl.*, vol. E68, p. 464, 1968.

[25] W. von Oertzen, M. Freer, and Y. Kanada-En'yo, "Nuclear clusters and nuclear molecules," *J. Phys. Rep.*, vol. 432, pp. 43–113, 2006.

[26] P. Schuck, "Alpha particle clusters and their condensation in nuclear systems," *Phys. Scr.*, vol. 91, pp. 123001, 2016.

[27] M. Freer, "The clustered nucleus - cluster structures in stable and unstable nuclei," *Rep. Prog. Phys.*, vol. 70, pp. 2149, 2007.

[28] D. Jenkins and O. Kirsebom, "The secret of life," *Physics World*, vol. 26, pp. 23, 2013.

[29] M. Kamimura, "Transition densities between the $0_1^+, 2_1^+, 4_1^+, 0_2^+, 2_2^+, 1_1^-$ and 3_1^- states in ^{12}C derived from the three-alpha resonating-group wave functions," *Nucl. Phys. A*, vol. 351, p. 456, 1981.

[30] E. Uegaki, S. Okave, Y. Abe, and H. Tanaka, "Structure of excited states in ^{12}C," *Prog. Theor. Phys.*, vol. 57, p. 1262, 1977.

[31] Y. Funaki, A. Tohsaki, H. Horiuchi, P. Schuck, and G. Ropke, "Analysis of previous microscopic calculations for the second 0^+ state in ^{12}C in terms of 3-α particle bose-condensed state," *Phys. Rev. C*, vol. 67, p. 051306, 2003.

[32] L. Morelli et al., "Full disassembly of excited ^{24}Mg into six α particles," *Phys. Rev. C*, vol. 99, p. 054610, 2019.

[33] B. Borderie et al., "Probing clustering in excited alpha-conjugate nuclei)," *Phys. Lett. B*, vol. 755, p. 475, 2016.

[34] J. Bishop et al., "Experimental investigation of α condensation in light nuclei," *Phys. Rev. C*, vol. 100, p. 034320, 2019.

[35] B. Borderie, M.F. Rivet, and L. Tassan-Got, "Heavy-ion peripheral collisions in the fermi energy domain: fragmentation processes or dissipative collisions?," *Annales de Physique*, vol. 95, pp. 287, 1990.

[36] P. Marini et al., "Signals of bose einstein condensation and fermi quenching in the decay of hot nuclear systems," *Phys. Lett. B*, vol. 756, p. 194, 2016.

[37] H. Schuler and T. Schmidt., "Deviations of the atomic nucleus from spherical symmetry," *Z. Physik*, vol. 94, p. 457, 1935.

[38] A. Bohr, "Nuclear magnetic moments and atomic hyperfine structure," *Phys. Rev.*, vol. 81, p. 331, 1951.

[39] A. Bohr and B. Mottelson, "Nuclear magnetic moments and atomic hyperfine structure," *Phys. Rev.*, vol. 89, p. 316, 1953.

[40] J. Rainwater, "Nuclear energy level argument for a spheroidal nuclear model," *Phys. Rev.*, vol. 79, p. 432, 1950.

[41] J. Griffin and J.A. Wheeler, "Collective motions in nuclei by the method of generator coordinates," *Phys. Rev.*, vol. 108, p. 311, 1957.

[42] S.G. Nilsson, *Binding states of individual nucleons in strongly deformed nuclei.* PhD thesis, Inst. Theor. Phys., Univ. Copenhagen, 1955.

[43] J.A. Wheeler, "Nucleonics notebook," *(unpublished)*, 1950. see also p. 297 in G. Gamow, Biography of Physics, Harper & Brothers Publishers, N. Y. 1961; Princeton University Graduate Course Physics 576 Take-Home Examination Problem 2, May 22, 1963 (unpublished).

[44] C.Y. Wong, "Toroidal nuclei," *Phys. Lett. B*, vol. 41, pp. 446, 1972.

[45] C.Y. Wong, "Toroidal and spherical bubble nuclei," *Ann. Phys.*, vol. 77, pp. 279, 1973.

[46] T. Ichikawa et al., "Pure collective precession motion of a high-spin torus isomer," *Phys. Rev. C*, vol. 89, p. 011305, 2014.

[47] P. Ring and P. Schuck, *The Nuclear Many-Body Problem*, p. 142. Theoretical and Mathematical Physics, Springer Berlin, Heidelberg, 1981.

[48] A. Staszczak and C.Y. Wong, "Toroidal high-spin isomers in light nuclei with N≠Z," *Phys. Scr.*, vol. 90, pp. 114006, 2015.

[49] X.G. Cao et al., "Evidence for resonances in the 7α disassembly of ^{28}Si," *AIP Conference Proceedings*, vol. 2018, p. 020021, 2018.

[50] A. Bohr and B. Mottelson, *Nuclear Structure*, vol. 2. Benjamin, New York, 1975.

[51] A. Gaamouci et al., "Exotic toroidal and superdeformed configurations in light atomic nuclei: Predictions using a mean-field Hamiltonian without parametric correlations," *Phys. Rev. C*, vol. 103, p. 054311, 2012.

[52] G. Gamow, "Mass defect curve and nuclear constitution," *Proc. Math. Phys. Eng.*, vol. 126, pp. 632–644, 1930.

[53] E. Pairam and A. Fernandez-Nieves, "Generation and stability of toroidal droplets in a viscous liquid," *Phys. Rev. Lett.*, vol. 102, p. 234501, 2009.

[54] J.D. McGraw et al., "Plateau-rayleigh instability in a torus: formation and breakup of a polymer ring," *Soft Matter*, vol. 6, pp. 1258–1262, 2009.

[55] M.A. Fontelos, V.J. García-Garrido, and U. Kindelán, "Evolution and breakup of viscous rotating drops," *SIAM Journal on Applied Mathematics*, vol. 71, pp. 1941–1964, 2011.

[56] S.E. Agbemava and A.V. Afanasjev, "Hyperheavy spherical and toroidal nuclei: The role of shell structure," *Phys. Rev. C*, vol. 103, p. 034323, 2021.

[57] R.P. Schmitt et al., "A flexible 4π neutron detector for in-beam studies: the Texas A&M neutron ball," *Nucl. Instrum. Methods*, vol. 354, pp. 487, 1995.

[58] S. Aiello, "Chimera: a project of a 4π detector for heavy ion reactions studies at intermediate energy," *Nucl. Phys. A*, vol. 583, pp. 461, 1995.

[59] J. Pouthas, "INDRA, a 4π charged product detection array at GANIL," *Nucl. Instr. and Meth. A*, vol. 357, pp. 418, 1995.

[60] S. Wuenschel et al., "NIMROD-ISiS, a versatile tool for studying the isotopic degree of freedom in heavy ion collisions," *Nucl. Instr. and Meth. A*, vol. 604, pp. 578–583, 2009.

[61] B. Davin et al., "LASSA: a large area silicon strip array for isotopic identification of charged particles," *Nucl. Instr. and Meth. A*, vol. 473, pp. 302, 2001.

[62] M.S. Wallace et al., "The high resolution array (HiRA) for rare isotope beam experiments," *Nucl. Instr. and Meth. A*, vol. 583, p. 302, 2007.

[63] A. S. Goldhaber, "Volume versus surface sampling of Maxwellian distributions in nuclear reactions," *Phys. Rev. C*, vol. 17, p. 2243, 1978.

[64] W.W. Wilcke et al., "Reaction parameters for heavy-ion collisions," *At. Data Nucl. Data Tables*, vol. 25, pp. 389–619, 1980.

[65] F. Gimeno-Nogues et al., "FAUST: a new forward array detector," *Nucl. Instr. and Meth. A*, vol. 399, pp. 94, 1997.

[66] M. Parlog et al., "Response of CsI(Tl) scintillators over a large range in energy and atomic number of ions. Part II: calibration and identification in the INDRA array," *Nucl. Instr. and Meth. A*, vol. 482, pp. 693–706, 2002.

[67] 360 Foothill Road Box 6910, Bridgewater, New Jersey, "Hammamatsu Corporation." http://www.hamamatsu.com, 2020.

[68] M. Suffert, "Silicon photodiode readout of scintillators and associated electronics," *Nucl. Instr. and Meth. A*, vol. 322, pp. 523–528, 1992.

[69] W. Skulski and M. Momayezi, "Particle identification in CsI(Tl) using digital pulse shape analysis," *Nucl. Instr. and Meth. A*, vol. 458, pp. 759–771, 2001.

[70] P. Kreutz et al., "Photodiode readout and pulse shape analysis of CsI(Tl) scintillator signals," *Nucl. Instr. and Meth. A*, vol. 260, pp. 120–123, 1987.

[71] L.A. Heilborn, *Proton-proton correlation functions measured using position-sensitive FAUST*. PhD thesis, Texas A&M University, 2018.

[72] P.J. Cammarata, *Ternary breaking of the reaction system in heavy-ion collisions below the fermi energy*. PhD thesis, Texas A&M University, 2007.

[73] A.L. Keksis, *N/Z equilibration in deep inelastic collisions and the fragmentation of the resulting quasiprojectiles*. PhD thesis, Texas A&M University, 2007.

[74] Struck Innovative Systeme GmbH, "22399 Hamburg, Germany." https://www.struck.de/.

[75] mesytec GmbH & Co. KG, "Wernher-von-Braun-Straße 1, 85640 Putzbrunn, Germany." https://www.mesytec.com/.

[76] W-Ie-Ne-R Plein & Baus Corporation, "202 N Limestone St 320, Springfield, OH 45503." https://www.wiener-us.com/.

[77] L.A. McIntosh et al., "Performance of position-sensitive resistive silicon detectors in the Forward Array Using Silicon Technology (FAUST)," *Nucl. Instr. and Meth. A*, vol. 985, p. 164642, 2021.

[78] Pico Systems, "543 Lindeman Rd, Kirkwood, MO 63122." https://pico-systems.com/.

[79] H. Spieler, "Measurements, IV: Signal processing." Lecture Notes - ICFA Instrumentation School, June 2002.

[80] Advanced Measurement Technology Inc (ORTEC/AMETEK), "801 S Illinois Ave, Oak Ridge, TN 37830." https://www.ortec-online.com/.

[81] K. Hagel et al., "Zero deadtime event readout for experiments at the Cyclotron Institute," *2020-2021 Texas A&M Cyclotron Institute Progress in Research*, 2021.

[82] V. Mishra, V. D. Srivastava, and S K Kataria, "Role of guard rings in improving the performance of silicon detectors," *J. Phys.*, vol. 65, pp. 259–272, 2005.

[83] R. Loveza et al., "A novel calorimeter telescope for identification of relativistic heavy-ion reaction channels," *Nucl. Instr. and Meth. A*, vol. 562, p. 298, 2006.

[84] A. Banu et al., "Performance evaluation of position-sensitive silicon detectors with four-corner readout," *Nucl. Instr. and Meth. A*, vol. 593, pp. 399–406, 2008.

[85] M. C. Solal, "The origin of duo-lateral position-sensitive detector distortions," *Nucl. Instr. and Meth. A*, vol. 572, p. 1047, 2007.

[86] L. McInnes, J. Healy, and S. Astels, "hdbscan: Hierarchical density based clustering," *The Journal of Open Source Software*, vol. 2, no. 11, 2017.

[87] C. Norhtcliffe and R. Schilling, "Range and stopping-power tables for heavy ions," *Nucl. Data Tables*, vol. A7, pp. 233, 1970.

[88] F. Hubert, R. Bimbot, H. Gauvin, "Range and stopping-power tables for 2.5-500 MeV/nucleon heavy ions in solids," *Nucl. Data Tables*, vol. 46, pp. 1, 1990.

[89] "The stopping and range of ions in matter." `http://www.srim.org/`. accessed July 2019.

[90] L.C. Northcliffe, "Passage of heavy ions through matter," *Annu. Rev. Nucl. Sci.*, vol. 13, p. 67, 1963.

[91] U. Fano, "Penetration of protons, alpha particles, and mesons," *Annu. Rev. Nucl. Sci.*, vol. 13, p. 1, 1963.

[92] D. Gruyer et al., "Semi-automatic charge and mass identification in two-dimensional matrices," *arXiv*, vol. 1607.08529, 2016.

[93] S. Wuenschel, K. Hagel, L.W. May, R. Wada, and S.J. Yennello, "Particle identification in the NIMROD-Isis detector array," *AIP Conference Proceedings*, vol. 1099, p. 816, 2009.

[94] Y. Ashida et al., "Separation of gamma-ray and neutron events with CsI(Tl) pulse shape analysis," *Prog. Theor. Exp. Phys.*, vol. 4, p. 043H01, 2018.

[95] M. Parlog et al., "Response of CsI(Tl) scintillators over a large range in energy and atomic number of ions. Part I: recombination and δ-electrons," *Nucl. Instr. and Meth. A*, vol. 482, pp. 674–692, 2002.

[96] E.K. Warburton, "R-matrix analysis of the $\beta^{\mp}$-delayed alpha spectra from the decay of ^{8}Li and ^{8}B," *Phys. Rev. C*, vol. 33, p. 303, 1986.

[97] A. Ono et al., "Antisymmetrized version of molecular dynamics with two nucleon collisions and its application to heavy ion reactions," *Prog. Theor. Phys*, vol. 87, pp. 1185–1206, 1992.

[98] A. Ono and H. Horiushi, "Antisymmetrized molecular dynamics for heavy ion collisions," *Prog. Part. Nucl. Phys.*, vol. 53, pp. 501–581, 2004.

[99] R. Wada et al., "Entrance channel dynamics in ^{40}Ca + ^{40}Ca at 35A MeV," *Phys. Lett. B*, vol. 422, pp. 6–12, 1998.

[100] R. Wada et al., "Reaction dynamics and multifragmentation in fermi energy heavy ion reactions," *Phys. Rev. C*, vol. 69, p. 044610, 2004.

[101] R. Charity, "GEMINI: A code to simulate the decay of a compound nucleus by a series of binary decays," *Joint ICTP-IAEA advanced workshop on model codes for spallation reactions*, pp. 139–148, 2008.

[102] N. Bohr and J.A. Wheeler, "The mechanism of nuclear fission," *Phys. Rev.*, vol. 56, p. 426, 1939.

[103] L. Moretto, "Statistical emission of large fragments: A general theoretical approach," *Nucl. Phys. A*, vol. 211-230, pp. 247, 1975.

[104] M.B. Tsang et al., "Comparisons of statistical multifragmentation and evaporation models for heavy-ion collisions," *Eur. Phys. J.*, vol. A 30, pp. 129–139, 2006.

[105] K. Hagel et al., "Violent collisions and multifragment final states in the ^{40}Ca+^{40}Ca reaction at 35 MeV/nucleon," *Phys. Rev. C*, vol. 50, p. 2017, 1994.

[106] A. Hannaman et al., "Isoscaling and nuclear reaction dynamics," *Phys. Rev. C*, vol. 101, pp. 034605, 2020.

[107] Y. Larochelle et al., "Dependence of intermediate mass fragment production on the reaction mechanism in light heavy-ion collisions at intermediate energy," *Phys. Rev. C*, vol. 53, p. 823, 1996.

[108] J. Pochodzalla et al., "Two-particle correlations at small relative momenta for ^{40}Ar-induced reactions on ^{197}Au at E/A=60 MeV," *Phys. Rev. C*, vol. 35, p. 1695, 1986.

[109] A.M. Lane and R.G. Thomas, "R-matrix theory of nuclear reactions," *Phys. Mod. Phys.*, vol. 30, p. 257, 1958.

[110] A.B. McIntosh et al., "Tidal effects and the proximity decay of nuclei," *Phys. Rev. Lett.*, vol. 99, p. 132701, 2007.

[111] G. Verde, A. Chibihi, R. Ghetti, and J. Helgesson, "Correlations and characterization of emitting sources," *Eur. Phys. J.*, vol. 30, pp. 81–108, 2006.

[112] D. Drijard, H.G. Fischer, and T. Nakada, "Study of event mixing and its application to the extraction of resonance signals," *Proceedings*, vol. 225, pp. 367–377, 1984.

[113] M Barbui et al., "Searching for states analogous to the ^{12}C Hoyle state in heavier nuclei using the thick target inverse kinematics technique," *Phys. Rev. C.*, vol. 98, p. 044601, 2018.

[114] A. F. Nassirpour, "Improved event mixing for resonance yield extraction," *Proceedings*, vol. 10, p. 26, 2019.

[115] K.W. Brown et al., "Proton-decaying states in light nuclei and the first observation of ^{17}Na," *Phys. Rev. C*, vol. 95, p. 044326, 2017.

[116] R.J. Charity et al., "Invariant-mass spectroscopy of ^{18}Ne, ^{16}O, and ^{10}C excited states formed in neutron-transfer reactions," *Phys. Rev. C*, vol. 99, p. 044304, 2019.

[117] C.B. Das et al., "Statistical simultaneous multifragmentation model for heavy ion collisions with entrance channel characteristics," *Phys. Rev. C*, vol. 53, p. 1833, 1996.

[118] A.S. Botvina and D.H.E. Gross, "Sequential or simultaneous multifragmentation of nuclei?," *Phys. Lett. B*, vol. 344, pp. 6–10, 1995.

[119] H.-Y. Wu et al., "Evolution of the decay of highly excited nuclei," *Phys. Rev. C*, vol. 57, p. 3178, 1998.

[120] M. Bruno et al., "Simple observables sensitive to the transition from sequential decay to simultaneous break-up of nuclear systems," *Nuov Cim A*, vol. 105, pp. 1629–1635, 1992.

[121] J. Manfredi et al., "α decay of the excited states in ^{12}C at 7.65 and 9.64 MeV," *Phys. Rev. C.*, vol. 85, p. 037603, 2012.

[122] Tz. Kokalova, N. Itagaki, W. von Oertzen, and C. Wheldon, "Signatures for multi-α-condensed states," *Phys. Rev. Lett.*, vol. 96, p. 192502, 2006.

[123] S. Adachi et al., "Signatures for multi-α-condensed states," *Phys. Lett. B.*, vol. 819, p. 136411, 2006.

[124] A.B. McIntosh et al., "Apparent temperatures of neutron-poor and neutron-rich compound nuclei," *Phys. Rev. C*, vol. 107, p. 024612, 2023.

[125] R. Yanez et al., "Excitation and decay of projectilelike fragments formed in dissipative peripheral collisions at intermediate energies," *Phys. Rev. C*, vol. 68, p. 011602, 2003.

[126] B.K. Nandi et al., "Search for DCC in relativistic heavy-ion collision through event shape analysis," *Phys. Lett. B*, vol. 449, pp. 109–113, 1999.

[127] D.A. Cebra et al., "Event-shape analysis: sequential versus simultaneous multifragment emission," *Phys. Rev. Lett.*, vol. 64, p. 2246, 1990.

[128] A. Badala et al., "^{16}O breakup on Al, Ni and Au targets at 95 MeV/nucleon," *Phys. Lett. B*, vol. 299, pp. 11–15, 1993.

[129] L. Beaulieu et al., "Breakup of highly excited ^{35}Cl projectiles on a gold target at 30 A MeV: an exclusive analysis," *Phys. Rev. C*, vol. 580, pp. 81–99, 1994.

[130] C.P. Montoya et al., "Fragmentation of necklike structures," *Phys. Rev. Lett.*, vol. 73, p. 3070, 1994.

[131] M. Rosenblatt, "Remarks on some nonparametric estimates of a density function," *Ann. Math. Statist.*, vol. 27, pp. 832–837, 1956.

[132] P.A.M. Dirac, "The quantum theory of the emission and absorption of radiation," *Proc. R. Soc. A*, vol. 114, pp. 243–265, 1927.

APPENDIX A

IKEDA DECAY CHANNELS OF ^{28}Si AND ^{32}S

All α-conjugate-containing decay configurations in the de-excitation of ^{28}Si (Figure A.1) and ^{32}S (Figure A.2) were examined for possible high excitation energy states that could possibly originate from high-spin toroidal isomer breakup. The overall excitation energies that each channel span are reasonable given the relative Q-value and Coulomb barrier associated with each channel. There are no significant, narrow peaks observed at high excitation energy in any channel. There are enhancements of yield at low excitation energy below the main distributions for the more symmetric breakups containing larger fragments (e.g. Figure A.1 panels (d,f) and Figure A.2 panels (f,g,i)). These channels have significant Coulomb barriers that suppress yield near the Q-value; however, the yield seen here is reasonably within the expected contamination of double beam-burst events as shown in Figure 4.13, prohibiting any claims of deep sub-barrier yield. The lower overall yield of channels that include fragments of $Z \gtrsim 10$ is due to many of these fragments saturating the DADL preamplifiers as discussed in Sections 4.1.1 and 4.1.2.

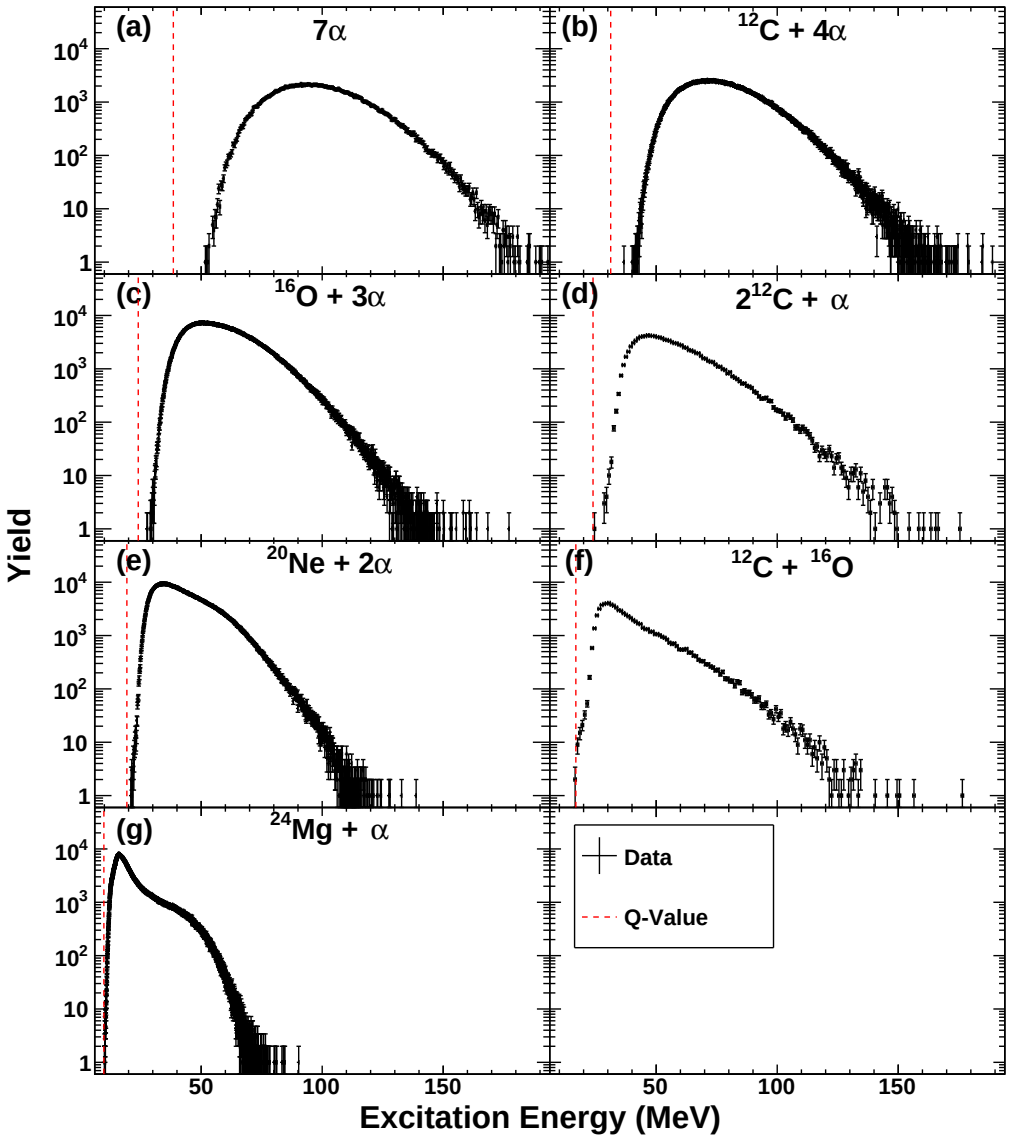

Figure A.1: Experimental excitation energy distributions for all α-conjugate decay channels of ^{28}Si in collisions of ^{28}Si + ^{12}C at 35 MeV/nucleon. The panels are ordered to have increasing Q-value (vertical dashed lines) for each channel.

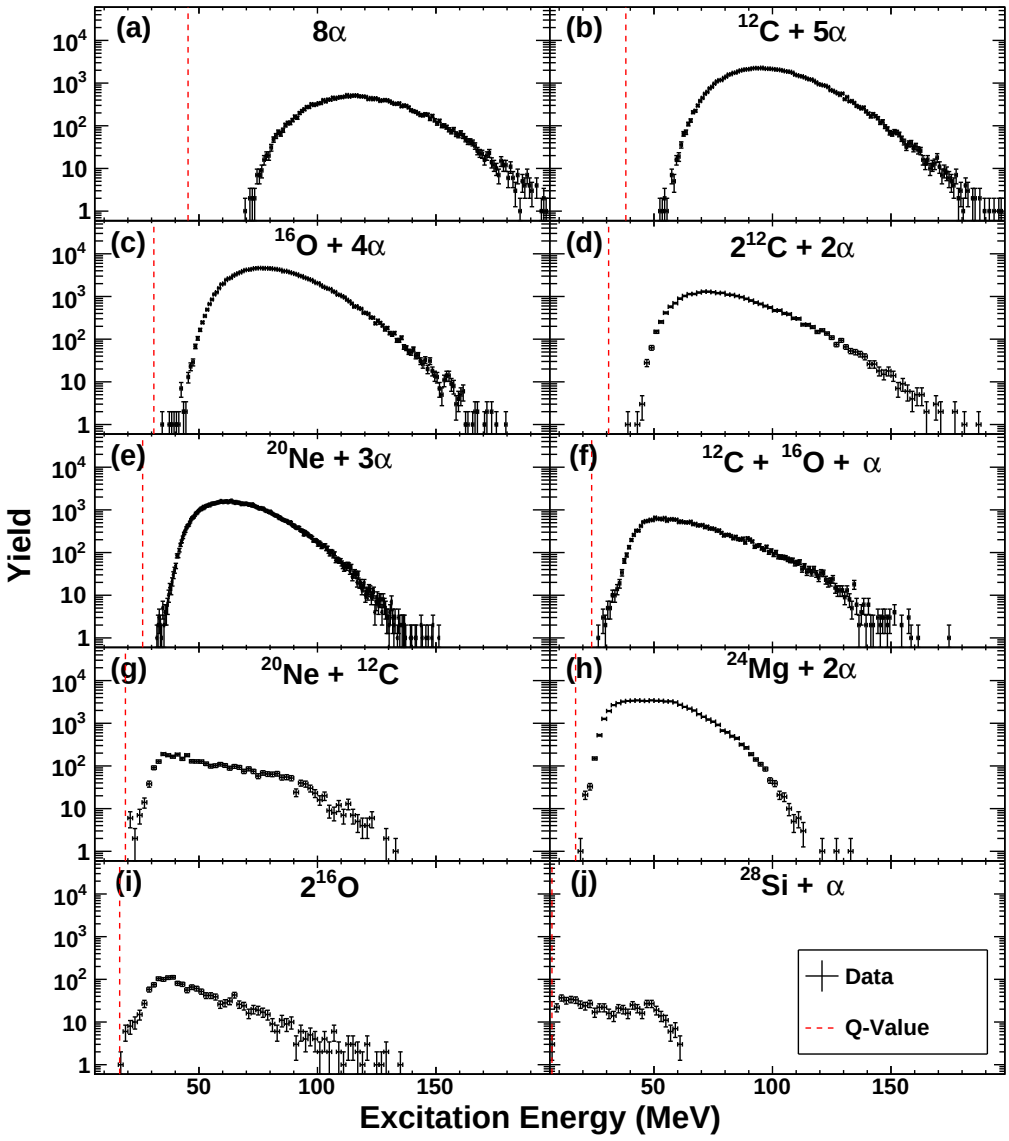

Figure A.2: Experimental excitation energy distributions for all α-conjugate decay channels of ^{32}S in collisions of ^{28}Si + ^{12}C at 35 MeV/nucleon. The panels are ordered to have increasing Q-value (vertical dashed lines) for each channel.